Large-scale and meso-scale surface heat flux patterns of Lake Geneva

THÈSE N^{O} 8650 (2018)

PRÉSENTÉE LE 16 AOÛT 2018

À LA FACULTÉ DE L'ENVIRONNEMENT NATUREL, ARCHITECTURAL ET CONSTRUIT
LABORATOIRE DE TECHNOLOGIE ÉCOLOGIQUE
PROGRAMME DOCTORAL EN GÉNIE CIVIL ET ENVIRONNEMENT

ÉCOLE POLYTECHNIQUE FÉDÉRALE DE LAUSANNE

POUR L'OBTENTION DU GRADE DE DOCTEUR ÈS SCIENCES

PAR

Abolfazl IRANI RAHAGHI

acceptée sur proposition du jury:

Prof. A. Berne, président du jury
Prof. D. A. Barry, directeur de thèse
Prof. G. Mariéthoz, rapporteur
Dr N. Le Dantec, rapporteur
Prof. J. Wüest, rapporteur

ÉCOLE POLYTECHNIQUE
FÉDÉRALE DE LAUSANNE
Suisse
2018

Acknowledgement

First and foremost, I am very grateful to my supervisor, **David Andrew Barry**, who gave me the opportunity to join and work in his group. He strongly supported me, gave me courage, taught me how to research, and initiated very interesting and deep discussions to keep me on the right track.
I also kindly thank the rest of my thesis committee, **Alfred Johny Wüest**, **Alexis Berne**, **Grégoire Mariéthoz** and **Nicolas Le Dantec** for their interest in my work.

I express my deepest and sincerest thanks to **Ulrich Lemmin** for his constructive remarks, advice, guidance and proofreading during my PhD period. I would also like to thank **Andrea Cimatoribus** and **Damien Bouffard** for many fruitful discussions and their constructive comments to improve my research. I really enjoyed collaborating with them. Many thanks to **Michael Riffler** and **Stefan Wunderle** for providing the AVHRR satellite data that their collaboration made the first half of this dissertation possible. I also wish to thank **Daniel Sage**, **Anton Ivanov** and **Stepan Tulyakov** for their help and advice on thermal image processing.

A very special thank to **Jean-Luc Liardon**, a magic microengineer, and to **Htet Kyi Wynn**, a fantastic lab technician, who made the measurement systems functional and helped me a lot during fieldwork. I would also like to thank **Philippe Paccaud**, **Beat Geissmann**, **Ludovic Zulliger**, **Jérôme Béguin**, **Pascal Klaus**, **Nawaaz Gujja Shaik**, **Samuel Benketaf**, **Karl Kangur**, **Marco Pagnamenta**, **Lukas Hostettler**, **Nicolas Bongard**, **Guillaume Ulrich**, **Bendicht Grossniklaus**, **Adrien Rosselet**, **Michael Bolay**, **Jean Rossier**, **Yannick Poffet** and **Nicolas Roussel** for their contribution to designing, testing, and improving of the measurement platforms used in this research. I would not forget the great times that we spent together on Lac Léman. Thanks to all my friends and colleagues in the Léman-Baikal project both in Switzerland and Russia, particularly **Natacha Pasche** for her effort in organization of meetings and fieldwork.

I would like to thank all my colleagues from ECOL for their support and the great time we had together, with special thanks to my office-mates with who I shared most of my days at EPFL: **Mohsen Cheraghi**, **Rafael Reiss** and **Qihao Jiang**, and to present and past members of the group (apart from those mentioned above): **Amir Razmi**, **Jonas Margot**, **Elisa Bruque Pozas**,

Setareh Nagheli, **Frédéric Soulignac** and **Benjamin Graf**. A big thanks to our lovely secretary, **Marie Sudki**, who made the administrative part very easy.

I am deeply thankful to my awesome friends in Lausanne, including **Nasser**, **Siamak**, **Shahrzad**, **Lida**, **Hossein**, **Mohsen**, **Sajjad**, **Firouzeh**, **Leila** and **Amin**, with whom I shared a lot of good memories and moments. Thanks to all my team-mates in **Persepolis de Lausanne** football club for lots of fun that we had together, and it is a shame that the club may lose an excellent striker!

Last but definitely the best, I express my warmest respects and gratitude to my lovely and sweet wife, **Mohaddeseh**, who was partly with me during this exciting but sometimes tough journey, to my parents, **Ahmad** and **Narges**, my siblings, **Fatemeh**, **Razieh** and **Amirhossein**, and especially to my uncle, **Asghar**, who were always unconditionally supportive, patient and encouraging.

Abstract

Diverse studies have confirmed the adverse impact of global climate change in lakes. In order to establish effective water quality management policies, it is essential to understand how the heat exchange between the atmosphere and the lake evolves under these conditions. Lake Surface Water Temperature (LSWT), which is the key coupling parameter at the interface of the Atmospheric Boundary Layer (ABL) and the lake surface layer is often considered the reference climate variable in this context. The temporal development of the lake heat content is mainly controlled by the net Surface Heat Flux (SurHF) at this interface. LSWT, ABL conditions and SurHF are linked and may vary in space and time. However, past studies often relied on single point measurements for SurHF estimation and this can result in significant errors in the heat budget analysis, particularly over large lakes.

In this thesis, the dynamics of SurHF over Lake Geneva, the largest water body in Western Europe, were investigated with an emphasis on the effect of spatial heterogeneity of the LSWT and meteorological parameters on two different scales. A large-scale study for the whole surface of the lake was carried out using meteorological data and satellite images with a pixel size of 1 km^2 that can depict large-scale thermal patterns, but not the meso- or small-scale processes. To address the SurHF aspects at the meso-scale level, an airborne system for resolving LSWT with a ~1 m pixel resolution was developed that allowed investigating the structure of the processes on scales within a satellite pixel.

In a multi-annual large-scale analysis, the SurHF of Lake Geneva was estimated for a 7-y period (2008 to 2014). Data sources included hourly maps of over-the-lake reanalysis meteorological data from a numerical weather model, LSWT from satellite imagery, and long-term temperature depth profiles at two locations. The most common formulas for different heat flux components were combined and calibrated at two locations based on the heat content balance in the water column. When optimized for one lake temperature profile location, SurHF models failed to predict the temperature profile at the other location due to the spatial variability of meteorological parameters. Consequently, a procedure for calibrating the optimal SurHF models was developed using two profile locations. The combination of the modified parameterization of the Brutsaert equation for incoming atmospheric radiation and of similarity theory bulk parameterization algorithms for turbulent SurHF provided the most accurate SurHF estimates. It was found that if a calibration was not carried out optimally, the calculated change in heat content could be much higher than the observed annual climate change-induced trend. The developed calibration procedure improved parameterization of bulk transfer coefficients, mainly under low wind regimes.

The optimized and calibrated set of bulk models was then used to compute the spatiotemporal SurHF. Model results indicated an average spatial range of > ± 20 Wm^{-2}. This was mainly caused by wind-sheltering over parts of the lake, which produced spatial anomalies in sensible and latent heat fluxes. During spring, much less spatial variability was evident compared to other seasons. The spring variability was caused by air-water temperature differences and, to a

lesser extent, global radiation variability, again due to sheltering by the surrounding topography. Analysis of the ABL showed statistically unstable conditions during the whole year except from March to early June and also that this regime change could explain the low SurHF spatial anomalies obtained during spring. In addition, investigation of lake heat content variations induced by SurHF indicated a cooling period from 2008 to 2012, with an onset of warming in 2013. This trend is consistent with the recorded long-term heat content variation of Lake Geneva, and other worldwide observations. The results emphasized that spatial variability in the meteorological and the LSWT patterns, and consequently the spatiotemporal SurHF data, should be taken into consideration when assessing the time evolution of the heat budget of large water bodies.

To resolve LSWT at meso-scales, a measurement platform for aerial thermography of inland water bodies was developed. It consists of a tethered Balloon Launched Imaging and Monitoring Platform (BLIMP), equipped with an uncooled InfraRed (IR) camera that records the LSWT, and an autonomous catamaran (called ZiviCat) that simultaneously measures in situ surface/near surface temperatures. Correcting the spatial and temporal noise of the IR camera (nonuniformity and shutter-based drift, respectively) was found to be vital prior to image registration. A feature matching-based algorithm, combining blob and region detectors, was implemented to create composite thermal images. The results indicate that a high overlapping field of view is essential for image fusion and noise reduction over such low-contrast scenes. Finally, by using the in situ temperatures for radiometric calibration, meso-scale LSWT maps were generated that revealed spatial LSWT variability with unprecedented detail.

The meso-scale patterns, based on four selected daytime (afternoon) LSWT maps resolving a sub-pixel satellite area of less than 1 km^2, indicated various cold-warm patches and streak-like structures over the lake with a LSWT contrast of > 2°C during spring and > 3.5°C during summer. The cold season data did not show significant meso-scale spatial LSWT heterogeneity, and hence SurHF variability. For representative spring and summer cases, the corresponding SurHF contrasts were found to be > 20 Wm^{-2} and > 40 Wm^{-2}, respectively. Implementing a spatial mean filter, the effect of LSWT spatial heterogeneity on the SurHF estimation of the satellite pixelwise results was studied. Increasing the averaging filter size reduced the standard deviation of the SurHF patterns, but did not show a major effect on the median values of the distributions. However, the spatial mean value of SurHF during the summer field campaign, where the ABL was very stable, showed a reduction of ~3.5 Wm^{-2} from high, O(1 m) to low O(1 km) pixel resolution. Investigating the effect of errors in the meteorological condition sampling revealed that higher wind speed, and lower air temperature and relative humidity result in higher surface cooling and SurHF spatial contrast. It was also found that increasing air temperature, and consequently shifting from unstable to very stable ABL conditions, tend to alter the SurHF distribution from negatively skewed to positively skewed, and hence affect the mean SurHF estimates. This was mainly attributed to the substantial variation of latent heat flux under near-neutral ABL conditions.

This thesis provides new concepts and insight for improving the heat budget analysis of inland water bodies. It highlights the challenges of SurHF model parameterization and calibration, and

estimates the effect of SurHF spatial variability on the total heat content evolution of a large lake, in particular under the threat of climate change. A measurement platform and an image processing procedure for the airborne thermography of lakes is proposed, and the effect of meso-scale LSWT heterogeneity on the estimation of SurHF is evaluated, since it is considered to be an important physical process in limnology.

Keywords: Surface heat flux, lake surface water temperature, meteorological forcing, Lake Geneva, meso-scale thermal pattern, thermal imagery, remote sensing, model calibration, heat content.

Zusammenfassung

Der Einfluss des globalen Klimawandels und dessen mögliche Folgen auf die Langzeitdynamik von Seen ist in der Literatur klar dokumentiert. Vielfach wird dabei die See-Oberflächentemperatur (SOT) als der beste Indikator für diese Entwicklung herangenommen, weil die SOT ein Schlüsselparameter für die Kopplung zwischen der atmosphärischen Grenzschicht (AGS) und der Seeoberfläche ist. Die zeitliche Entwicklung des thermischen Zustandes von Seen, d.h. ihr Wärmeinhalt, wird hauptsächlich durch den Netto-Oberflächenwärmestrom (OWS) an dieser Grenzfläche bestimmt. SOT, AGS-Bedingungen und OWS hängen miteinander zusammen und können sowohl räumlich als auch zeitlich variieren. Dennoch wurden in der Vergangenheit zur der Berechnung des OWS vielfach Daten eines einzigen Messpunktes im See verwendet, was insbesondere bei großen Seen zu Fehlern in der Wärmebilanz führen kann.

Die vorliegende Arbeit befasst sich mit der Dynamik des OWS über Westeuropas größtem Binnengewässer, dem Genfer See. Der Schwerpunkt liegt dabei auf der Beurteilung der Bedeutung der räumlichen Heterogenität von OWS und den meteorologischen Parametern auf zwei verschiedenen Skalen. Zunächst werden die großskaligen Prozesse, die die gesamte Oberfläche des Sees einbeziehen, mit Hilfe von Satellitendaten, die eine räumlich Auflösung von etwa 1 km^2 haben, untersucht. Satelliten-Daten können zwar großskalige thermische Muster erfassen, nicht aber meso- oder kleinskalige Prozesse. Um die Dynamik des OWS im Mesoskalenbereich zu studieren, wurde ein Ballon-gestütztes Thermographie System und ein Bildverarbei-tungskonzept mit einer Auflösung von ~1m entwickelt, das die Auflösung und somit Verifizierung von Satellitendaten im Subpixelbereich ermöglicht.

In der Großskalen-Analyse wurde der OWS des Genfer Sees für eine Siebenjahresperiode (2008-2014) abgeschätzt. Als Datengrundlage dienten unter anderem stündliche, aufgearbeitete meteorologische Daten eines numerischen Wettermodells, SOT-Daten basierend auf Satellitenbildern sowie Langzeit-Wasser Temperaturprofile an zwei Stellen im See.

Zunächst wurden die zwei gängigsten Ansätze zur Berechnung der einzelnen Komponenten des Wärmestroms kombiniert und anhand einer Wärmeinhalts-Bilanz an zwei Stellen kalibriert. Wurden die OWS-Modelle lediglich für eine Stelle optimiert, waren sie nicht in der Lage das Temperaturprofil an der anderen Stelle vorherzusagen. Dies ist auf die räumliche Variabilität der meteorologischen Parameter zurückzuführen. Folglich wurde ein Verfahren entwickelt mit dessen Hilfe die OWS-Modelle anhand von Profilen an zwei Stellen im See kalibriert wurden. Eine Kombination aus einer modifizierten Parametrisierung der Brutsaert Gleichung für die atmosphärische Strahlung mit, auf der Ähnlichkeitstheorie basierenden Bulk-Parametrisierungen für den turbulenten OWS lieferten die genausten Schätzungen des OWS. Es konnte gezeigt werden, dass eine Vernachlässigung der zwei Punkt Kalibrierung Unterschiede im berechneten Wärmeinhalt zur Folge haben kann, welche wesentlich grösser sind als der jährlich beobachtete, durch den Klimawandel verursachte Trend. Die Kalibrierung

verbesserte die Parametrisierung der Bulk-Transferkoeffizienten hauptsächlich unter windarmen Bedingungen.

Im nächsten Schritt wurde mithilfe der optimierten und kalibrierten Bulk-Modelle der räumlich-zeitliche OWS berechnet. Die mittlere räumliche Variabilität lag dabei im Bereich von 20 W/m². Dies ist in erster Linie darauf zurückzuführen, dass einige Teile des Sees windgeschützt sind, was zu räumlichen Unterschieden der fühlbaren und latenten Wärmeströme führt. Im Frühling war eine erheblich geringere räumliche Variabilität zu erkennen im Vergleich zu den übrigen Jahreszeiten. Die Variabilität im Frühling wurde in erste Linie durch Temperaturunterschiede zwischen Wasseroberfläche und Atmosphäre und in geringerem Masse durch topographiebedinge Unterschiede in der Globalstrahlung verursacht. Basierend auf einer Analyse der AGS herrschten, mit Ausnahme von März bis Anfang Juni, ganzjährig statistisch instabile AGS Bedingungen. Dieser Wechsel von instabilen zu stabilen atmosphärischen Bedingungen erklärt die geringe räumliche Variabilität des OWS im Frühling. Einer Analyse der OWS bedingten Änderungen des Wärmeinhalts zufolge, gab es zwischen 2008 und 2012 eine Abkühlungsperiode, wohingegen das Jahr 2013 den Beginn einer Erwärmungsperiode markiert. Dieser Trend spiegelt sich auch in den Langzeit-Schwankungen des, auf den zuvor erwähnten zwei Punkt-Messungen basierenden, Wärmeinhalts des Genfer Sees sowie in anderen weltweiten Beobachtungen wider. Die hier vorgestellten Ergebnisse verdeutlichen, daß räumliche Unterschiede in meteorologischen Bedingungen und der See-Oberflächentemperatur, und folglich räumlich-zeitlich variable OWS-Daten, bei der Bestimmung der zeitlichen Entwicklung der Wärmebilanz von großen Seen berücksichtig werden sollten.

Um die SOT Dynamik im Mesoskalenbereich aufzulösen, wurde ein Messsystem für Ballon gestützte Thermographie von Binnengewässern entwickelt. Das System besteht aus einer Ballon-gebundenen Plattform (Balloon Launched Imaging and Monitoring Platform - BLIMP), ausgestattet mit einer ungekühlten Infrarot (IR) Kamera zur Aufzeichnung der SOT, sowie einem autonomen Katamaran (ZiviCat), welcher gleichzeitig in-situ Messungen von Oberflächenwasser- und Lufttemperatur durchführt. Eine Korrektur des räumlich-zeitlichen Rauschens der IR-Kamera vor der Bildregistrierung hat sich als unverzichtbar erwiesen. Ein auf Feature-Matching basierender Algorithmus, welcher Blob- und Regions-Erkennung kombiniert, wurde implementiert um zusammenhängende thermische Bildfolgen zu generieren. Aus den Untersuchungen lässt sich schließen, daß zur Bildfusion und Rauschreduktion solch kontrastarmer Szenen wie man sie an der Seeoberfläche findet, eine hohe Überlappung der Bildfelder notwendig ist. Unter Verwendung der gemessenen in-situ Temperaturen zur Kalibrierung des Radiometers, wurden mesoskalen SOT-Karten erstellt, welche eine räumliche Variabilität der SOT in einem bisher nicht dagewesenem Detailgrad erkennen lassen.

Basierend auf SOT-Karten, welche an vier ausgewählten Nachmittagen aufgenommen wurden und den Subpixelbereich von Satelliten auflösen (< 1 km²), konnten verschiedene kalt-warm Bereiche und schlierenartige Strukturen mit einem SOT Unterschied von > 2°C im Frühlings und > 4°C im Sommers identifiziert werden. Während der kalten Jahreszeit konnte keine

signifikante räumliche SOT-Heterogenität und somit OWS-Variabilität festgestellt werden. Die OWS-Unterschiede waren typischerweise im Frühling > 20 Wm^{-2}, während des Sommers > 40 Wm^{-2}. Mithilfe eines räumlichen Mittelungsfilters wurde der Effekt einer räumlichen OWS-Heterogenität auf die OWS-Abschätzung basierend auf pixelweisen Satellitendaten untersucht. Eine Vergrößerung des Mittelungsbereichs führte zu einer Reduktion der Standardabweichung von OWS-Mustern, hatte aber keinen erheblichen Einfluss auf die Medianwerte der Verteilungen. Der räumliche Mittelwert des OWS während der Sommermessreihe, mit einer sehr stabilen AGS, wies hingegen eine Reduktion von ca. 3 Wm^{-2} zwischen einer hohen (d.h. O(1 m)) und einer niedrigen (d.h. O(1 km)) Pixelauflösung auf. Eine Untersuchung des Effekts von Fehlern bei der Messung der meteorologischen Bedingungen zeigte, dass höhere Windgeschwindigkeiten sowie eine niedrigere Lufttemperatur und relative Luftfeuchtigkeit sowohl zu einer höheren Oberflächenkühlung als auch zu größeren räumlichen Kontrasten im OWS führen. Des Weiteren konnte gezeigt werden, daß eine zunehmende Lufttemperatur und der damit einhergehende Wechsel von einer instabilen zu einer sehr stabilen AGS, dazu neigt, die OWS-Verteilung von einer linksschiefen zu einer rechtsschiefen Verteilung zu verschieben. Somit beeinflusst eine Änderung der Lufttemperatur ebenfalls den Mittelwert des OWS, was in erster Linie darauf zurückzuführen ist, dass sich die Richtung des fühlbaren Wärmestroms von Abkühlung zu Aufwärmung ändert.

Diese Doktorarbeit hat neue Konzepte und Perspektiven für die Analyse der Wärmebilanz von Binnengewässern aufgezeigt und dabei die Herausforderungen bei der Parametrisierung und Kalibrierung von OWS-Modellen hervorgehoben. Der Einfluß einer räumlichen Variabilität der SOT auf die Entwicklung des gesamten Wärmeinhalts von großen Seen wurde untersucht und dessen signifikante Bedeutung im Genfer See nachgewiesen. Abschließend wurde eine Messplattform und ein Bildverarbeitungs-konzept zur Ballon gestützten Thermographie von Seen vorgestellt sowie der Effekt der Heterogenität der SOT im Mesoskalenbereich auf die Abschätzung des OWS abgeschätzt.

Stichwörter: Oberflächenwärmestrom, See-Oberflächentemperatur, meteorologische Bedingungen, Genfer See, mesoskale thermische Muster, Wärmebildkamera, Fernerkundung, Modell-Kalibrierung, Wärmeinhalt.

Table of contents

Acknowledgement ..... **I**
Abstract ..... **IV**
Zusammenfassung ..... **VII**
Table of contents ..... **X**
1. Introduction **1**
1.1. Lake surface water temperature and surface heat flux 2
1.1.1. Response to climate change: Worldwide spatial heterogeneity 2
1.1.2. Measurement and estimation methodologies 3
1.2. Study site: Lake Geneva 5
1.2.1. General overview 5
1.2.2. Surface water temperature and heat content variability 6
1.3. Research objectives and approaches 9
References 12
2. Improving surface heat flux estimation of a large lake through model optimization and 2-point calibration: The case of Lake Geneva **17**
2.1. Introduction 19
2.2. Materials and procedures 20
2.2.1. Study site 20
2.2.2. Energy balance in a water column 21
2.2.3. Water temperature profiles 23
2.2.4. Satellite data 23
2.2.5. Meteorological data 24
2.2.6. Model calibration procedure 25
2.3. Assessment and results 28
2.3.1. Model calibration and assessment 28
2.3.1.1. Calibrated versus uncalibrated net surface heat flux models 28
2.3.1.2. Two-point versus one-point calibration 30
2.3.1.3. Intercomparison of lake heat content variation 31
2.3.1.4. Intercomparison of net surface heat flux 33
2.3.2. Surface heat flux estimation 34
2.4. Discussion 36
2.4.1. Bulk transfer coefficients 36

2.4.2. Sensitivity of the calibration factors 39
2.5. Comments and recommendations 41
References 43
Supplemental Information for Chapter 2 49
3. Multi-annual surface heat flux dynamics over Lake Geneva: The importance of spatial variability 69
3.1. Introduction 71
3.2. Materials and methods 72
3.2.1. Study site 72
3.2.2. Meteorological data 73
3.2.3. Lake surface water temperature (satellite data) 74
3.2.4. Spatiotemporal variation of meteorological data and LSWT 74
3.2.5. Bulk modeling of surface heat fluxes 78
3.3. Results 78
3.3.1. Mean annual spatiotemporal variability of surface heat flux 78
3.3.2. Spatial variability of surface heat flux components 80
3.3.3. Statistical analysis of the spatial heat flux variability 83
3.4. Discussion 85
3.4.1. Effects of spatial variability of meteorological forcing on SurHF 85
3.4.2. Atmospheric boundary layer stability 87
3.4.3. Spatial clustering using the k-means method 91
3.4.4. Lake surface thermal energy (heat content) variability 93
3.5. Conclusions 96
References 98
Supplemental Information for Chapter 3 103
4. LSWT imagery: Aerial remote sensing and image registration 110
4.1. Introduction 112
4.2. Materials and methods 114
4.2.1. Study site 114
4.2.2. Measurement platforms 115
4.2.3. Image enhancement, registration and calibration procedure 118
4.3. Results and discussion 126
4.4. Summary and conclusions 131
References 133

Supplemental Materials for Chapter 4 ..... **137**

5. Meso-scale surface water temperature heterogeneity effect on the surface cooling estimates of a large lake: Airborne remote sensing results from Lake Geneva **140**

5.1. Introduction 142

5.2. Materials and methods 143

5.2.1. Lake surface cooling formulas 143

5.2.2. Data set and study site 145

5.3. Results and discussion 148

5.3.1. Spatial heterogeneity of LSWT at meso-scales 148

5.3.2. Meso-scale surface cooling patterns and distributions 150

5.3.3. Effect of area-averaged surface water temperatures on the surface cooling estimates 155

5.3.4. Effect of biases in the meteorological parameters on the surface cooling spatial distribution 158

5.3.5. Effect of turbulent heat flux parameterization on the surface cooling spatial distribution 159

5.4. Summary and conclusions 161

References 163

Supplemental Information for Chapter 5 ..... **166**

6. Conclusions and perspectives **168**

6.1. Summary and conclusions 169

6.1.1. Large-scale investigation 169

6.1.2. Meso-scale investigation 170

6.2. Future work 171

References 173

Appendix A: Temporal variation of lake surface heat flux and heat content **175**

Curriculum Vitae **183**

Chapter 1

Introduction

1.1. Lake surface water temperature and surface heat flux

1.1.1. Response to climate change: Worldwide spatial heterogeneity

Lakes, as an essential part of the water cycle, play a vital role in supplying domestic water as well as in agricultural and industrial applications. Therefore, monitoring and investigation of their physical, chemical and biological states, both in short-term and long-term, are crucial for water resource management (Carpenter et al. 2011). The on-going global and regional impacts of climate change on the water cycle underscore the need for the relevant data acquisition and analysis schemes to monitor and characterize the lake water status. In a global-scale, development of some networks to measure the environmental data around the world, and share them among the research communities have been growing in the last decade. In this context, the Global Lake Ecological Observatory Network (GLEON, last accessed 5 March 2018) is motivated by researchers having the goal to share and interpret the "high resolution sensor data to understand, predict and communicate the role and response of lakes in a changing global environment" (Hanson et al. 2018), and has led to some publications in the physical limnology (e.g., O'Reilly et al. 2015; Sharma et al. 2015; Woolway et al. 2017).

Lake Surface Water Temperature (LSWT), which is the key coupling parameter at the interface of the Atmospheric Boundary Layer (ABL) and the lake surface layer, has been listed as an essential climate variable (Adrian et al. 2009; Arvola et al. 2010). A worldwide study by O'Reilly et al. (2015) indicated a mean warming rate of 0.34 °C decade^{-1} for summer LSWT between 1985 to 2009 by investigating more than 200 lakes around the globe. However, a high level of spatial heterogeneity in warming rates (or cooling rates in some cases) was found. They attributed this to the diversity of airside climate variables (Eastman and Warren 2013; Ji et al. 2014), and of morphometric properties of the lakes that may influence the efficiency of the heat transfer (Toffolon et al. 2014), and hence the LSWT warming rate. The lake thermal status, i.e., lake heat content, depends on the net Surface Heat Flux (SurHF), thermal energy variation by inflows and geothermal heat flux. In lakes with a large surface area, SurHF, when integrated over time, is the dominant factor controlling lake temperatures (Henderson-Sellers 1986; Van Emmerik et al. 2013; Fink et al. 2014). In addition, on the airside, climate change affects air temperature, wind speed, relative humidity and cloud cover, which directly impact SurHF (Adrian et al. 2009). The LSWT, SurHF and ABL conditions, which are coupled (Woolway et al. 2015; Tozuka et al. 2017), not only reflect the response of a water body to climate change (Woolway and Merchant 2017), they also indirectly affect gas exchange and other chemical

and biological reactions at the air-water interface (Garbe et al. 2004; Cole et al. 2010; Bonvin et al. 2013).

These parameters, i.e., LSWT, SurHF and ABL conditions, are likely to vary between lakes (as discussed above), and also be spatially heterogeneous within large lakes (discussed in section 1.1.2.). To ascertain their spatial and temporal variability, accurate data gathered at appropriate intervals as well as properly calibrated formulas are essential.

1.1.2. Measurement and estimation methodologies

The LSWT data include in situ measurements and remote sensing. Depending on the measurement depth, surface water temperature is commonly classified as skin (less than a millimeter) or bulk (more than a few centimeters) temperature, while the former is usually < 0.5 °C colder than the latter (Fairall et al. 1996; Minnett et al. 2011; Wilson et al. 2013). For the in situ data, an in-air radiometer or an in-water thermistor is usually used to measure the skin (Wilson et al. 2013) or bulk (e.g., Gillet and Quetin 2006; Van Emmerik et al. 2013) LSWT, respectively. In a novel approach, the long-term variation of LSWT at a point can also be estimated from the air temperatures by using a simple lumped model (Piccolroaz et al. 2013). This approach requires tuning of a SurHF model for individual lakes (Toffolon et al. 2014). Using multiple points in large lakes, the tuning may also be spatially variable (Piccolroaz et al. 2018).

Spaceborne satellite thermal images are frequently employed to resolve the large-scale thermal patterns (e.g., Schwab et al. 1992; Sima et al. 2013; Riffler et al. 2015). These data reveal a remarkable (compared to the global warming rate) LSWT spatial variability over large lakes. For instance, an average LSWT spatial contrast of > 3 °C and > 4 °C was reported for Lake Garda (Italy) (Pareeth et al. 2016) and Lake Superior (USA/Canada) (Xue et al. 2015), respectively, using the summertime satellite images. However, the satellite data cannot depict meso- or small-scale processes. Hereinafter, by large-scale, meso-scale and small-scale patterns we mean horizontal structures with O(>100 m), O(1-100 m) and O(<1 m) dimensions, respectively (this is different from the definition in oceanography). Satellite data are usually validated against point measurements, considered to be representative for a sizeable surface area (typical pixel size ~1 km^2). Airborne thermography using an infrared camera, which has received little attention, allows one to spatially resolve meso-scale surface water patterns (Ferri

et al. 2000; Castro et al. 2017). Such data are also valuable for quantification of the uncertainty associated with the satellite-based thermal investigation of a water body. A large-scale analysis using satellite date is discussed in chapter 3, while chapters 4 and 5 describe an airborne platform and the obtained meso-scale data for the study site (see section 1.2.).

SurHF depends on incoming and outgoing radiation (incoming solar shortwave and infrared from the sky, outgoing radiation from the water), latent (evaporative) and sensible (convective) heat fluxes, and precipitation. The effect of precipitation on the SurHF of European lakes is neglected due to its minimal influence on SurHF (Livingstone and Imboden 1989; Rimmer et al. 2009; Fink et al. 2014). SurHF is commonly determined based on (i) direct measurement using the eddy covariance technique and a net radiometer, or (ii) employing bulk formulas that requires LSWT and meteorological data. While the former is usually performed at a single location (e.g., Laird and Kristovich 2002; Assouline et al. 2008; Rouse et al. 2008; Blanken et al. 2011; Nordbo et al. 2011; Van Emmerik et al. 2013; Zhang and Liu 2014; Li et al. 2015), the latter can be done at a single point (e.g., Schertzer 1978; Henderson-Sellers 1986; Lenters et al. 2005; Woolway et al. 2015), at multiple points (e.g., Rimmer et al. 2009; Verburg and Antenucci 2010; Spence et al. 2011), or over the entire water body (e.g., Schneider and Mauser 1991; Lofgren and Zhu 2000; Phillips et al. 2016; Moukomla and Blanken 2017), depending on the availability of LSWT and meteorological data. The reported results from large lakes emphasize that the spatial variability of SurHF, principally due to LSWT heterogeneity and variable meteorological conditions, can be important, and potentially can influence long-term climate studies. For example, the monthly spatial standard deviation of SurHF over Lake Huron (USA/Canada) was estimated to vary between 7 to 21 Wm^{-2} for summertime (Lofgren and Zhu 2000). The reported spatial variability of SurHF in large lakes is mainly due to turbulent SurHF heterogeneity. A comprehensive multi-annual study on the spatiotemporal variation of SurHF over a large lake, and the critical factors underlying such variability is given in chapter 3.

The thermal behavior of a water body can also be obtained by numerical simulation. It can be done using a one-dimensional (1D) (e.g., Tanentzap et al. 2007; Momii and Ito 2008; Austin and Allen 2011; Stepanenko et al. 2014; Thiery et al. 2014a; Thiery et al. 2014b; Yang et al. 2017), or three-dimensional (3D) (e.g., Bai et al. 2013; Beletsky et al. 2013; Wahl and Peeters 2014; Xue et al. 2015) hydrodynamic modeling. In numerical modeling, an error in the temperature of the near-surface layer is attenuated with time (about one month for 1°C

temperature deviation in the near-surface layer), a behavior that is attributed to "self-restoration". This behavior can lead to deviations from the observed surface thermal patterns (Xue et al. 2015). In a recent study, Dommenget and Rezny (2018) reported that the flux correction (as the surface boundary condition) could result in better simulated climate responses than the numerical model tuning. In this context, reliable spatiotemporal patterns of SurHF are preferred (and required) for the lake thermal modeling.

As discussed before, bulk formulas are usually employed to calculate SurHF. There are various formulations in the literature for the radiative, evaporative and convective SurHF terms (Brutsaert 1975; Henderson-Sellers 1986; Brunke et al. 2002; Brodeau et al. 2017). These formulas are based on different concepts and require specific parameters. Ideally, these parameters are known for a given set of conditions (e.g., a lake), but, in practice, they should be calibrated. Furthermore, their possible combinations give rise to numerous net SurHF models. The functionality of such models over a water body, particularly for long-term analysis, needs to be investigated. This is discussed in details in chapter 1.

1.2. Study site: Lake Geneva

1.2.1. General overview

This dissertation is focused on the LSWT and SurHF spatial variation, using Lake Geneva (Local name: *Lac Léman*) as an outdoor "laboratory". It is the largest lake in Western Europe which plays a vital role in providing drinking water, and supporting tourism, fishery and transportation for the surrounding area. Located between Switzerland and France, Lake Geneva is a deep, crescent-shaped perialpine lake with a mean surface altitude of 372 m. It is approximately 70-km long, with a maximum width of 14 km, a surface area of 582 km² and a volume of 89 km³. The mean residence time of the lake is ~11.3 y (The "*Commision Internationale de la Protection des Eaux du Leman*"; CIPEL, last accessed 1 February 2018). Lake Geneva is composed of two basins: an eastern, large basin called the *Grand Lac*, with a maximum depth of 309 m, and a western, small, narrow basin called the *Petit Lac*, with a maximum depth of approximately 70 m (Fig. 1.1). The high solar radiation in spring and summer results in a thermally stratified profile in the lake. During winter, the thermocline deepens, but usually does not disappear.

The surrounding topography has a major influence on the wind-induced pattern over large lakes (e.g., Lemmin and D'Adamo 1996; Rueda et al. 2005; Valerio et al. 2017). The lake is

surrounded by the Jura Mountains in the northwest, and by the Alps in the south and, to a lesser extent, the northeast (Fig. 1.1). This topography creates a "corridor" through which two strong dominant winds pass over most of the lake surface, namely the *Bise*, coming from the northeast, and the *Vent*, from the southwest (Fig. 1). Wind speeds are generally weak and barely exceed 5 ms^{-1}. However, Lemmin and D'Adamo (1996) showed that on average, the western part of the *Grand Lac* and most of the *Petit Lac* experience higher wind speeds than the eastern part of the *Grand Lac* due to topographic sheltering. In addition, due to topographic sheltering, a small region on the eastern end of the lake experiences minimal average wind speeds throughout the year. Another consequence is the occurrence of lower near-shore wind speeds, particularly along the southern shore. The time variation of spatial anomalies of wind patterns, along with other parameters, over Lake Geneva are presented in chapter 3.

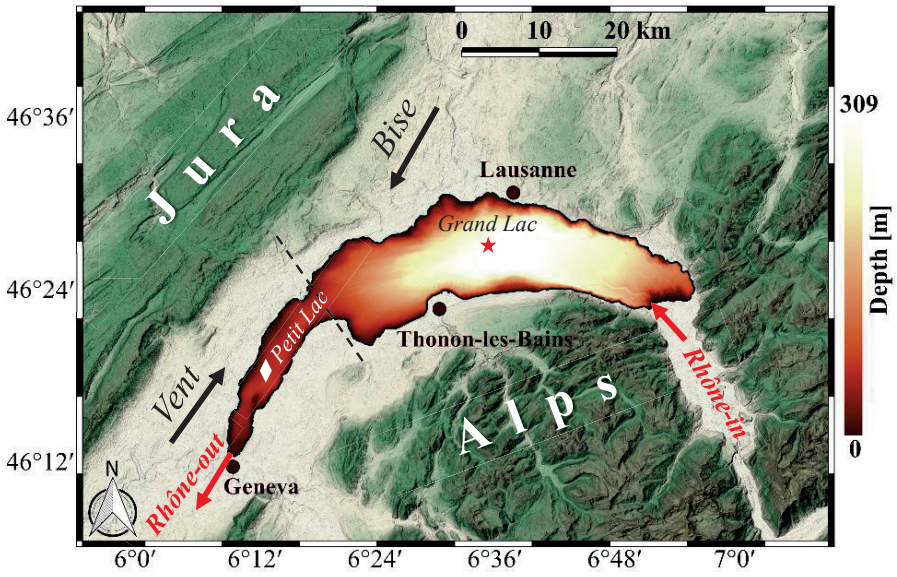

Fig. 1.1. Location and bathymetry (see the legend in the right part) of Lake Geneva, adapted from a public domain satellite image (NASA World Wind, last accessed 1 February 2018) and bathymetry data (SwissTopo, last accessed 1 February 2018). SHL2 (red star, 46.45° N, 6.59° E) and GE3 (white diamond, 46.3° N, 6.22° E) are two historical monitoring points in the lake. Arrows labeled *Bise* and *Vent* indicate the direction of the strongest winds that pass over the lake. *Rhône-in* and *Rhône-out* show the lake's main river inflow and outflow locations, respectively.

1.2.2. **Surface water temperature and heat content variability**

CIPEL (last accessed 1 February 2018) has measured Conductivity-Temperature-Depth (CTD) profiles regularly since 1957 at locations SHL2 (309 m depth) and GE3 (70 m depth) in the *Grand Lac* and *Petit Lac* (Fig. 1.1.), respectively, at a frequency of 1 to 2 profiles per month.

These data were used in some studies for numerical model tuning and validation, out of which the multi-annual thermal response of the lake to climate change was investigated using 1D models (Perroud et al. 2009; Perroud and Goyette 2010; Goyette and Perroud 2012). Although the overall trends seem reasonable, the temperature profiles at the mid and deep parts were not captured very well. Their results show a temperature increase of 2.32-3.8 °C and 2.2-2.33 °C over a13-decade period in monthly epilimnic and hypolimnic temperatures, respectively.

Some near-shore measured data were also employed to study the thermal behavior of Lake Geneva. A warming rate of ~0.065 °Cyr^{-1} was reported for the near-surface water temperature of Lake Geneva using a 28-y daily recorded data at 2 m on the south bank of the lake (Gillet and Quetin 2006). The effect of small-scale turbulence on over-lake water vapor, and hence heat flux and vertical energy balance of Lake Geneva were reported (Vercauteren et al. 2008; 2009; Vercauteren et al. 2011). The measurements used collected on Aug-Oct 2006, 100 m from the northern shore close to Buchillon, in a 3-m deep section of the lake. They obtained the sensible and latent heat fluxes using the eddy covariance method. A method was then proposed to estimate wet surface evaporation. This required estimation of sensible heat flux and air temperature, humidity and wind speed values at one level only.

The focus of this dissertation is on thermal patterns of Lake Geneva. Since the near-shore data may be affected by coastal mixing, they are not suitable for the selected heat balance methodology (see chapter 2). Therefore, the temperature profiles at SHL2 and GE3 locations are used to calibrate the SurHF models. The concept of water column heat content (G_o, [Jm^{-2}]) is used in this study:

$$G_o(t) = \int_0^H \rho_w C_{p,w} T(z,t)\, dz \tag{1.1}$$

where ρ_w and $C_{p,w}$ are the density [kgm^{-3}] and the specific heat capacity of water at constant pressure [Jkg^{-1}°C^{-1}], respectively, and $T(z,t)$ represents vertical temperature profile [°C] at time t down to water column depth $z = H$ [m]. Based on this, the heat content difference between SHL2 and GE3 for a 35-y period (1970 to 2014) was calculated and plotted in Fig. 1.2. The results illustrate that the heat content variation may include positive and negative rates, which can be an indicator of the temporal variation of the climate patterns over Lake Geneva. It also demonstrates that the observed warming of the lake is usually damped by a cooling period, although the overall trend shows a net warming (dashed line in Fig. 1.2). This analysis suggests

that a multi-annual study is needed for SurHF model calibration and heat budget investigation of the lake.

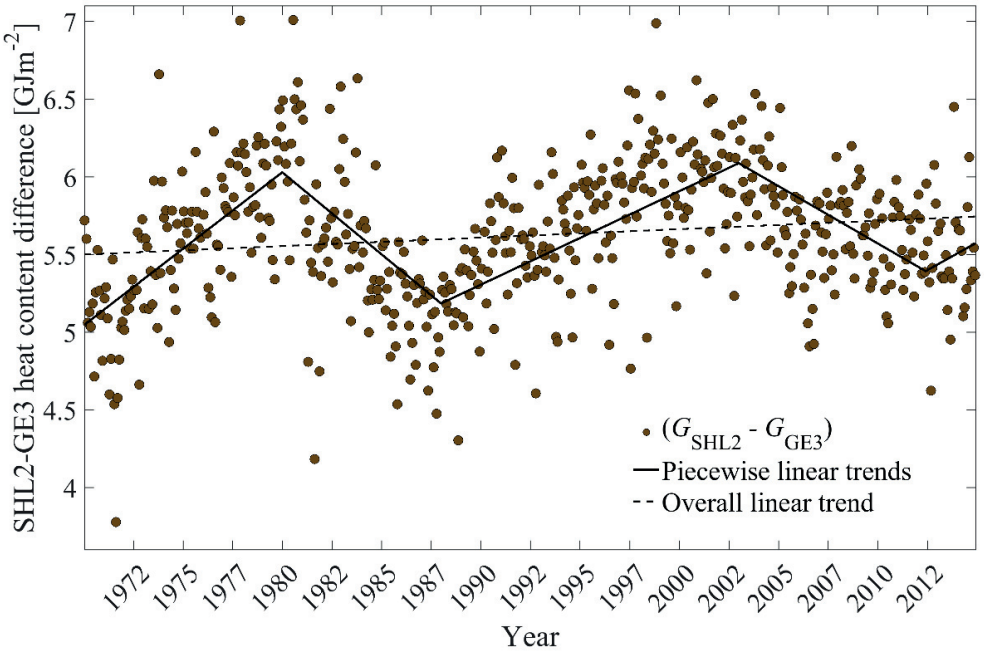

Fig. 1.2. Temporal evolution of heat content difference between SHL2 and GE3 estimated from temperature profiles from 1970 to 2014. The solid black lines show the piecewise linear trends by setting the intervals manually. The dashed line indicates the linear trend for the entire period.

Satellite data indicate that the spatial heterogeneity of LSWT can be significant over water bodies (discussed in section 1.1.2.). A few studies examined the spatial variability of LSWT over Lake Geneva (Oesch et al. 2005; 2008). Advanced very high resolution radiometer (AVHRR) together with moderate resolution imaging spectroradiometer (MODIS) satellite imagery were employed to monitor the diurnal/nocturnal LSWT patchiness during a 13-d period in summer 2003. They suggest that the observed warm/cold LSWT regions may result from thermocline undulations, lake-land breezes and large-scale circulation forced by the wind field over the lake (Lemmin and D'Adamo 1996).

Figure 1.3 shows two daily (before noon) examples of LSWT spatial anomaly maps of Lake Geneva using Landsat-8 and (AVHRR) satellite data on 15 August 2013 (with less than 1.5 h time lag). The two images show similar large-scale patterns with a significant temperature contrast (~4 °C) over the entire lake. The effect of this variability on the mean SurHF, and hence

the total heat content of the lake has to be quantified. Furthermore, the comparison with the high resolution data can be used to assess the uncertainty associated with coarse resolution images. Landsat 8 (Fig. 1.3a) provides higher resolution images, and consequently a better indication of LSWT patchiness, than AVHRR (Fig. 1.3b). However, the imaging frequency is every 16 d (USGS, last accessed 1 February 2018) which makes it unsuitable for statistical analysis. Therefore, AVHRR data are used to study the multi-annual large-scale thermal patterns of Lake Geneva (see chapters 2 and 3). Thermography at the meso-scale level allows resolution of LSWT heterogeneity at the sub-pixel scale. As yet, to our knowledge, such data are available neither for Lake Geneva nor for other European lakes (Dörnhöfer and Oppelt 2016). This is presumably due to the challenges intrinsic to the airborne thermal imagery over natural waters (discussed in chapter 4).

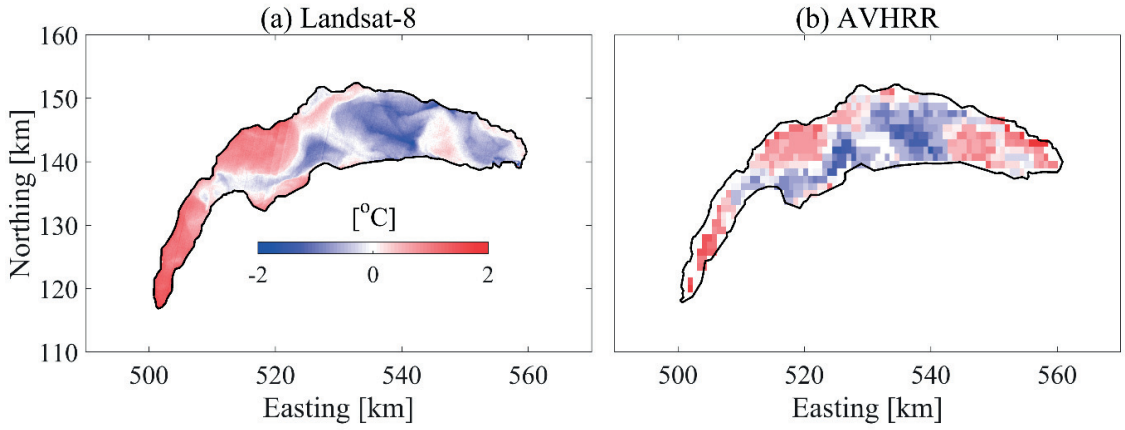

Fig. 1.3. Examples of LSWT spatial anomaly maps of Lake Geneva on 15 August 2013 using: (a) Landsat-8 image (100-m resolution interpolated to 30 m), and (b) AVHRR image (~1 km resolution). The Swiss coordinate system with km length-based units (CH1903) is used in these plots. Colors are identified in the legend in (a).

1.3. Research objectives and approaches

With respect to the literature and illustrations given above, the main objectives of this dissertation are (i) to characterize the large-scale spatial variability of LSWT, meteorological parameters and SurHF over Lake Geneva (an archetype of a large, mid-latitude lake), (ii) to quantify the effect of SurHF spatial heterogeneity on the total heat content estimates of a large lake, (iii) to identify the critical factors underlying the SurHF spatial variability of Lake Geneva,

and (iv) to resolve the LSWT at meso-scales, and accordingly quantify the uncertainty of SurHF estimates at large-scales due to in-pixel LSWT heterogeneity.

LSWT patterns from AVHRR (~1 km resolution), hourly maps of over-the-lake assimilated meteorological data from a numerical weather model (COSMO; 2.2-km resolution) run by the Swiss Federal Office of Meteorology and Climatology (MeteoSwiss, last accessed 1 February 2018) and long-term temperature depth profiles at two locations (SHL2 and GE3 in Fig. 1.1) were used for the large-scale thermal investigation. A SurHF model was optimized and calibrated for a 7-y period (March 2008 to December 2014) to achieve the first three objectives. A measurement platform including a balloon-launched platform for aerial thermography and a catamaran for ground-truthing was proposed for meso-scale study. An image processing procedure was then proposed to create the composite LSWT maps at meso-scales (~1 m resolution). A few examples of field measurements covering different ABL conditions were then selected to quantify the effect of LSWT meso-scale heterogeneity on SurHF estimations at sub-pixel satellite scales.

This dissertation is comprised of the following chapters:

Chapter 2- focusses on the SurHF model optimization and calibration for a 7-y period study. A quasi-1D water column heat balance approach was used at two locations in the lake. In a comprehensive study, the functionality of various SurHF bulk formulas (combinations of existing formulas for different heat flux components) in reproducing the lake's heat content was assessed. In addition, the impact of estimating the lake's heat content based on profile data from two measurement locations, as opposed to calibrations based on a single station, was investigated. Based on that, optimal formulas and parameterizations for SurHF calculation of Lake Geneva were obtained. This model was used in chapters 3 and 5. The sensitivity of the lake heat budget to the variation of the optimal calibration factors in a long-term analysis was also evaluated.

Chapter 3- uses the results of chapter 2 to obtain the typical monthly range of SurHF spatial variability over Lake Geneva. The full AVHRR data and meteorological patters were used for this study. The major meteorological factors controlling the dominant heat flux terms that determine spatial thermal patterns were obtained through statistical analyses.

Chapter 4- describes the measurement platform and the image processing algorithm to obtain the meso-scale LSWT patterns over a large water body. (i) Correction of spatial and temporal

noise inherent within uncooled thermal cameras and intensified for water thermography, (ii) implementation of a procedure for thermal image fusion and registration, and (iii) georeferencing and radiometric calibration of the composite image were illustrated in this chapter.

Chapter 5- uses the developed tools in chapters 2 and 4 to compute the surface cooling patterns with 1-m resolution. With these results, the impact of meso-scale LSWT heterogeneity on the large-scale SurHF (obtained in chapter 3) was quantified. Four different field campaigns containing different ABL conditions were selected and analyzed for this purpose.

Chapter 6- includes a conclusion of the previous chapters of this dissertation as well as some possible future research questions.

Appendix A- presents the temporal variation of lake-wide mean SurHF components and heat content using the results of chapter 3. A cross-correlation analysis was carried out to obtain the dominant SurHF terms underlying the total heat content variation. The results also demonstrate the time-lag between the lake's thermal responses to each of SurHF terms.

The dissertation structure is based on the manuscripts that are (or will be) submitted to peer-reviewed journals. For consistency and continuity within each of them, they are presented in their unedited form (except for some minor changes). Therefore, the content of the chapters may be in part repetitive.

References

Adrian, R., C. M. O'Reilly, H. Zagarese, S. B. Baines, D. O. Hessen, W. Keller, D. M. Livingstone, R. Sommaruga, D. Straile, E. Van Donk, G. A. Weyhenmeyer, and M. Winder. 2009. Lakes as sentinels of climate change. Limnol. Oceanogr. **54:** 2283-2297. doi: 10.4319/lo.2009.54.6_part_2.2283.

Arvola, L., G. George, D. M. Livingstone, M. Järvinen, T. Blenckner, M. T. Dokulil, E. Jennings, C. N. Aonghusa, P. Nõges, T. Nõges, and G. A. Weyhenmeyer. 2010. The impact of the changing climate on the thermal characteristics of lakes, p. 85-101. *In* G. George [ed.], The impact of climate change on European Lakes. Springer Netherlands. doi: 10.1007/978-90-481-2945-4_6.

Assouline, S., S. W. Tyler, J. Tanny, S. Cohen, E. Bou-Zeid, M. B. Parlange, and G. G. Katul. 2008. Evaporation from three water bodies of different sizes and climates: Measurements and scaling analysis. Adv. Water Resour. **31:** 160-172. doi: 10.1016/j.advwatres.2007.07.003.

Austin, J. A., and J. Allen. 2011. Sensitivity of summer Lake Superior thermal structure to meteorological forcing. Limnol. Oceanogr. **56:** 1141-1154. doi: 10.4319/lo.2011.56.3.1141.

Bai, X. Z., J. Wang, D. J. Schwab, Y. Yang, L. Luo, G. A. Leshkevich, and S. Z. Liu. 2013. Modeling 1993-2008 climatology of seasonal general circulation and thermal structure in the Great Lakes using FVCOM. Ocean Model. **65:** 40-63. doi: 10.1016/j.ocemod.2013.02.003.

Beletsky, D., N. Hawley, and Y. R. Rao. 2013. Modeling summer circulation and thermal structure of Lake Erie. J. Geophys. Res.: Oceans **118:** 6238-6252. doi: 10.1002/2013JC008854.

Blanken, P. D., C. Spence, N. Hedstrorn, and J. D. Lenters. 2011. Evaporation from Lake Superior: 1. Physical controls and processes. J. Great Lakes Res. **37:** 707-716. doi: 10.1016/j.jglr.2011.08.009.

Bonvin, F., A. M. Razmi, D. A. Barry, and T. Kohn. 2013. Micropollutant dynamics in Vidy Bay-A coupled hydrodynamic-photolysis model to assess the spatial extent of ecotoxicological risk. Environ. Sci. Technol. **47:** 9207-9216. doi: 10.1021/es401294c.

Brodeau, L., B. Barnier, S. K. Gulev, and C. Woods. 2017. Climatologically significant effects of some approximations in the bulk parameterizations of turbulent air-sea fluxes. J. Phys. Oceanogr. **47:** 5-28. doi: 10.1175/Jpo-D-16-0169.1.

Brunke, M. A., X. B. Zeng, and S. Anderson. 2002. Uncertainties in sea surface turbulent flux algorithms and data sets. J. Geophys. Res.: Oceans **107:** 3141. doi: 10.1029/2001jc000992.

Brutsaert, W. 1975. Derivable formula for long-wave radiation from clear skies. Water Resour. Res. **11:** 742-744. doi: 10.1029/Wr011i005p00742.

Carpenter, S. R., E. H. Stanley, and M. J. Vander Zanden. 2011. State of the world's freshwater ecosystems: Physical, chemical, and biological changes. Annu Rev Env Resour **36:** 75-99. doi: 10.1146/annurev-environ-021810-094524.

Castro, S. L., W. J. Emery, G. A. Wick, and W. Tandy. 2017. Submesoscale sea surface temperature variability from UAV and satellite measurements. Remote Sens. **9:** 1089. doi: 10.3390/Rs9111089.

Cole, J. J., D. L. Bade, D. Bastviken, M. L. Pace, and M. Van de Bogert. 2010. Multiple approaches to estimating air-water gas exchange in small lakes. Limnol. Oceanogr.: Methods **8:** 285-293. doi: 10.4319/lom.2010.8.285.

Dommenget, D., and M. Rezny. 2018. A caveat note on tuning in the development of coupled climate models. J Adv Model Earth Sy **10:** 78-97. doi: 10.1002/2017MS000947.

Dörnhöfer, K., and N. Oppelt. 2016. Remote sensing for lake research and monitoring – Recent advances. Ecol. Indic. **64:** 105-122. doi: 10.1016/j.ecolind.2015.12.009.

Eastman, R., and S. G. Warren. 2013. A 39-yr survey of cloud changes from land stations worldwide 1971-2009: Long-term trends, relation to aerosols, and expansion of the tropical belt. J. Clim. **26:** 1286-1303. doi: 10.1175/Jcli-D-12-00280.1.

Fairall, C. W., E. F. Bradley, D. P. Rogers, J. B. Edson, and G. S. Young. 1996. Bulk parameterization of air-sea fluxes for Tropical Ocean Global Atmosphere Coupled Ocean Atmosphere Response Experiment. J. Geophys. Res.: Oceans **101:** 3747-3764. doi: 10.1029/95jc03205.

Ferri, R., N. Pierdicca, and S. Talice. 2000. Mapping sea surface temperature from aircraft using a multi-angle technique: An experiment over the Orbetello lagoon. Int. J. Remote Sens. **21:** 3003-3024. doi: 10.1080/01431160050144929.

Fink, G., M. Schmid, B. Wahl, T. Wolf, and A. Wüest. 2014. Heat flux modifications related to climate-induced warming of large European lakes. Water Resour. Res. **50:** 2072-2085. doi: 10.1002/2013wr014448.

Garbe, C. S., U. Schimpf, and B. Jahne. 2004. A surface renewal model to analyze infrared image sequences of the ocean surface for the study of air-sea heat and gas exchange. J. Geophys. Res.: Oceans **109:** C08s15. doi: 10.1029/2003jc001802.

Gillet, C., and P. Quetin. 2006. Effect of temperature changes on the reproductive cycle of roach in Lake Geneva from 1983 to 2001. J. Fish Biol. **69:** 518-534. doi: 10.1111/j.1095-8649.2006.01123.x.

Goyette, S., and M. Perroud. 2012. Interfacing a one-dimensional lake model with a single-column atmospheric model: Application to the deep Lake Geneva, Switzerland. Water Resour. Res. **48:** Artn W04507. doi: 10.1029/2011wr011223.

Hanson, P. C., K. C. Weathers, H. A. Dugan, and C. Gries. 2018. The global lake ecological observatory network, p. 415-433. *In* F. Recknagel and W. K. Michener [eds.], Ecological Informatics: Data Management and Knowledge Discovery. Springer International Publishing. doi: 10.1007/978-3-319-59928-1_19.

Henderson-Sellers, B. 1986. Calculating the surface energy balance for lake and reservoir modeling: A review. Rev. Geophys. **24:** 625-649. doi: 10.1029/Rg024i003p00625.

Ji, F., Z. H. Wu, J. P. Huang, and E. P. Chassignet. 2014. Evolution of land surface air temperature trend. Nat. Clim. Change **4:** 462-466. doi: 10.1038/Nclimate2223.

Laird, N. F., and D. A. R. Kristovich. 2002. Variations of sensible and latent heat fluxes from a Great Lakes buoy and associated synoptic weather patterns. J. Hydrometeorol. **3:** 3-12. doi: 10.1175/1525-7541(2002)003<0003:Vosalh>2.0.Co;2.

Lemmin, U., and N. D'Adamo. 1996. Summertime winds and direct cyclonic circulation: Observations from Lake Geneva. Ann. Geophys., Ser. A **14:** 1207-1220. doi: 10.1007/s005850050384.

Lenters, J. D., T. K. Kratz, and C. J. Bowser. 2005. Effects of climate variability on lake evaporation: Results from a long-term energy budget study of Sparkling Lake, northern Wisconsin (USA). J. Hydrol. **308:** 168-195. doi: 10.1016/j.jhydrol.2004.10.028.

Li, Z. G., S. H. Lyu, Y. H. Ao, L. J. Wen, L. Zhao, and S. Y. Wang. 2015. Long-term energy flux and radiation balance observations over Lake Ngoring, Tibetan Plateau. Atmos. Res. **155:** 13-25. doi: 10.1016/j.atmosres.2014.11.019.

Livingstone, D. M., and D. M. Imboden. 1989. Annual heat balance and equilibrium temperature of Lake Aegeri, Switzerland. Aquat. Sci. **51:** 351-369. doi: 10.1007/Bf00877177.

Lofgren, B. M., and Y. C. Zhu. 2000. Surface energy fluxes on the Great Lakes based on satellite-observed surface temperatures 1992 to 1995. J. Great Lakes Res. **26:** 305-314. doi: 10.1016/S0380-1330(00)70694-0.

Minnett, P. J., M. Smith, and B. Ward. 2011. Measurements of the oceanic thermal skin effect. Deep-Sea Res. Part II. **58:** 861-868. doi: 10.1016/j.dsr2.2010.10.024.

Momii, K., and Y. Ito. 2008. Heat budget estimates for Lake Ikeda, Japan. J. Hydrol. **361:** 362-370. doi: 10.1016/j.jhydrol.2008.08.004.

Moukomla, S., and P. D. Blanken. 2017. The estimation of the North American Great Lakes turbulent fluxes using satellite remote sensing and MERRA reanalysis data. Remote Sens. **9:** 141. doi: 10.3390/Rs9020141.

Nordbo, A., S. Launiainen, I. Mammarella, M. Lepparanta, J. Huotari, A. Ojala, and T. Vesala. 2011. Long-term energy flux measurements and energy balance over a small boreal lake using eddy covariance technique. J. Geophys. Res.: Atmos. **116:** D02119. doi: 10.1029/2010jd014542.

O'Reilly, C. M., S. Sharma, D. K. Gray and others 2015. Rapid and highly variable warming of lake surface waters around the globe. Geophys. Res. Lett. **42:** 10773-10781. doi: 10.1002/2015GL066235.

Oesch, D., J. M. Jaquet, R. Klaus, and P. Schenker. 2008. Multi-scale thermal pattern monitoring of a large lake (Lake Geneva) using a multi-sensor approach. Int. J. Remote Sens. **29:** 5785-5808. doi: 10.1080/01431160802132786.

Oesch, D. C., J. M. Jaquet, A. Hauser, and S. Wunderle. 2005. Lake surface water temperature retrieval using Advanced Very High Resolution Radiometer and Moderate Resolution Imaging Spectroradiometer data: Validation and feasibility study. J. Geophys. Res.: Oceans **110:** C12014. doi: 10.1029/2004jc002857.

Pareeth, S., N. Salmaso, R. Adrian, and M. Neteler. 2016. Homogenised daily lake surface water temperature data generated from multiple satellite sensors: A long-term case study of a large sub-Alpine lake. Sci Rep-Uk **6:** 31251. doi: 10.1038/Srep31251.

Perroud, M., and S. Goyette. 2010. Impact of warmer climate on Lake Geneva water-temperature profiles. Boreal Environ. Res. **15:** 255-278. http://hdl.handle.net/10138/233095.

Perroud, M., S. Goyette, A. Martynov, M. Beniston, and O. Anneville. 2009. Simulation of multiannual thermal profiles in deep Lake Geneva: A comparison of one-dimensional lake models. Limnol. Oceanogr. **54:** 1574-1594. doi: 10.4319/lo.2009.54.5.1574.

Phillips, R. C., J. R. Saylor, N. B. Kaye, and J. M. Gibert. 2016. A multi-lake study of seasonal variation in lake surface evaporation using MODIS satellite-derived surface temperature. Limnology **17:** 273-289. doi: 10.1007/s10201-016-0481-z.

Piccolroaz, S., N. C. Healey, J. D. Lenters, S. G. Schladow, S. J. Hook, G. B. Sahoo, and M. Toffolon. 2018. On the predictability of lake surface temperature using air temperature in a changing climate: A case study for Lake Tahoe (USA). Limnol. Oceanogr. **63:** 243-261. doi: 10.1002/lno.10626.

Piccolroaz, S., M. Toffolon, and B. Majone. 2013. A simple lumped model to convert air temperature into surface water temperature in lakes. Hydrol. Earth Syst. Sci. **17:** 3323-3338. doi: 10.5194/hess-17-3323-2013.

Riffler, M., G. Lieberherr, and S. Wunderle. 2015. Lake surface water temperatures of European Alpine lakes (1989-2013) based on the Advanced Very High Resolution Radiometer (AVHRR) 1 km data set. Earth Sys. Sci. Data **7:** 1-17. doi: 10.5194/essd-7-1-2015.

Rimmer, A., R. Samuels, and Y. Lechinsky. 2009. A comprehensive study across methods and time scales to estimate surface fluxes from Lake Kinneret, Israel. J. Hydrol. **379:** 181-192. doi: 10.1016/j.jhydrol.2009.10.007.

Rouse, W. R., P. D. Blanken, N. Bussieres, C. J. Oswald, W. M. Schertzer, C. Spence, and A. E. Walker. 2008. Investigation of the thermal and energy balance regimes of Great Slave and Great Bear Lakes. J. Hydrometeorol. **9:** 1318-1333. doi: 10.1175/2008JHM977.1.

Rueda, F. J., S. G. Schladow, S. G. Monismith, and M. T. Stacey. 2005. On the effects of topography on wind and the generation of currents in a large multi-basin lake. Hydrobiologia **532:** 139-151. doi: 10.1007/s10750-004-9522-4.

Schertzer, W. M. 1978. Energy budget and monthly evaporation estimates for Lake Superior, 1973. J. Great Lakes Res. **4:** 320-330. doi: 10.1016/S0380-1330(78)72201-X.

Schneider, K., and W. Mauser. 1991. On the estimation of energy fluxes at the surface of Lake Constance using NOAA-AVHRR data, p. 373-376. IGARSS 91-Remote Sensing : Global Monitoring for Earth Management. IEEE Xplore Conference, Espoo, Finland. doi: 10.1109/IGARSS.1991.579158.

Schwab, D. J., G. A. Leshkevich, and G. C. Muhr. 1992. Satellite measurements of surface water temperature in the Great Lakes: Great Lakes Coastwatch. J. Great Lakes Res. **18:** 247-258. https://www.glerl.noaa.gov/pubs/fulltext/1992/19920009.pdf.

Sharma, S., D. K. Gray, J. S. Read and others 2015. A global database of lake surface temperatures collected by in situ and satellite methods from 1985-2009. Sci Data **2:** 150008. doi: 10.1038/Sdata.2015.8.

Sima, S., A. Ahmadalipour, and M. Tajrishy. 2013. Mapping surface temperature in a hyper-saline lake and investigating the effect of temperature distribution on the lake evaporation. Remote Sens. Environ. **136:** 374-385. doi: 10.1016/j.rse.2013.05.014.

Spence, C., P. D. Blanken, N. Hedstrom, V. Fortin, and H. Wilson. 2011. Evaporation from Lake Superior: 2-Spatial distribution and variability. J. Great Lakes Res. **37:** 717-724. doi: 10.1016/j.jglr.2011.08.013.

Stepanenko, V., K. D. Johnk, E. Machulskaya, M. Perroud, Z. Subin, A. Nordbo, I. Mammarella, and D. Mironov. 2014. Simulation of surface energy fluxes and stratification of a small boreal lake by a set of one-dimensional models. Tellus, Ser. A. **66:** 21389. doi: 10.3402/Tellusa.V66.21389.

Tanentzap, A. J., D. P. Hamilton, and N. D. Yan. 2007. Calibrating the Dynamic Reservoir Simulation Model (DYRESM) and filling required data gaps for one-dimensional thermal profile predictions in a boreal lake. Limnol. Oceanogr.: Methods **5:** 484-494. doi: 10.4319/lom.2007.5.484.

Thiery, W., A. Martynov, F. Darchambeau, J. P. Descy, P. D. Plisnier, L. Sushama, and N. P. M. van Lipzig. 2014a. Understanding the performance of the FLake model over two African Great Lakes. Geosci. Model Dev. **7:** 317-337. doi: 10.5194/gmd-7-317-2014.

Thiery, W., V. M. Stepanenko, X. Fang, K. D. Johnk, Z. S. Li, A. Martynov, M. Perroud, Z. M. Subin, F. Darchambeau, D. Mironov, and N. P. M. Van Lipzig. 2014b. LakeMIP Kivu: Evaluating the representation of a large, deep tropical lake by a set of one-dimensional lake models. Tellus, Ser. A. **66:** 21390. doi: 10.3402/Tellusa.V66.21390.

Toffolon, M., S. Piccolroaz, B. Majone, A. M. Soja, F. Peeters, M. Schmid, and A. Wuest. 2014. Prediction of surface temperature in lakes with different morphology using air temperature. Limnol. Oceanogr. **59:** 2185-2202. doi: 10.4319/lo.2014.59.6.2185.

Tozuka, T., S. Ohishi, and M. F. Cronin. 2017. A metric for surface heat flux effect on horizontal sea surface temperature gradients. Climate Dynam. doi: 10.1007/s00382-017-3940-2.

Valerio, G., A. Cantelli, P. Monti, and G. Leuzzi. 2017. A modeling approach to identify the effective forcing exerted by wind on a prealpine lake surrounded by a complex topography. Water Resour. Res. **53:** 4036-4052. doi: 10.1002/2016WR020335.

Van Emmerik, T. H. M., A. Rimmer, Y. Lechinsky, K. J. R. Wenker, S. Nussboim, and N. C. van de Giesen. 2013. Measuring heat balance residual at lake surface using distributed temperature sensing. Limnol. Oceanogr.: Methods **11:** 79-90. doi: 10.4319/lom.2013.11.79.

Verburg, P., and J. P. Antenucci. 2010. Persistent unstable atmospheric boundary layer enhances sensible and latent heat loss in a tropical great lake: Lake Tanganyika. J. Geophys. Res.: Atmos. **115:** D11109. doi: 10.1029/2009jd012839.

Vercauteren, N., E. Bou-Zeid, H. Huwald, M. B. Parlange, and W. Brutsaert. 2009. Estimation of wet surface evaporation from sensible heat flux measurements. Water Resour. Res. **45:** W06424. doi: 10.1029/2008wr007544.

Vercauteren, N., E. Bou-Zeid, M. B. Parlange, U. Lemmin, H. Huwald, J. Selker, and C. Meneveau. 2008. Subgrid-scale dynamics of water vapour, heat, and momentum over a lake. Bound-Lay. Meteor. **128:** 205-228. doi: 10.1007/s10546-008-9287-9.

Vercauteren, N., H. Huwald, E. Bou-Zeid, J. S. Selker, U. Lemmin, M. B. Parlange, and I. Lunati. 2011. Evolution of superficial lake water temperature profile under diurnal radiative forcing. Water Resour. Res. **47:** W09522. doi: 10.1029/2011wr010529.

Wahl, B., and F. Peeters. 2014. Effect of climatic changes on stratification and deep-water renewal in Lake Constance assessed by sensitivity studies with a 3D hydrodynamic model. Limnol. Oceanogr. **59:** 1035-1052. doi: 10.4319/lo.2014.59.3.1035.

Wilson, R. C., S. J. Hook, P. Schneider, and S. G. Schladow. 2013. Skin and bulk temperature difference at Lake Tahoe: A case study on lake skin effect. J. Geophys. Res.: Atmos. **118:** 10332-10346. doi: 10.1002/Jgrd.50786.

Woolway, R. I., I. D. Jones, D. P. Hamilton, S. C. Maberly, K. Muraoka, J. S. Read, R. L. Smyth, and L. A. Winslow. 2015. Automated calculation of surface energy fluxes with high-frequency lake buoy data. Environ. Model. Softw. **70:** 191-198. doi: 10.1016/j.envsoft.2015.04.013.

Woolway, R. I., and C. J. Merchant. 2017. Amplified surface temperature response of cold, deep lakes to inter-annual air temperature variability. Sci Rep-Uk **7:** 4130. doi: 10.1038/S41598-017-04058-0.

Woolway, R. I., P. Verburg, C. J. Merchant, J. D. Lenters, D. P. Hamilton, J. Brookes, S. Kelly, S. Hook, A. Laas, D. Pierson, A. Rimmer, J. A. Rusak, and I. D. Jones. 2017. Latitude and lake size are important predictors of over-lake atmospheric stability. Geophys. Res. Lett. **44:** 8875-8883. doi: 10.1002/2017GL073941.

Xue, P. F., D. J. Schwab, and S. Hu. 2015. An investigation of the thermal response to meteorological forcing in a hydrodynamic model of Lake Superior. J. Geophys. Res.: Oceans **120:** 5233-5253. doi: 10.1002/2015JC010740.

Yang, J., Z.-H. Wang, Q. Li, N. Vercauteren, E. Bou-Zeid, and M. B. Parlange. 2017. A novel approach for unraveling the energy balance of water surfaces with a single depth temperature measurement. Limnol. Oceanogr. **62:** 89-103. doi: 10.1002/lno.10378.

Zhang, Q., and H. Liu. 2014. Seasonal changes in physical processes controlling evaporation over inland water. J. Geophys. Res.: Atmos. **119:** 9779-9792. doi: 10.1002/2014JD021797.

Chapter 2

Improving surface heat flux estimation of a large lake through model optimization and 2-point calibration: The case of Lake Geneva

Abolfazl Irani Rahaghi[a], Ulrich Lemmin[a], Andrea Cimatoribus[a], Damien Bouffard[b,c], Michael Riffler[d,e], Stefan Wunderle[d], David Andrew Barry[a]

[a] Ecological Engineering Laboratory (ECOL), Environmental Engineering Institute (IIE), Faculty of Architecture, Civil and Environmental Engineering (ENAC), Ecole Polytechnique Fédérale de Lausanne (EPFL), 1015 Lausanne, Switzerland

[b] Physics of Aquatic Systems Laboratory (APHYS), Margaretha Kamprad Chair, Environmental Engineering Institute (IIE), Faculty of Architecture, Civil and Environmental Engineering (ENAC), Ecole Polytechnique Fédérale de Lausanne (EPFL), 1015 Lausanne, Switzerland

[c] Aquatic Physics Group, Department of Surface Waters Research & Management, Eidgenössische Anstalt für Wasserversorgung, Abwasserreinigung und Gewässerschutz (EAWAG), 6047 Kastanienbaum, Switzerland

[d] Institute of Geography and Oeschger Centre for Climate Change Research, Faculty of Science, University of Bern, Bern, Switzerland

[e] Geoville Information Systems GmbH, Innsbruck, Austria

Submitted to *Limnology and Oceanography: Methods*

Abstract

Net surface heat flux (SurHF) was estimated from 2008 to 2014 for Lake Geneva (Switzerland/France), using long-term temperature depth profiles at two locations, hourly maps of reanalysis meteorological data from a numerical weather model and lake surface water temperatures from calibrated satellite imagery. Existing formulas for different heat flux components were combined into 54 different total SurHF models. The coefficients in these models were calibrated based on SurHF optimization. Four calibration factors characterizing the incoming long-wave radiation, sensible and latent heat fluxes were further investigated for the six best performing models. The combination of the modified parameterization of the Brutsaert equation for incoming atmospheric radiation and of similarity theory based bulk parameterization algorithms for latent and sensible surface heat fluxes provided the most accurate SurHF estimates. When optimized for one lake temperature profile location, SurHF models failed to predict the temperature profile at the other location due to the spatial variability of meteorological parameters between the two locations. Consequently, the optimal SurHF models were calibrated using two profile locations. The results emphasize that even relatively small changes in calibration factors, particularly in the atmospheric emissivity, significantly modify the estimated long-term heat content. Lack of calibration can produce changes in the calculated heat content that are much higher than the observed annual climate change-induced trend. The calibration improved parameterization of bulk transfer coefficients, mainly under low wind regimes.

Keywords: Surface heat flux, meteorological forcing, Lake Geneva, model calibration, bulk parameterization algorithm, radiation heat flux, turbulent heat flux

2.1. Introduction

Surface heat flux (SurHF) and wind forcing control stratification dynamics and have a major influence on the physical, chemical and biological properties of lakes (e.g., MacIntyre et al. 2002; Churchill and Charles Kerfoot 2007; Bonvin et al. 2013; Finlay et al. 2015). For many lakes, changes in heat content are mainly due to SurHF variations, as shown in both short-term investigations (Van Emmerik et al. 2013) and long-term climate change studies (Arvola et al. 2010; Fink et al. 2014). SurHF temporal variations are often obtained from measurements taken at a single location, e.g., at the deepest point in the lake (e.g., Heikinheimo et al. 1999; Laird and Kristovich 2002; Rouse et al. 2003; Rouse et al. 2008; Nordbo et al. 2011; Van Emmerik et al. 2013; Woolway et al. 2015a), using bulk formulas (e.g., Schertzer 1978; Henderson-Sellers 1986; Lenters et al. 2005; Woolway et al. 2015b) or 1D numerical modeling (e.g., Tanentzap et al. 2007; Momii and Ito 2008; Austin and Allen 2011; Stepanenko et al. 2014; Thiery et al. 2014a; Thiery et al. 2014b; Yang et al. 2017). Such quasi one-dimensional (1D) estimates are then considered representative for the whole lake. Although the single location approach might be suitable for small water bodies, spatial variability of SurHF due to variable meteorological conditions can be important for large lakes (e.g., Lofgren and Zhu 2000; Xue et al. 2015; Moukomla and Blanken 2017). Data from multiple locations permit the investigation of SurHF spatial variability, and the availability of such data is growing (e.g., Rimmer et al. 2009; Verburg and Antenucci 2010; Spence et al. 2011). A systematic evaluation of the validity and performance of SurHF models at more than one location has received little attention in the literature, especially for long-term studies. Here, we examine the impact of using data taken at two locations on the bulk SurHF model optimization and calibration, and then compare it to the common one-point approach.

An additional source of uncertainty is the selected SurHF model itself. SurHF models involve several terms for the relevant physical processes. For each of these terms, different formulations exist. Some studies aimed to improve and optimize individual SurHF terms (e.g., Fairall et al. 1996; Zeng et al. 1998; Crawford and Duchon 1999; Rimmer et al. 2009; Wang et al. 2014). However, the effect of combining different equations for all the relevant SurHF terms and optimizing them as a set has not been evaluated.

In this study, we calibrated different combinations of SurHF term equations (with each term describing a different heat exchange mechanism) to quantify the heat content variation of a

large lake for a 7-y period (2008-2014). We also assessed the impact of using time series of temperature profiles taken at two measurement points, instead of at only one point, for the calibration and estimation of SurHF. Lake Geneva, the largest freshwater lake in Western Europe, is a suitable study site since the required data are available. Specifically, the following questions were addressed:

(i) What is the optimal combination of bulk formulas for modeling SurHF in a given lake?
(ii) What is the impact of estimating the lake's heat content based on profile data from two measurement locations, as opposed to calibrations based on a single station?
(iii) Using the example of Lake Geneva, how sensitive is the lake heat budget variation to the optimal calibration factors in a long-term analysis?

The methodology is developed here using two locations. However, it can be extended to more than two locations. In fact, by increasing the number of locations, it can be expected that the performance of the lakewide SurHF model will be further improved.

2.2. Materials and procedures

2.2.1. Study site

Located between Switzerland and France, Lake Geneva (Local name: *Lac Léman*) is a large, deep perialpine lake with a mean surface altitude of 372 m. It is approximately 70-km long, with a maximum width of 14 km, a surface area of 582 km² and a volume of 89 km³. The lake is composed of two basins: an eastern, large basin called the *Grand Lac*, with a maximum depth of 309 m, and a western, small narrow basin, the *Petit Lac*, with a maximum depth of approximately 70 m (Fig. 1.1). The main inflow (*Rhône-in*) and outflow (*Rhône-out*) of the lake are shown in Fig. 1.1. The lake is surrounded by the Jura Mountains in the northwest, and by the Alps in the south and, to a lesser extent, the northeast (Fig. 1.1). This topography leads to two dominant wind fields, namely the *Bise* coming from the northeast, and the *Vent* from the southwest (Lemmin and D'Adamo 1996). On average, due to topographic sheltering, the eastern part of the *Grand Lac* experiences lower wind speeds than the western part of the *Grand Lac* and most of the *Petit Lac*. However, the two monitoring locations, SHL2 located in the *Grand Lac* and GE3 in the *Petit Lac* (Fig. 1.1), for which all the required data for model calibration are available, are located in the part of the lake where the surrounding topography is flat and topographical sheltering effects can be neglected.

2.2.2. Energy balance in a water column

The total heat content of a water column, G_o [Jm^{-2}], is given by:

$$G_o(t) = \int_0^H \rho_w C_{p,w} T(z,t)\, dz \tag{2.1}$$

where ρ_w and $C_{p,w}$ are the density [kgm^{-3}] and the specific heat capacity of water at constant pressure [Jkg^{-1}°C^{-1}], respectively, and $T(z,t)$ represents vertical temperature profile [°C] at time t down to water column depth $z = H$ [m]. The heat content variation from time t_1 to time t_2 then can be quantified by:

$$\Delta G_o(t_1 \to t_2) = G_o(t_2) - G_o(t_1) \tag{2.2}$$

The heat content variation in the water column over the full lake depth (ΔG_m) is the sum of the net energy flux into it and includes net SurHF, Q_N, advective (lateral) heat transport, Q_{ad}, and geothermal heat flux, Q_{ge}:

$$\Delta G_m(t_1 \to t_2) = \int_{t_1}^{t_2} \left[Q_N(\hat{t}) + Q_{ad}(\hat{t}) + Q_{ge}(\hat{t}) \right] d\hat{t} \tag{2.3}$$

The contribution of the Q_{ad} and Q_{ge} terms to ΔG_m were compared with that of Q_N. For advective heat transport, note that the measurement locations in the present study are far from shore and the river mouth (Fig. 1.1), and so river input effects can be considered to be small, as is evident from the long theoretical residence time of Lake Geneva (11.3 y, CIPEL, last accessed 18 January 2018). The contribution of advective heat flux, Q_{ad}, to the heat content variation in the water column, ΔG_m, may be important in lakes with short flushing times due to river inflows (Carmack 1979). In large lakes, the advective heat flux may be significant in certain areas where persistent currents move water from one thermal regime to another, such as the Keewenaw current in Lake Superior (Zhu et al. 2001), or the bi-directional flow in the Straits of Mackinac (Anderson and Schwab 2017). However, the mean circulation pattern that is most often observed in large lakes is primarily a cyclonic circulation, with well-developed along-shore currents in the near shore zone and mostly weak currents of more random orientation in the central region of the lake (e.g., Emery and Csanady 1973; Simons 1980; Boyce et al. 1989; Beletsky et al. 1999; Beletsky and Schwab 2008). With this circulation pattern, steady shore-perpendicular currents advecting heat towards the center of the lake are rare. In their numerical modeling of Lake Superior, Bennington et al. (2010) observed that cyclonic circulation dominates and that there is no correlation between the daily anomalies of the local temperature

gradient in the meridional direction and the daily anomalies of the current speed in the zonal direction outside the near shore boundary layer. Derecki (1976) reported that heat advection can be ignored for Lake Erie during most of the year. Based on numerical modeling, a two-gyre (Simons 1980) or three-gyre (Akitomo et al. 2004) large-scale circulation pattern may sometimes be present in large lakes.

In most studies cited in the literature, contributions by Q_{ad} and Q_{ge} are ignored and it is assumed that ΔG_m can be approximated by only considering Q_N. In order to determine whether such a quasi-1D approach is justified in Lake Geneva, we estimated the contribution of Q_{ad} using a 3D hydrodynamic model. A detailed simulation was performed for a representative period (January to October 2010), as described in the Supplemental Information (SI) section. The results (Fig. S2.3) show that far from shore and the main inflow, the *Rhône* river (Fig. 1.1), at the locations where the present study is carried out, the contribution of SurHF, Q_N, to the heat content variation is much higher than that of lateral advection, Q_{ad}. For the whole lake, the heat content variation due to advective heat flux is high in the near shore zone and low in the center of the lake (Fig. S2.4), in agreement with Bennington et al. (2010). Thus, in the present analysis, advective heat flux, $Q_{ad,}$ is ignored.

Although the geothermal heat flux, Q_{ge}, is not known for Lake Geneva, it is reported to be small in many Swiss lakes, typically ~ 0.1 Wm^{-2} (Finckh 1976), and its contribution is ignored here. However, we briefly quantify below the impact of this (potential) flux on the estimated parameter values.

The net input energy, ΔG_m [J m^{-2}], is calculated by time-integrating the net SurHF, Q_N [Wm^{-2}], for a given period (Eq. 2.3). The energy balance in the water column can then be written as (Van Emmerik et al. 2013; Fink et al. 2014; Nussboim et al. 2017):

$$\Delta G_o = \Delta G_m \cong \int_{t_1}^{t_2} Q_N\left(\hat{t}\right) d\hat{t} \tag{2.4}$$

The net heat flux at the air-water interface (positive when directed into the water), Q_N, in Eq. 2.4 is given by:

$$Q_N = Q_{sn} + Q_{an} + Q_{br} + Q_{ev} + Q_{co} + Q_{pr} \tag{2.5}$$

where the right-hand side terms describe the flux due to solar shortwave radiation, Q_{sn}, incoming long-wave radiation from the sky, Q_{an}, back long-wave radiation, Q_{br}, latent (evaporation, Q_{ev}), sensible (convection, Q_{co}), and precipitation (Q_{pr}) heat fluxes. The effect of precipitation, Q_{pr}, on the SurHF of European lakes is neglected due to its minimal influence on SurHF (Livingstone and Imboden 1989; Rimmer et al. 2009; Fink et al. 2014). In order to use Eqs. 2.1, 2.4 and 2.5, water and atmospheric field data input are required.

2.2.3. Water temperature profiles

CIPEL has measured water temperature profiles (for Eq. 2.1) since 1957 at locations SHL2 (309 m depth) and GE3 (70 m depth) in the *Grand Lac* and *Petit Lac* (Fig. 1.1), respectively, at a frequency of 1 to 2 profiles per month. In total, 130 Conductivity-Temperature-Depth (CTD) profiles at SHL2 and 78 profiles at GE3 are available for the study period (2008 - 2014). Based on these temperature profiles, the water column heat content variation (Eq. 2.1) at these two locations was calculated (Fig. S2.5).

2.2.4. Satellite data

Lake Surface Water Temperatures (LSWT) are needed for Eq. 2.5. Riffler et al. (2015) determined the LSWT for 25 lakes in and near the Alps from a long-term archive of AVHRR satellite imagery (1.1 km × 1.1 km pixel size). The satellite-based temperatures agreed well with the near-surface in situ measurements for our study with a bias and RMSE within the range of -0.5 to 0.6 K and 1.0 to 1.6 K, respectively. This range of values favorably corresponds with another long-term LSWT calibration for Lake Geneva (Oesch et al. 2005). In this study, we use the same data set as Riffler et al. (2015) (4384 images from 1 March 2008 to 31 December 2014) to retrieve LSWT at the SHL2 and GE3 locations. Images with more than 70% lake coverage were selected, resulting in a total of 856 diurnal images and 308 nocturnal images. Missing pixels in these images were interpolated spatially using Barnes interpolation (Koch et al. 1983; Liston and Elder 2006). The present analysis requires a pixelwise spatially resolved time series of surface temperature. These were derived from the spatially interpolated LSWT maps. Time series were produced using Piecewise Cubic Hermite polynomials (Fritsch and Carlson 1980). Figure 2.1a shows the variation of LSWT (labeled T_w in the figures) at the SHL2 and GE3 locations (the nearest pixels in the satellite images) smoothed with a 30-d moving average. On average, SHL2 has a higher skin temperature than GE3 in summer and winter (Fig.

2.1a). A shift in the T_w distribution at the two locations is evident from the smoothed Probability Density Function (PDF) of the LSWT (Fig. S2.6a).

2.2.5. Meteorological data

Meteorological data over Lake Geneva are not measured. However, since 2008, the Swiss Federal Office of Meteorology and Climatology (MeteoSwiss, last accessed 18 January 2018) has run a numerical weather model, COSMO-2, which provides hourly output on a 2.2 km × 2.2 km grid. Lakes are distinguished from land by using a lake model in COSMO-2 (Mironov 2008). COSMO-2 data include spatiotemporal maps of wind speed (10 m above the lake), air temperature (2 m above the lake), relative humidity (2 m above the lake), cloudiness, global radiation and air pressure. Model results are systematically verified against over-land surface data in Switzerland and Europe (MeteoSwiss). This study is based on reanalysis COSMO-2 datasets (assimilated results are based on past field observations) for the period from 1 March 2008 to 31 December 2014. To investigate the quality of COSMO-2 results further, we compared these data with measurements taken at meteorological stations located around the lake (Fig. S2.7a). Our analysis indicates a high correlation between these measurements and the COSMO-2 outputs (Fig. S2.7b), with the exception of wind speed, which has a higher local spatiotemporal variability. For wind speed, the cross correlation between different stations is similar for COSMO-2 results and in situ measurements, which confirms the capability of the COSMO-2 model to represent realistic large-scale wind patterns over Lake Geneva (Fig. S2.7c).

Smoothed meteorological data with a 30-d moving average are shown in Figs. 2.1b-f, for the SHL2 and GE3 locations (PDFs of the raw hourly data are presented in Figs. S2.6b-f). The differences between the two locations in variation and distribution of wind speed, U_{10}, (Figs. 2.1b and S2.6b), and relative humidity, ϕ_{rel}, (Figs. 2.1e and S2.6e), are pronounced. In particular, the average wind speed is higher at GE3 than at SHL2 (Fig. 2.1b). The probability density of low wind speeds (1-3 ms^{-1}) is also lower at GE3 (Fig. S2.6b). This is due to the differences between the characteristics and fetch of the two dominant winds, *Bise* and *Vent*, as described above (Fig. 1.1).

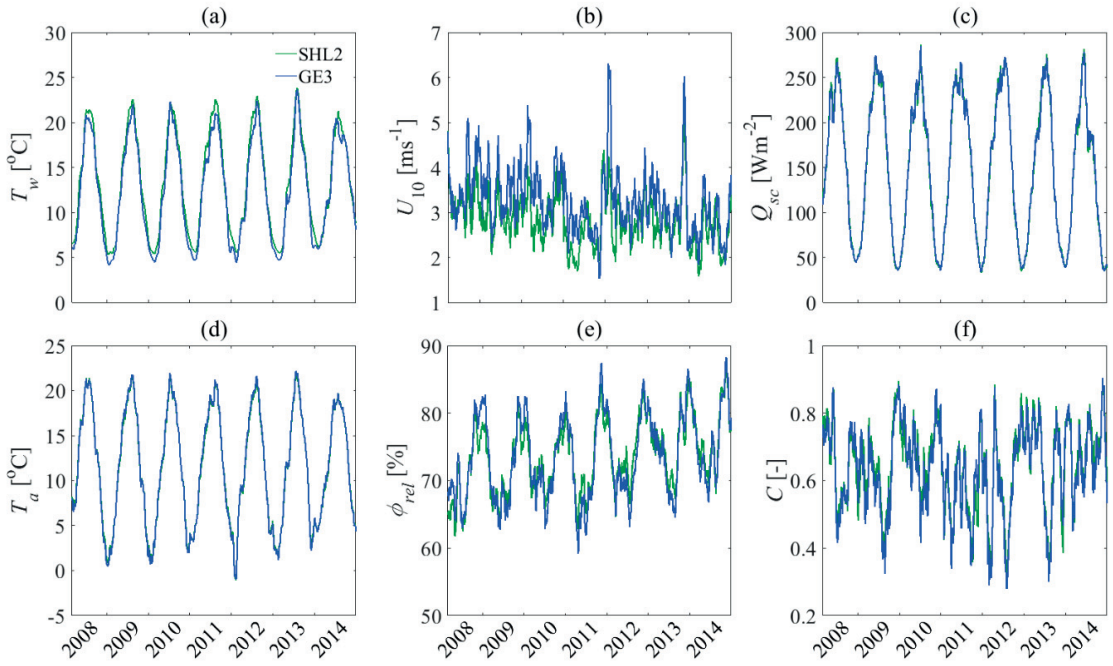

Fig. 2.1. Time series of Lake Surface Water Temperature (LSWT) and meteorological data smoothed with a 30-d moving average at SHL2 and GE3 employed in the SurHF calculations: (a) LSWT, T_w, (b) wind speed, U_{10}, (c) global radiation, Q_{sc}, (d) air temperature, T_a, (e) relative humidity, ϕ_{rel}, and (f) cloudiness, C.

2.2.6. Model calibration procedure

The net SurHF, i.e., the air-water heat exchange in Eq. 2.5, is usually estimated using bulk formulas. These formulas are based on different concepts and require specific parameters. Ideally, these parameters are known for a given set of conditions (e.g., a lake), but, in practice, they should be calibrated.

For each of the five SurHF terms in Eq. 2.5 that remain to be solved, there are various formulations available in the literature, and their possible combinations give rise to numerous net SurHF models. In this study, we evaluated 54 net SurHF model combinations and report here in more detail the results for the six combinations considered optimal. Details of the formulas and parameters are presented in the SI (Tables S2.1-S2.4). The relative contributions of the incoming long-wave radiation and latent heat flux (evaporation) on the long-term variation of lake heat budgets are more significant compared to other heat flux terms (Kuhn 1978), a finding confirmed in our study (details not reported). There is a similarity between the

formulas for the Q_{ev} and Q_{co} estimation that is attributed to the physical analogy between processes controlling humidity and air temperature. Therefore, we re-examined Q_{an}, Q_{ev} and Q_{co}, and recalibrated them. We used one model for Q_{sn} and Q_{br}, two models for Q_{an}, and three models for the Q_{ev}/Q_{co} calculations in Eq. 2.5. Table 2.1 summarizes the references and the corresponding calibration factors for each SurHF component. The combination of equations used in each of the six SurHF models is given in Table 2.2.

Table 2.1. Selected bulk formulas and their corresponding calibration coefficients for five surface heat flux (SurHF) components, Details of each model are given in Tables S2.1-S2.4

SurHF components and equations			**References**	**Corresponding calibration factors**
Solar shortwave radiation	Q_{sn}	Eq. S2.1	Cogley (1979); Fink et al. (2014)	-
Atmospheric long-wave radiation	Q_{an1}	Eq. S2.2	Brutsaert (1975)	C_{an} and C_{cloud}
	Q_{an2}	Eq. S2.3	Crawford and Duchon (1999)	C_{lc} and C_{lt}
Back radiation	Q_{br}	Eq. S2.4	Livingstone and Imboden (1989); Fink et al. (2014)	-
Latent (evaporation) and sensible (convection) heat fluxes	$(Q_{ev} + Q_{co})_1$	Eq. S2.5	Bowen (1926); Murakami et al. (1985)	C_{mur} and C_b
	$(Q_{ev} + Q_{co})_2$	Eq. S2.6	Ryan et al. (1974); Gill (1982)	$C_{e,r}$ and $C_{h,r}$
	$(Q_{ev} + Q_{co})_3$	Eq. S2.7	Monin and Obukhov (1954); Woolway et al. (2015b)	C_{m2} and C_{q1}

Table 2.2. Equations used in each of the six selected surface heat flux (SurHF) models. See Table 2.1 for references for each heat flux term (details are given in Tables S2.1-S2.4)

Model Number	Constituent Equations
1	$Q_{sn} + Q_{an1} + Q_{br} + (Q_{ev} + Q_{co})_1$
2	$Q_{sn} + Q_{an1} + Q_{br} + (Q_{ev} + Q_{co})_2$
3	$Q_{sn} + Q_{an1} + Q_{br} + (Q_{ev} + Q_{co})_3$
4	$Q_{sn} + Q_{an2} + Q_{br} + (Q_{ev} + Q_{co})_1$
5	$Q_{sn} + Q_{an2} + Q_{br} + (Q_{ev} + Q_{co})_2$
6	$Q_{sn} + Q_{an2} + Q_{br} + (Q_{ev} + Q_{co})_3$

The calibration factors listed in Table 2.1 were optimized based on energy conservation over time, (Eq. 2.4). The Generalized Likelihood Uncertainty Estimation (GLUE) methodology (Beven and Binley 1992) was applied to calibrate the six SurHF models in Table 2.2. This methodology requires a validity range for each parameter, a sampling strategy for the parameter space and a likelihood measure for each parameter set. The range of different parameters was chosen according to physical limitations as well as their reported ranges in the literature, particularly for Swiss lakes. The details on the range of parameters and the sampling strategy can be found in the SI. To evaluate the temporal variation of the model heat content, the Root Mean Square Error (RMSE) with respect to observations was selected as the minimized optimization metric:

$$RMSE = \sqrt{\frac{\sum_{i=1}^{N}\left\{\left[G_o(t_i) - G_o(t_1)\right] - \left[G_m(t_i) - G_m(t_1)\right]\right\}^2}{N}} \tag{2.6}$$

where N is the number of total observations at the two measurement locations (SHL2 and GE3, Fig. 1.1) at time t_i. However, in cases where RMSEs are close for different models, other metrics, such as correlation coefficient and standard deviation were used.

2.3. Assessment and results

2.3.1. Model calibration and assessment

2.3.1.1. Calibrated versus uncalibrated net surface heat flux models

Various combinations of SurHF models were studied applying the water column energy balance First, we examined the performance of the different models using coefficient values given in the literature, with an emphasis on those used in other lake studies in Switzerland. These include C_{cloud} = 0.17, C_{an} = 1.0592 and C_b = 0.62 as in Fink et al. (2014), C_{lt} = 0.06 and C_{lc} = 1.22 (Crawford and Duchon 1999), $C_{mur} = 1.2 \times 10^{-7}$ (Murakami et al. 1985), $C_{e,r} = 2.1 \times 10^{-3}$ and $C_{h,r} = 1.45 \times 10^{-3}$ (Wahl and Peeters 2014), C_{m2} = 0.11 and C_{q1} = -2.67 (Zeng et al. 1998).

A Taylor diagram (Taylor 2001) was used to determine how well the results of the six SHF models matched the observations (Eq. 2.4). The Taylor diagram (Fig. 2.2) provides a comparison between a group of models and a reference observation by combining correlation coefficients, RMSE and standard deviations in a single figure. Here, the reference is the heat content variation at the SHL2 and GE3 locations, ΔG_o, calculated by Eqs. 2.1 and 2.2. The comparison groups are the heat content variation calculated with these six different net SurHF models, ΔG_m, estimated by Eq. 2.3. These models and their corresponding SurHF terms are described in Tables 2.1 and 2.2. The results reveal that the models using the predefined (uncalibrated) values lead to a high standard deviation and RMSE (1.2-7.7 GJm^{-2}), and a low correlation coefficient (less than 0.4) compared to the observations. These substantial deviations emphasize the significance of performing a pre-analysis before applying the SurHF models for long-term air-water heat exchange investigations. Furthermore, the model-observation deviation is higher for uncalibrated models using atmospheric emissivity as proposed by Crawford and Duchon (1999), ε_{an2} (Eq. S2.3b, Table S2.1), resulting from an overestimation of Q_{an2} due to a presumably high (uncalibrated) C_{lc} value, 1.22. Crawford and Duchon (1999) reported a monthly mean bias error of -9 to 4 W m^{-2} based on their data for a 1-y period using this formula. In summary, all six models using these predefined coefficients failed to reproduce the heat content variation at both the SHL2 and GE3 locations.

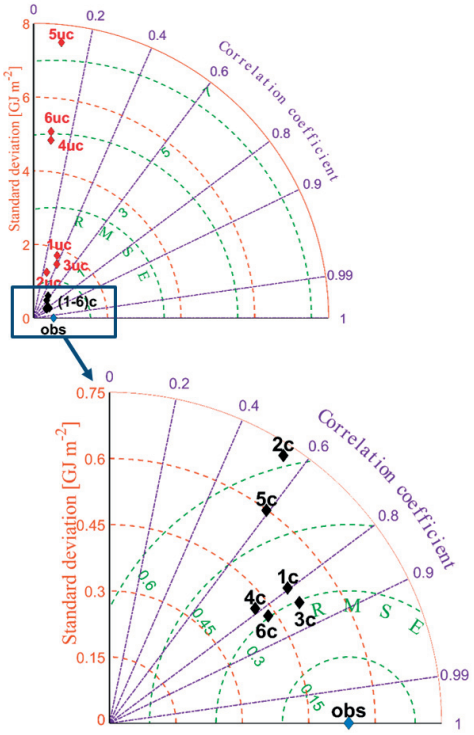

Fig. 2.2. Taylor diagrams showing a statistical comparison of the individual net surface heat flux (SurHF) models with respect to observations. Both uncalibrated, "uc" (in red), and calibrated, "c" (in black), models are shown by their corresponding numbers (see Table 2.2). Green dashed lines, orange dashed lines and purple dashed lines indicate RMSE, standard deviation and correlation coefficient, respectively. The lower diagram is a zoom of the blue rectangle in the upper diagram. For details, see the text.

Therefore, we followed the optimization and calibration procedure for all model combinations, as explained above, using a two-location calibration approach. The zoomed lower panel of Fig. 2.2 presents the model-observation comparison for the optimum (calibrated) net SurHF models and the combined observations at SHL2 and GE3. The results show a great improvement over the uncalibrated estimations. Models 1 and 4 (Table 2.2), which calculate turbulent heat fluxes using $(Q_{ev} + Q_{co})_1$ have a higher correlation coefficient, lower RMSE and smaller standard deviation than Models 2 and 5 using $(Q_{ev} + Q_{co})_2$. The simple Murikami's and Bowen's formulations, $(Q_{ev} + Q_{co})_1$, yield a better estimation of Lake Geneva's surface heat exchange than considering the effect of both free and forced convection in $(Q_{ev} + Q_{co})_2$. For the model of Ryan et al. (1974), turbulent heat fluxes, $(Q_{ev} + Q_{co})_2$, were derived under laboratory conditions where forced convection is not significant compared to free convection and the air-water temperature difference was greater than in natural systems. However, the similarity theory, $(Q_{ev} + Q_{co})_3$ in Table 2.1, applied in Models 3 and 6, reproduces the temporal variation of turbulent heat fluxes far better than the other two algorithms.

Since the calibrated Models 3 and 6 have similar RMSEs, we applied additional statistical methods, i.e., correlation coefficient and standard deviation, to select the best model for SurHF

estimation. We also calculated the bias between the observed and modeled heat contents for each model. Models 3 and 6 result in nearly identical correlation coefficients and RMSEs (purple lines and green lines in Fig. 2.2). However, Model 3 gives a slightly better standard deviation than Model 6 (blue lines in Fig. 2.2) while the estimated bias using Model 6 is slightly smaller than Model 3. Although the temporal variation of heat contents by implementing Model 3 and Model 6 are not noticeably different (results not shown), Model 3 was selected as the best model resulting from the Taylor diagram comparison (Fig. 2.2).

2.3.1.2. Two-point versus one-point calibration

Our analysis (Fig. 2.2) shows that, regardless of the chosen model, recalibration greatly improves the estimation of the long-term surface heat exchange for Lake Geneva. In order to determine whether there is a significant difference between the one-point and two-point calibrations, we calibrated the six SurHF models using either SHL2 or GE3 temperature profiles. Figure 4 shows the heat content variation comparison between observations ΔG_o and Model 3 results ΔG_m. The SurHF model calibrated at SHL2 overestimates the SurHF at GE3 (Fig. 2.3a), while SurHF values are underestimated at SHL2 using only the GE3 temperature profiles for model calibration (Fig. 2.3b). Therefore, SurHF models calibrated using only one temperature profile location fail to predict the profile at the other location. Similar results were obtained using the other five net SurHF models (results not shown). This confirms that there is a significant difference between the one-point and two-point calibration.

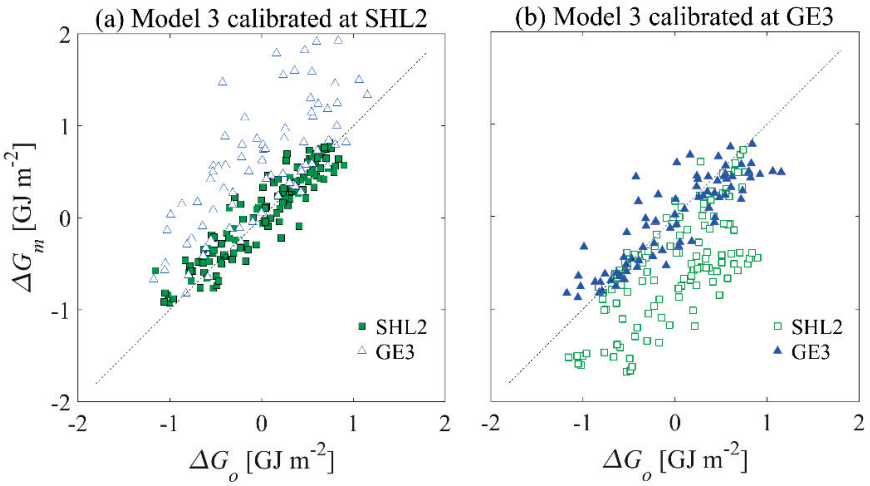

Fig. 2.3. Heat content variation comparison between observations at SHL2 (green squares) and GE3 (blue triangles) employing Model 3 with a calibration at (a) SHL2, and (b) GE3.

2.3.1.3. Intercomparison of lake heat content variation

A group of four optimal calibration factors was obtained for each of the six models, listed in Table 2.2, using the two-point calibration. For the remaining analysis, only these values are employed. The observed heat content variation, ΔG_o, and the corresponding heat content variation using the six different calibrated models, ΔG_m, are compared in Fig. 2.4. Here, the model performances at SHL2 and GE3 are investigated separately. Using Models 2 and 5, the SHL2 and GE3 results are roughly distributed below and above the optimal dashed line, respectively, and have the largest scatter. This demonstrates that the worst combination of sensible-latent heat flux terms, $(Q_{ev} + Q_{co})_2$ (Eq. S2.6, Table S2.3), underestimates the SurHF at SHL2, while it is overestimated at GE3. Although this two-point separation is less pronounced using Models 1 and 4 (left panels of Fig. 2.4), these models still have a relatively higher RMSE and lower correlation coefficient compared to the best models (Fig. 2.2). Models 3 and 6, which are the best models in terms of RMSE, employ similarity theory, $(Q_{ev} + Q_{co})_3$ (Eq. S2.7, Table S2.3), for turbulent heat flux estimation. Model 3 uses Brutsaert's formulation (Eq. S2.2, Table S2.1), while Crawford-Duchon's approach (Eq. S2.3, Table S2.1) quantifies atmospheric radiation in Model 6. Therefore, using a more advanced model for the sensible-latent SurHF calculation, Eq. S2.7, Table S2.3, not only leads to better model-observation statistics, but it also reproduces the heat content of individual points better than the other models.

When comparing Models 1-3 (top panels) with Models 4-6 (bottom panels) in Fig. 2.4, it should be noted that in the top panels, the results for SHL2 mainly cluster above the optimal line, whereas those for GE3 are mainly below that line. Such a clear separation between the results of the two stations is less obvious in the bottom panels. Models 1-3 use the Brutsaert (1975) formulation for cloud cover, and the remaining models use the more complex model of Crawford and Duchon (1999). This latter formulation gives more realistic results in terms of the model bias.

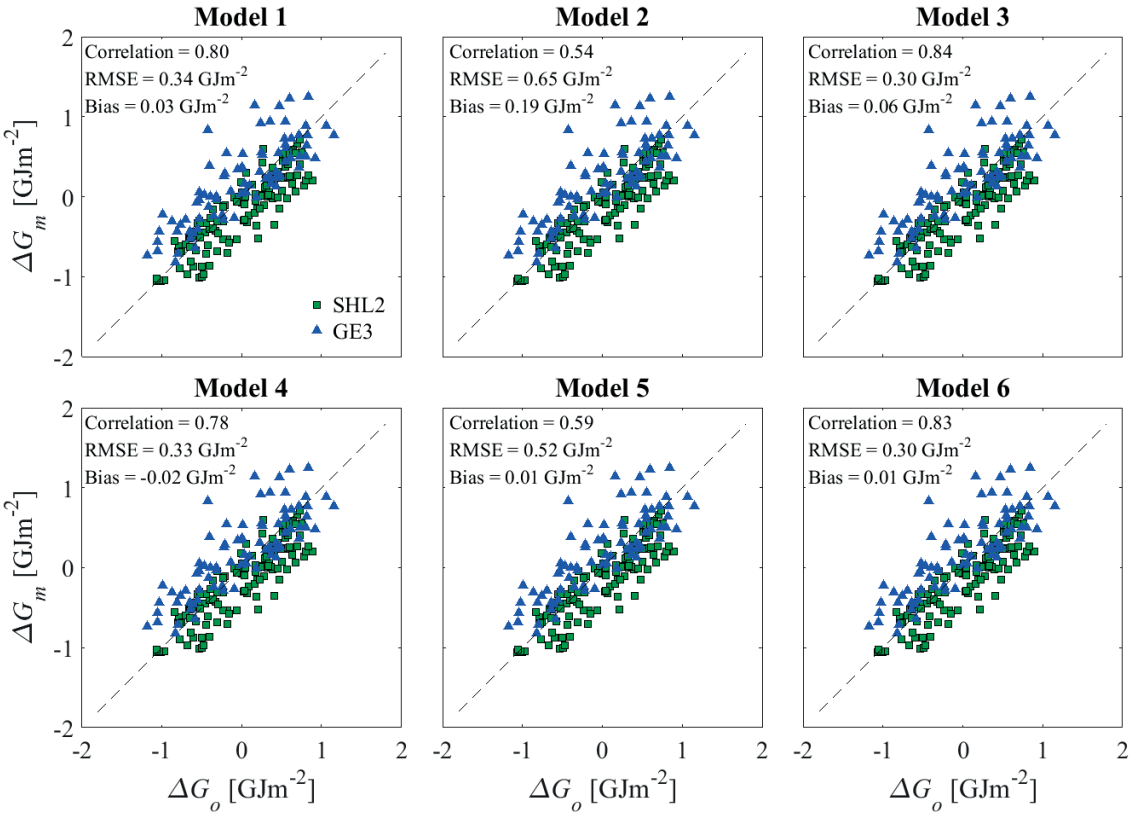

Fig. 2.4. Heat content variation comparison between observations at SHL2 (green squares) and GE3 (blue triangles) for six different model combinations. The individual formulas used in each model are given in Table 2.2 (see Tables S2.1-S2.4 for more details).

Using the best and worst models (respectively, Model 3, closest to "obs" in Fig. 2.2, and Model 2, furthest from "obs" in Fig. 2.2), time series of the modeled lake heat content at the calibration locations are compared with observations in Fig. 2.5. As stated above, the calibration factors are assumed constant. However, if each location is treated independently in the calibration process, there is little or no difference between the models (results not shown). This, again, demonstrates the significant improvement resulting from the two-point calibration and the use of optimal heat flux term concepts.

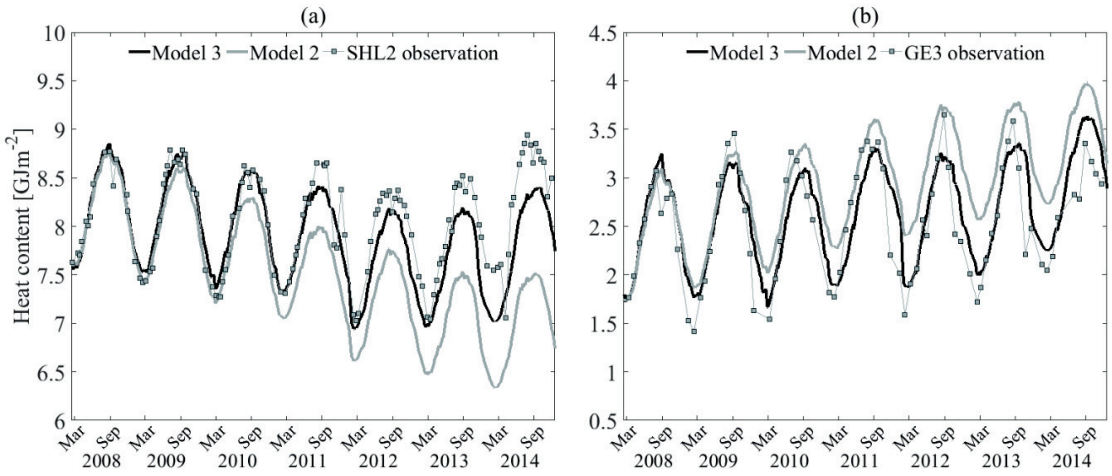

Fig. 2.5. Temporal evolution of the lake heat content. Model results compared to observations (points) at (a) SHL2, and (b) GE3 (see Fig. 1.1 for station location). Only the best (Model 3, black lines) and the worst (Model 2, grey lines) models are presented. Note that due to the difference in depth at the two locations, i.e., 309 m at SHL2 and 70 m at GE3, the absolute values of heat content (vertical axis) have different magnitudes in (a) and (b).

2.3.1.4. Intercomparison of net surface heat flux

In order to compare the net SurHF, Q_N [Wm^{-2}], at SHL2 and GE3 obtained with the six selected models using the best-fit parameters, the mean and standard deviation of Q_N were calculated for the period 1 January 2009 to 31 December 2014 (due to missing data, the January-February 2008 results were excluded). The mean value of SurHF at GE3 is higher than at SHL2 in all models (Table 2.3). The mean SurHF difference ranges from 4 to 10.7 Wm^{-2} for Models 6 and 2, respectively. In terms of mean net SurHF, Model 6, and to a lesser extent Model 1, are close to Model 3, while Model 2 has the largest deviation. The results of Models 5 and 6 have the maximum and minimum standard deviation differences with respect to Model 3 at the two locations. Consequently, there will be marked differences between the models if integrated over the entire lake and considered over an annual cycle.

The mean net SurHF at SHL2 and GE3 are -1 and 3.4 Wm^{-2}, respectively, for 2009-2014. The results indicate that on average, some parts of the lake, e.g., GE3, are warming at the same time as other regions are cooling down, e.g., SHL2, for this period. This emphasizes the importance of using multiple locations (or ideally the entire lake) instead of only one location for SurHF and lake heat content studies, especially for long-term analyses. The high standard deviation

values in Table 2.3 result from using hourly estimates. When the data are smoothed with a 30-d moving average, standard deviations of 88.9 and 95.6 Wm^{-2} for SHL2 and GE3, respectively, are obtained with Model 3. Although the difference between these standard deviations is small, it shows that the SurHF distribution can vary systematically from one point to another over a large lake. Furthermore, the SurHF values are spread over a slightly wider range at GE3 than at SHL2. This distribution is the response to the combined contribution of various meteorological parameters, for which spatial variations are likely to occur. Figures 2.1 and S2.3, for example, illustrate this variability at the two studied locations.

Table 2.3. Mean and standard deviation of net surface heat flux (SurHF), Q_N, at SHL2 and GE3 using the six SurHF models specified in Table 2.2 for the period 2009-2014. Model 3, in bold, is the best model based on the results in the Taylor diagram (Figs. 2.2 and 2.4)

	Location	Model 1	Model 2	**Model 3**	Model 4	Model 5	Model 6
Mean [Wm^{-2}]	SHL2	-1.1	-6.2	**-1.0**	0.4	-2.5	-0.7
	GE3	4.7	4.5	**3.4**	4. 8	6.1	3.3
Standard deviation [Wm^{-2}]	SHL2	221.9	219.4	**232.4**	219. 6	219.4	228.6
	GE3	223.2	220.2	**238.9**	222.2	219.6	235.8

2.3.2. Surface heat flux estimation

We calculated SurHF terms at two locations using the best model (Model 3), with the four best-fit coefficient values $C_{cloud,opt}$ = 0.11, $C_{an,opt}$ = 0.983, $C_{m2,opt}$ = 0.01 and $C_{q1,opt}$ = -1.52. The $C_{cloud,opt}$ value is lower than C_{cloud} = 0.17 determined by Kuhn (1978) and used in other studies in Switzerland (Livingstone and Imboden 1989; Fink et al. 2014). The parameter $C_{an,opt}$ is also slightly lower than the values of 1.09 and 1.0592 employed in those studies. To verify the calibrated values for C_{cloud} and C_{an}, we evaluated the computed atmospheric emissivity for the SHL2 and GE3 stations. The emissivity values, ε_{an1} (Eq. S2.2b, Table S2.1), fluctuate between 0.6 and 1, with the lower emissivity values being valid for clear skies and low air temperatures

in winter and the highest values during warm and fully cloudy summertime conditions. The C_{m2} and C_{q1} factors will be further discussed in the next section.

The calculated temporal variation of five SurHF terms and the net SurHF for the study period using Model 3 is presented in Fig. 2.6 (results were smoothed with a 30-d moving average). There is a high correlation (> 0.97) for the radiative heat fluxes, Q_{sn}, Q_{an} and Q_{br} at SHL2 and GE3. However, due to the difference in variation of wind speed, relative humidity and LSWT at SHL2 and GE3 (U_{10}, ϕ_{rel}, and T_w in Figs. 2.2 and S2.6), the correlation coefficients of sensible, Q_{co}, and latent, Q_{ev}, heat fluxes between SHL2 and GE3 are 0.8 and 0.63, respectively, based on hourly values. A correlation coefficient of 0.93 was found between the net SurHF Q_N at SHL2 and GE3. The mean and standard deviation of the different SurHF terms at both locations for the period 1 January 2009 to 31 December 2014 are given in Table 2.4. Examining the results for different SurHF terms reveals that radiative components mainly contribute to the variation of the mean net SurHF at each location. The higher standard deviation of the net SurHF at the GE3 location compared to SHL2 (Table 2.3) can be explained by the higher standard deviation values of turbulent heat fluxes at this location (Table 2.4).

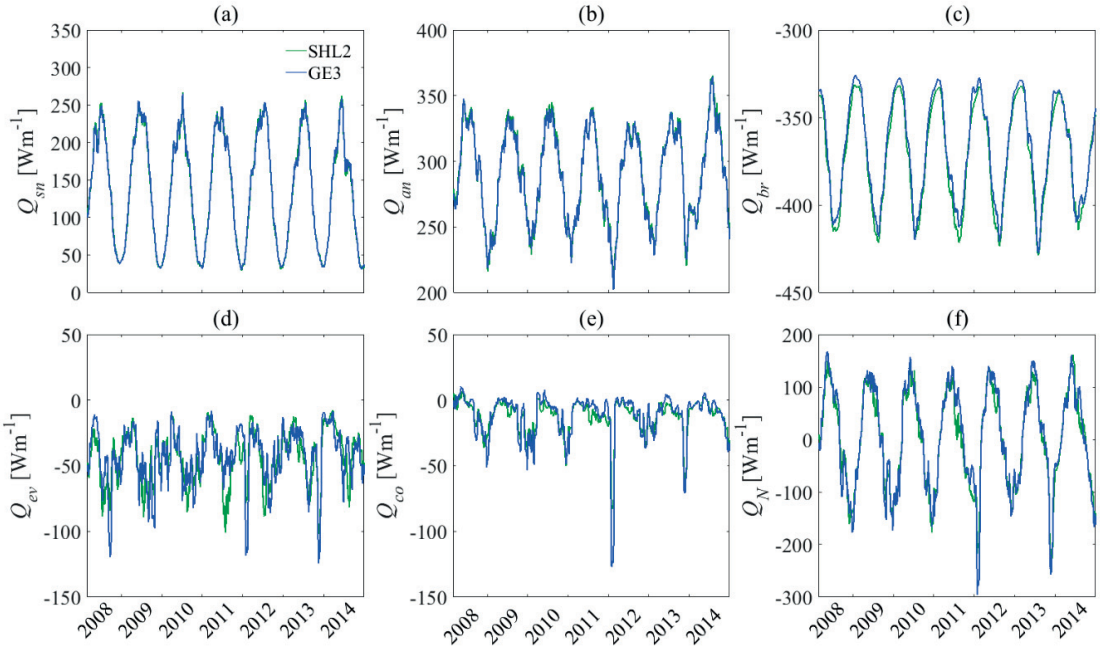

Fig. 2.6. Long-term time series of the surface heat flux (SurHF) terms and net SurHF of Lake Geneva at SHL2 (green lines) and GE3 (blue lines) smoothed with a 30-d moving average obtained with Model 3: (a) solar radiation, Q_{sn}, (b) atmospheric radiation, Q_{an}, (c) back radiation, Q_{br}, (d) latent heat flux, Q_{ev}, (e) sensible heat flux, Q_{co}, and (f) net SurHF, Q_N. The horizontal axis indicates the year.

Table 2.4. Mean and standard deviation of different surface heat flux (SurHF) terms at SHL2 and GE3 using Model 3 for the period 2009-2014

	Location	Q_{sn}	Q_{an}	Q_{br}	Q_{ev}	Q_{co}
Mean [Wm^{-2}]	SHL2	136.4	289.7	-371.4	-42.8	-12.9
	GE3	137.2	288.7	-367.5	-42.7	-12.3
Standard deviation [Wm^{-2}]	SHL2	210.4	50.6	30.8	58.4	31.1
	GE3	210.7	50.2	30.6	64.7	39.8

2.4. Discussion

2.4.1. Bulk transfer coefficients

The model assessment shows that using an appropriate model for the sensible-latent heat flux estimation is essential for the two-point calibration. The results indicate that some models fail to reflect the long-term heat content variation at two points. Based on the RSME, the bulk aerodynamic algorithm using the similarity theory and empirical relationships, $(Q_{ev} + Q_{co})_3$ in Table 2.2 (details in Eq. S2.7, Table S2.3), was the best model. Two components must be defined in this algorithm: turbulence stability functions, f_m, f_e and f_h, and roughness lengths for momentum, temperature and humidity, z_0, z_{0t} and z_{0q}, respectively. Details of the calculation procedure are given in the SI. Unlike the other selected models, i.e., $(Q_{ev} + Q_{co})_1$ and $(Q_{ev} + Q_{co})_2$ in Table 2.2, the heat transfer coefficients are not constant in this algorithm. The spatiotemporal values of the transfer coefficients, $C_{d,m}$, $C_{e,m}$ and $C_{h,m}$, are defined as a function of the atmospheric stability parameter (ζ, Eq. S2.7e, Table S2.3) using the Monin-Obukhov theory (Monin and Obukhov 1954). Even though wind speed is often considered to be the main physical parameter affecting the transfer coefficient values, other processes such as waves and relative humidity may also contribute (Toffoli et al. 2012).

The obtained optimal values, $C_{m2,opt}$ = 0.01 and $C_{q1,opt}$ = -1.52, are, respectively, lower and higher than the optimum values of Zeng et al. (1998), i.e., $C_{m2,uc}$ = 0.11 and $C_{q1,uc}$ = -2.57.

Figure 2.7 illustrates the variation of $C_{e,m}$ and $C_{d,m}$ as a function of wind speed, U_{10}, comparing the uncalibrated and calibrated factors. The coefficient $C_{h,m}$ has a similar shape to $C_{e,m}$ (not shown here). These curves were obtained by randomly sampling 2000 points from the dataset under unstable conditions (negative stability parameter, $\zeta < 0$). Following the sensitivity analysis in Fig. S2.8, the difference between calibrated and uncalibrated factors results in lower (higher) humidity and temperature bulk transfer coefficients under low (high) wind speed conditions (Fig. 2.7a). We assumed a constant value of 0.013 for the Charnock parameter (Charnock 1955) in the calculation of the momentum roughness length, z_0 (Eq. S2.8). Therefore, the drag coefficient, $C_{d,m}$, under high wind conditions (> 7 ms^{-1}) is similar for uncalibrated and calibrated conditions (Fig. 2.7b).

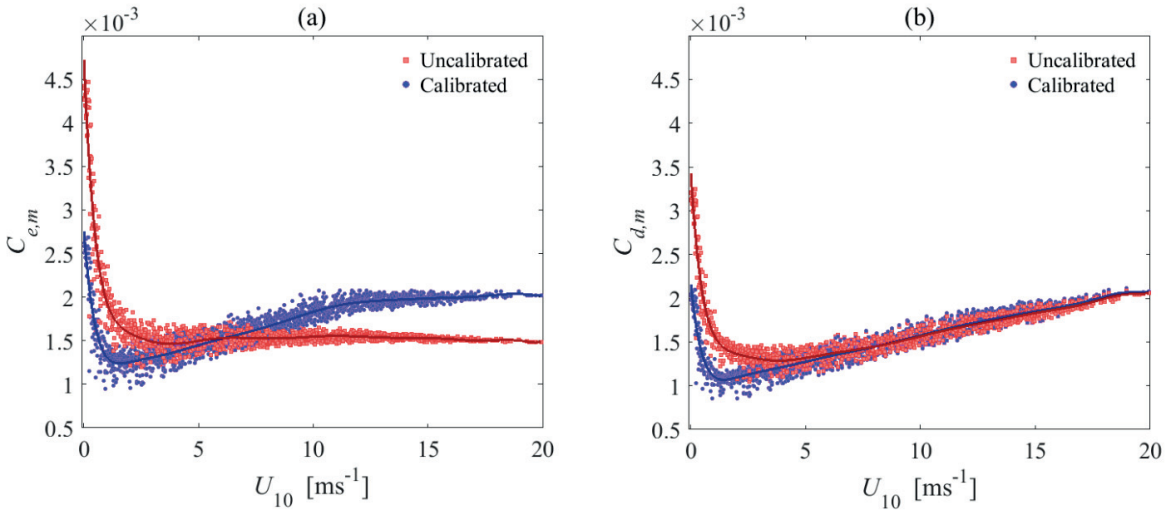

Fig. 2.7. (a) Humidity bulk transfer coefficient, $C_{e,m}$, and (b) drag coefficient, $C_{d,m}$, as a function of wind speed, $U_{10,}$ using uncalibrated ($C_{m2,uc}$ = 0.11 and $C_{q1,uc}$ = -2.57; in red) and calibrated parameters ($C_{m2,opt}$ = 0.01 and $C_{q1,opt}$ = -1.52; in blue).

To verify the calibration factors, we compare the shape and range of these curves with some measurements taken over water. The general form of theses curves is similar to the measured values over inland and open waters (e.g., Wüest and Lorke 2003; Wei et al. 2016). Since we obtained lower values for both C_{m2} and C_{q1} than Zeng et al. (1998), the calibrated transport coefficients are smaller (higher) at low (high) winds than the uncalibrated coefficients in Fig. 2.7. These coefficients are sensitive to the choice of parameterization, especially in low wind regimes (Webster and Lukas 1992). For weak winds, the measured data cover a wide range of

drag coefficients from ~ 2×10^{-3} to 2×10^{-2}. Higher coefficient values (~ 2×10^{-2}) are reported mainly for ocean experiments (Geernaert et al. 1988; Bradley et al. 1991) while lower values (~ 2×10^{-3}) were observed over shallow coastal waters (Mahrt et al. 1996) and estuaries (Lin et al. 2002). Wei et al. (2016) found a high drag coefficient value of ~ 10^{-2} at a wind speed of ~ 1 ms^{-1} for Lake Kasumigaura (Japan), while a value of ~ 2.5×10^{-3} was measured for Lake Neuchatel (Switzerland), for the same wind speed (Simon 1997). For Lake Kasumigaura, however, the humidity transfer coefficient was ~ 3×10^{-3} at 1 ms^{-1} wind speed, which is closer to our estimated values (Fig. 2.7a). Under high wind regimes, the calibrated value (~ 2×10^{-3}) and the almost linear variation of the transfer coefficients are in agreement with reported measurements (Graf and Prost 1980; Merzi and Graf 1988; Mahrt et al. 1996; Babanin and Makin 2008; Toffoli et al. 2012; Wei et al. 2016). Although the transfer coefficient values are consistent with other studies, there is a shift in the wind speed under which these minima are observed. The minimum values of the transfer coefficients (~ 10^{-3}) were obtained at a low wind speed of ~ 2 ms^{-1} (Fig. 2.7), whereas the minima reported in the literature are, for example, at ~ 4 ms^{-1} (Mahrt et al. 1996; Lin et al. 2002) or ~ 5 ms^{-1} (Wüest and Lorke 2003; Wei et al. 2016).

The large scatter seen in the transport coefficients under weak wind regimes could be due to the measurement technique, method of statistical calculation, or site-dependent parameters. Recently, Wei et al. (2016) suggested some possible reasons for high values at low wind speeds, e.g., the lake surface current, wave effects, gustiness, etc. However, the behavior of transfer coefficients under low wind speeds is less clear. Mahrt et al. (1996) investigated the influence of fetch on the drag coefficient curve. They reasoned that the drag coefficient for a short fetch (< 4 km) is greater than for a long fetch, particularly for high wind speeds. They associated this variation to the wave field difference under different fetches. Their results also indicate that the drag coefficient for short fetches has a minimum at a wind speed of ~ 3 m s^{-1}. Our results agree with the short-fetch results of Mahrt et al. (1996), especially for low wind speeds (< 3 ms^{-1}). The variation of transport coefficients in this regime is mainly due to the second term in the right-hand side of Eq. S2.8, $C_{m2}v_a/u_*$. Compared to measurements by Zeng et al. (1998), Wüest and Lorke (2003) and Wei et al. (2016), the lower transport coefficients at low wind speeds reported here are due to the small C_{m2} value, 0.01, compared to the commonly used value of 0.11. Other parameterizations for this term are proposed, e.g., $C_{m3}\sigma_w/\rho_w u_*^2$ (Jin 1994; Bourassa et al. 1999), where C_{m3} is a calibration factor and σ_w is the surface tension. Better insight into

realistic parameterizations could be obtained from systematic direct measurements of the atmospheric boundary layer.

2.4.2. Sensitivity of the calibration factors

We quantified the effect of uncertainty associated with the four calibration factors using a straightforward sensitivity analysis in which one parameter was varied over a specific range while keeping the remaining three constant. The difference in heating/cooling caused by the different parameters is expressed as the temperature change in the near surface water layer, e.g., the upper 10 m of the water column, ΔT [°Cy^{-1}], using:

$$\Delta T = \frac{\Delta G_{m,sen}}{\rho_w C_{p,w} H_{sl}} \tag{2.7}$$

where $\Delta G_{m,sen}$ [Jm^{-2}y^{-1}] is the mean annual heat content change due to variation of the corresponding parameter, and H_{sl} is the surface layer depth [m]. This metric was used to compare the cooling/heating induced by employing uncalibrated SurHF box models with a warming water temperature trend. In this context, a ±1°Cy^{-1} variation is approximately equal to a ±1.3 Wm^{-2} bias in the estimation of the net SurHF.

Figure 2.8 shows the effect on the heat content variation at SHL2 and GE3. The results indicate that relatively small deviations in calibration factors, particularly in C_{an}, affect the lake's temperature trend significantly and can be much higher than the annual climate change trend of 0.065 °Cy^{-1} reported by Gillet and Quetin (2006) for the near surface layer. Variations in C_{an} and C_{cloud} have a linear influence on the heat flux estimation (Figs. 2.8a and b) while the effect of an uncalibrated C_{q1} and C_{m2} is non-linear (Figs. 2.8c and d). This is due to non-linearity inherent in the turbulent heat flux parameterization. The sensitivity of the results to C_{an} variations is striking (Fig. 2.8a), whereas variations of C_{q1} are less marked (Fig. 2.8c). A small deviation in C_{an} (< 1%) results in a noticeable change in the SurHF estimation (> 2.5 Wm^{-2}), and consequently the lake heat content. The results are also sensitive to C_{cloud}. A ±10% variation of C_{cloud} leads to a bias of ~ ±1.6 Wm^{-2} in the estimation of net SurHF.

The results also indicate that the responses to C_{q1} and C_{m2} at SHL2 and GE3 are different. The C_{m2} variation has a more pronounced effect at SHL2 (Fig. 2.8c) while GE3 is more sensitive to C_{q1} (Fig. 2.8d) due to the spatial variability of meteorological forcing and LSWT over Lake

Geneva. The differences in wind speed, LSWT and relative humidity are quite noticeable between the two locations (Figs. 2.1 and S2.6). Wind speed variations (Fig. 2.1b), for example, are on average higher at GE3 than at SHL2. Since the value of C_{m2} mainly affects the intensity of turbulent heat fluxes at low wind regimes (Fig. S2.8a), the tendency for weak winds to occur at SHL2 reflects its sensitivity to C_{m2}. In contrast, stronger wind forcing at GE3 makes it more sensitive to the value of C_{q1}, which controls heat flux for high wind regimes (Fig. S2.8b). Again, these differences underscore the possible significant errors arising from single-point model calibration.

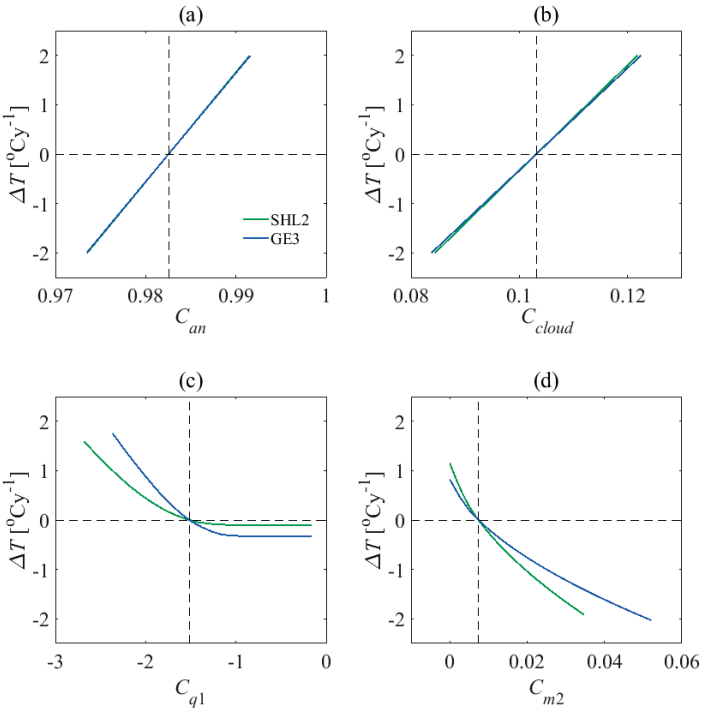

Fig. 2.8. Sensitivity analysis of model-induced cooling/warming for the upper 10 m of Lake Geneva at SHL2 (green lines) and GE3 (blue lines) depending on the optimum calibration factors for (a) C_{an}, (b) C_{cloud}, (c) C_{q1}, and (d) C_{m2}. The vertical dashed lines indicate the position at the optimum values for each calibration factor resulting from our analysis. Note that there is a high amount of overlap between the green and blue lines in panels (a) and (b).

The same analysis can be applied to quantify the effect of geothermal heat flux on the model calibration. The water column heat content variation due to geothermal bottom heating is ~ 0.003 $GJm^{-2}y^{-1}$ using the typical value for the geothermal heat flux, i.e., ~ 0.1 Wm^{-2} (Finckh

1976), which is 100 times smaller than the calculated RMSE employing Model 3 (legends in Fig. 2.4). Since this variation is small, we did not repeat the optimization procedure with the updated heat content values. Instead, we used the sensitivity analysis results to estimate its effect on the obtained calibration factors. The calculated geothermal induced slight warming (0.003 $GJm^{-2}y^{-1}$) corresponds to a 0.08 $°Cy^{-1}$ variation in a 10-m water column.

2.5. Comments and recommendations

Large lakes can be characterized by considerable spatial variability in meteorological parameters. For example, the surrounding topography can exert a strong influence on the wind patterns and solar radiation, and hence on SurHF. LSWT may likewise exhibit significant spatial variability, mainly during the summertime. Therefore, the determination of SurHF at a single location only provides a partial understanding of the energy exchange dynamics over the whole lake surface and could result in significant errors in the estimation of SurHF for the whole lake. In addition, various formulations and parameterizations exist for different heat flux components, in particular for sensible and latent heat fluxes. Thus far, a systematic analysis of their optimal combination, which determines the net SurHF, has not been reported. In this study, we addressed these questions by expanding the net SurHF estimation for a 7-y period using a two-point calibration, instead of the commonly used one-point calibration. We tested 54 different net SurHF models Q_N, and presented the results for the best six models associated with different combinations of one model for solar shortwave radiation Q_{sn}, two models for atmospheric radiation Q_{an}, one model for longwave radiation from the water surface Q_{br}, and three models for turbulent heat fluxes, i.e., sensible Q_{co} and latent Q_{ev} heat fluxes. For the period 2008 to 2014, we evaluated the heat content response of Lake Geneva to these models by implementing frequently used coefficients given in the literature for comparable water bodies.

The analysis emphasizes the importance of choosing appropriate calibration factors when estimating the heat budgets of large lakes. Since none of the coefficients given in the literature provided acceptable SurHF estimates, optimization was used to find the best calibration factors for the selected SurHF models. However, the common approach of computing SurHF based on a single location did not result in satisfactory SurHF predictions at both locations. We found a high sensitivity of SurHF estimations to certain calibration factors indicating that a systematic calibration of bulk models is required for each study site. We demonstrated that a small

variation in calibration factors, especially those controlling atmospheric radiation, leads to a significant change in the heating/cooling estimation of the lake.

The results indicate that multi-point (two-point in this study) calibration is best performed using a comprehensive model for sensible-latent heat flux calculation. The parameterization in the bulk formula based on similarity theory was found to account for the spatial variability adequately. On the other hand, the temporal variation of the air-water heat exchange is highly sensitive to the atmospheric radiation modeling. Note that all the tested models gave reasonable RMSE values for short periods, i.e., less than 2 y (Fig. 2.5). However, only a few of them gave satisfactory calibration over two points for longer periods, i.e., more than 3 y. Therefore, an accurate model selection and calibration is important for long-term climate studies, assuming that the calibration remains valid for a shifting temperature pattern.

The results show that, for heat exchange analysis of large lakes, a properly calibrated atmospheric radiation model and an appropriate turbulent SurHF model are essential. The quality of the results is affected by model simplifications/limitations, errors in temperature measurements and AVHRR data retrieval, and uncertainties associated with meteorological data. However, the results are still reliable in terms of showing the need for optimized SurHF models, the advantage of two-point versus one-point calibration, and the sensitivity of the lake heat exchange to the actual values of different calibration factors. In this study, we used a 3D numerical simulation of Lake Geneva to quantify the negligible contribution of lateral heat exchange to the heat content variation of the water column far from the shore. In general, direct measurements of different heat flux terms and advective heat transport in the water body should be carried out, since this may further refine the validation of the different SurHF terms and the heat balance algorithm applied. Likewise, measurements from more than two points would extend and enhance the present survey. The methodology developed in this study and the results obtained improve the computation of the spatiotemporal SurHF over large lakes, and consequently give a better estimation of the total energy exchange at the air-water interface. At the same time, these results may increase the reliability of numerical weather modeling by better accounting for lake-atmosphere heat exchanges.

Acknowledgments

We thank the Federal Office of Meteorology and Climatology in Switzerland, MeteoSwiss, for providing us with spatiotemporal meteorological data. We also extend our appreciation to the Commission International pour la Protection des Eaux du Léman (CIPEL) for organizing the systematic in situ temperature measurements over Lake Geneva. We thank the Eco-Informatics ORE INRA Team at the French National Institute for Agricultural Research (SOERE OLA-IS, INRA Thonon-les-Bains) for collecting water temperature profiles at the SHL2 station over the period 1970-2014, and SECOE Direction générale de l'Eau du Canton de Genève (CH) for water temperature measurements at the GE3 station for the period 2008-2014. This research was supported by the Fondation pour l'Etude des Eaux du Léman (FEEL). We thank the reviewers for their constructive comments that helped improve the paper.

References

Akitomo, K., M. Kurogi, and M. Kumagai. 2004. Numerical study of a thermally induced gyre system in Lake Biwa. Limnology **5:** 103-114. doi: 10.1007/s10201-004-0122-9.

Anderson, E. J., and D. J. Schwab. 2017. Meteorological influence on summertime baroclinic exchange in the Straits of Mackinac. J. Geophys. Res.: Oceans **122:** 2171-2182. doi: 10.1002/2016JC012255.

Arvola, L., G. George, D. M. Livingstone, M. Järvinen, T. Blenckner, M. T. Dokulil, E. Jennings, C. N. Aonghusa, P. Nõges, T. Nõges, and G. A. Weyhenmeyer. 2010. The impact of the changing climate on the thermal characteristics of lakes, p. 85-101. *In* G. George [ed.], The impact of climate change on European Lakes. Springer Netherlands. doi: 10.1007/978-90-481-2945-4_6.

Austin, J. A., and J. Allen. 2011. Sensitivity of summer Lake Superior thermal structure to meteorological forcing. Limnol. Oceanogr. **56:** 1141-1154. doi: 10.4319/lo.2011.56.3.1141.

Babanin, A. V., and V. K. Makin. 2008. Effects of wind trend and gustiness on the sea drag: Lake George study. J. Geophys. Res.: Oceans **113:** C02015. doi: 10.1029/2007jc004233.

Beletsky, D., J. H. Saylor, and D. J. Schwab. 1999. Mean circulation in the Great Lakes. J. Great Lakes Res. **25:** 78-93. doi: 10.1016/S0380-1330(99)70718-5.

Beletsky, D., and D. J. Schwab. 2008. Climatological circulation in Lake Michigan. Geophys. Res. Lett. **35:** L21604. doi: 10.1029/2008gl035773.

Bennington, V., G. A. McKinley, N. Kimura, and C. H. Wu. 2010. General circulation of Lake Superior: Mean, variability, and trends from 1979 to 2006. J. Geophys. Res.: Oceans **115:** C12015. doi: 10.1029/2010jc006261.

Beven, K., and A. Binley. 1992. The future of distributed models: Model calibration and uncertainty prediction. Hydrol. Processes **6:** 279-298. doi: 10.1002/hyp.3360060305.

Bonvin, F., A. M. Razmi, D. A. Barry, and T. Kohn. 2013. Micropollutant dynamics in Vidy Bay-A coupled hydrodynamic-photolysis model to assess the spatial extent of ecotoxicological risk. Environ. Sci. Technol. **47:** 9207-9216. doi: 10.1021/es401294c.

Bourassa, M. A., D. G. Vincent, and W. L. Wood. 1999. A flux parameterization including the effects of capillary waves and sea state. J. Atmos. Sci. **56:** 1123-1139. doi: 10.1175/1520-0469(1999)056<1123:Afpite>2.0.Co;2.

Bowen, I. S. 1926. The ratio of heat losses by conduction and by evaporation from any water surface. Phys. Rev. **27:** 779-787. doi: 10.1103/Physrev.27.779.

Boyce, F. M., M. A. Donelan, P. F. Hamblin, C. R. Murthy, and T. J. Simons. 1989. Thermal structure and circulation in the Great Lakes. Atmos. Ocean **27:** 607-642. doi: 10.1080/07055900.1989.9649358.

Bradley, E. F., P. A. Coppin, and J. S. Godfrey. 1991. Measurements of sensible and latent heat flux in the western equatorial Pacific Ocean. J. Geophys. Res.: Oceans **96:** 3375-3389. doi: 10.1029/90JC01933.

Brutsaert, W. 1975. Derivable formula for long-wave radiation from clear skies. Water Resour. Res. **11:** 742-744. doi: 10.1029/Wr011i005p00742.

Carmack, E. C. 1979. Combined influence of inflow and lake temperatures on spring circulation in a riverine lake. J. Phys. Oceanogr. **9:** 422-434. doi: 10.1175/1520-0485(1979)009<0422:Cioial>2.0.Co;2.

Charnock, H. 1955. Wind stress on a water surface. Q. J. Roy. Meteor. Soc. **81:** 639-640. doi: 10.1002/qj.49708135027.

Churchill, J. H., and W. Charles Kerfoot. 2007. The impact of surface heat flux and wind on thermal stratification in Portage Lake, Michigan. J. Great Lakes Res. **33:** 143-155. doi: 10.3394/0380-1330(2007)33[143:TIOSHF]2.0.CO;2.

Cogley, J. G. 1979. Albedo of water as a function of latitude. Mon. Weather Rev. **107:** 775-781. doi: 10.1175/1520-0493(1979)107<0775:Taowaa>2.0.Co;2.

Crawford, T. M., and C. E. Duchon. 1999. An improved parameterization for estimating effective atmospheric emissivity for use in calculating daytime downwelling longwave radiation. J. Appl. Meteorol. **38:** 474-480. doi: 10.1175/1520-0450(1999)038<0474:Aipfee>2.0.Co;2.

Derecki, J. A. 1976. Heat storage and advection in Lake Erie. Water Resour. Res. **12:** 1144-1150. doi: 10.1029/Wr012i006p01144.

Emery, K. O., and G. T. Csanady. 1973. Surface circulation of lakes and nearly land-locked seas. P. Natl. Acad. Sci. USA. **70:** 93-97. doi: 10.1073/Pnas.70.1.93.

Fairall, C. W., E. F. Bradley, D. P. Rogers, J. B. Edson, and G. S. Young. 1996. Bulk parameterization of air-sea fluxes for Tropical Ocean Global Atmosphere Coupled Ocean Atmosphere Response Experiment. J. Geophys. Res.: Oceans **101:** 3747-3764. doi: 10.1029/95jc03205.

Finckh, P. 1976. Wärmeflussmessungen in Randalpenseen. ETH Zürich, Switzerland. Dissertation No. 5787. doi: 10.3929/ethz-a-000101336.

Fink, G., M. Schmid, B. Wahl, T. Wolf, and A. Wüest. 2014. Heat flux modifications related to climate-induced warming of large European lakes. Water Resour. Res. **50:** 2072-2085. doi: 10.1002/2013wr014448.

Finlay, K., R. J. Vogt, M. J. Bogard, B. Wissel, B. M. Tutolo, G. L. Simpson, and P. R. Leavitt. 2015. Decrease in CO_2 efflux from northern hardwater lakes with increasing atmospheric warming. Nature **519:** 215-218. doi: 10.1038/nature14172.

Fritsch, F. N., and R. E. Carlson. 1980. Monotone piecewise cubic interpolation. Siam. J. Numer. Anal. **17:** 238-246. doi: 10.1137/0717021.

Geernaert, G. L., K. L. Davidson, S. E. Larsen, and T. Mikkelsen. 1988. Wind stress measurements during the Tower Ocean Wave and Radar Dependence Experiment. J. Geophys. Res.: Oceans **93:** 13913-13923. doi: 10.1029/Jc093ic11p13913.

Gill, A. E. 1982. Atmosphere-ocean dynamics. Academic Press. San Diego, USA. doi: 10.1002/qj.49711046322.

Gillet, C., and P. Quetin. 2006. Effect of temperature changes on the reproductive cycle of roach in Lake Geneva from 1983 to 2001. J. Fish Biol. **69:** 518-534. 10.1111/j.1095-8649.2006.01123.x.

Graf, W. H., and J. P. Prost. 1980. Aerodynamic drag and its relation to the sea state: With data from Lake Geneva. Arch. Meteorol. Geophy. A. **29:** 67-87. doi: 10.1007/Bf02247734.

Heikinheimo, M., M. Kangas, T. Tourula, A. Venalainen, and S. Tattari. 1999. Momentum and heat fluxes over lakes Tamnaren and Raksjo determined by the bulk-aerodynamic and eddy-correlation methods. Agric. For. Meteorol. **98-9:** 521-534. doi: 10.1016/S0168-1923(99)00121-5.

Henderson-Sellers, B. 1986. Calculating the surface energy balance for lake and reservoir modeling: A review. Rev. Geophys. **24:** 625-649. doi: 10.1029/Rg024i003p00625.

Jin, W. 1994. The sea-surface is aerodynamically rough even under light winds. Bound-Lay. Meteor. **69:** 149-158. doi: 10.1007/BF00713300.

Koch, S. E., M. Desjardins, and P. J. Kocin. 1983. An interactive Barnes objective map analysis scheme for use with satellite and conventional data. J. Clim. Appl. Meteorol. **22:** 1487-1503. doi: 10.1175/1520-0450(1983)022<1487:Aiboma>2.0.Co;2.

Kuhn, V. W. 1978. Aus Wärmehaushalt und Klimadaten berechnete Verdunstung des Zürichsees. Vjschr. Naturf. Ges. Zürich **123:** 261-283. http://www.ngzh.ch/publikationen/vjs/123/4.

Laird, N. F., and D. A. R. Kristovich. 2002. Variations of sensible and latent heat fluxes from a Great Lakes buoy and associated synoptic weather patterns. J. Hydrometeorol. **3:** 3-12. doi: 10.1175/1525-7541(2002)003<0003:Vosalh>2.0.Co;2.

Lemmin, U., and N. D'Adamo. 1996. Summertime winds and direct cyclonic circulation: Observations from Lake Geneva. Ann. Geophys., Ser. A **14:** 1207-1220. doi: 10.1007/s005850050384.

Lenters, J. D., T. K. Kratz, and C. J. Bowser. 2005. Effects of climate variability on lake evaporation: Results from a long-term energy budget study of Sparkling Lake, northern Wisconsin (USA). J. Hydrol. **308:** 168-195. doi: 10.1016/j.jhydrol.2004.10.028.

Lin, W. Q., L. P. Sanford, S. E. Suttles, and R. Valigura. 2002. Drag coefficients with fetch-limited wind waves. J. Phys. Oceanogr. **32:** 3058-3074. doi: 10.1175/1520-0485(2002)032<3058:Dcwflw>2.0.Co;2.

Liston, G. E., and K. Elder. 2006. A meteorological distribution system for high-resolution terrestrial modeling (MicroMet). J. Hydrometeorol. **7:** 217-234. doi: 10.1175/Jhm486.1.

Livingstone, D. M., and D. M. Imboden. 1989. Annual heat balance and equilibrium temperature of Lake Aegeri, Switzerland. Aquat. Sci. **51:** 351-369. doi: 10.1007/Bf00877177.

Lofgren, B. M., and Y. C. Zhu. 2000. Surface energy fluxes on the Great Lakes based on satellite-observed surface temperatures 1992 to 1995. J. Great Lakes Res. **26:** 305-314. doi: 10.1016/S0380-1330(00)70694-0.

MacIntyre, S., J. R. Romero, and G. W. Kling. 2002. Spatial-temporal variability in surface layer deepening and lateral advection in an embayment of Lake Victoria, East Africa. Limnol. Oceanogr. **47:** 656-671. doi: 10.4319/lo.2002.47.3.0656.

Mahrt, L., D. Vickers, J. Howell, J. Hojstrup, J. M. Wilczak, J. Edson, and J. Hare. 1996. Sea surface drag coefficients in the Riso Air Sea Experiment. J. Geophys. Res.: Oceans **101:** 14327-14335. doi: 10.1029/96jc00748.

Merzi, N., and W. H. Graf. 1988. Wind stress over water waves: Field experiments on Lake of Geneva. Meteorol. Atm. Phys. **39:** 14-24. doi: 10.1007/Bf01029894.

Mironov, D. V. 2008. Parameterization of lakes in numerical weather prediction: Description of a lake model, p. 1-44. *In* M. Milelli [ed.], COSMO technical reports: http://www.cosmo-model.org/content/model/documentation/techReports/docs/techReport11.pdf.

Momii, K., and Y. Ito. 2008. Heat budget estimates for Lake Ikeda, Japan. J. Hydrol. **361:** 362-370. doi: 10.1016/j.jhydrol.2008.08.004.

Monin, A. S., and A. M. Obukhov. 1954. Basic laws of turbulent mixing in the ground layer of the atmosphere. Tr. Akad. Nauk SSSR Geofiz. Inst. **24:** 163-187.

Moukomla, S., and P. D. Blanken. 2017. The estimation of the North American Great Lakes turbulent fluxes using satellite remote sensing and MERRA reanalysis data. Remote Sens. **9:** 141. doi: 10.3390/Rs9020141.

Murakami, M., Y. Oonishi, and H. Kunishi. 1985. A numerical simulation of the distribution of water temperature and salinity in the Seto Inland Sea. J. Oceanogr. Soc. Jpn. **41:** 213-224. doi: 10.1007/BF02109271.

Nordbo, A., S. Launiainen, I. Mammarella, M. Lepparanta, J. Huotari, A. Ojala, and T. Vesala. 2011. Long-term energy flux measurements and energy balance over a small boreal lake using eddy covariance technique. J. Geophys. Res.: Atmos. **116:** D02119. doi: 10.1029/2010jd014542.

Nussboim, S., A. Rimmer, Y. Lechinsky, P.-O. Gutman, and D. Broday. 2017. Improving the estimation of Lake Kinneret's heat balance and surface fluxes using the Kalman Filter algorithm. Limnol. Oceanogr.: Methods **15:** 467-479. doi: 10.1002/lom3.10173.

Oesch, D. C., J. M. Jaquet, A. Hauser, and S. Wunderle. 2005. Lake surface water temperature retrieval using Advanced Very High Resolution Radiometer and Moderate Resolution Imaging Spectroradiometer data: Validation and feasibility study. J. Geophys. Res.: Oceans **110:** C12014. doi: 10.1029/2004jc002857.

Riffler, M., G. Lieberherr, and S. Wunderle. 2015. Lake surface water temperatures of European Alpine lakes (1989-2013) based on the Advanced Very High Resolution Radiometer (AVHRR) 1 km data set. Earth Sys. Sci. Data **7:** 1-17. doi: 10.5194/essd-7-1-2015.

Rimmer, A., R. Samuels, and Y. Lechinsky. 2009. A comprehensive study across methods and time scales to estimate surface fluxes from Lake Kinneret, Israel. J. Hydrol. **379:** 181-192. doi: 10.1016/j.jhydrol.2009.10.007.

Rouse, W. R., P. D. Blanken, N. Bussieres, C. J. Oswald, W. M. Schertzer, C. Spence, and A. E. Walker. 2008. Investigation of the thermal and energy balance regimes of Great Slave and Great Bear Lakes. J. Hydrometeorol. **9:** 1318-1333. doi: 10.1175/2008JHM977.1.

Rouse, W. R., C. M. Oswald, J. Binyamin, P. D. Blanken, W. M. Schertzer, and C. Spence. 2003. Interannual and seasonal variability of the surface energy balance and temperature of central Great Slave Lake. J. Hydrometeorol. **4:** 720-730. doi: 10.1175/1525-7541(2003)004<0720:Iasvot>2.0.Co;2.

Ryan, P. J., D. R. F. Harleman, and K. D. Stolzenbach. 1974. Surface heat loss from cooling ponds. Water Resour. Res. **10:** 930-938. doi: 10.1029/Wr010i005p00930.

Schertzer, W. M. 1978. Energy budget and monthly evaporation estimates for Lake Superior, 1973. J. Great Lakes Res. **4:** 320-330. doi: 10.1016/S0380-1330(78)72201-X.

Simon, A. 1997. Turbulent mixing in the surface boundary layer of lakes. ETH Zürich, Switzerland. Dissertation No. 12272. doi: 10.3929/ethz-a-001843543.

Simons, T. J. 1980. Circulation models of lakes and inland seas. Can. B. Fish Aquat. Sci.**:** 1-146.

Spence, C., P. D. Blanken, N. Hedstrom, V. Fortin, and H. Wilson. 2011. Evaporation from Lake Superior: 2-Spatial distribution and variability. J. Great Lakes Res. **37:** 717-724. doi: 10.1016/j.jglr.2011.08.013.

Stepanenko, V., K. D. Johnk, E. Machulskaya, M. Perroud, Z. Subin, A. Nordbo, I. Mammarella, and D. Mironov. 2014. Simulation of surface energy fluxes and stratification of a small boreal lake by a set of one-dimensional models. Tellus, Ser. A. **66:** 21389. doi: 10.3402/Tellusa.V66.21389.

Tanentzap, A. J., D. P. Hamilton, and N. D. Yan. 2007. Calibrating the Dynamic Reservoir Simulation Model (DYRESM) and filling required data gaps for one-dimensional thermal profile predictions in a boreal lake. Limnol. Oceanogr.: Methods **5:** 484-494. doi: 10.4319/lom.2007.5.484.

Taylor, K. E. 2001. Summarizing multiple aspects of model performance in a single diagram. J. Geophys. Res.: Atmos. **106:** 7183-7192. doi: 10.1029/2000jd900719.

Thiery, W., A. Martynov, F. Darchambeau, J. P. Descy, P. D. Plisnier, L. Sushama, and N. P. M. van Lipzig. 2014a. Understanding the performance of the FLake model over two African Great Lakes. Geosci. Model Dev. **7:** 317-337. doi: 10.5194/gmd-7-317-2014.

Thiery, W., V. M. Stepanenko, X. Fang, K. D. Johnk, Z. S. Li, A. Martynov, M. Perroud, Z. M. Subin, F. Darchambeau, D. Mironov, and N. P. M. Van Lipzig. 2014b. LakeMIP Kivu: Evaluating the representation of a large, deep tropical lake by a set of one-dimensional lake models. Tellus, Ser. A. **66:** 21390. doi: 10.3402/Tellusa.V66.21390.

Toffoli, A., L. Loffredo, P. Le Roy, J. M. Lefevre, and A. V. Babanin. 2012. On the variability of sea drag in finite water depth. J. Geophys. Res.: Oceans **117:** C00J25. doi: 10.1029/2011jc007857.

Van Emmerik, T. H. M., A. Rimmer, Y. Lechinsky, K. J. R. Wenker, S. Nussboim, and N. C. van de Giesen. 2013. Measuring heat balance residual at lake surface using distributed temperature sensing. Limnol. Oceanogr.: Methods **11:** 79-90. doi: 10.4319/lom.2013.11.79.

Verburg, P., and J. P. Antenucci. 2010. Persistent unstable atmospheric boundary layer enhances sensible and latent heat loss in a tropical great lake: Lake Tanganyika. J. Geophys. Res.: Atmos. **115:** D11109. doi: 10.1029/2009jd012839.

Wahl, B., and F. Peeters. 2014. Effect of climatic changes on stratification and deep-water renewal in Lake Constance assessed by sensitivity studies with a 3D hydrodynamic model. Limnol. Oceanogr. **59:** 1035-1052. doi: 10.4319/lo.2014.59.3.1035.

Wang, W., W. Xiao, C. Cao, Z. Q. Gao, Z. H. Hu, S. D. Liu, S. H. Shen, L. L. Wang, Q. T. Xiao, J. P. Xu, D. Yang, and X. H. Lee. 2014. Temporal and spatial variations in radiation and energy balance across a large freshwater lake in China. J. Hydrol. **511:** 811-824. doi: 10.1016/j.jhydrol.2014.02.012.

Webster, P. J., and R. Lukas. 1992. Toga Coare: The Coupled Ocean-Atmosphere Response Experiment. B. Am. Meteorol. Soc. **73:** 1377-1416. doi: 10.1175/1520-0477(1992)073<1377:Tctcor>2.0.Co;2.

Wei, Z. W., A. Miyano, and M. Sugita. 2016. Drag and bulk transfer coefficients over water surfaces in light winds. Bound-Lay. Meteor. **160:** 319-346. doi: 10.1007/s10546-016-0147-8.

Woolway, R. I., I. D. Jones, H. Feuchtmayr, and S. C. Maberly. 2015a. A comparison of the diel variability in epilimnetic temperature for five lakes in the English Lake District. Inland Waters **5:** 139-154. doi: 10.5268/Iw-5.2.748.

Woolway, R. I., I. D. Jones, D. P. Hamilton, S. C. Maberly, K. Muraoka, J. S. Read, R. L. Smyth, and L. A. Winslow. 2015b. Automated calculation of surface energy fluxes with high-frequency lake buoy data. Environ. Model. Softw. **70:** 191-198. doi: 10.1016/j.envsoft.2015.04.013.

Wüest, A., and A. Lorke. 2003. Small-scale hydrodynamics in lakes. Ann. Rev. Fluid Mech. **35:** 373-412. doi: 10.1146/annurev.fluid.35.101101.161220.

Xue, P. F., D. J. Schwab, and S. Hu. 2015. An investigation of the thermal response to meteorological forcing in a hydrodynamic model of Lake Superior. J. Geophys. Res.: Oceans **120:** 5233-5253. doi: 10.1002/2015JC010740.

Yang, J., Z.-H. Wang, Q. Li, N. Vercauteren, E. Bou-Zeid, and M. B. Parlange. 2017. A novel approach for unraveling the energy balance of water surfaces with a single depth temperature measurement. Limnol. Oceanogr. **62:** 89-103. doi: 10.1002/lno.10378.

Zeng, X. B., M. Zhao, and R. E. Dickinson. 1998. Intercomparison of bulk aerodynamic algorithms for the computation of sea surface fluxes using TOGA COARE and TAO data. J. Clim. **11:** 2628-2644. doi: 10.1175/1520-0442(1998)011<2628:Iobaaf>2.0.Co;2.

Zhu, J. R., C. S. Chen, E. Ralph, S. A. Green, J. W. Budd, and F. Y. Zhang. 2001. Prognostic modeling studies of the Keweenaw current in Lake Superior. Part II: Simulation. J. Phys. Oceanogr. **31:** 396-410. doi: 0.1175/1520-0485(2001)031<0396:Pmsotk>2.0.Co;2.

Supplemental Information for Chapter 2:

Improving surface heat flux estimation of a large lake through model optimization and 2-point calibration: The case of Lake Geneva

Abolfazl Irani Rahaghi[a], Ulrich Lemmin[a], Andrea Cimatoribus[a], Damien Bouffard[b,c], Michael Riffler[d,e], Stefan Wunderle[d], David Andrew Barry[a]

[a] Ecological Engineering Laboratory (ECOL), Environmental Engineering Institute (IIE), Faculty of Architecture, Civil and Environmental Engineering (ENAC), Ecole Polytechnique Fédérale de Lausanne (EPFL), 1015 Lausanne, Switzerland

[b] Physics of Aquatic Systems Laboratory (APHYS), Margaretha Kamprad Chair, Environmental Engineering Institute (IIE), Faculty of Architecture, Civil and Environmental Engineering (ENAC), Ecole Polytechnique Fédérale de Lausanne (EPFL), 1015 Lausanne, Switzerland

[c] Aquatic Physics Group, Department of Surface Waters Research & Management, Eidgenössische Anstalt für Wasserversorgung, Abwasserreinigung und Gewässerschutz (EAWAG), 6047 Kastanienbaum, Switzerland

[d] Institute of Geography and Oeschger Centre for Climate Change Research, Faculty of Science, University of Bern, Bern, Switzerland

[e] Geoville Information Systems GmbH, Innsbruck, Austria

Text S2.1. Contribution of lateral (horizontal) advection to the water column energy balance

In order to quantify the effect of lateral (horizontal) advection on the energy content of the water column, particularly at the SHL2 and GE3 locations, we used a 3D numerical model to calculate the effect of horizontal advection over the entire lake. This included locations SHL2 and GE3.

The MITgcm code (Marshall et al. 1997) was applied to solve the Navier-Stokes equations under the Boussinesq and hydrostatic approximations. The 3D velocity and temperature fields were solved by the model with a finite-volume approach. Since salinity plays a minor role in determining the density of Lake Geneva, a constant value of 0.05 p.s.u. was assumed. COSMO-2 hourly meteorological patterns provided the surface forcing. The model also includes the *Rhône-in* (Fig. 1.1) discharge and temperature data provided by Swiss Federal Office for the Environment (FOEN, last accessed 18 January 2018) and the Rhone outflow (*Rhône-out* in Fig. 1.1) for water mass balance. A grid with a horizontal resolution of 173 m to 260 m, and 35 depth layers (ranging in thickness from 0.5 m at the top to 37 m at the bottom) was generated. The model parameters were determined through a comprehensive study of Lake Geneva (Cimatoribus et al. 2018). The same model configuration was employed to study the effect of lateral heat exchange on the total heat content variation at SHL2 and GE3.

We performed the modeling from January to October 2010. The model was initialized from rest on 16 November 2009 at 12:00, using the temperature profile recorded at SHL2 on that date as the initial condition. The model spin up finished by April 2010, and the simulation was run until the end of October 2010. Here, we present the results for the six-month period May to October 2010. The measured temperature profiles up to 70-m depth at SHL2 and GE3 and the model results at these locations (Figs. S2.1 and S2.2) are in good agreement.

At each grid cell, the 6-h average advective temperature fluxes, $F_{ad,x}$, $F_{ad,y}$, and $F_{ad,z}$ [$^{o}Cm^{3}s^{-1}$], were recorded. The horizontal advective temperature fluxes at each cell were then calculated following MITgcm guidelines (MITgcm, last accessed 18 January 2018). These fluxes were integrated over the entire column and multiplied by $\rho_w C_{p,w}$ to determine the rate of horizontal thermal energy transfer [W] into the water column. To compare this with the SurHF estimations [W per m^2 of the surface], the values were averaged over ~ 1 km^2 (satellite pixel resolution), and then multiplied by (surface area/lateral area) to obtain Q_{ad} [Wm^{-2}] (hereinafter m^2 refers to

the m^2 of the lake surface). Mean monthly absolute values were less than 10 Wm^{-2} (results not shown). We also computed the horizontal diffusive fluxes at each grid cell. As expected, they are much lower than the horizontal advective fluxes and thus were neglected in this analysis.

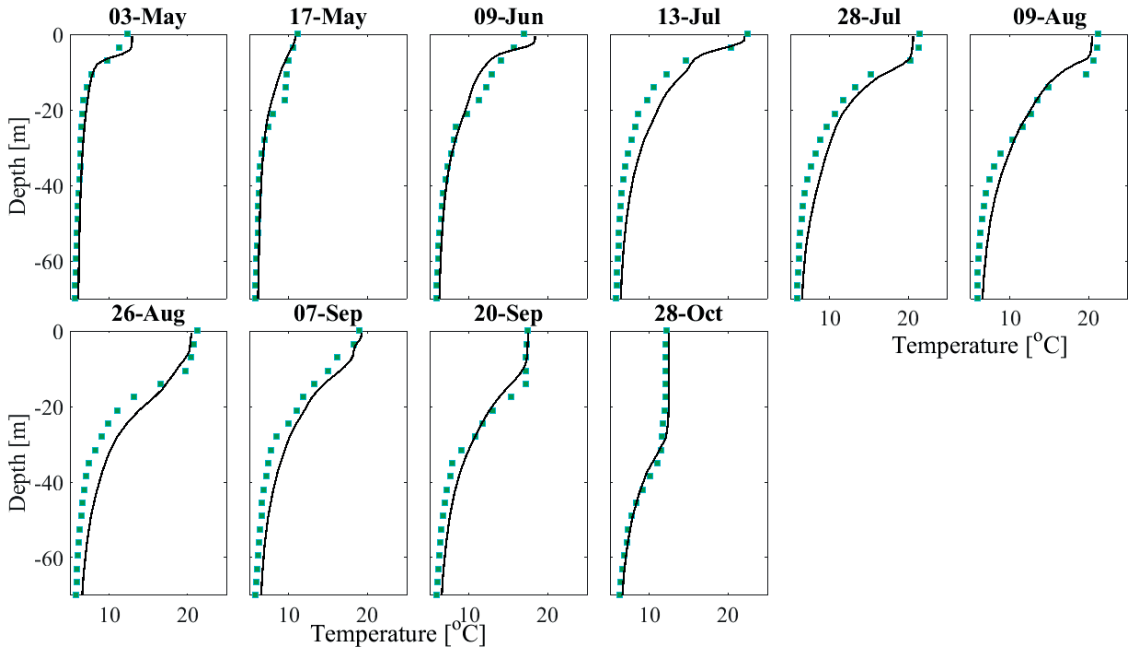

Fig. S2.1. Comparison of measured temperature profiles (green squares) at SHL2 (for station location see Fig. 1.1) with the MITgcm model results (black lines) for May to October 2010. The water depth is ~ 309 m at this point. However, for visualization purposes only the first 70 m are shown (results for deeper depths are similar).

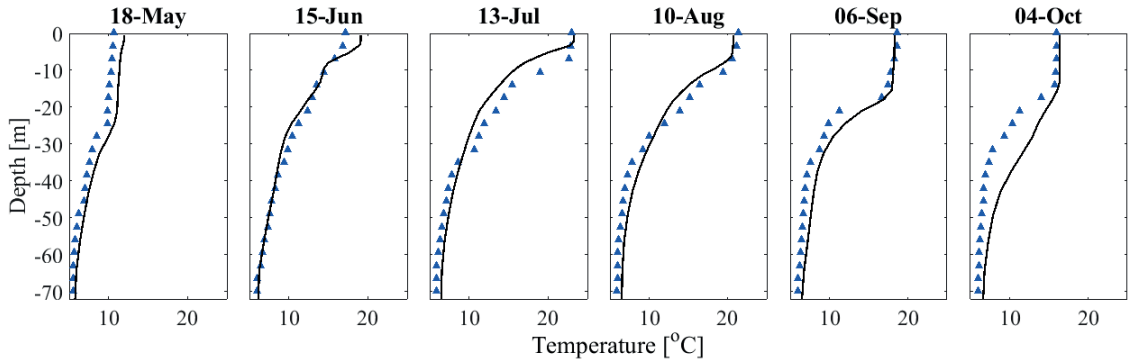

Fig. S2.2. Comparison of measured temperature profiles (blue triangles) at GE3 (for station location see Fig. 1.1) with the MITgcm model results (black lines) for May to October 2010.

To determine the contribution of advective heat flux, Q_{ad}, to the lake heat content (Eq. 2.3), the heat content variation due to Q_{ad} was compared with the heat content variation resulting from

the estimated SurHF Q_N for the numerical simulation period. The 6-h advective fluxes were used for Q_{ad}, and the hourly results for Q_N. Results (Fig. S2.3) indicate that the temporal heat content variation resulting from the advective heat fluxes remains nearly constant and is negligible compared to the net SurHF for the spatiotemporal scales of this study. Oscillations in ΔQ_{ad}, more clearly seen for GE3, indicate that large-scale mixing and homogenization are more significant than unidirectional transport.

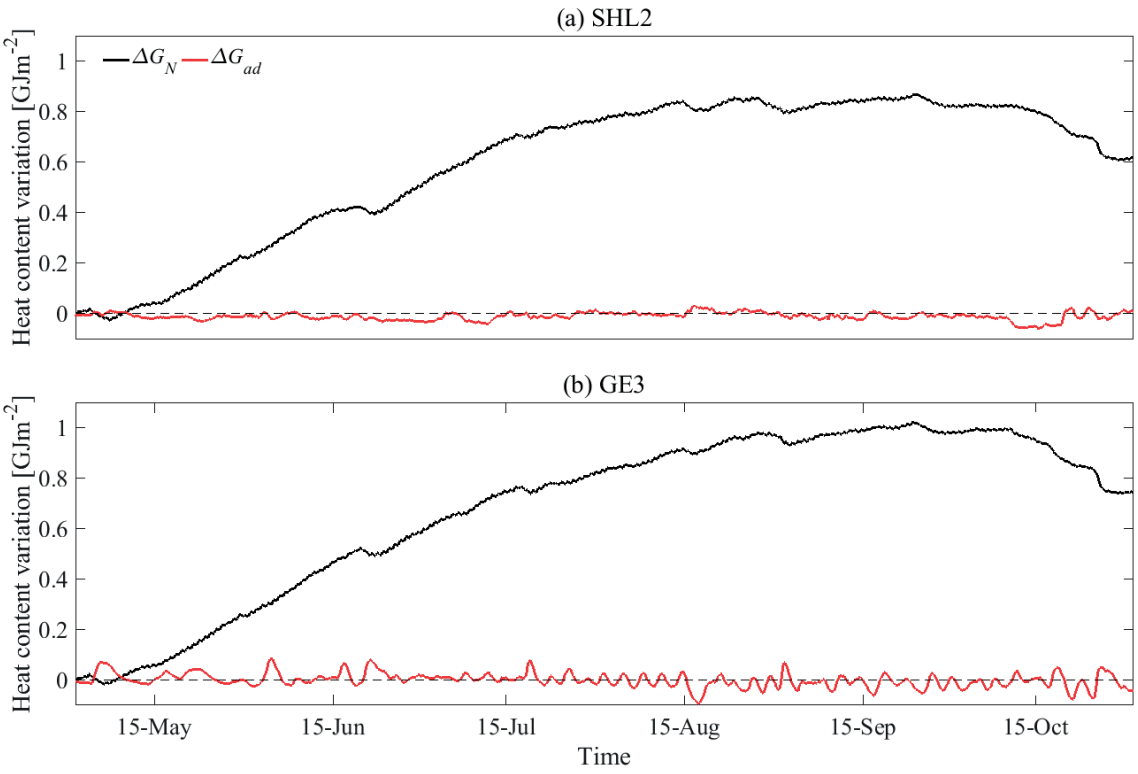

Fig. S2.3. Comparison of cumulative heat content variation due to (i) the net SurHF (ΔG_N obtained from bulk modeling) and (ii) to lateral advection (ΔG_{ad} determined from 3D numerical modeling) at SHL2 and GE3 for the period May to October 2010.

The standard deviation for the time series of water column heat content due to advective heat fluxes, i.e., the standard deviation of ΔG_{ad} , was also calculated over the entire lake. Figure S2.4 shows the map of this statistical parameter for the simulation period. It can be seen that the contribution of the advective heat fluxes is important for near-shore regions, whereas it is negligible for the central region of the lake where stations SHL2 and GE3 are located (for station location see Fig. 1.1).

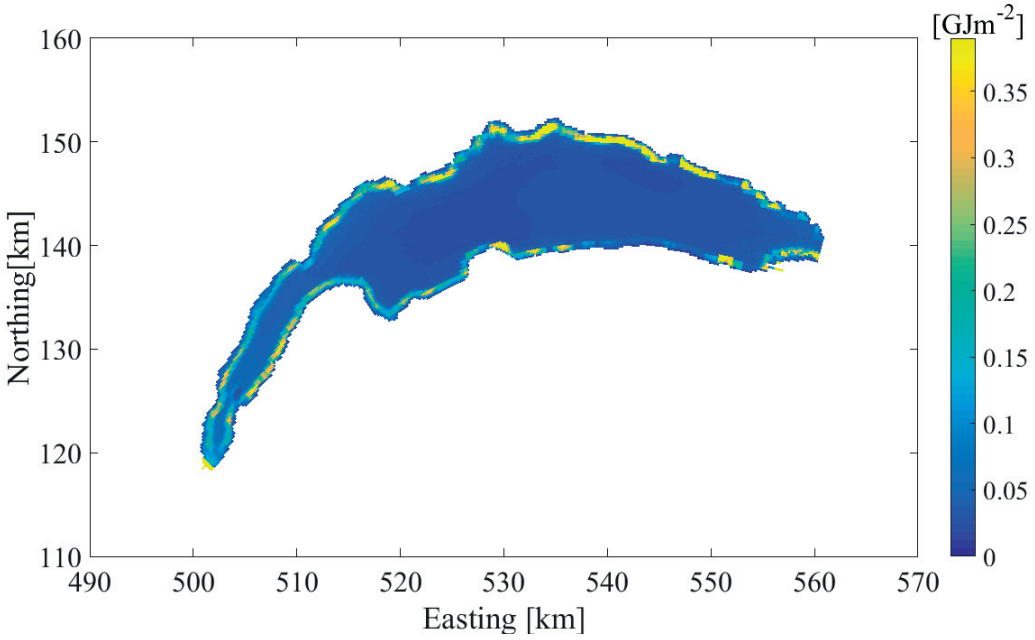

Fig. S2.4. Spatial pattern of the standard deviation of the water column energy content variation, $\sigma_{\Delta G_{ad}}$ [GJm^{-2}], due to horizontal advective energy fluxes (Q_{ad}, [Wm^{-2}]) for the period May to October 2010. In order to compare it with the energy content variation due to SurHF, the range of the color bar is equal to the standard deviation of ΔG_N at SHL2 and GE3 (black lines in Fig. S2.3). The Swiss coordinate system with km length-based units (CH1903) was used.

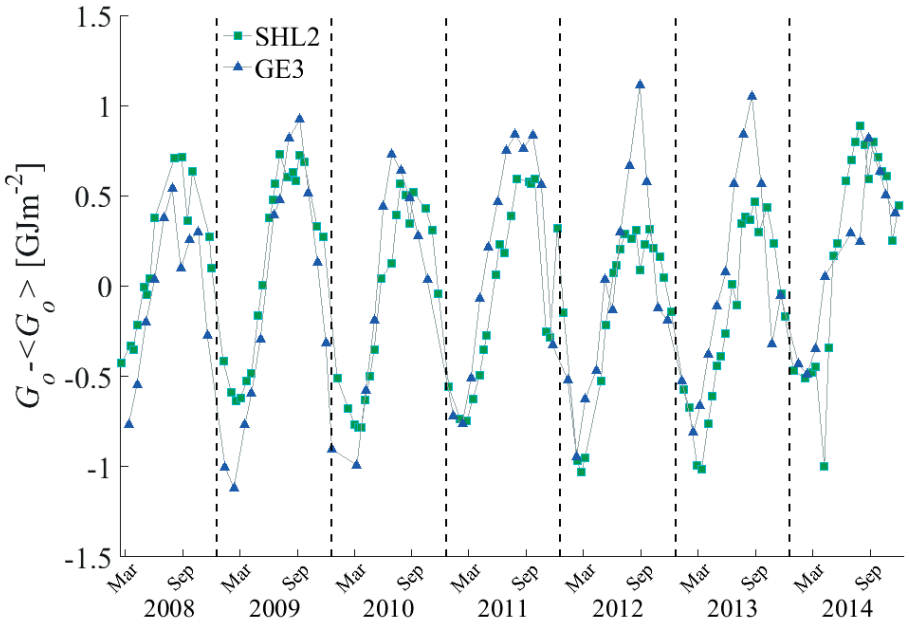

Fig. S2.5. Temporal evolution of lake heat content variation (the mean value is removed) using the measured temperature profiles at SHL2 (green squares) and GE3 (blue triangles).

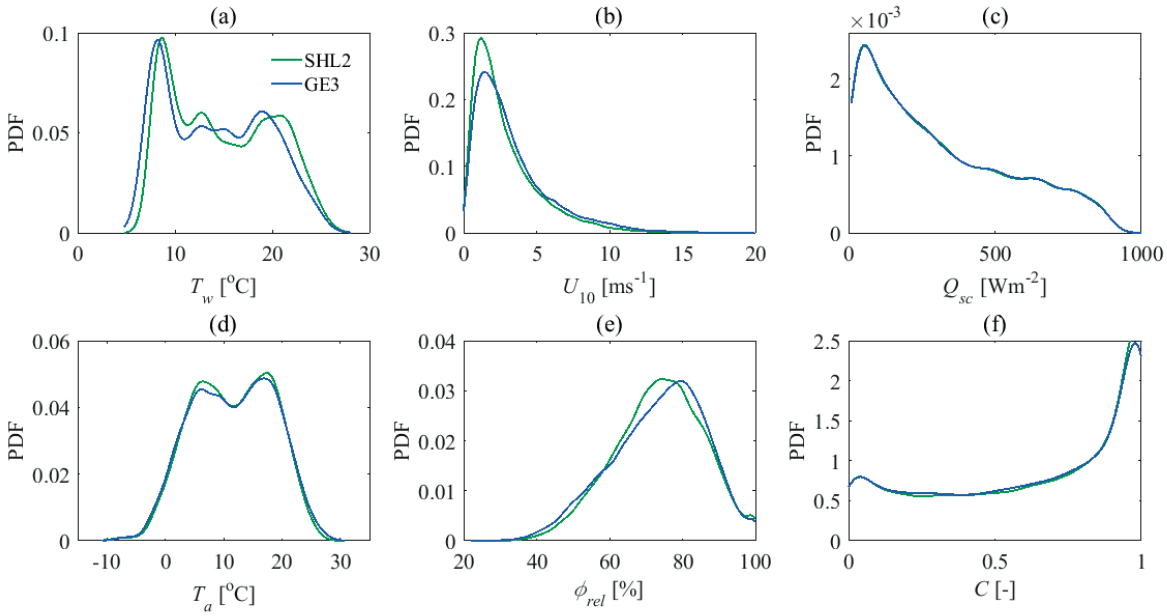

Fig. S2.6. Probability density functions (PDFs) for hourly input data at SHL2 and GE3. (a) Lake surface water temperature (LSWT), T_w, (b) wind speed, U_{10}, (c) global radiation, Q_{sc}, (d) air temperature, T_a, (e) relative humidity, ϕ_{rel}, and (f) cloudiness, C.

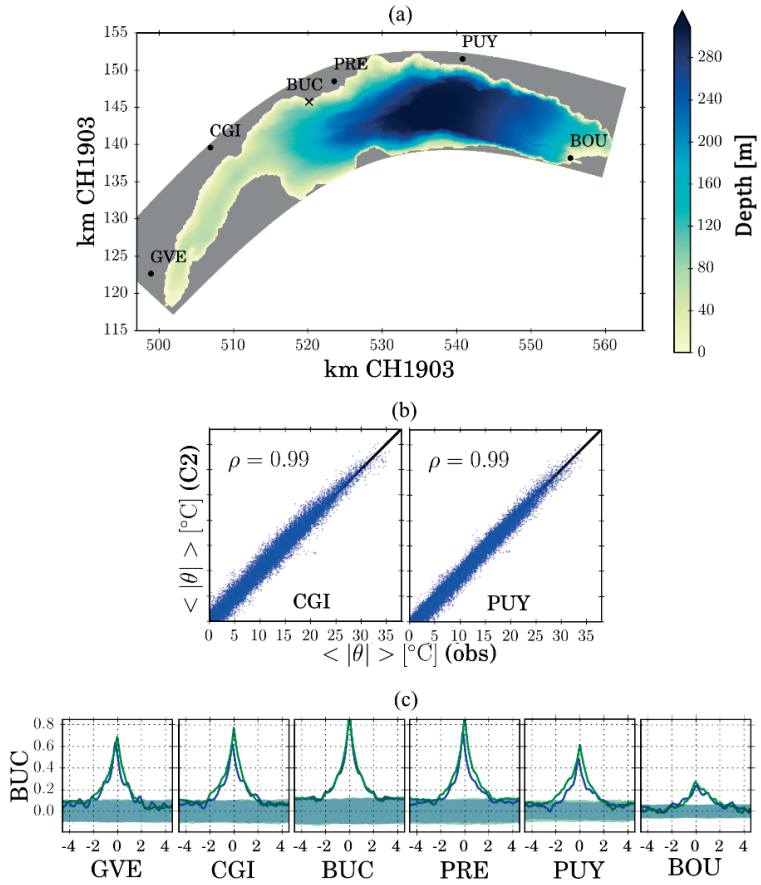

Fig. S2.7. (a) Location of meteorological stations on the Swiss side of Lake Geneva operated by MeteoSwiss (black circles; GVE: Geneva airport, CGI: Changins, PRE: Saint-Prex, PUY: Pully, and BOU: Bouveret), and our station 100 m offshore (black cross; BUC: Buchillon). The shaded color shows the lake bathymetry, (b) Correlation coefficient, ρ, between hourly averaged ($\langle |\theta| \rangle$) in situ air temperature (obs) and COSMO-2 outputs (C2) at Changins and Pully for 2013, and (c) Cross correlation (including autocorrelation) values between BUC and the other stations for in situ measurements (blue lines) and COSMO-2 outputs (green lines). The values on the abscissa of (c) are in hours.

Text S2.2. Selected surface heat flux (SurHF) models

Radiation

Tables S2.1 and S2.2 summarize formulas and coefficient values for estimating the radiative SurHF components, Q_{sn}, Q_{an} and Q_{br}, Eqs. S2.1 to S2.4 in Table S2.1, respectively. Part of the incident solar radiation is reflected at the water surface, denoted by the albedo coefficient, r_s, which is divided into direct and diffusive parts. Several empirical formulas exist for the determination of the atmospheric long-wave radiation, Q_{an}. Here, we considered two concepts that represent the relevant physics and provide widely used formulas. In Eq. S2.2b, C_{cloud} is a calibration factor that depends on the cloud type. Factor C_{an} is another calibration factor that corrects the so-called leading coefficient proposed by Brutsaert (1975), i.e., 1.24 in Eq. S2.2b. This means that ε_{an} can physically reach a maximum value of unity under completely covered skies, i.e., $C = 1$ where C is cloudiness. The parameter ε_{an2} was calculated employing the improved methods of Crawford and Duchon (1999). They added a seasonal adjustment, C_{lt}, in Table S2.1-Eq. S2.3b, to the leading coefficient, C_{lc}. According to their analysis, this time-variable atmospheric emissivity better represents the monthly mean bias and root mean square errors of the observations.

Table S2.1. Bulk models used to calculate radiative surface heat flux (SurHF) components

	$Q_{sn} = Q_{sc}F_{dir}\left(1-r_{s,dir}\right)+Q_{sc}F_{diff}\left(1-r_{s,diff}\right)$	(S2.1a)
Cogley (1979); Fink et al. (2014)	$F_{dir} = \left(1-C\right)\left[\left(1-C\right)+\frac{C}{2}\right]^{-1}$	(S2.1b)
	$F_{diff} = 1-F_{dir}$	(S2.1c)
Stefan-Boltzmann law	$Q_{an1} = \varepsilon_{an1}\sigma\left(T_a+273.15\right)^4$	(S2.2a)
Brutsaert (1975)	$\varepsilon_{an1} = 1.24C_{an}\left(1+C_{cloud}C^2\right)\left(\frac{e_a}{T_a+273.15}\right)^{1/7}$	(S2.2b)
Stefan-Boltzmann law	$Q_{an2} = \varepsilon_{an2}\sigma\left(T_a+273.15\right)^4$	(S2.3a)
Crawford and Duchon (1999)	$\varepsilon_{an2} = \left\{C+\left(1-C\right)\left(C_{lc}+C_{lt}\sin\left[\left(t_m+2\right)\frac{\pi}{6}\right]\right)\left(\frac{e_a}{T_a+273.15}\right)^{1/7}\right\}$	(S2.3b)
Stefan-Boltzmann law	$Q_{br} = -\varepsilon_w\sigma\left(T_w+273.15\right)^4$	(S2.4)

Table S2.2. Definition and values/formulas of the symbols used in Table S2.1

Definitions		Value
C	Cloudiness	From COSMO-2
C_{an}	Calibration factor	-
C_{cloud}	Calibration factor	-
C_{lc}	Calibration factor	-
C_{lt}	Calibration factor	-
e_a	Water vapor pressure [hPa]	$e_a = 23.38\phi_{rel} \exp\left(18.1 - \frac{5303.3}{T_a + 273.15}\right)$
F_{diff}	Solar radiation diffusive fraction	-
F_{dir}	Solar radiation direct fraction	-
Q_{sc}	Global radiation [Wm^{-2}]	From COSMO-2
$r_{s,diff}$	Diffusive albedo [a]	0.066
$r_{s,dir}$	Direct albedo [b]	From Cogley (1979)
T_a	Air temperature [°C]	From COSMO-2
t_m	Numerical month	e.g., 15 January = 1
T_w	Lake surface water temperature [°C]	From satellite imagery
ε_a	Atmospheric emissivity	-
ε_w	Water surface emissivity [c]	0.972
ϕ_{rel}	Relative humidity	From COSMO-2
σ	Stefan-Boltzmann constant [$Wm^{-2}°C^{-4}$]	5.67×10^{-8}

[a] Burt (1954); Fink et al. (2014)

[b] In the present study, the modified mean monthly direct albedo for 46° latitude (Cogley 1979) was used. For the SurHF calculation, hourly values were estimated by applying the Piecewise Cubic Hermite polynomials interpolation method (Fritsch and Carlson 1980). The effects of other atmospheric conditions, e.g., air pollution, and solar zenith angle on the direct/diffusive fraction are neglected. The daily variation of Q_{sn} is mainly due to Q_{sc}, which is taken into account.

[c] Davies et al. (1971) and Sweers (1976) recommended a value of $\varepsilon_w = 0.972$, which was used by Livingstone and Imboden (1989) and Fink et al. (2014), whereas Octavio (1977) suggested $\varepsilon_w = 0.956$. We applied the first value, i.e., 0.972, following previous studies in Switzerland.

Sensible and latent heat fluxes

Due to the similarity between sensible, Q_{co}, and latent, Q_{ev}, heat fluxes, they are often calculated with formulas having a similar form. To estimate them, three different pairs of equations, Eqs. S2.5 to S2.7 in Table S2.3, were selected, representing different concepts. The level of complexity in these formulas increases from Eq. S2.5 to Eq. S2.7. Table S2.4 shows the definition and values of the parameters in those equations.

Murakami's formulation, Eq. S2.5a, corresponds to the turbulent bulk latent heat flux formula without the influence of free convection, following a constant Dalton number. A constant Bowen ratio in Eq. S2.5b, C_b, was used to estimate the sensible heat flux with values of the latent heat flux, Q_{ev1}. The factor C_b is proportional to air pressure even though an average value is usually employed in SurHF estimation. Equation S2.6 takes into account the contribution of free convection to the sensible and latent heat flux calculations. Here, $C_{e,r}$ and $C_{h,r}$ are the Dalton and Stanton numbers, respectively, both of which are calibrated. In a more sophisticated approach, the turbulent SurHF is calculated by applying the bulk parameterization algorithms based on similarity theory and empirical relationships, Eq. S2.7. This formulation relates the surface layer data to surface momentum and heat fluxes. More information is given in the "Details of the model calibration procedure" section below.

Table S2.3. Selected bulk models for sensible and latent surface heat fluxes

Murakami et al. (1985)	$Q_{ev1} = -C_{mur} U_{10} \rho_w L_v \left(e_s - e_a\right)$	(S2.5a)
Bowen (1926) [a]	$Q_{co1} = -Q_{ev1} C_b \left(\frac{T_w - T_a}{e_s - e_a}\right)$	(S2.5b)
Ryan et al. (1974); Gill (1982)	$Q_{ev2} = Q_{ev2,forced} + Q_{ev2,free}$	(S2.6a)
	$Q_{co2} = Q_{co2,forced} + Q_{co2,free}$	(S2.6b)
	$Q_{ev2,forced} = -C_{e,r} U_{10} L_v \rho_a \left(q_s - q_a\right)$	(S2.6c)
	$Q_{ev2,free} = -k_s L_v \bar{\rho}_a \left(q_s - q_a\right)$	(S2.6d)
	$Q_{co2,forced} = -\rho_a C_{p,a} C_{h,r} U_{10} \left(T_w - T_a\right)$	(S2.6e)
	$Q_{co2,free} = -k_s \bar{\rho}_a C_{p,a} \left(T_w - T_a\right)$	(S2.6f)
	$k_s = C_{fr.conv.} \left[\frac{g D_a^{\,2}}{\upsilon_a \bar{\rho}_a} \left(\rho_a - \rho_s\right)\right]^{1/3}$	(S2.6g)
	$\rho_s = \frac{\frac{100 P_{atm} - 100 e_s}{R_{dry}} + \frac{100 e_s}{R_{vap}}}{T_w + 273.15},\ \rho_a = \frac{\frac{100 P_{atm} - 100 e_a}{R_{dry}} + \frac{100 e_a}{R_{vap}}}{T_a + 273.15}$	(S2.6h)
	$\bar{\rho}_a = \frac{\rho_a + \rho_s}{2}$	(S2.6i)
Monin-Obukhov similarity theory (Monin and Obukhov 1954)	$Q_{ev3} = -C_{e,m} \rho_z L_v u_z \left(q_s - q_z\right) = \rho_z L_v u_* q_*$	(S2.7a)
	$Q_{co3} = -\rho_z C_{p,a} C_{h,m} u_z \left(T_s - T_z\right) = \rho_z C_{p,a} u_* T_*$	(S2.7b)
	$\tau = C_{d,m} \rho_z u_z^2 = \rho_z u_*^2$	(S2.7c)
	$f_m(\zeta) = \frac{\kappa z_u}{u_*} \frac{\partial u}{\partial z},\ f_e(\zeta) = \frac{\kappa z_q}{q_*} \frac{\partial q}{\partial z},\ f_h(\zeta) = \frac{\kappa z_t}{T_*} \frac{\partial T}{\partial z}$	(S2.7d)
	$\zeta = z L_w^{-1} = \frac{z \kappa g \left[\frac{Q_{co3}}{C_{p,a}} + 0.61 \frac{\left(T_z + 273.15\right) Q_{ev3}}{L_v}\right]}{\rho_z u_*^3 T_v}$	(S2.7e)

[a] Assuming an analogy between heat exchange and mass transfer, the convective heat flux can be related to the evaporative flux through the Bowen ratio, $R_b = \frac{Q_{co,b}}{Q_{ev}} = -C_b \left(\frac{T_w - T_a}{e_s - e_a}\right)$.

Table S2.4. Definition and values/formulas of the symbols used in Table S2.3

Definitions		Value
C_b	Calibration factor (Bowen coefficient) [hPaK^{-1}]	-
C_e	Calibration factor (Dalton number)	-
$C_{fr.conv.}$	The free convection coefficient [a]	0.14
C_d	Momentum transfer coefficient	-
C_h	Calibration factor (Stanton number)	-
C_{mur}	Calibration factor	-
$C_{p,a}$	Specific heat capacity of air [Jkg^{-1}°C^{-1}]	1004
D_a	Air molecular diffusivity [m^{2}s^{-1}]	$D_a = \frac{\nu_a}{\mathrm{Pr}}$
e_s	Saturated water vapor pressure [hPa] [b]	$e_s = 6.112\exp\left(\frac{17.62T_w}{T_w + 243.12}\right)$
g	Gravitational acceleration [ms^{-2}]	9.81
k_s	Exchange velocity [ms^{-1}]	-
L_v	Latent heat of vaporization [Jkg^{-1}]	$L_v = 2.5\times10^6 - 2.3\times10^3 T_w$
L_w	Monin-Obukhov length	-
P_{atm}	Air pressure [hPa]	From COSMO-2
Pr	Prandtl number	0.7
q_a	Actual air specific humidity [kgkg^{-1} dry air]	$q_a = \frac{0.62e_a}{P_{atm} - 0.38e_a}$
q_s	Saturated air specific humidity [kgkg^{-1} dry air]	$q_s = \frac{0.62e_s}{P_{atm} - 0.38e_s}$
q_z	Specific humidity at height z_q [kgkg^{-1} dry air]	-
q_*	Scaling humidity [kgkg^{-1} dry air]	
R_{dry}	Dry air gas constant [Jkg^{-1}°C^{-1}]	287.05
R_{vap}	Water vapor gas constant [Jkg^{-1}°C^{-1}]	461.495
S_L	Lake surface area [m^2]	5.8×10^8
T_z	Air temperature at height z_t [°C]	-
T_v	Virtual air temperature [°C]	$T_v = \left(T_z + 273.15\right)\left(1 + 0.61q_z\right)$
T_*	Scaling temperature [°C]	-
U_{10}	Wind speed at 10 m above the free surface [m s^{-1}]	From COSMO-2
u_z	Wind speed at height z_u [ms^{-1}]	-
u_*	Air friction velocity [ms^{-1}]	-
z_q	Height of humidity data [m]	From COSMO-2
z_t	Height of air temperature data [m]	From COSMO-2

Table S2.4. Definition and values/formulas of the symbols used in Table S2.3 (continued)

Definitions		Value
z_u	Height of wind speed data [m]	From COSMO-2
κ	Von Karman constant	0.41
ν_a	Air viscosity [m^2s^{-1}]	1.6×10^{-5}
ρ_a	Actual air density [kgm^{-3}]	-
$\overline{\rho}_a$	Average air density [kgm^{-3}]	-
ρ_s	Saturated air density [kgm^{-3}]	-
ρ_w	Water density [kgm^{-3}]	$\frac{\rho_w}{1000} = \left[1 - \frac{(T_w + 288.941)(T_w - 3.986)^2}{5089292(T_w + 68.1296)}\right]$ (Read et al. 2011)
ρ_z	Air density at height z [kgm^{-3}]	$\rho_z = \frac{\frac{100P_{atm} - 100e_z}{R_{dry}} + \frac{100e_z}{R_{vap}}}{T_z + 273.15}$
τ	Air-water momentum flux [Nm^{-2}]	-
ζ	Stability parameter	-

[a] Estimated by Ryan et al. (1974).

[b] Estimated with the Magnus formula (WMO 2008).

Text S2.3. Details of the model calibration procedure

In Tables 2.1 and S2.3, the level of complexity in the turbulent heat flux models increases from $(Q_{ev} + Q_{co})_1$ to $(Q_{ev} + Q_{co})_3$. The calculations in the first two formulas are not complicated. The latter, i.e., $(Q_{ev} + Q_{co})_3$, uses the bulk parameterization algorithms based on the similarity theory and empirical relationships (Eq. S2.7, Table S2.3). Two components must be defined in this algorithm: the turbulence stability functions, f_m, f_e and f_h, and the roughness lengths for wind, temperature and humidity (z_0, z_{0t} and z_{0q}, respectively). The differential equations for f_m, f_e and f_h (Eq. S2.7d) are integrated between the roughness lengths and the measurement heights to obtain the wind, temperature and specific humidity gradients in the atmospheric boundary layer, and the corresponding drag, humidity and temperature bulk transfer coefficients, $C_{d,m}$, $C_{e,m}$ and $C_{h,m}$, respectively, to calculate the turbulent surface fluxes. The Monin-Obukhov similarity theory (Monin and Obukhov 1954) was used for the turbulence stability functions, which depend on the atmospheric stability parameter, ζ (Eq. S2.7e). Details of these functions are given elsewhere (e.g., Zeng et al. 1998; Woolway et al. 2015).

The empirical parameterization of two roughness lengths was investigated in order to reduce the calibration factor for the calculation of $(Q_{ev} + Q_{co})_3$. The roughness momentum length, z_0, was calculated using (Smith 1988):

$$z_0 = C_{m1}\frac{u_*^2}{g} + C_{m2}\frac{v_a}{u_*} \tag{S2.8}$$

where C_{m1}, the Charnock constant (Charnock 1955), and C_{m2} are calibration factors. The functional form of Brutsaert (1982) was applied for the roughness lengths of humidity, z_{0q}, and temperature, z_{0t}:

$$z_{0q} = z_{0t} = z_0 \exp\left(C_{q1}\,\mathrm{Re}_*^{0.25} + C_{q2}\right) \tag{S2.9}$$

where C_{q1} and C_{q2} are calibration factors, and $\mathrm{Re}_* = u_* z_0 / v_a$ is the roughness Reynolds number. Zeng et al. (1998), employing the bulk parametrization in Eqs. S2.8 and S2.9 with some other algorithms, obtained the following values: $C_{m1} = 0.013$, $C_{m2} = 0.11$, $C_{q1} = -2.67$ and $C_{q2} = 2.57$. These four calibration factors were based on the data of the Tropical Ocean-Global Atmosphere Coupled-Ocean Atmosphere Response (TOGA CORE) experiment (Fairall et al. 1996) and

define the variation of drag, humidity and temperature bulk transfer coefficients as a function of meteorological parameters, especially wind speed. A sensitivity analysis of these calibration factors reveals that the shape of humidity and temperature transfer coefficients are mainly controlled by C_{m2} and C_{q1} (Fig. S2.8). These results illustrate that C_{m2} affects the low wind speed regime (up to 5 ms^{-1}) while C_{q1} controls higher wind speeds (over 5 m s^{-1}). Rearranging Eq. S2.8 indicates that C_{m2} is equal to a constant Re_* as the wind speed approaches zero. In addition to other meteorological parameters and LSWT, the wind speed distribution also changes at SHL2 and GE3 (Figs. 2.1b and S2.6b). In this study, we assumed $C_{m1} = 0.013$ and $C_{q2} = 2.57$ and examine and calibrate C_{m2} and C_{q1}. Their values are found through an optimization procedure.

The Generalized Likelihood Uncertainty Estimation (GLUE) methodology employed for the optimization requires values within a certain range for each calibration parameter. These are based on values reported in the literature (Table S2.5). For each of the six net SurHF models, there are four calibration factors: viz., C_{cloud}/C_{an} or C_{lc}/C_{lt} in the atmospheric radiation component, and C_{mur}/C_b or $C_{e,r}/C_{h,r}$ or C_{m2}/C_{q1} in the turbulent, i.e., sensible and latent heat fluxes. Monte Carlo realizations (10^5) using uniform random sampling across the parameter ranges were implemented as the sampling strategy.

For the calibration, the following five-step procedure was carried out for each SurHF model: (i) the meteorological data including U_{10}, T_a, ϕ_{rel}, Q_{sc}, C, P_{atm} from the COSMO-2 model and T_w from AVHRR satellite images were extracted at the SHL2 and GE3 locations (Fig. 1.1), (ii) the net SurHF model and its corresponding calibration factors, [(C_{an}/C_{cloud}) | (C_{lc}/C_{lt})] and [(C_{mur}/C_b) | ($C_{h,r}/C_{e,r}$) | (C_{m2}/C_{q1})], were chosen, (iii) Q_N and G_m were calculated at the two locations for different Monte Carlo model realizations, (iv) the measured temperature profiles at SHL2 and GE3 were taken from the CIPEL data set and G_o was calculated, and (v) model performance was ranked based on Eq. 2.6.

The data set was divided into two parts: The period March 2008 to 7 July 2011 was used for calibration, and August 2011 to December 2014 for validation.

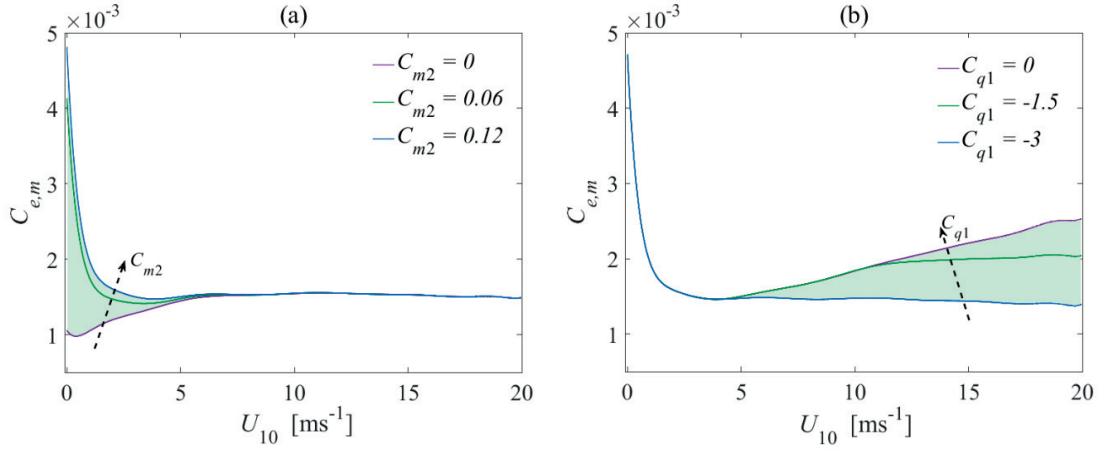

Fig. S2.8. Sensitivity of humidity bulk transfer coefficient, $C_{e,m}$, to the calibration factors given in the legend: (a) C_{m2}, and (b) C_{q1}. Dashed arrows indicate the change in values as given in the legend.

Table S2.5. Literature values for the selected calibration factors

Calibration factors	Reported values	References	Selected range for GLUE methodology
C_{an}	1.09, 0.943, 1.05	Livingstone and Imboden (1989), Herrero and Polo (2012), Fink et al. (2014)	[0.8, 1.3]
C_{cloud}	0.17, 0.42, 0.17	Livingstone and Imboden (1989), Herrero and Polo (2012), Fink et al. (2014)	[0.04, 0.45]
C_{lc}	1.22	Crawford and Duchon (1999)	[0.8, 1.3]
C_{lt}	0.06	Crawford and Duchon (1999)	[0.02, 0.2]
C_{mur}	1.2×10^{-7}	Murakami et al. (1985)	$[5\times10^{-8}, 2\times10^{-7}]$
C_b	0.65, 0.6, 0.62	Sweers (1976), Livingstone and Imboden (1989), Fink et al. (2014)	[0.58, 0.7]
$C_{e,r}$	2.1×10^{-3}	Wahl and Peeters (2014)	$[10^{-4}, 5\times10^{-2}]$
$C_{h,r}$	1.45×10^{-3}	Wahl and Peeters (2014)	$[10^{-4}, 5\times10^{-2}]$
C_{m2}	0.11	Zeng et al. (1998)	[0, 0.12][a]
C_{q1}	-2.67	Zeng et al. (1998)	[-3, 0][a]

[a] See the sensitivity analysis above for the details of the range selection.

References

Bowen, I. S. 1926. The ratio of heat losses by conduction and by evaporation from any water surface. Phys. Rev. **27:** 779-787. doi: 10.1103/Physrev.27.779.

Brutsaert, W. 1975. Derivable formula for long-wave radiation from clear skies. Water Resour. Res. **11:** 742-744. doi: 10.1029/Wr011i005p00742.

Brutsaert, W. 1982. Evaporation into the atmosphere: Theory, history and applications. Springer Netherlands. doi: 10.1007/978-94-017-1497-6.

Burt, W. V. 1954. Albedo over wind-roughened water. J. Meteorol. **11:** 283-290. doi: 10.1175/1520-0469(1954)011<0283:Aowrw>2.0.Co;2.

Charnock, H. 1955. Wind stress on a water surface. Q. J. Roy. Meteor. Soc. **81:** 639-640. doi: 10.1002/qj.49708135027.

Cimatoribus, A. A., U. Lemmin, D. Bouffard, and D. A. Barry. 2018. Nonlinear dynamics of the near-shore boundary layer of a large lake (Lake Geneva). J. Geophys. Res.: Oceans **123:** 1016-1031. doi: 10.1002/2017JC013531.

Cogley, J. G. 1979. Albedo of water as a function of latitude. Mon. Weather Rev. **107:** 775-781. doi: 10.1175/1520-0493(1979)107<0775:Taowaa>2.0.Co;2.

Crawford, T. M., and C. E. Duchon. 1999. An improved parameterization for estimating effective atmospheric emissivity for use in calculating daytime downwelling longwave radiation. J. Appl. Meteorol. **38:** 474-480. doi: 10.1175/1520-0450(1999)038<0474:Aipfee>2.0.Co;2.

Davies, J. A., P. J. Robinson, and M. Nunez. 1971. Field determinations of surface emissivity and temperature for Lake Ontario. J. Appl. Meteorol. **10:** 811-819. doi: 10.1175/1520-0450(1971)010<0811:FDOSEA>2.0.CO;2.

Fairall, C. W., E. F. Bradley, D. P. Rogers, J. B. Edson, and G. S. Young. 1996. Bulk parameterization of air-sea fluxes for Tropical Ocean Global Atmosphere Coupled Ocean Atmosphere Response Experiment. J. Geophys. Res.: Oceans **101:** 3747-3764. doi: 10.1029/95jc03205.

Fink, G., M. Schmid, B. Wahl, T. Wolf, and A. Wüest. 2014. Heat flux modifications related to climate-induced warming of large European lakes. Water Resour. Res. **50:** 2072-2085. doi: 10.1002/2013wr014448.

Fritsch, F. N., and R. E. Carlson. 1980. Monotone piecewise cubic interpolation. Siam. J. Numer. Anal. **17:** 238-246. doi: 10.1137/0717021.

Gill, A. E. 1982. Atmosphere-ocean dynamics. Academic Press. San Diego, USA. doi: 10.1002/qj.49711046322.

Herrero, J., and M. J. Polo. 2012. Parameterization of atmospheric longwave emissivity in a mountainous site for all sky conditions. Hydrol. Earth Syst. Sci. **16:** 3139-3147. doi: 10.5194/hess-16-3139-2012.

Livingstone, D. M., and D. M. Imboden. 1989. Annual heat balance and equilibrium temperature of Lake Aegeri, Switzerland. Aquat. Sci. **51:** 351-369. doi: 10.1007/Bf00877177.

Marshall, J., A. Adcroft, C. Hill, L. Perelman, and C. Heisey. 1997. A finite-volume, incompressible Navier Stokes model for studies of the ocean on parallel computers. J. Geophys. Res.: Oceans **102:** 5753-5766. doi: 10.1029/96jc02775.

Monin, A. S., and A. M. Obukhov. 1954. Basic laws of turbulent mixing in the ground layer of the atmosphere. Tr. Akad. Nauk SSSR Geofiz. Inst. **24:** 163-187.

Murakami, M., Y. Oonishi, and H. Kunishi. 1985. A numerical simulation of the distribution of water temperature and salinity in the Seto Inland Sea. J. Oceanogr. Soc. Jpn. **41:** 213-224. doi: 10.1007/BF02109271.

Octavio, K. A. H. 1977. Vertical heat transport mechanisms in lakes and reservoirs. Ralph M. Parsons Laboratory for Water Resources and Hydrodynamics. Mass. Inst. Tech., Cambridge, Massachusetts, USA. http://hdl.handle.net/1721.1/52844.

Read, J. S., D. P. Hamilton, I. D. Jones, K. Muraoka, L. A. Winslow, R. Kroiss, C. H. Wu, and E. Gaiser. 2011. Derivation of lake mixing and stratification indices from high-resolution lake buoy data. Environ. Model. Softw. **26:** 1325-1336. doi: 10.1016/j.envsoft.2011.05.006.

Ryan, P. J., D. R. F. Harleman, and K. D. Stolzenbach. 1974. Surface heat loss from cooling ponds. Water Resour. Res. **10:** 930-938. doi: 10.1029/Wr010i005p00930.

Smith, S. D. 1988. Coefficients for sea-surface wind stress, heat flux, and wind profiles as a function of wind speed and temperature. J. Geophys. Res.: Oceans **93:** 15467-15472. doi: 10.1029/Jc093ic12p15467.

Sweers, H. E. 1976. Nomogram to estimate heat exchange coefficient at air-water interface as a function of wind speed and temperature: Critical survey of some literature. J. Hydrol. **30:** 375-401. doi: 10.1016/0022-1694(76)90120-7.

Wahl, B., and F. Peeters. 2014. Effect of climatic changes on stratification and deep-water renewal in Lake Constance assessed by sensitivity studies with a 3D hydrodynamic model. Limnol. Oceanogr. **59:** 1035-1052. doi: 10.4319/lo.2014.59.3.1035.

WMO. 2008. Guide to meteorological instruments and methods of observation. World Meteorological Organization (http://www.wmo.int/pages/prog/gcos/documents/gruanmanuals/CIMO/CIMO_Guide-7th_Edition-2008.pdf).

Woolway, R. I., I. D. Jones, D. P. Hamilton, S. C. Maberly, K. Muraoka, J. S. Read, R. L. Smyth, and L. A. Winslow. 2015. Automated calculation of surface energy fluxes with high-frequency lake buoy data. Environ. Model. Softw. **70:** 191-198. doi: 10.1016/j.envsoft.2015.04.013.

Zeng, X. B., M. Zhao, and R. E. Dickinson. 1998. Intercomparison of bulk aerodynamic algorithms for the computation of sea surface fluxes using TOGA COARE and TAO data. J. Clim. **11:** 2628-2644. doi: 10.1175/1520-0442(1998)011<2628:Iobaaf>2.0.Co;2.

Chapter 3

Multi-annual surface heat flux dynamics over Lake Geneva: The importance of spatial variability

Abolfazl Irani Rahaghi[a], Ulrich Lemmin[a], Andrea Cimatoribus[a], David Andrew Barry[a]

[a] Ecological Engineering Laboratory (ECOL), Environmental Engineering Institute (IIE), Faculty of Architecture, Civil and Environmental Engineering (ENAC), Ecole Polytechnique Fédérale de Lausanne (EPFL), 1015 Lausanne, Switzerland

To be submitted to *Water resources research*

Abstract

The spatiotemporal surface heat flux (SurHF) of Lake Geneva, the largest lake in Western Europe, was estimated for a 7-y period (2008 to 2014). Data sources included hourly maps of over-the-lake assimilated meteorological data from a numerical weather model and lake surface water temperatures (LSWT) from satellite imagery. A set of bulk algorithms, optimized and calibrated previously at two locations in Lake Geneva, was used. Analysis results indicate an average spatial range of > 40 Wm^{-2}. This is mainly due to wind sheltering over parts of the lake, which in turn produces spatial variability in sensible and latent heat fluxes. During spring, much less spatial variability was evident compared to other seasons. The spring variability was caused by air-water temperature differences and, to a lesser extent, global radiation variability, again due to shielding by the surrounding topography. Analysis of the atmospheric thermal boundary layer showed unstable conditions except from March to early June. This regime change can explain the low SurHF spatial variability observed during spring. The results emphasize that spatial variability in the meteorological and LSWT patterns, and consequently the spatiotemporal SurHF data, should be taken into consideration when assessing the time evolution of the heat budget of large water bodies.

Keywords: Surface heat flux, meteorological forcing, spatial variability, Lake Geneva, atmospheric boundary layer stability, heat content

3.1. Introduction

Wind forcing and Surface Heat Flux (SurHF) are the main external parameters affecting lake thermodynamics and hydrodynamics, which in turn influence the chemical and biological properties of aquatic systems (Honrath et al. 1997; MacIntyre et al. 2002; Churchill and Charles Kerfoot 2007; Bonvin et al. 2013; Finlay et al. 2015). In many lakes, SurHF is the most important process controlling total lake heat content and thus water temperatures that are often used as a climate change indicator (Adrian et al. 2009). Frequently, SurHF is determined from eddy covariance measurements or a surface heat balance using Lake Surface Water Temperature (LSWT) and meteorological data. A single-point approach is applied in many studies based on (i) direct measurements (e.g., Laird and Kristovich 2002; Assouline et al. 2008; Rouse et al. 2008; Blanken et al. 2011; Nordbo et al. 2011; Van Emmerik et al. 2013; Zhang and Liu 2014; Li et al. 2015), (ii) bulk formula calculations (e.g., Schertzer 1978; Henderson-Sellers 1986; Lenters et al. 2005; Woolway et al. 2015), or (iii) one-dimensional (1D) numerical modeling (e.g., Tanentzap et al. 2007; Momii and Ito 2008; Austin and Allen 2011; Stepanenko et al. 2014; Thiery et al. 2014a; Thiery et al. 2014b; Yang et al. 2017). Relying on a one-point approach can result in significant errors in the SurHF estimation of large lakes (Mahrer and Assouline 1993). With increasing size of the water body, variations of LSWT and meteorological conditions potentially induce larger spatial variability of SurHF, a topic that has received little attention in the literature. Data from multiple locations capture more of the SurHF spatial variability over lakes than the one-point approach (Rimmer et al. 2009; Verburg and Antenucci 2010; Rahaghi et al. 2018). Unfortunately, for most lakes, data from multiple locations are scarce, and these are often located close to shore.

Spatially resolved meteorological and LSWT data permit investigating SurHF spatial patterns over water bodies. The former are provided by numerical weather models (e.g., Kourzeneva et al. 2012; Mironov et al. 2012), while the latter are usually available from satellite remote sensing (e.g., Schwab et al. 1992; Politi et al. 2012; Sima et al. 2013; Riffler et al. 2015). Satellite data that are collected on a regular basis are suitable for long-term thermal analyses, although pixel sizes may be large (at the km scale) and clouds can reduce coverage. The combination of LSWT patterns and meteorological data from stations located around the shore (Schneider and Mauser 1991; Lofgren and Zhu 2000; Alcantara et al. 2010; Phillips et al. 2016) or numerical weather models (Spence et al. 2011; Xue et al. 2015; Moukomla and Blanken

2017) have been used to estimate the surface thermal patterns of inland water bodies. Satellite data were used to investigate the diurnal/nocturnal LSWT evolution of Lake Geneva (Oesch et al. 2005; 2008). They suggest that the observed warm/cold LSWT regions may result from thermocline undulations, lake-land breezes and large-scale circulation forced by the wind field over the lake (Lemmin and D'Adamo 1996).

Spatial thermal patterns can be also obtained via three-dimensional (3D) hydrodynamic modeling (e.g., Bai et al. 2013; Beletsky et al. 2013; Wahl and Peeters 2014; Xue et al. 2015). However, these models rely on bulk temperatures for back radiation and non-radiative heat flux calculations, whereas LSWT is preferred (Minnett et al. 2011; Wilson et al. 2013). In numerical modeling, an error in the temperature of the near-surface layer is attenuated with time (about one month for 1°C temperature deviation in the near-surface layer), a behavior that is attributed to "self-restoration". However, it can lead to deviations from the observed surface thermal patterns (Xue et al. 2015).

Despite the diversity of thermal structure analyses of inland water bodies, investigations of spatial SurHF variability of large lakes are scarce due to the lack of (i) spatiotemporal LSWTs, (ii) over-the-lake meteorological data, (iii) multi-station over-lake measurements, or multiple temperature profiles for determining the overall energy balance. However, Lake Geneva, the largest lake in Western Europe, is a suitable study site to investigate the spatial variability of SurHF, since all the required data mentioned above are available.

In this study, we quantify the impact of spatiotemporal SurHF variability of Lake Geneva on its overall energy balance. Specifically, the following questions are addressed: (i) What is the typical monthly range of SurHF spatial variability using optimized and calibrated bulk formulas?, and (ii) What are the major meteorological factors controlling the dominant heat flux terms that determine spatial thermal patterns? This study is based on the 2-point calibrated SurHF model using the same data sets as in chapter 2 (Rahaghi et al. 2018; Unpublished work).

3.2. Materials and methods

3.2.1. Study site

Located between Switzerland and France, Lake Geneva (Local name: *Lac Léman*) is a large, deep, crescent-shaped perialpine lake with a mean surface altitude of 372 m. It is approximately

70-km long, with a maximum width of 14 km, a surface area of 582 km² and a volume of 89 km³. The lake is composed of two basins: an eastern, large basin called the *Grand Lac*, with a maximum depth of 309 m, and a western, small, narrow basin called the *Petit Lac*, with a maximum depth of approximately 70 m (Fig. 1.1).

The lake is surrounded by the Jura Mountains in the northwest, and by the Alps in the south and, to a lesser extent, the northeast (Fig. 1.1). The eastern part of the *Grand Lac* basin is also referred to as the *Haut Lac*. The surrounding mountains there can reach over 1000 m above the lake surface within 2 km from shore. This topography creates a "corridor" through which two strong dominant winds pass over most of the lake surface, namely the *Bise,* coming from the northeast, and the *Vent,* from the southwest (Fig. 1.1). Lemmin and D'Adamo (1996) showed that on average, the western part of the *Grand Lac* and most of the *Petit Lac* experience higher wind speeds than the eastern part of the *Grand Lac* due to topographic sheltering by the high mountains surrounding the *Haut Lac* area.

3.2.2. Meteorological data

Meteorological data over Lake Geneva are not measured. However, the Swiss Federal Office of Meteorology and Climatology (MeteoSwiss, last accessed 1 February 2018) runs a numerical weather model, COSMO-2 that provides hourly output on a 2.2-km grid for the studied period. COSMO-2 data include spatiotemporal maps of wind speed (10 m above the lake), air temperature (2 m above the lake), relative humidity (2 m above the lake), cloudiness, global radiation and air pressure. Model results are systematically verified against over-land surface data in Switzerland and Europe by MeteoSwiss. The present study is based on COSMO-2 data sets for the period from 1 March 2008 to 31 December 2014. We used the assimilated results (called analysis data) based on the field observations rather than pure forecast data.

To investigate the quality of analysis COSMO-2 results, these data were compared with in situ measurements taken at meteorological stations located around the lake in chapter 2 (Rahaghi et al. 2018). A high correlation coefficient (more than 0.96) between those measurements and the COSMO-2 data was found, with the exception of wind speed, which has higher local spatiotemporal variability. For wind speed, the cross correlation between different stations was similar for COSMO-2 data and in situ measurements, thus confirming the capability of the COSMO-2 model to represent large-scale wind patterns over Lake Geneva. A cubic

interpolation method was applied to map the meteorological data in the LSWT satellite grid cells which have a pixel resolution of ~1 km. Although COSMO-2 can distinguish lakes from land by using a lake model only for the momentum transfer calculation (Mironov 2008), COSMO-2 cannot spatially resolve LSWT.

3.2.3. Lake surface water temperature (satellite data)

Riffler et al. (2015) determined LSWT for 25 lakes in and near the Alps from a long-term archive of Advanced Very High Resolution Radiometer (AVHRR) satellite imagery (~ 1 km pixel size). The satellite-based temperatures agreed well with the near-surface in situ measurements with a bias and Root Mean Square Error (RMSE) within the range of −0.5 to 0.6 °C and 1.0 to 1.6 °C, respectively. This range of values favorably corresponds with another long-term LSWT calibration for Lake Geneva (Oesch et al. 2005). In the present study, we use the same dataset as Riffler et al. (2015), i.e., 4384 images from 1 March 2008 to 31 December 2014, to retrieve LSWT. Images with more than 70% lake coverage were selected, resulting in a total of 856 diurnal images and 308 nocturnal images. Missing pixels in these images were interpolated spatially using Barnes interpolation (Koch et al. 1983; Liston and Elder 2006). The present analysis requires a pixel-wise spatially-resolved time series of lake surface temperature, which was derived from the spatially interpolated LSWT maps. Time series were produced using Piecewise Cubic Hermite Polynomials. For a large surface area, the effect of diel temperature variation on the pixel-wise interpolated data is expected to be small (Woolway et al. 2016). A simple cross-validation analysis was performed on the interpolation algorithms by randomly and repeatedly removing some measured points. A correlation coefficient of ~ 0.99 and a RMSE of ~ 0.85°C are found when comparing actual measurements and the virtually interpolated points.

3.2.4. Spatiotemporal variation of meteorological data and LSWT

The monthly mean spatial anomalies of wind speed for March, June, September and December, representative of different seasons, averaged over the study period (1 March 2008 to 31 December 2014) are plotted in Fig. 3.1a (maps for other months are presented in the Supplementary Information (SI), Fig. S3.1) section. A distinct pattern is evident for all seasons, with the highest winds over the western part of the *Grand Lac* basin and often slightly lower winds over the *Petit Lac* basin. Lowest wind speeds are systematically found over the *Haut*

Lac, the eastern part of the *Grand Lac* basin where high mountains surround the basin. On average, wind speeds over the western half of Lake Geneva are twice as high as those over its eastern half, and are higher from September to March compared to the summer period (April to August). The lake-wide mean wind speed also shows a seasonal pattern with high speeds measured during fall and in particular winter, and low speeds during the summer.

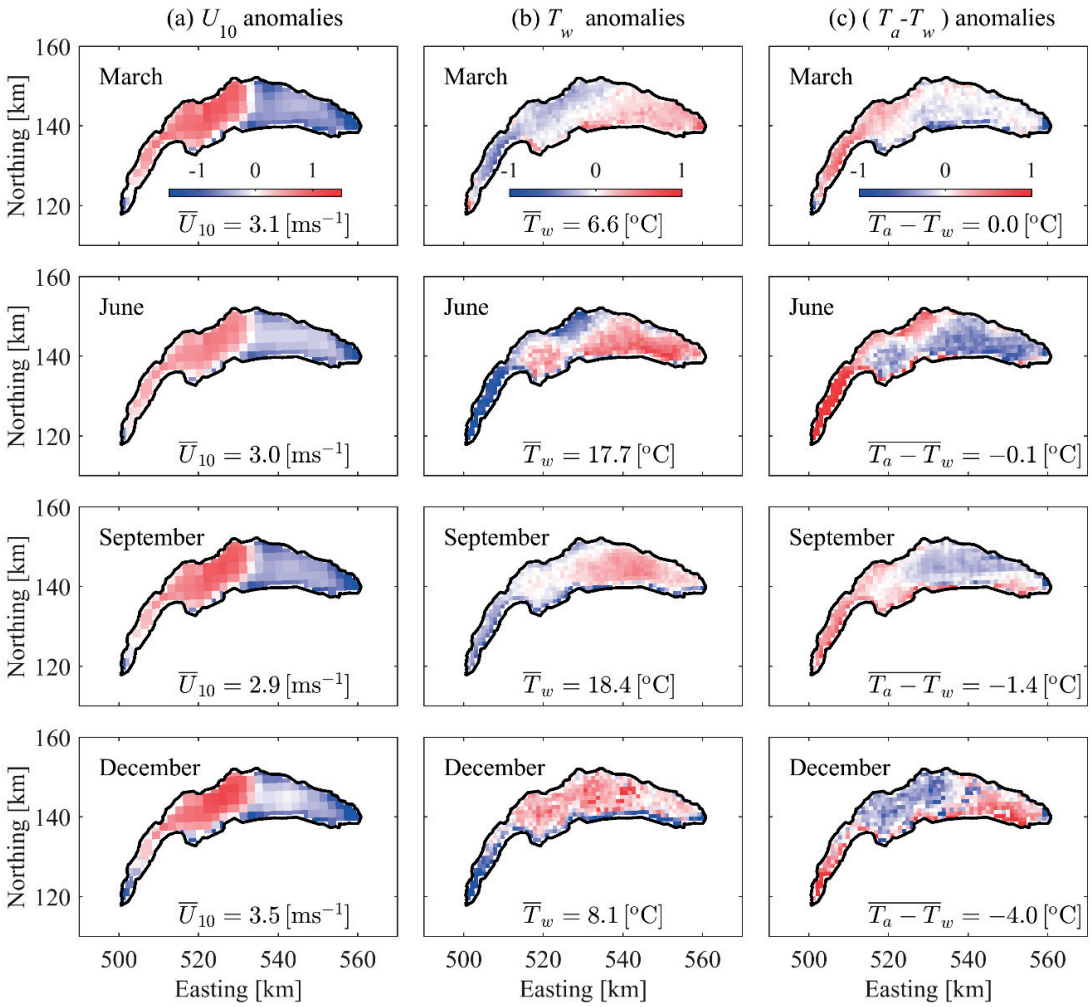

Fig. 3.1. Mean monthly anomaly patterns of (a) wind speed at 10 m above the surface (U_{10}), (b) LSWT (T_w), and (c) air-water surface temperature difference (T_a - T_w). Spatial averages are noted on each map. For a better comparison, the deviations from the mean spatial value within a range of ±1.5 ms^{-1} and ±1 °C are plotted in panels (a), and (b)-(c), respectively. The Swiss coordinate system with km length-based units (CH1903) is used in these plots. Legends of the color range are given in the top panels.

The monthly mean LWST distribution over the lake surface for selected months, averaged over the period 1 March 2008 to 31 December 2014 (Fig. 3.1b), shows that the temperatures in the

Petit Lac are most of the time below the lake-wide mean LWST and above the lake-wide mean LWST in the eastern part of the *Grand Lac* (see maps for other months in Fig. S3.2). A typical pattern for the summer months (April to August) is seen in the June image of Fig. 3.1b with a strong North-South temperature gradient across the *Grand Lac* basin, most pronounced in the western and central parts. During fall and winter, a band of below-average LSWT is observed along the southern shore due to shielding of solar radiation by the high mountains along the southern shore. Temperatures in the *Haut Lac* area of the lake remain above the lake-wide average year round, and in the western part of the *Grand Lac,* they may be close to average or slightly above. Lake-wide mean LWSTs follow the seasonal cycle that is characteristic for the mid-latitude climate zone. The monthly mean spatial patterns of air-water temperature difference, which will be discussed below, are also plotted (Figs. 3.1c and S3.3).

Time evolution of meteorological data and LSWT (labeled T_w), smoothed with a 30-d moving average, shows the mean annual cycle typical for this latitude for LWST, air temperature and global radiation with maxima in the summer and minima in the winter (Fig. S3.4). Wind speed reaches its highest mean values during the fall to spring period. To further investigate the temporal variability of the spatial distribution of these parameters, an InterQuartile Range (IQR) analysis based on the 25-75 percentile was carried out in order to determine how spread out the actual values are with respect to the spatial median value. To better visualize the results, the mean time trend seen in Fig. S3.4 was subtracted, and to facilitate the interpretation of the IQR results, we included the 1-99 percentile, called P1-99 hereinafter, which is indicative for the total range.

The spatial distribution range over the lake of the above parameters, identified via IQR and P1-99 and smoothed with a 30-d running mean (Fig. 3.2) reveals that spatial variability is noticeable. Figure 3.2a gives the temporal evolution of LSWT spatial anomalies. The negatively skewed distribution, which is dominant in Fig. 3.2a, is due to the colder mean LSWT values in the *Petit Lac* compared to the *Grand Lac* and the narrow cold band close to the southern shore of the lake (Fig. 3.1b). Spatial variability in wind speed, U_{10} (Fig. 3.2b), is considerable. The IQR band shows seasonal variations with widest bands usually during the fall to spring period. Comparing the median to the quartile values reveals that the wind speed distribution over the lake has a higher proportion of low speeds, and therefore the median is closer to the first quartile (Figs. 3.2b and S3.4b). Significant peaks, mainly during winter, are seen in the total range of

P1-99 band (Fig. 3.2b). Air temperature has the narrowest IQR band with respect to the standard deviation, indicating that air temperatures over the lake are more evenly distributed (Fig. 3.2c). However, the total range (P1-99) suggests that often, in particular from fall to spring, significant temperature differences can be expected over the lake. The IQR band of the global radiation is narrowest during winter and widest during summer (Fig. 3.2d). The total range is wide with more pronounced negative peaks mainly occurring during the summer season. This may be related to different types of cloud cover during the different seasons. Shielding by the high mountains along the southern shore in the central to eastern part of the *Grand Lac* basin may also contribute. The above results confirm the significance of spatial variability of LSWT and the meteorological parameters that most strongly affect the heat flux dynamics over Lake Geneva.

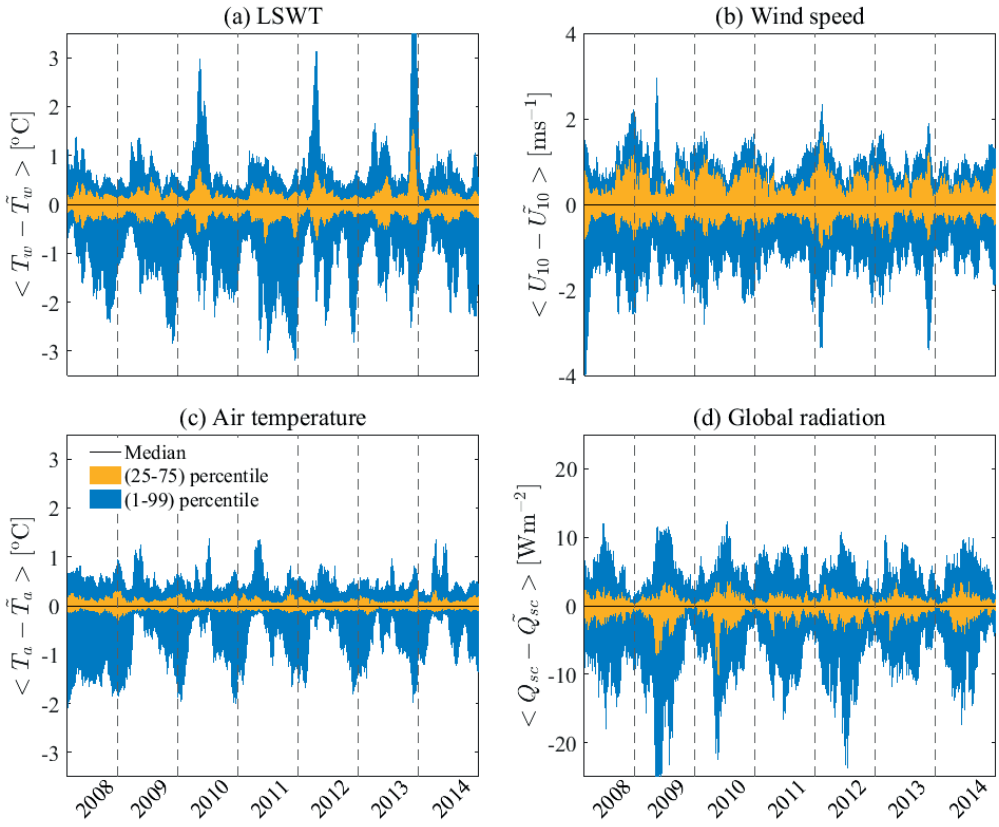

Fig. 3.2. Time series of the spatial anomalies, IQR and P1-99, of lake surface water temperature (LSWT) and meteorological data. The time series are smoothed with a 30-d running window and the median has been removed. (a) LSWT (T_w), (b) wind speed (U_{10}), (c) air temperature (T_a), and (d) global radiation (Q_{sc}). These plots show the time evolution of the colored areas in Fig. S3.4 in the Supplemental Information (SI) section. Colors are identified in the legend in (c).

3.2.5. Bulk modeling of surface heat fluxes

The net (total) heat flux at the air-water interface, SurHF, also called Q_N, is given by:

$$Q_N = Q_{sn} + Q_{an} + Q_{br} + Q_{ev} + Q_{co} \quad (3.1)$$

The effect of precipitation on the SurHF is neglected, since it has a minimal influence on the surface heat exchange of central European lakes (Livingstone and Imboden 1989; Rimmer et al. 2009; Fink et al. 2014). SurHF is often estimated using bulk formulas. These formulas are based on different concepts and require specific parameters. Ideally, these parameters are known for a given site (e.g., a lake), but, in practice, lake-specific calibrated parameter sets are required (Phillips et al. 2016). For each of the five SurHF terms on the right hand side of Eq. 3.1, there are various formulations available in the literature, and their possible combinations give rise to numerous net SurHF models. In a comprehensive study by Rahaghi et al. (2018; Unpublished work), various combinations of SurHF models were evaluated for Lake Geneva based on the total heat content variation concept (Van Emmerik et al. 2013; Fink et al. 2014). A 2-point calibration and optimization (Rahaghi et al. 2018; Unpublished work) was performed using long-term detailed water temperature profiles at two locations far from the shore (SHL2 and GE3 in Fig. 1.1). The present analysis is based on the obtained optimal models. These models are then assumed to be valid over the entire lake. Details about the calibration procedure were given in chapter 2.

3.3. Results

3.3.1. Mean annual spatiotemporal variability of surface heat flux

The lake-wide average net SurHF and its terms for the study period, smoothed with a 30-d running mean, are presented in Fig. 3.3. The mean shortwave solar radiation Q_{sn} follows the annual sun cycle (Fig. 3.3a), with a maximum and minimum around the summer and winter solstices, respectively. Most years, the mean Q_{sn} curve shows sub-monthly temporal fluctuations most often from the end of the spring to the summer that reflect cloud cover variability. Atmospheric longwave radiation, Q_{an}, is the largest warming contributor to SurHF with the second largest annual amplitude after solar radiation (Fig. 3.3b). It is compensated by the longwave back radiation from the lake, Q_{br} (Fig. 3.3c). The Q_{an} and Q_{br} terms approximately follow the same periodic variation but are shifted in phase by half an annual cycle. The mean

annual radiative heat fluxes were estimated to be 135.6 for Q_{sn}, 292.7 for Q_{an}, and –370.2 Wm^{-2} for Q_{br}, respectively, for the period of 1 January 2009 to 31 December 2014 (due to the missing data of January-February, 2008 results were excluded for the mean annual analyses).

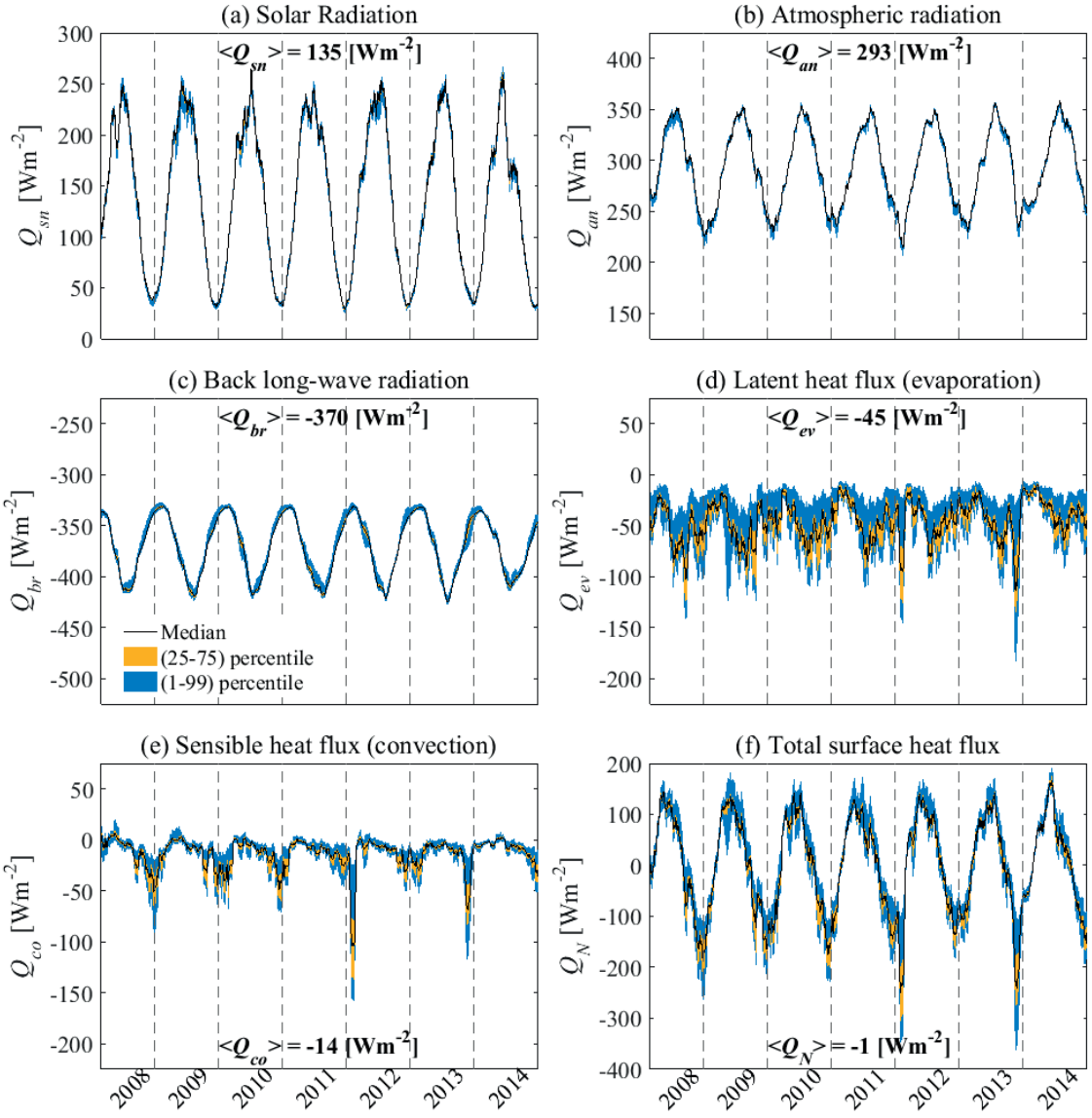

Fig. 3.3. Time series of the median (black lines) and percentiles (colored areas for IQR, and P1-99; colors are identified in the legend in (c)) of the distribution of spatially resolved surface heat flux (SurHF) terms and net SurHF for Lake Geneva smoothed with a 30-d running mean: (a) solar radiation, Q_{sn}, (b) atmospheric radiation, Q_{an}, (c) back radiation, Q_{br}, (d) latent heat flux, Q_{ev}, (e) sensible heat flux, Q_{co}, and (f) net SurHF (Q_N). For a better comparison, all plots (except f) have the same range of 300 Wm^{-2} on the ordinate axis. The mean annual values of each term and the net SurHF, averaged over the 2009 to 2014 period, are also noted on each diagram.

The contributions of the non-radiative (turbulent) heat flux terms are smaller in magnitude compared to the radiative components, but they show larger variability in both time and space. On average, the evaporative heat loss (Q_{ev}, Fig. 3.3d) is lower during the spring and higher in the summer. The mean annual evaporative cooling for the period 2009 to 2014 is –45.0 Wm^{-2}. Convective heat loss (Q_{co}, Fig. 3.3e) is usually highest in winter when both wind speed and air-water temperature differences are high. In contrast to evaporation, which always cools the lake, convection may occasionally warm the lake during spring, mainly in April and May, when the lake-wide average LSWT can be colder than the air temperature. Overall, the mean annual convective cooling is –14.1 Wm^{-2} for the period 2009 to 2014.

The net SurHF (Fig. 3.3f) follows an annual cycle with occasional exceptionally strong cooling (e.g., January 2012, December 2013) and warming (e.g., May and June 2014) events (see the mean annual plot in Fig. S3.5). Due to the phase shift in cooling and warming of the lake, the range of mean net SurHF from Eq. 3.1 (> 350 Wm^{-2}, Fig. 3.3f) is higher than the range of each of the individual SurHF terms (< 250 Wm^{-2}, Figs. 3.3a-e). The spatial variability of IQR and P1-99 will be discussed below.

3.3.2. Spatial variability of surface heat flux components

The monthly spatially resolved variability of the net SurHF maps (Fig. 3.4) indicates that, on average, the SurHF in the western part of the *Grand Lac* is below the lake-wide mean value, whereas it is above in most of its eastern part. This non-uniformity in SurHF is accentuated during the cooling season, and the spatial pattern changes little in shape during this period. Thus, the eastern part of the *Grand Lac* cools less rapidly than its western part. A minimum SurHF spatial variation is found in March to May, with a spatial standard deviation, σ_s, of ~ 8 Wm^{-2}. In the *Petit Lac*, the SurHF is either above the lake-wide mean or close to it and the least spatial variability is again seen during March to May.

Mean monthly $\bar{Q}_N$ and σ_s values, as well as the mean SurHF spatial range (min/max difference), R_s ($\bar{Q}_N$), are listed in Table 3.1. A relatively high spatial standard deviation of > 20 Wm^{-2} (equivalent to a temperature change of 0.88 °Cy^{-1} in the whole water body of Lake Geneva) was obtained during February, October and December (25%, 32% and 17% of mean $\bar{Q}_N$, respectively). The results also indicate that during certain months, on average, some parts of

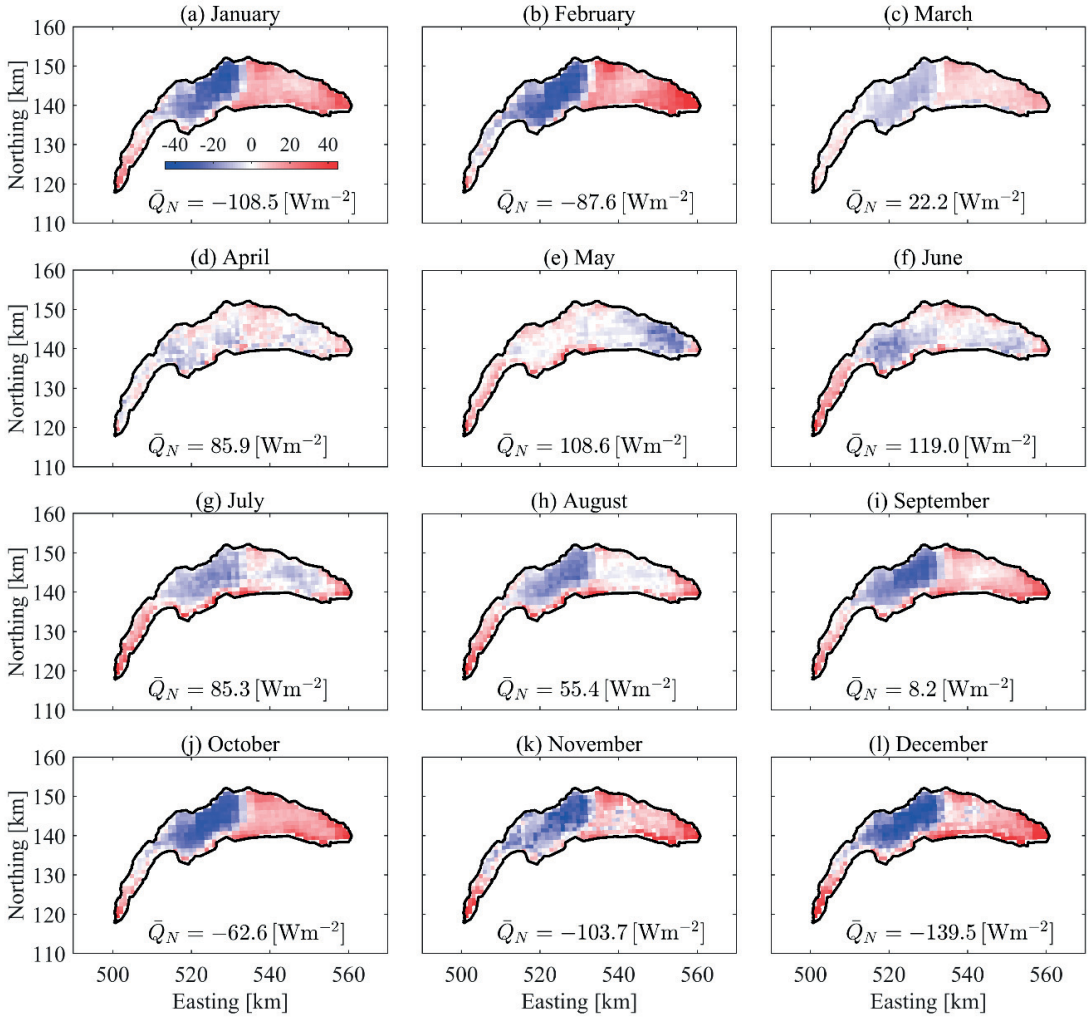

Fig. 3.4. Mean monthly net SurHF anomaly patterns of Lake Geneva averaged over the period from March 2008 to December 2014. The lake-wide mean values are indicated on each map. For a better comparison, all panels use the same scale, showing deviations from the mean value within a range of ± 45 Wm^{-2}. The Swiss coordinate system with km length-based units (CH1903) is used. Colors are identified in the legend in (a).

the lake warm up, while other parts cool down. This behavior is pronounced during September and to a lesser extent in March. During these months the mean lake-wide SurHF is low. Lofgren and Zhu (2000) estimated the monthly SurHF for Lake Huron using satellite LSWT and data from on-shore meteorological stations. They found a maximum spatial standard deviation of ~20 Wm^{-2} during August and December. A close-to-zero mean net SurHF was reported for March and September that agrees with the results from Lake Geneva. Over Lake Constance, a

total SurHF spatial range was estimated to be 60 Wm^{-2} during May 1989 (Schneider and Mauser 1991). We obtain a value of 63 Wm^{-2} for that month over Lake Geneva. The effect of the spatial SurHF variation on the spatial lake heat content variation will be addressed below.

Table 3.1. The lake-wide average $\bar{Q}_N$, standard deviation σ_s and range $R_s(\bar{Q}_N)$ of monthly SurHF patterns shown in Fig. 3.4

Month	$\bar{Q}_N$ [Wm^{-2}]	σ_s [Wm^{-2}]	$R_s(\bar{Q}_N)$ [Wm^{-2}]
Jan	–108	18	74
Feb	–88	22	90
Mar	22	8	33
Apr	86	7	46
May	109	10	63
Jun	119	11	75
Jul	85	14	76
Aug	55	15	88
Sep	8	17	73
Oct	–63	20	79
Nov	–104	19	98
Dec	–139	23	102

The average spatial pattern of the net SurHF for the 2009 to 2014 period (Fig. 3.5) shows a mean spatial standard deviation and a range of ~13 and > 40 Wm^{-2}, respectively. This variability emphasizes that a single-point analysis can lead to sizable errors in the estimation of the SurHF and hence the heat budget of a large water body (Rahaghi et al. 2018; Unpublished work). In addition, a small negative mean spatiotemporal heat flux of –1 Wm^{-2} (indicated in Fig. 3.5) is found for the entire period considered, i.e., the lake slightly cooled during the period from 2009 to 2014, if we assume that the SurHF dominates the lake's energy budget. Since a close-to-zero value is expected for the mean spatiotemporal SurHF of Lake Geneva, this small value confirms the validity of the methods and formulas employed in this study. However, due to various sources of uncertainty, e.g., errors in data retrieval, model assumptions, etc., the mean absolute

value (-1 Wm^{-2}) must be interpreted with caution. The physical parameters controlling the obtained spatial SurHF anomalies and the effect of such variability on the estimation of lake heat content will be discussed in the following sections.

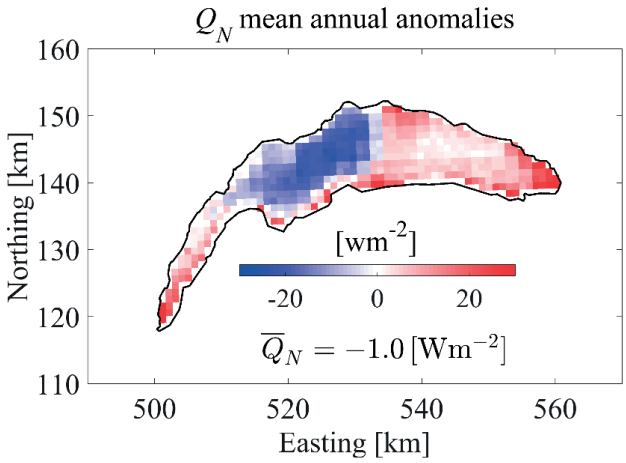

Fig. 3.5. Mean annual pattern of net SurHF in Lake Geneva, based on data from 1 January 2009 to 31 December 2014. The spatial pattern shows deviations from the mean value within a range of ± 30 Wm^{-2}. The Swiss coordinate system with km length-based units (CH1903) is used. Colors are identified in the legend.

3.3.3. Statistical analysis of the spatial heat flux variability

To characterize the factors underlying the observed spatial SurHF anomalies (Figs. 3.4 and 3.5), we computed statistics relating the spatial variability of the net SurHF to that of the different SurHF terms. The correlation coefficient and Root Mean Square Difference (RMSD) between spatially resolved hourly maps of different SurHF terms and the total SurHF were calculated. The results were smoothed with a 30-d running mean window, and then for each hour in the year averaged over the corresponding time during the 6-y period from 1 January 2009 to 31 December 2014 (for leap years the additional day in February was removed). Higher correlation coefficients and smaller RMSD values indicate a more significant contribution of the corresponding SurHF term to the spatial variability of the net SurHF. The radiative heat flux components, Q_{sn}, Q_{an} and Q_{br}, have relatively low correlation coefficients and high RMSDs (Fig. 3.6) pointing towards the low probability of spatial variability of these terms. Evaporation (latent heat flux, Q_{ev}) patterns have the highest correlation coefficient (Fig. 3.6a) and the lowest RMSD (Fig. 3.6b) for all months and is followed by convection, Q_{co}. Therefore, spatial evaporation and convection variations are mainly responsible for the observed spatial anomalies of SurHF over Lake Geneva. This is in agreement with the findings in other large lakes, e.g., Lake Superior (Xue et al. 2015) and Lake Huron (Lofgren and Zhu 2000). However, there is

more spatial variability in global radiation and air temperature over Lake Huron due to its larger surface area (~10 times greater than Lake Geneva). Therefore, the spatial variability of the net radiative flux on Lake Huron is more than two times higher than that of Lake Geneva. Similar to Lake Geneva, a significant spatial variability of evaporation was also reported for other large lakes, e.g., Lake Tanganyika (Verburg and Antenucci 2010) and Great Lakes (Moukomla and Blanken 2017).

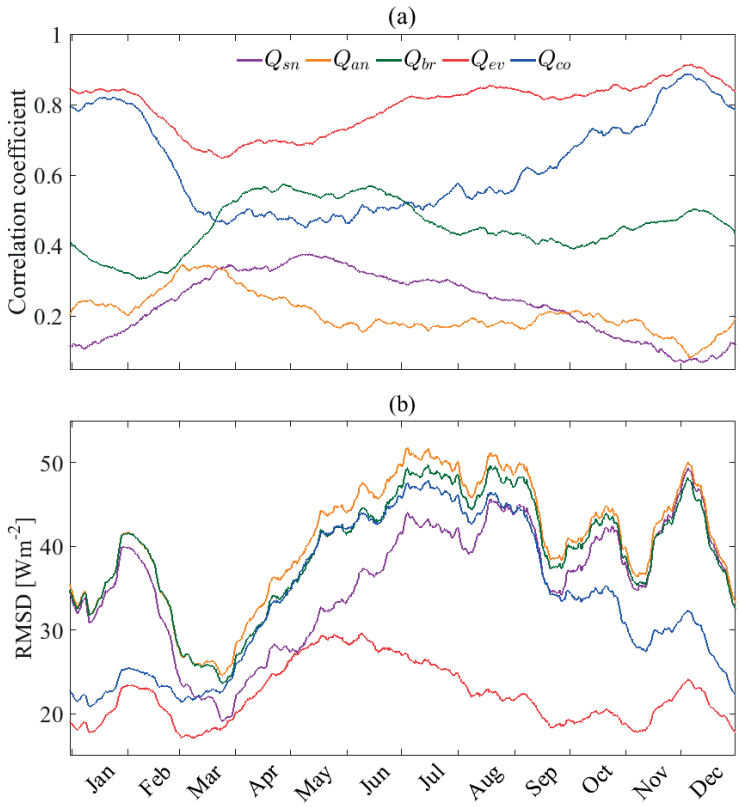

Fig. 3.6. Statistical comparison of spatial patterns of individual SurHF components with respect to spatial patterns of net SurHF: (a) correlation coefficient, and (b) root mean square difference (RMSD). The results are smoothed with a 30-d running mean. Colors are identified in the legend in (a).

Figure 3.6 also indicates that the correlation and RMSD between the SurHF components and net SurHF vary throughout the year. Evaporation has a high correlation (> 0.8) with net SurHF from July to February that is reduced to about 0.7 in March and April. In March, and to a lesser extent in April, the RMSD curves converge due to the overall small spatial variability of the net SurHF (Fig. 3.4) and the various SurHF terms (not shown). The convective (sensible heat flux, Q_{co}) component demonstrates a behavior similar to Q_{ev} from November to February, while it deviates from Q_{ev} from March to June. Generally, a change of the SurHF forcing regime during the March to June period with respect to the rest of the year is observed for the net SurHF spatial

patterns (Fig. 3.4) and the analysis of SurHF components (Fig. 3.6, see the Q_{br} correlation curve as a clear example). This will be further discussed below.

Time series of IQR of the spatial variability of the net SurHF and its components with their median values removed (Fig. 3.7) show that the spatial variability of the radiative components (Fig. 3.7a) is small throughout the study period and hardly changes with time, thus confirming the correlation analysis results above. The spatial variability of SurHF in IQR is dominated by the spatial variability of the two turbulent flux components, in particular evaporation, Q_{ev} (Fig. 3.7b). Seasonal variability of Q_{ev} is obvious with smaller spatial variability occurring during spring. However, a year-to-year variability is also seen in this pattern reflecting changing large-scale weather conditions. During most years, convective heat flux, Q_{co}, has small spatial variability except from late fall to early spring, when it may reach spatial variability values similar to those of Q_{ev}. Individual events of strong spatial SurHF variability such as in early 2012 and late 2013 are exclusively caused by the variability of the turbulent heat flux components. The P1-99 distribution (not shown) is similar to the IQR distribution, but spread out over a wider range. This indicates that spatial variability of turbulent heat fluxes significantly contributes to the spatial variability of SurHF over Lake Geneva.

3.4. Discussion

3.4.1. Effects of spatial variability of meteorological forcing on SurHF

In order to determine the major meteorological factors controlling the spatial thermal variability patterns, we computed the correlation coefficients of hourly spatial patterns (over 7 y) of each meteorological parameter and the net SurHF at the corresponding time. The hourly (spatial) correlation coefficients thus obtained were smoothed with a 30-d running mean, and then averaged over a year (i.e., the correlation coefficients for a given hour in the year were averaged over the six or seven years considered; for leap years the additional day in February was removed). The results are shown in Fig. 3.8. Spatial LSWT (T_w) and wind speed (U_{10}) are negatively correlated with the spatial SurHF pattern. Global radiation, Q_{sc}, reaches a maximum correlation coefficient of around 0.5 during March and April, the months with the lowest spatial variability in net SurHF (Fig. 3.4). Except for spring, wind speed has a correlation of > 0.6 and is the dominant meteorological parameter controlling net SurHF spatial variability.

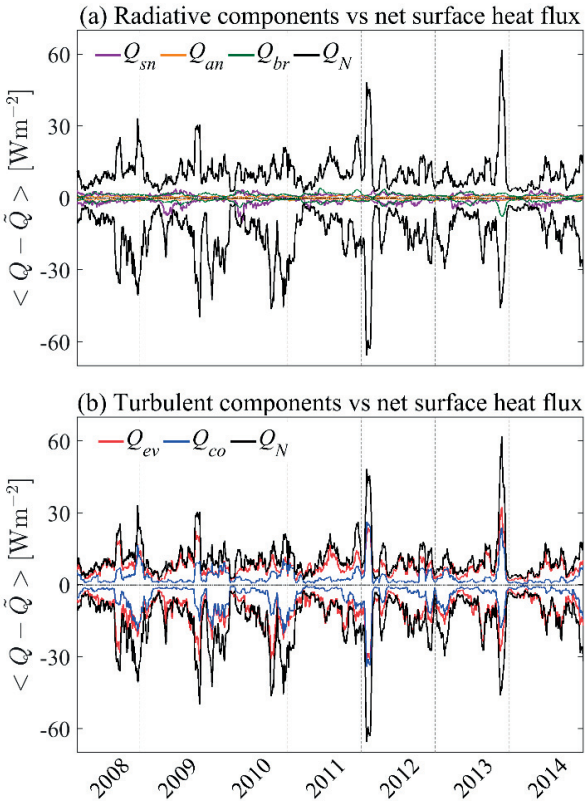

Fig. 3.7. Time series of the spatial anomalies with respect to the median value ($\tilde{Q}$), i.e., IQR (25-75 percentile), of the surface heat flux (SurHF) components as compared with the net SurHF of Lake Geneva: (a) radiative heat flux terms, and (b) turbulent heat fluxes terms. The results are smoothed with a 30-d running mean.

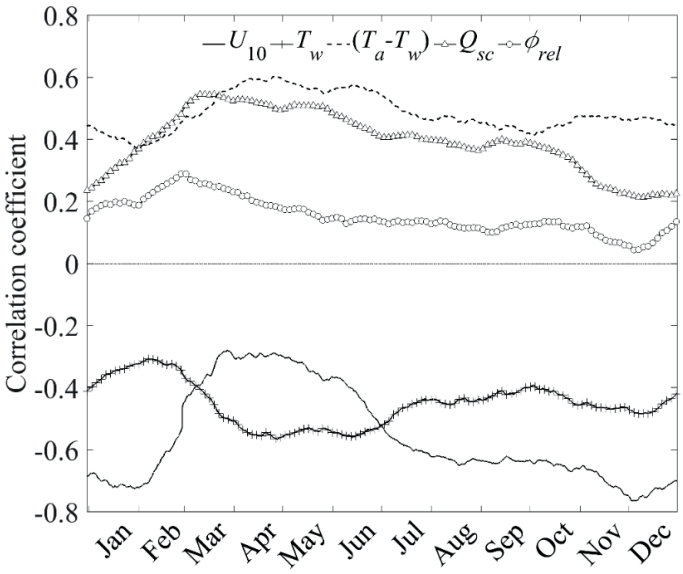

Fig. 3.8. Temporal variation of correlation coefficients between lake-wide meteorological parameters and lake-wide net SurHF.

The air-water temperature difference is close to zero in early spring over a large portion of the lake (March and April in Figs. 3.1c and S3.3). The wind speed is also relatively low during that period, in particular during April (Figs. 3.1a and S3.1). As a result, the spatial SurHF variability due to evaporation and convection is lowest in early spring, as indicated by the low spatial correlation coefficients during this time (Fig. 3.6). During the March-to-June period, when wind speeds are low (Figs. 3.1a and S3.1), LSWT and the air-water temperature difference are the most important parameters, with correlation coefficients of approximately 0.6 (Fig. 3.8). During this period, the convective net cooling effect due to the air-water temperature difference ($T_w - T_a$) is larger in the eastern part of Lake Geneva than in the western part of the lake (not shown). Thus, the wind-sheltering effect in the eastern part of the lake is partially compensated by the air-water temperature difference during spring, and consequently there is a less noticeable difference in SurHF between the eastern and western parts of the *Grand Lac* (Fig. 3.4). Schneider and Mauser (1991) suggested the same reason for the estimated spatial variation of SurHF over Lake Constance during May 1989. Using point data over three small lakes, Granger and Hedstrom (2011) found that wind speed, land-water temperature difference and land-water vapor pressure contrasts were the dominant factors causing turbulent SurHF variations. As is the case in the present study, they reported a minimum in turbulent cooling during spring.

The patterns in Figs. 3.1c and S3.3 demonstrate that the convective net heating effect due to the air-water temperature difference is smaller in the eastern part of the lake during March to June compared to the western part of the lake. On average, LSWT (Figs. 3.1b and S3.2), and hence longwave cooling is lower in the *Petit Lac* than the *Grand Lac*. Furthermore, the effect of strong winds on convective cooling is partially balanced by higher ($T_a - T_w$) in the *Petit Lac*. These factors explain the higher SurHF in the *Petit Lac* compared to the western *Grand Lac* (Figs. 3.4 and 3.5).

3.4.2. Atmospheric boundary layer stability

It was shown above that evaporation and convection are the most important heat flux components affecting the spatial variability of net SurHF. The main variable in these terms is the Obukhov ABL stability parameter, ζ, which characterizes the relative contribution of buoyancy and wind shear to the turbulence generation over the lake surface (Yusup and Liu 2016). When $\zeta < 0$, the ABL is unstable, and turbulent cooling of the surface is higher. In contrast, under stable ABL conditions ($\zeta > 0$), the turbulent heat exchange is less important.

ABL stability is determined by several meteorological parameters, such as wind speed (U_{10}), LSWT (T_w), air-water temperature difference ($T_a - T_w$) and relative humidity (ϕ_{rel}). To examine the combined effect of the dominant controlling factors, i.e., U_{10}, T_w and ($T_w - T_a$), the mean temporal variation and the mean spatial pattern of the ABL stability parameter (ζ) for different months were calculated.

The annual time series of the median and the spatial anomalies of the ABL stability parameter (ζ) are shown in Fig. 3.9. The results (smoothed with a 30-d running mean) demonstrate that the ABL is unstable over Lake Geneva, except for a stable period from early March to early June. The transition to a stable period in spring coincides with the strong change in the values of the various correlation coefficients observed before in Figs. 3.6 and 3.8. Evaporation, as discussed above, was at its minimum during the stable period ($\zeta > 0$). Woolway et al. (2017), using data from different lakes, observed that unstable ABL conditions are least common during spring. Our results indicate that on an annual basis, the ABL is unstable ~ 74% of the time over Lake Geneva and that the unstable period accounts for ~ 90% of total evaporation. Woolway et al. (2017) reported unstable ABL conditions ~ 72% of the time (annual basis). Persistent unstable conditions were observed over tropical lakes (Verburg and Antenucci 2010; Woolway et al. 2017).

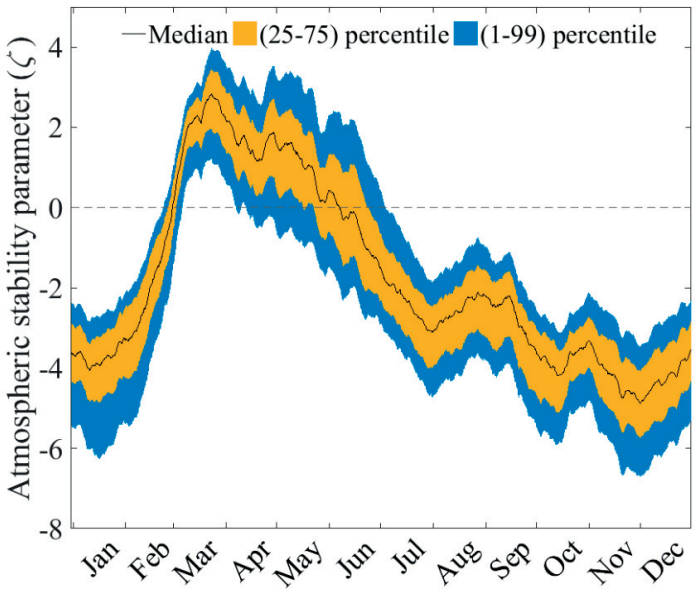

Fig. 3.9. Temporal variation of lake-wide mean atmospheric stability parameter (ζ), smoothed with a 30-d running mean window. The colored areas indicate the spatial distribution (IQR and P1-99) of ζ. Colors are identified in the legend.

The range of spatial anomalies of ζ as indicated by IQR and P1-99 is approximately constant in time except in late February and early March, when the stability changes rapidly from unstable to stable and the spatial variability is reduced (colored areas in Fig. 3.9). Since the ABL is more stable during spring, the air-water temperature difference is close to zero over most of the lake (Fig. 3.1c), resulting in lower turbulent heat fluxes, Q_{ev} and Q_{co}. In early spring, this stability is due to intense solar radiation, and the capacity of water to absorb heat is high, because surface layer water temperatures are colder and the stratification is weaker than in summertime. Comparing T_w and T_a spatial patterns (not shown) suggests that the spatial distribution of air-water temperature differences over Lake Geneva, and hence the spatial variability of the atmospheric thermal boundary layer, is predominantly controlled by LSWT, not air temperatures.

Maps of the mean ABL stability parameter based on the six years of analysis were created for each month as described above for SurHF (Fig. 3.4). The spatial variability of ζ is large compared to its mean throughout the year (Fig. 3.10) for all months. The narrowest range of spatial variability is found during the period of stable stratification (March to May). This corresponds to the narrowest range of spatial variability of SurHF observed in Fig. 3.4. During the unstable period ($\zeta < 0$) from July to February, the ABL is less unstable in the western *Grand Lac* where the SurHF is at the lowest below the monthly mean value (Fig. 3.4). Thus, in this area, the less unstable the ABL is, the greater the heat loss is from the lake. This agrees with Yusup and Liu (2016) who found that the maxima of turbulent heat fluxes did not occur in the most unstable conditions, but rather at low values of ζ. On average, the ABL is more unstable in the eastern *Grand Lac* where wind speeds are generally lower than in the western *Grand Lac.* In the eastern part of Lake Geneva, gradients from the less unstable southern part to the more unstable northern part are evident for some months. Yusup and Liu (2016) had already indicated that low wind speeds usually correspond to very unstable ABL conditions as seen in the eastern *Grand Lac*. They also mentioned that due to mixing in the near-surface water layers caused by wind stirring, the feedback mechanism between ABL stability and turbulent heat fluxes may at times make the interpretation of the relationship between these parameters difficult. For the *Petit Lac,* it is more difficult to establish a clear link between ζ and SurHF.

The ABL stability concept appears in the Monin-Obukhov similarity theory, Eq. S2.7 in Table S2.3. Yusup and Liu (2016) suggested that the Monin-Obukhov similarity theory may have

limited validity beyond the stability range of $|\zeta| < 1$. Studying the effect of thermal inertia and water advection on the Monin-Obukhov scaling, Assouline et al. (2008) concluded that for the case of small advection and large thermal inertia, as seen in Lake Geneva in the spring, the transport efficiency of humidity is higher than that of temperature, whereas they are usually assumed to be equal in the similarity theory (Zeng et al. 1998; Woolway et al. 2015). This can also be a source of error in the presented results.

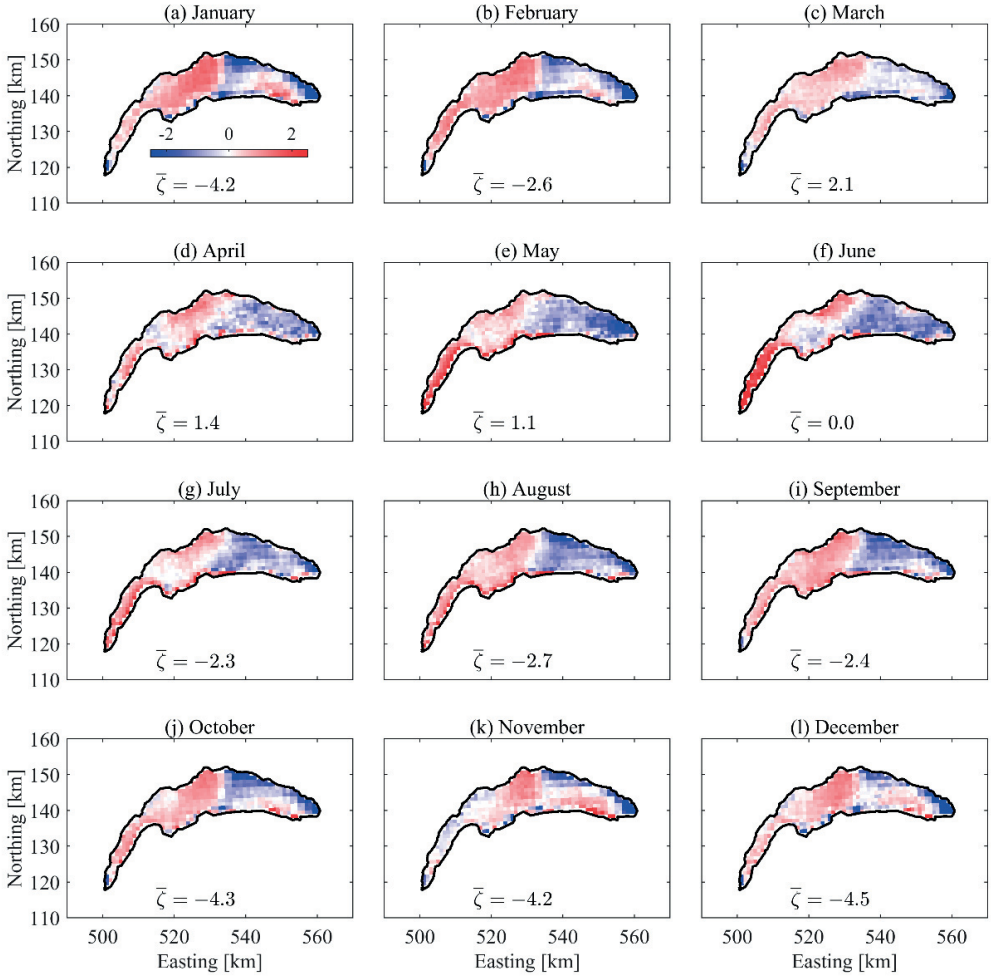

Fig. 3.10. Mean monthly anomaly patterns of Atmospheric Boundary Layer (ABL) stability (ζ) for Lake Geneva averaged over the period from March 2008 to December 2014. The lake-wide mean values of ζ for each month are indicated on each map. For a better comparison, deviations from the mean value within a range of ±2.5 are plotted. The Swiss coordinate system with km length-based units (CH1903) is used. Colors are identified in the legend in (a).

3.4.3. Spatial clustering using the *k*-means method

To further explore similarities in the SurHF spatial patterns and those of meteorological parameters, the *k*-means clustering method (Jain 2010) was applied to the seasonal data. In the present analysis, this method is used to spatially partition SurHF and the meteorological parameters that affect SurHF spatial variability into clusters. The number of clusters used ($k \geq 1$) is arbitrary for a given data set. However, the overall variance of the data set decreases with increasing k, and the "optimal" value of k is usually taken at the point where the variance reduction rate becomes relatively small, because the variance first reduces rapidly, then more slowly (e.g., Tibshirani et al. 2001). The method was applied to the hourly data sets of the net SurHF (Q_N) and the three meteorological parameters that affect its spatial variability the most, i.e., LSWT (T_w), wind speed (U_{10}), and global radiation (Q_s). Results for spring and fall (Fig. 3.11; results for the other two seasons are presented in Fig. S3.6) show that the net SurHF splits into four clusters (Fig. 3.11a-b), thus indicating four lake areas within which SurHF values vary little from the mean of the cluster. These compare well with the pattern seen in Fig. 3.4. There are only minor differences between the patterns in the different seasons (Figs. 3.11a-b and S6a-b). LSWT and wind speed also split into four clusters in spring (Fig. 3.11c and e, respectively). The actual pattern of the former more closely resembles that of the clustering of the net SurHF.

Due to convective surface cooling, and therefore strong mixing at the surface, only two LWST clusters (one in the *Grand Lac* and one mainly in the *Petit Lac*) were obtained for the fall season (Fig. 3.11d), while there is more consistency between the SurHF clustering (Fig. 3.11b) and that of the wind speed (Fig. 3.11f) in this season. Therefore, wind speed, which is a key parameter in the evaporative and convective SurHF terms (Eq. S2.7), is significant in controlling SurHF spatial variability during fall. Air-water temperature differences ($T_w - T_a$) are also higher in fall compared to spring (Figs. 3.1c and S3.3) when lower values of ($T_w - T_a$) weaken the effect of the convective and evaporative heat fluxes. As a result, the contribution of the spatial variability of the longwave emission to the observed variability in the total SHF becomes more significant during spring. The similarity between the net SurHF clusters (Fig. 3.11a) and that of LSWT (Fig. 3.11c) confirms this.

In all seasons, the global radiation, Q_s, splits into three clusters (Figs. 3.11g-h and S3.6g-h) that hardly change in shape or extent. The pattern of three clusters probably is a reflection of the effect of the topography surrounding the lake and cloud cover. In general, the results of the

seasonal *k*-means analysis are in agreement with the temporal correlation coefficient trends presented in Fig. 3.8 and coincide with spatial variability in the SurHF patterns (Fig. 3.4). For most of the year, spatial variability is organized in zones aligned along the lake axis from the west to the east.

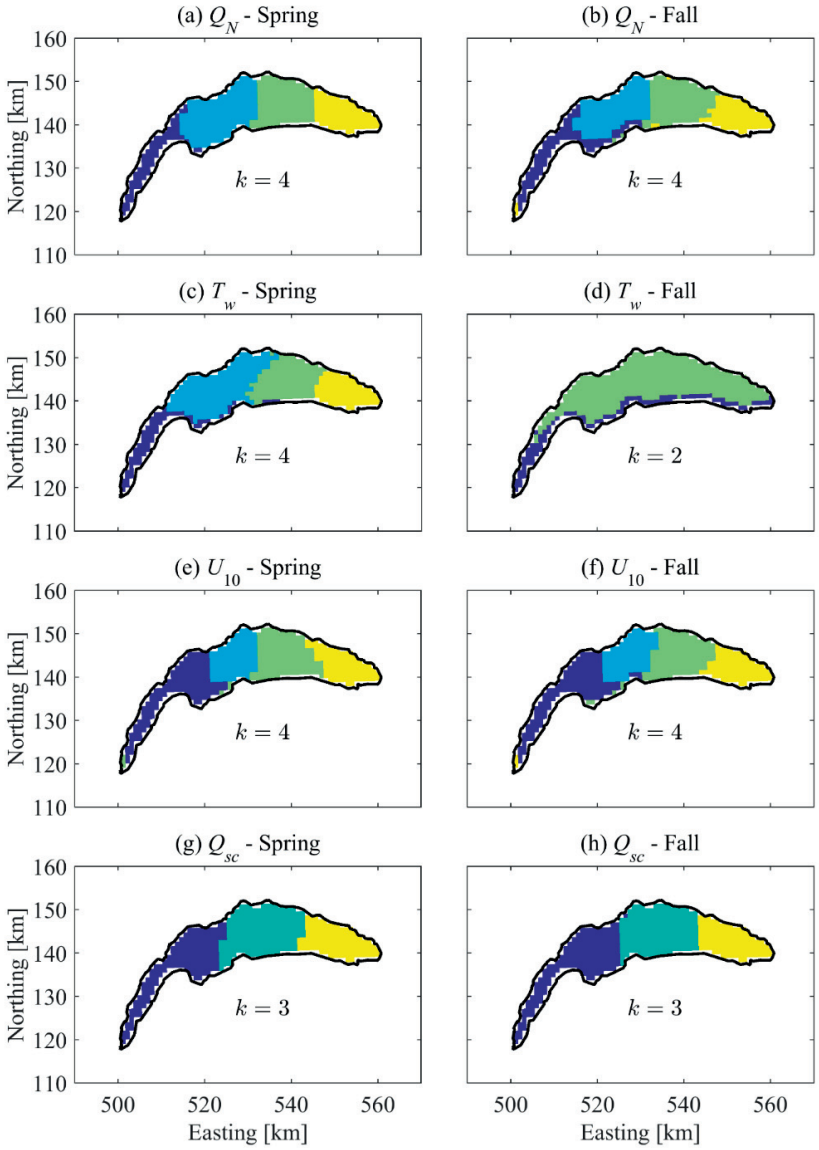

Fig. 3.11. Dominant patterns (clusters) of (a) and (b) net SHF (Q_N), (c) and (d) LSWT (T_w), (e) and (f) wind speed at 10 m above surface (U_{10}), and (g) and (h) global radiation (Q_s), during spring (plots in left panel) and fall (plots in right panel) for the period 2008 to 2014. Shading identifies the different clusters; *k* is given in each panel and is the number of clusters.

A source of error in the above results (Figs. 3.3 to 3.11) may be related to the horizontal heterogeneity due to the relatively large LSWT pixel resolution (~ 1 km) and meteorological data (~ 2.2 km). The area-averaged SurHF may be overestimated or underestimated, particularly when air-water temperature differences are small (Mahrt and Khelif 2010). The change of the ABL regime from unstable to stable and vice versa, results in a drastic change of bulk transfer coefficients (Deardorff 1968). Therefore, we expect higher uncertainties during near-neutral conditions at the end of February and beginning of March (Fig. 3.9). The above-mentioned errors become more significant when the absolute value of the SurHF is at its minimum in the springtime. However, regardless of these uncertainties, the general findings of our study, showing the spatiotemporal variation of SurHF (Figs. 3.3, 3.4 and 3.5) and the change of the dominant controlling regimes (Figs. 3.6, 3.8 and 3.9), are not affected. Better quantification of the associated uncertainties requires higher resolution maps of LSWT and meteorological data, which, to our knowledge, are presently not available.

3.4.4. Lake surface thermal energy (heat content) variability

The heat content variation in the water column over the full lake depth is the sum of the net energy flux into it. In order to determine whether and how the effect of the spatial variability of the SurHF affects the heat content of the lake, the temporal variation of the water column thermal energy is used (Van Emmerik et al. 2013; Fink et al. 2014; Nussboim et al. 2017):

$$\Delta G_m(t) = \int_0^t Q_N(\hat{t})\, d\hat{t} \tag{3.2}$$

Here, the net input energy, ΔG_m [Jm^{-2}] into the lake, is calculated by time-integrating the net SurHF, Q_N [Wm^{-2}], for a given period (Eq. 3.1). This calculation was carried out for one area in the western *Grand Lac* where SurHF is below the lake-wide mean and one in the eastern *Grand Lac* where SurHF is above the lake-wide mean (Fig. 3.5). Time series of Q_N were averaged over a small area in these regions instead of single points to be more representative for these regions. They are shown by shaded areas in Fig. 3.12a, denoted by EG and PG. For the 2009 to 2014 period, the spatiotemporal average net SurHF, $\langle \bar{Q}_N \rangle$, is 3.2 Wm^{-2} (above the mean value of –1 Wm^{-2} obtained for the whole lake and for the same period) in the EG area and –6.7 Wm^{-2} (below the mean value) in the PG area. Time series of the heat content calculated with Eq. 3.2 for the areas EG and PG (Fig. 3.12b) indicate that the heat content changes in the

two areas follow the same seasonal pattern. However, they occur systematically at higher values in the EG area than those in the PG area. Thus, spatial variability of SurHF results in spatial variability of the heat content in the lake. Unfortunately, no measured water temperature profiles in these areas are available for the period 2008 to 2014 to verify these results.

However, monthly temperature profiles in these areas were taken for the period July 1986 to June 1995 at several stations in the lake. From these measured temperature profiles, the total heat content of a water column in the lake, G_o [Jm^{-2}], is obtained employing Eq. 2.1. By using Eq. 2.2, the change in heat content from time t_1 to time t_2 can then be quantified between two consecutive profiles. These calculations were carried out for stations P1 and P2 in the EG area, and P3 and P4 in the PG area. It can be seen (Fig. 3.12c) that the seasonal variation and the amplitude of the variation are similar at all four stations. However, the heat content time change at P1 and P2 in EG is systematically above that of stations P3 and P4 in the PG area. This result is consistent with the difference in the time variation of the heat content in the EG and PG areas computed from the SurHF (Fig. 3.12b), and thus confirms that the heat content in the eastern *Grand Lac* is above that of the western *Grand Lac.* Furthermore, it shows that the SurHF (Q_N) for Lake Geneva is the dominant source of heat input into the lake and that other processes such as advective heat flux only play a minor role, as was demonstrated previously in chapter 2 (Rahaghi et al. 2018; Unpublished work). This also indicates that in a large lake the effect of spatial variability of heat flux on the heat content may be important and that estimating heat content dynamics of a lake from a single station may not be representative for the whole lake. It is suggested that the trend towards higher heat content values and the spread between the eastern and the western *Grand Lac* regions over the study periods, as seen in Figs. 3.12b and c, is related to the effects of climate change (Lemmin and Amouroux 2013). They reported an average warming trend in Lake Geneva between 1970 to 2010, which follows the climate-related warming trend in ABL.

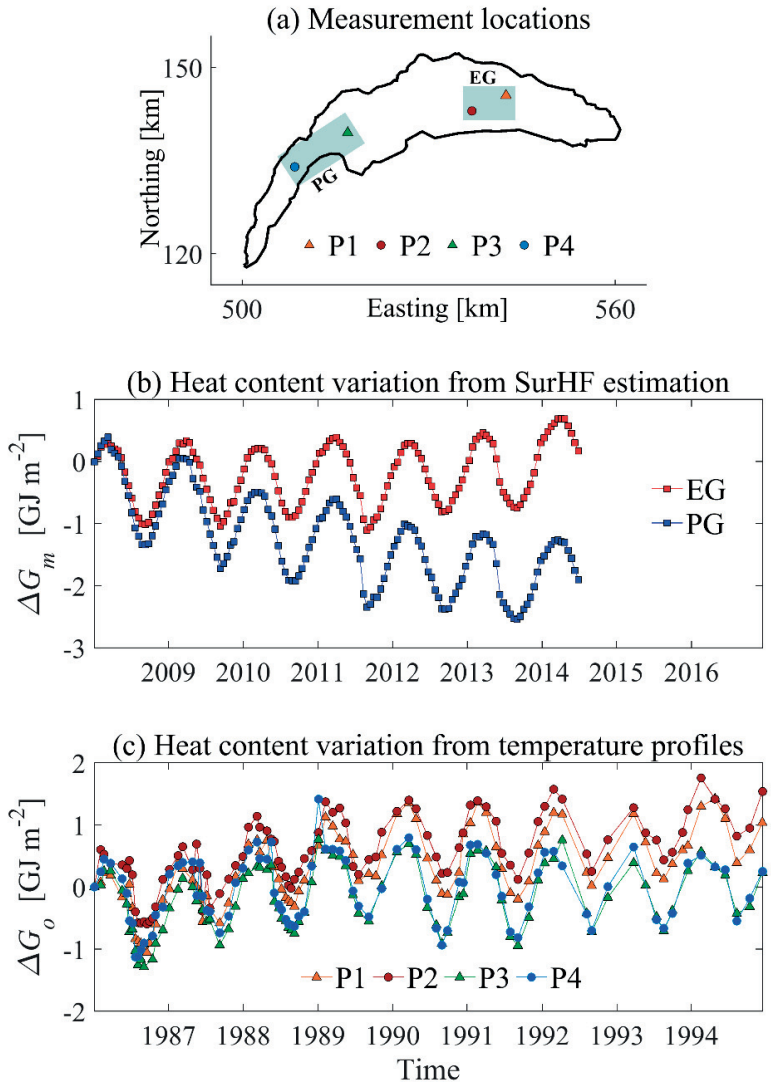

Fig. 3.12. (a) Location of long-term monitoring points in Lake Geneva; see legend for details, (b) heat content evolution in the lake based on SurHF estimation for the period 4 July 2008 to 31 December 2014. The shaded regions in (a), denoted by EG and PG, represents the areas used for net SurHF, Q_N, estimation (see the text for more details), and (c) temporal evolution of heat content estimated by ~ monthly temperature profiles at P1-P3 for the period 4 July 1986 to 14 June 1995. For comparison with the curves in figures (b) and (c), the horizontal axes of the two plots are made for the same number of years. For a better comparison, all curves in (b) and (c) are plotted relative to their heat content value on the initial date.

3.5. Conclusions

It can be expected that large lakes exhibit spatial variability in meteorological parameters. For example, the surrounding topography can influence wind patterns and solar radiation. As a result, LSWT may exhibit considerable spatial variability, in particular during the summertime. The combination of meteorological and LSWT surface patterns can induce significant spatial variability in SurHF. Therefore, the determination of SurHF at a single location (or at best a few locations) where SurHF or water temperature profiles are measured regularly, only provides a partial understanding of the overall energy exchange dynamics in large lakes. In this study, we addressed this question by calculating the spatiotemporal distribution of net SurHF and its five main components over a 7-y period for Lake Geneva. The optimized and calibrated bulk algorithms, based on observations at 2 locations (discussed in chapter 2), were used to compute the SurHF terms.

The calibrated SurHF model permitted quantifying the spatial variability of SurHF. We found a monthly spatial variability of up to ~ ± 40 Wm^{-2} (Fig. 3.4), which indicates the significance of spatial patterns of meteorological forcing patterns and LSWT in SurHF estimation in large lakes. From the results, it is clear that the latent and sensible heat fluxes are the main factors affecting the observed spatial variability of SurHF (Fig. 3.6). These fluxes are controlled by the variability of wind patterns, LSWT and air-water temperature difference, all of which affect the ABL stability, and hence the air-water heat exchange dynamics.

The spatiotemporal variation of these meteorological forces follows a seasonal pattern. Our analyses show a noticeable change of the main controlling forcing in spring compared to the rest of the year (Fig. 3.8). The spatial variability of SurHF values predominantly reflects the variation in wind patterns during the summer-winter period, while the LSWT variability is more important during springtime (Fig. 3.8). The data show relatively low spatial anomalies for air temperature over Lake Geneva for all months. Therefore, LSWT mainly determines the spatial temperature difference in the ABL. The change of the controlling regime was evident in the ABL stability conditions curve (Fig. 3.9). Our results indicate that on average, the ABL over Lake Geneva is statically unstable 74% of the time, except during the springtime, when it is stable. The rate of evaporation is lower under stable ABL conditions (only ~ 10% of evaporation occurs during this period). Due to intense solar radiation and a higher potential of heat absorption during the onset of stratification (March-April), the air-water temperature

difference, and therefore the non-radiative heat fluxes are lower in the springtime. In addition, due to relatively low wind speeds, combined with the reduced air-water temperature difference, less spatial anomalies were observed during this period (Figs. 3.4c-d and S3.5). With increasing LSWT, the back radiation into the atmosphere becomes significant in the summertime. This, together with the reduced solar radiation, decreases the stability of the ABL (Fig. 3.9). Accordingly, the turbulent heat fluxes, mainly evaporation, increase. The wind pattern, as the dominant factor in the non-radiative SurHF terms, then controls the spatial variability of SurHF. This can explain the change of the dominant parameters shown in Fig. 3.8.

The area-averaged (pixelwise) analyses are restricted by the LSWT satellite pixel resolution (~1 km). However, the results are dependable in terms of showing the range and distribution of spatiotemporal variability of SurHF and surface thermal energy (heat content) over a large lake. More detailed spatiotemporal in situ measurements of the thermal parameters, in both water and air are desirable in order to further improve the understanding of spatial variability of energy exchange dynamics.

Acknowledgments

We would like to thank Michael Riffler and Stefan Wunderle for providing the AVHRR satellite data for the study period (2008-2014). The spatiotemporal meteorological data were kindly provided by the Federal Office of Meteorology and Climatology in Switzerland, MeteoSwiss. We also extend our appreciation to the Commission International pour la Protection des Eaux du Léman (CIPEL) for in situ temperature measurements. Water temperature profiles at the SHL2 station over the period 1970-2014 were collected by the Eco-Informatics ORE INRA Team at French National Institute for Agricultural Research (SOERE OLA-IS, INRA Thonon-les-Bains, France). Damien Bouffard is gratefully acknowledged for his scientific comments during the project. This research was supported by the Fondation pour l'Etude des Eaux du Léman (FEEL).

References

Adrian, R., C. M. O'Reilly, H. Zagarese, S. B. Baines, D. O. Hessen, W. Keller, D. M. Livingstone, R. Sommaruga, D. Straile, E. Van Donk, G. A. Weyhenmeyer, and M. Winder. 2009. Lakes as sentinels of climate change. Limnol. Oceanogr. **54:** 2283-2297. doi: 10.4319/lo.2009.54.6_part_2.2283.

Alcantara, E. H., J. L. Stech, J. A. Lorenzzetti, M. P. Bonnet, X. Casamitjana, A. T. Assireu, and E. M. L. D. Novo. 2010. Remote sensing of water surface temperature and heat flux over a tropical hydroelectric reservoir. Remote Sens. Environ. **114:** 2651-2665. doi: 10.1016/j.rse.2010.06.002.

Assouline, S., S. W. Tyler, J. Tanny, S. Cohen, E. Bou-Zeid, M. B. Parlange, and G. G. Katul. 2008. Evaporation from three water bodies of different sizes and climates: Measurements and scaling analysis. Adv. Water Resour. **31:** 160-172. doi: 10.1016/j.advwatres.2007.07.003.

Austin, J. A., and J. Allen. 2011. Sensitivity of summer Lake Superior thermal structure to meteorological forcing. Limnol. Oceanogr. **56:** 1141-1154. doi: 10.4319/lo.2011.56.3.1141.

Bai, X. Z., J. Wang, D. J. Schwab, Y. Yang, L. Luo, G. A. Leshkevich, and S. Z. Liu. 2013. Modeling 1993-2008 climatology of seasonal general circulation and thermal structure in the Great Lakes using FVCOM. Ocean Model. **65:** 40-63. doi: 10.1016/j.ocemod.2013.02.003.

Beletsky, D., N. Hawley, and Y. R. Rao. 2013. Modeling summer circulation and thermal structure of Lake Erie. J. Geophys. Res.: Oceans **118:** 6238-6252. doi: 10.1002/2013JC008854.

Blanken, P. D., C. Spence, N. Hedstrorn, and J. D. Lenters. 2011. Evaporation from Lake Superior: 1. Physical controls and processes. J. Great Lakes Res. **37:** 707-716. doi: 10.1016/j.jglr.2011.08.009.

Bonvin, F., A. M. Razmi, D. A. Barry, and T. Kohn. 2013. Micropollutant dynamics in Vidy Bay-A coupled hydrodynamic-photolysis model to assess the spatial extent of ecotoxicological risk. Environ. Sci. Technol. **47:** 9207-9216. doi: 10.1021/es401294c.

Churchill, J. H., and W. Charles Kerfoot. 2007. The impact of surface heat flux and wind on thermal stratification in Portage Lake, Michigan. J. Great Lakes Res. **33:** 143-155. doi: 10.3394/0380-1330(2007)33[143:TIOSHF]2.0.CO;2.

Deardorff, J. W. 1968. Dependence of air-sea transfer coefficients on bulk stability. J. Geophys. Res. **73:** 2549-2557. doi: 10.1029/JB073i008p02549.

Fink, G., M. Schmid, B. Wahl, T. Wolf, and A. Wüest. 2014. Heat flux modifications related to climate-induced warming of large European lakes. Water Resour. Res. **50:** 2072-2085. doi: 10.1002/2013wr014448.

Finlay, K., R. J. Vogt, M. J. Bogard, B. Wissel, B. M. Tutolo, G. L. Simpson, and P. R. Leavitt. 2015. Decrease in CO_2 efflux from northern hardwater lakes with increasing atmospheric warming. Nature **519:** 215-218. doi: 10.1038/nature14172.

Granger, R. J., and N. Hedstrom. 2011. Modelling hourly rates of evaporation from small lakes. Hydrol. Earth Syst. Sci. **15:** 267-277. doi: 10.5194/hess-15-267-2011.

Henderson-Sellers, B. 1986. Calculating the surface energy balance for lake and reservoir modeling: A review. Rev. Geophys. **24:** 625-649. doi: 10.1029/Rg024i003p00625.

Honrath, R. E., C. I. Sweet, and C. J. Plouff. 1997. Surface exchange and transport processes governing atmospheric PCB levels over Lake Superior. Environ. Sci. Technol. **31:** 842-852. doi: 10.1021/Es960645s.

Jain, A. K. 2010. Data clustering: 50 years beyond K-means. Pattern Recogn. Lett. **31:** 651-666. 10.1016/j.patrec.2009.09.011.

Koch, S. E., M. Desjardins, and P. J. Kocin. 1983. An interactive Barnes objective map analysis scheme for use with satellite and conventional data. J. Clim. Appl. Meteorol. **22:** 1487-1503. doi: 10.1175/1520-0450(1983)022<1487:Aiboma>2.0.Co;2.

Kourzeneva, E., E. Martin, Y. Batrak, and P. Le Moigne. 2012. Climate data for parameterisation of lakes in Numerical Weather Prediction models. Tellus, Ser. A. **64**. doi: 10.3402/Tellusa.V64i0.17226.

Laird, N. F., and D. A. R. Kristovich. 2002. Variations of sensible and latent heat fluxes from a Great Lakes buoy and associated synoptic weather patterns. J. Hydrometeorol. **3:** 3-12. doi: 10.1175/1525-7541(2002)003<0003:Vosalh>2.0.Co;2.

Lemmin, U., and A. Amouroux. 2013. The influence of climate change on Lake Geneva, p. 201-217. In: Climatic change and global warming of inland waters (Eds: C.R. Goldman, M. Kumagai and R.D. Robarts). John Wiley & Sons, Ltd. Chichester, UK. doi: 10.1002/9781118470596.ch12.

Lemmin, U., and N. D'Adamo. 1996. Summertime winds and direct cyclonic circulation: Observations from Lake Geneva. Ann. Geophys., Ser. A **14:** 1207-1220. doi: 10.1007/s005850050384.

Lenters, J. D., T. K. Kratz, and C. J. Bowser. 2005. Effects of climate variability on lake evaporation: Results from a long-term energy budget study of Sparkling Lake, northern Wisconsin (USA). J. Hydrol. **308:** 168-195. doi: 10.1016/j.jhydrol.2004.10.028.

Li, Z. G., S. H. Lyu, Y. H. Ao, L. J. Wen, L. Zhao, and S. Y. Wang. 2015. Long-term energy flux and radiation balance observations over Lake Ngoring, Tibetan Plateau. Atmos. Res. **155:** 13-25. doi: 10.1016/j.atmosres.2014.11.019.

Liston, G. E., and K. Elder. 2006. A meteorological distribution system for high-resolution terrestrial modeling (MicroMet). J. Hydrometeorol. **7:** 217-234. doi: 10.1175/Jhm486.1.

Livingstone, D. M., and D. M. Imboden. 1989. Annual heat balance and equilibrium temperature of Lake Aegeri, Switzerland. Aquat. Sci. **51:** 351-369. doi: 10.1007/Bf00877177.

Lofgren, B. M., and Y. C. Zhu. 2000. Surface energy fluxes on the Great Lakes based on satellite-observed surface temperatures 1992 to 1995. J. Great Lakes Res. **26:** 305-314. doi: 10.1016/S0380-1330(00)70694-0.

MacIntyre, S., J. R. Romero, and G. W. Kling. 2002. Spatial-temporal variability in surface layer deepening and lateral advection in an embayment of Lake Victoria, East Africa. Limnol. Oceanogr. **47:** 656-671. doi: 10.4319/lo.2002.47.3.0656.

Mahrer, Y., and S. Assouline. 1993. Evaporation from Lake Kinneret. 2. Estimation of the horizontal variability using a 2-dimensional numerical mesoscale model. Water Resour. Res. **29:** 911-916. doi: 10.1029/92wr02433.

Mahrt, L., and D. Khelif. 2010. Heat fluxes over weak SST heterogeneity. J. Geophys. Res.: Atmos. **115:** D11103. doi: 10.1029/2009jd013161.

Minnett, P. J., M. Smith, and B. Ward. 2011. Measurements of the oceanic thermal skin effect. Deep-Sea Res. Part II. **58:** 861-868. doi: 10.1016/j.dsr2.2010.10.024.

Mironov, D., B. Ritter, J. P. Schulz, M. Buchhold, M. Lange, and E. Machulskaya. 2012. Parameterisation of sea and lake ice in numerical weather prediction models of the German Weather Service. Tellus, Ser. A. **64:** 17330. doi: 10.3402/Tellusa.V64i0.17330.

Mironov, D. V. 2008. Parameterization of lakes in numerical weather prediction: Description of a lake model, p. 1-44. *In* M. Milelli [ed.], COSMO technical reports: http://www.cosmo-model.org/content/model/documentation/techReports/docs/techReport11.pdf.

Momii, K., and Y. Ito. 2008. Heat budget estimates for Lake Ikeda, Japan. J. Hydrol. **361:** 362-370. doi: 10.1016/j.jhydrol.2008.08.004.

Moukomla, S., and P. D. Blanken. 2017. The estimation of the North American Great Lakes turbulent fluxes using satellite remote sensing and MERRA reanalysis data. Remote Sens. **9:** 141. doi: 10.3390/Rs9020141.

Nordbo, A., S. Launiainen, I. Mammarella, M. Lepparanta, J. Huotari, A. Ojala, and T. Vesala. 2011. Long-term energy flux measurements and energy balance over a small boreal lake using eddy covariance technique. J. Geophys. Res.: Atmos. **116:** D02119. doi: 10.1029/2010jd014542.

Nussboim, S., A. Rimmer, Y. Lechinsky, P.-O. Gutman, and D. Broday. 2017. Improving the estimation of Lake Kinneret's heat balance and surface fluxes using the Kalman Filter algorithm. Limnol. Oceanogr.: Methods **15:** 467-479. doi: 10.1002/lom3.10173.

Oesch, D., J. M. Jaquet, R. Klaus, and P. Schenker. 2008. Multi-scale thermal pattern monitoring of a large lake (Lake Geneva) using a multi-sensor approach. Int. J. Remote Sens. **29:** 5785-5808. doi: 10.1080/01431160802132786.

Oesch, D. C., J. M. Jaquet, A. Hauser, and S. Wunderle. 2005. Lake surface water temperature retrieval using Advanced Very High Resolution Radiometer and Moderate Resolution Imaging Spectroradiometer data: Validation and feasibility study. J. Geophys. Res.: Oceans **110:** C12014. doi: 10.1029/2004jc002857.

Phillips, R. C., J. R. Saylor, N. B. Kaye, and J. M. Gibert. 2016. A multi-lake study of seasonal variation in lake surface evaporation using MODIS satellite-derived surface temperature. Limnology **17:** 273-289. doi: 10.1007/s10201-016-0481-z.

Politi, E., M. E. J. Cutler, and J. S. Rowan. 2012. Using the NOAA Advanced Very High Resolution Radiometer to characterise temporal and spatial trends in water temperature of large European lakes. Remote Sens. Environ. **126:** 1-11. doi: 10.1016/j.rse.2012.08.004.

Rahaghi, A. I., U. Lemmin, A. Cimatoribus, D. Bouffard, M. Riffler, S. Wunderle, and D. A. Barry. 2018. Improving surface heat flux estimation of a large lake through model optimization and 2-point calibration: The case of Lake Geneva. Limnol. Oceanogr.: Methods**:** Under review.

Riffler, M., G. Lieberherr, and S. Wunderle. 2015. Lake surface water temperatures of European Alpine lakes (1989-2013) based on the Advanced Very High Resolution Radiometer (AVHRR) 1 km data set. Earth Sys. Sci. Data **7:** 1-17. doi: 10.5194/essd-7-1-2015.

Rimmer, A., R. Samuels, and Y. Lechinsky. 2009. A comprehensive study across methods and time scales to estimate surface fluxes from Lake Kinneret, Israel. J. Hydrol. **379:** 181-192. doi: 10.1016/j.jhydrol.2009.10.007.

Rouse, W. R., P. D. Blanken, N. Bussieres, C. J. Oswald, W. M. Schertzer, C. Spence, and A. E. Walker. 2008. Investigation of the thermal and energy balance regimes of Great Slave and Great Bear Lakes. J. Hydrometeorol. **9:** 1318-1333. doi: 10.1175/2008JHM977.1.

Schertzer, W. M. 1978. Energy budget and monthly evaporation estimates for Lake Superior, 1973. J. Great Lakes Res. **4:** 320-330. doi: 10.1016/S0380-1330(78)72201-X.

Schneider, K., and W. Mauser. 1991. On the estimation of energy fluxes at the surface of Lake Constance using NOAA-AVHRR data, p. 373-376. IGARSS 91-Remote Sensing : Global Monitoring for Earth Management. IEEE Xplore Conference, Espoo, Finland. doi: 10.1109/IGARSS.1991.579158.

Schwab, D. J., G. A. Leshkevich, and G. C. Muhr. 1992. Satellite measurements of surface water temperature in the Great Lakes: Great Lakes Coastwatch. J. Great Lakes Res. **18:** 247-258. https://www.glerl.noaa.gov/pubs/fulltext/1992/19920009.pdf.

Sima, S., A. Ahmadalipour, and M. Tajrishy. 2013. Mapping surface temperature in a hyper-saline lake and investigating the effect of temperature distribution on the lake evaporation. Remote Sens. Environ. **136:** 374-385. doi: 10.1016/j.rse.2013.05.014.

Spence, C., P. D. Blanken, N. Hedstrom, V. Fortin, and H. Wilson. 2011. Evaporation from Lake Superior: 2-Spatial distribution and variability. J. Great Lakes Res. **37:** 717-724. doi: 10.1016/j.jglr.2011.08.013.

Stepanenko, V., K. D. Johnk, E. Machulskaya, M. Perroud, Z. Subin, A. Nordbo, I. Mammarella, and D. Mironov. 2014. Simulation of surface energy fluxes and stratification of a small boreal lake by a set of one-dimensional models. Tellus, Ser. A. **66:** 21389. doi: 10.3402/Tellusa.V66.21389.

Tanentzap, A. J., D. P. Hamilton, and N. D. Yan. 2007. Calibrating the Dynamic Reservoir Simulation Model (DYRESM) and filling required data gaps for one-dimensional thermal profile predictions in a boreal lake. Limnol. Oceanogr.: Methods **5:** 484-494. doi: 10.4319/lom.2007.5.484.

Thiery, W., A. Martynov, F. Darchambeau, J. P. Descy, P. D. Plisnier, L. Sushama, and N. P. M. van Lipzig. 2014a. Understanding the performance of the FLake model over two African Great Lakes. Geosci. Model Dev. **7:** 317-337. doi: 10.5194/gmd-7-317-2014.

Thiery, W., V. M. Stepanenko, X. Fang, K. D. Johnk, Z. S. Li, A. Martynov, M. Perroud, Z. M. Subin, F. Darchambeau, D. Mironov, and N. P. M. Van Lipzig. 2014b. LakeMIP Kivu: Evaluating the representation of a large, deep tropical lake by a set of one-dimensional lake models. Tellus, Ser. A. **66:** 21390. doi: 10.3402/Tellusa.V66.21390.

Tibshirani, R., G. Walther, and T. Hastie. 2001. Estimating the number of clusters in a data set via the gap statistic. J. Roy. Stat. Soc.: B. **63:** 411-423. doi: 10.1111/1467-9868.00293.

Van Emmerik, T. H. M., A. Rimmer, Y. Lechinsky, K. J. R. Wenker, S. Nussboim, and N. C. van de Giesen. 2013. Measuring heat balance residual at lake surface using distributed

temperature sensing. Limnol. Oceanogr.: Methods **11:** 79-90. doi: 10.4319/lom.2013.11.79.

Verburg, P., and J. P. Antenucci. 2010. Persistent unstable atmospheric boundary layer enhances sensible and latent heat loss in a tropical great lake: Lake Tanganyika. J. Geophys. Res.: Atmos. **115:** D11109. doi: 10.1029/2009jd012839.

Wahl, B., and F. Peeters. 2014. Effect of climatic changes on stratification and deep-water renewal in Lake Constance assessed by sensitivity studies with a 3D hydrodynamic model. Limnol. Oceanogr. **59:** 1035-1052. doi: 10.4319/lo.2014.59.3.1035.

Wilson, R. C., S. J. Hook, P. Schneider, and S. G. Schladow. 2013. Skin and bulk temperature difference at Lake Tahoe: A case study on lake skin effect. J. Geophys. Res.: Atmos. **118:** 10332-10346. doi: 10.1002/Jgrd.50786.

Woolway, R. I., I. D. Jones, D. P. Hamilton, S. C. Maberly, K. Muraoka, J. S. Read, R. L. Smyth, and L. A. Winslow. 2015. Automated calculation of surface energy fluxes with high-frequency lake buoy data. Environ. Model. Softw. **70:** 191-198. doi: 10.1016/j.envsoft.2015.04.013.

Woolway, R. I., I. D. Jones, S. C. Maberly and others 2016. Diel surface temperature range scales with lake size. PLoS One **11:** e0152466. doi: 10.1371/journal.pone.0152466.

Woolway, R. I., P. Verburg, C. J. Merchant, J. D. Lenters, D. P. Hamilton, J. Brookes, S. Kelly, S. Hook, A. Laas, D. Pierson, A. Rimmer, J. A. Rusak, and I. D. Jones. 2017. Latitude and lake size are important predictors of over-lake atmospheric stability. Geophys. Res. Lett. **44:** 8875-8883. doi: 10.1002/2017GL073941.

Xue, P. F., D. J. Schwab, and S. Hu. 2015. An investigation of the thermal response to meteorological forcing in a hydrodynamic model of Lake Superior. J. Geophys. Res.: Oceans **120:** 5233-5253. doi: 10.1002/2015JC010740.

Yang, J., Z.-H. Wang, Q. Li, N. Vercauteren, E. Bou-Zeid, and M. B. Parlange. 2017. A novel approach for unraveling the energy balance of water surfaces with a single depth temperature measurement. Limnol. Oceanogr. **62:** 89-103. doi: 10.1002/lno.10378.

Yusup, Y., and H. P. Liu. 2016. Effects of atmospheric surface layer stability on turbulent fluxes of heat and water vapor across the water-atmosphere interface. J. Hydrometeorol. **17:** 2835-2851. doi: 10.1175/Jhm-D-16-0042.1.

Zeng, X. B., M. Zhao, and R. E. Dickinson. 1998. Intercomparison of bulk aerodynamic algorithms for the computation of sea surface fluxes using TOGA COARE and TAO data. J. Clim. **11:** 2628-2644. doi: 10.1175/1520-0442(1998)011<2628:Iobaaf>2.0.Co;2.

Zhang, Q., and H. Liu. 2014. Seasonal changes in physical processes controlling evaporation over inland water. J. Geophys. Res.: Atmos. **119:** 9779-9792. doi: 10.1002/2014JD021797.

Supplemental Information for Chapter 3:

Multi-annual surface heat flux dynamics over Lake Geneva: The importance of spatial variability

Abolfazl Irani Rahaghi[a], Ulrich Lemmin[a], Andrea Cimatoribus[a], David Andrew Barry[a]

[a] Ecological Engineering Laboratory (ECOL), Environmental Engineering Institute (IIE), Faculty of Architecture, Civil and Environmental Engineering (ENAC), Ecole Polytechnique Fédérale de Lausanne (EPFL), 1015 Lausanne, Switzerland

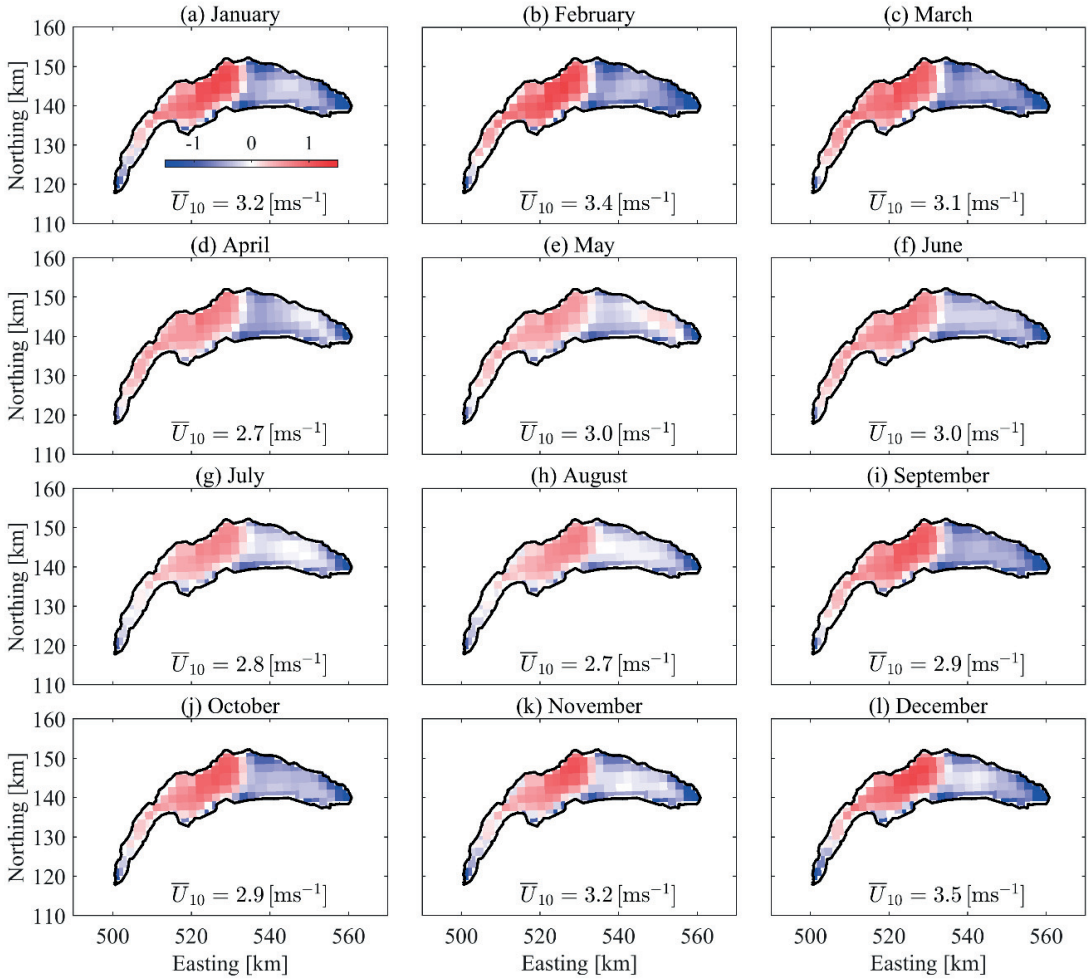

Fig. S3.1. Mean monthly anomaly patterns of wind speed at 10 m above the surface, U_{10}. Spatial averages are noted on each map. For a better comparison, the deviations from the mean spatial value within a range of ±1.5 ms^{-1} are plotted. The Swiss coordinate system with km length-based units (CH1903) is used in these plots. The legend in (a) indicates the color range.

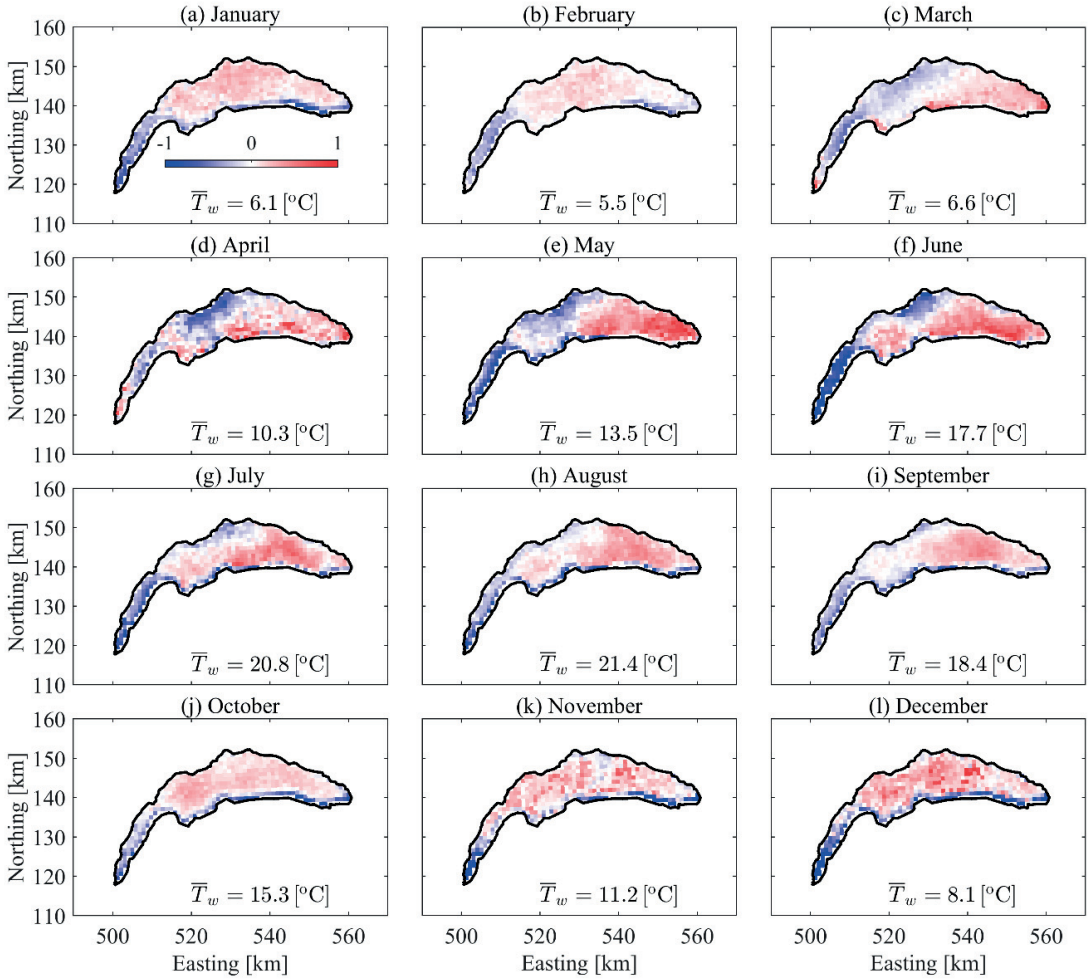

Fig. S3.2. Mean monthly anomaly patterns of lake surface water temperature, T_w. Spatial averages are noted on each map. For a better comparison, the deviations from the mean spatial value within a range of ±1 °C are plotted. The Swiss coordinate system with km length-based units (CH1903) is used in these plots. The legend in (a) indicates the color range.

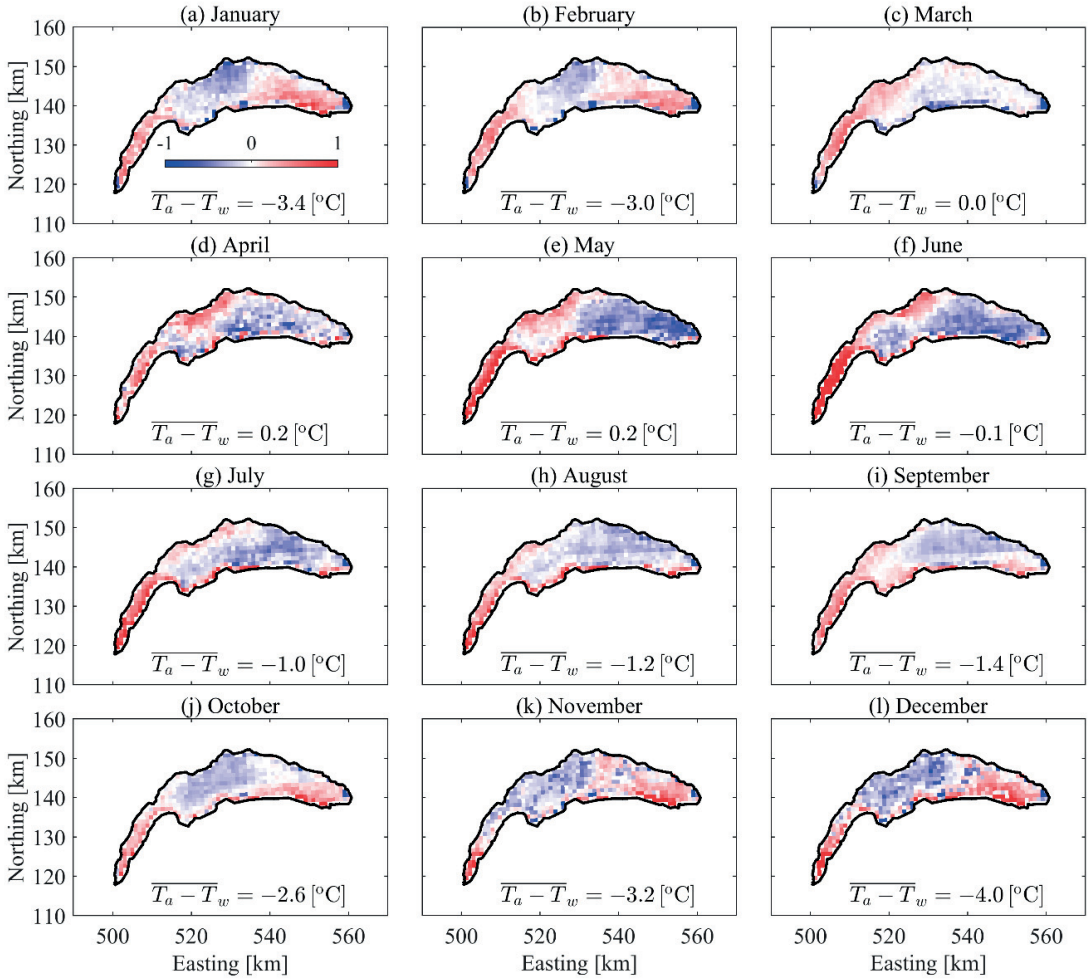

Fig. S3.3. Mean monthly anomaly patterns of air-water surface temperature difference, T_a - T_w. Spatial averages are noted on each map. For a better comparison, the deviations from the mean spatial value within a range of ±1 °C are plotted. The Swiss coordinate system with km length-based units (CH1903) is used in these plots. The legend in (a) indicates the color range.

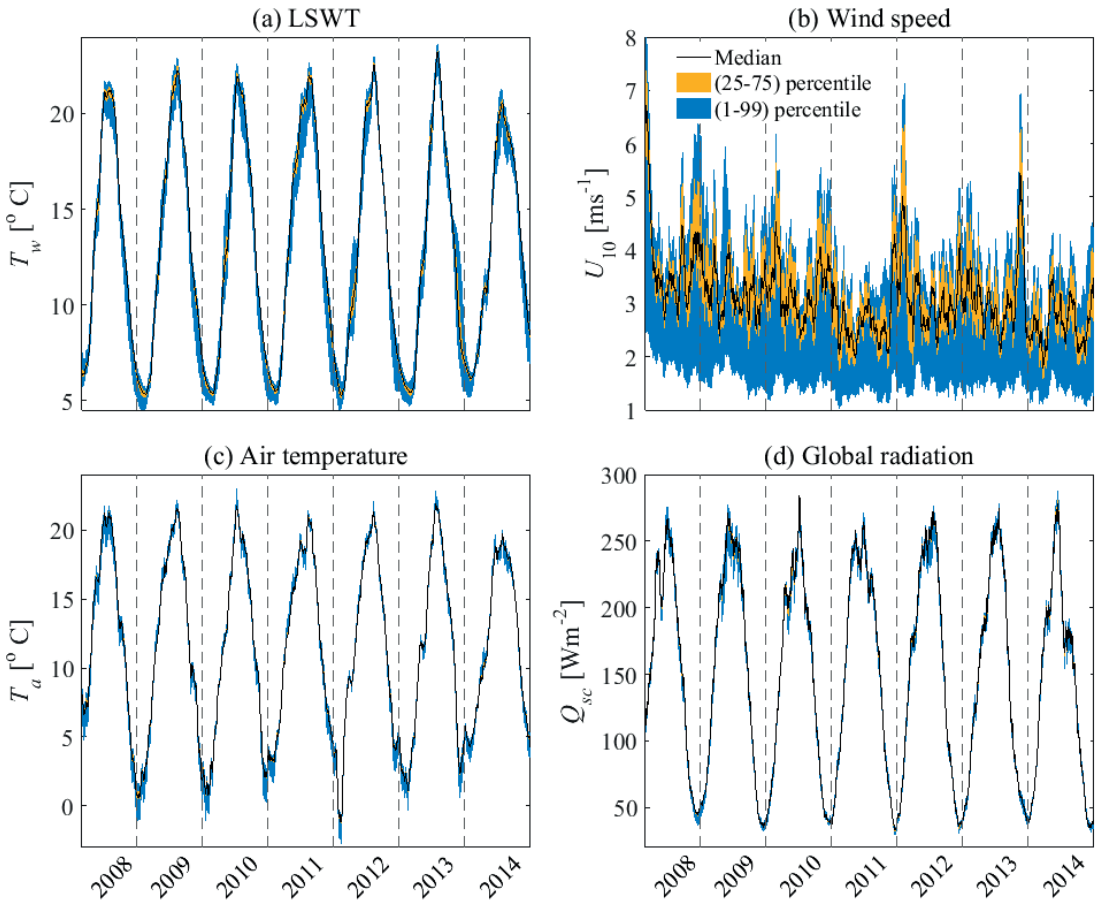

Fig. S3.4. Time series of the mean (black lines) and percentiles of the distribution of spatially resolved data (areas filled between IQR, i.e., 25-75 percentile, and P1-99, i.e.,1-99 percentile, see the legend in (b) for color coding) of lake surface water temperature (LSWT) and meteorological data smoothed with a 30-d running window: (a) LSWT (T_w), (b) wind speed (U_{10}), (c) air temperature (T_a), and (d) global radiation (Q_{sc}).

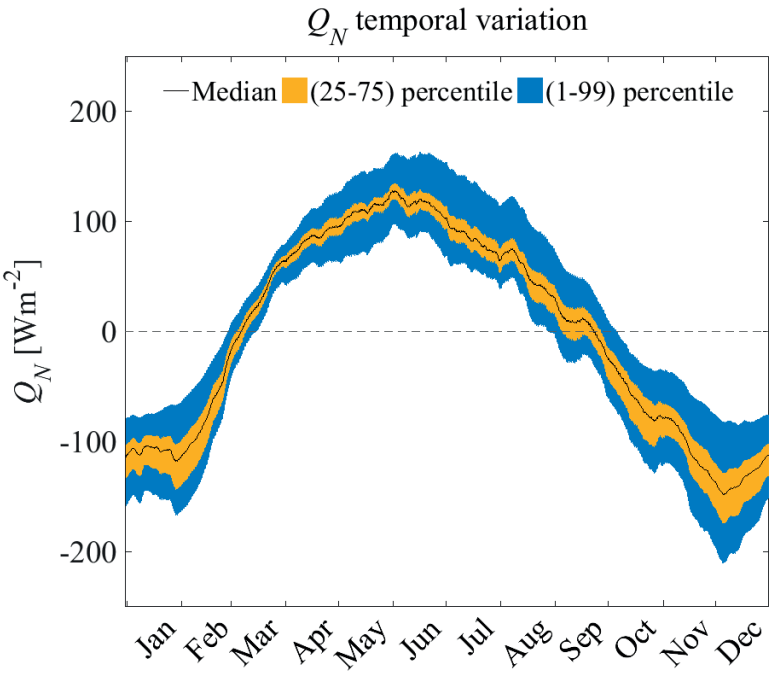

Fig. S3.5. Temporal variation of lake-wide mean net SurHF of Lake Geneva, based on data from 1 January 2009 to 31 December 2014 smoothed with a 30-d running mean. The colored areas show the spatial distribution (IQR and P1-99) of net SurHF; see legend for color coding.

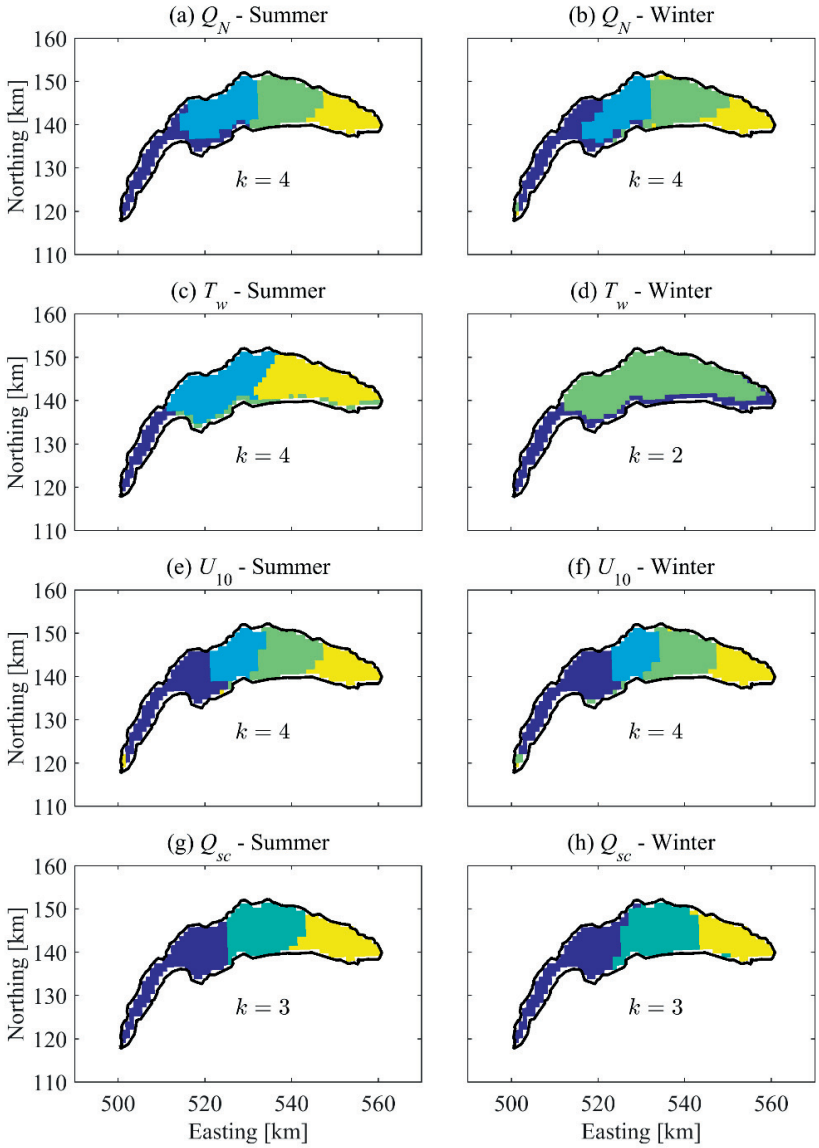

Fig. S3.6. Dominant patterns (clusters) of (a) and (b) net SHF (Q_N), (c) and (d) LSWT (T_w), (e) and (f) wind speed at 10 m above surface (U_{10}), and (g) and (h) global radiation (Q_s), during summer (plots in left panel) and winter (plots in right panel) for the period 2008 to 2014. Shading identifies the different clusters; k is given in each panel and is the number of clusters.

Chapter 4

LSWT imagery: Aerial remote sensing and image registration

Abolfazl Irani Rahaghi[a], Ulrich Lemmin[a], Daniel Sage[b], David Andrew Barry[a]

[a] Ecological Engineering Laboratory (ECOL), Environmental Engineering Institute (IIE), Faculty of Architecture, Civil and Environmental Engineering (ENAC), Ecole Polytechnique Fédérale de Lausanne (EPFL), 1015 Lausanne, Switzerland

[b] Biomedical Imaging Group (BIG), School of Engineering (STI), Ecole Polytechnique Fédérale de Lausanne (EPFL), 1015 Lausanne, Switzerland

Submitted to *Remote Sensing of Environment*

Abstract

An airborne system for realizing thermography of the Lake Surface Water Temperature (LSWT) with ~0.8 m pixel resolution is presented. It consists of a tethered Balloon Launched Imaging and Monitoring Platform (BLIMP) that records the LSWT and an autonomous catamaran (called ZiviCat) that measures in situ surface/near surface temperatures and permits simultaneous ground-truthing of the BLIMP data. The BLIMP was equipped with an uncooled InfraRed (IR) camera. The ZiviCat was designed to measure autonomously along predefined trajectories on a lake. Since LSWT spatial variability is expected to be low in each frame, poor estimation of spatial and temporal noise of the IR camera (nonuniformity and shutter-based drift, respectively) leads to errors in the thermal maps obtained. Nonuniformity was corrected by applying a pixelwise two-point linear correction method based on laboratory experiments. A Probability Density Function (PDF) matching in regions of overlap between sequential images was used for the drift correction. A feature matching-based algorithm, combining blob and region detectors, was implemented to create composite thermal images, and a mean value of the overlapped images at each location was considered as a representative value of that pixel. The results indicate that a high overlapping field of view is essential for image fusion and noise reduction over such low-contrast scenes. Finally, the measured in situ temperatures were used for the radiometric calibration. This resulted in the generation of meso-scale LSWT maps that revealed spatial LSWT variability with unprecedented detail.

Keywords: Remote sensing, thermal imagery, lake surface water temperature, image registration, uncooled infrared camera

4.1. Introduction

Lake Surface Water Temperature (LSWT) varies in space and time and is thus a powerful indicator of the meteorological and climatological forcing dynamics of water bodies (Livingstone and Dokulil 2001; Adrian et al. 2009). Data sources for LSWT mapping include remote sensing and in situ measurements. Depending on cloud cover, satellite data can depict large-scale thermal patterns, but not meso- or small-scale processes. Satellite thermal images are usually validated against point measurements (e.g., Oesch et al. 2005; Riffler et al. 2015), considered to be representative for a sizeable surface area (typical pixel size ~1 km^2). Thermography at the meso-scale level allows resolving (and hence ground-truthing) lake surface features at the sub-pixel scale ranging from several hundreds of meters to less than a meter. LSWT and air-water heat exchange are strongly coupled (Woolway et al. 2015; Tozuka et al. 2017) and so spatial heterogeneity of LSWT affects area-averaged surface heat flux estimates (Mahrt and Khelif 2010). Airborne thermography using an infrared camera (IR) can better resolve meso-scale LSWT spatial patterns.

In recent years, commercial and scientific applications of IR cameras grew substantially (e.g., Mounier 2011; Lahiri et al. 2012). Thermal detectors used in IR cameras can be cooled or uncooled (Williams 2009; Vollmer and Möllmann 2011). Cooled cameras provide a higher and more stable thermal sensitivity compared to uncooled detectors, but they are more expensive and heavier than uncooled ones; this limits their use on small airborne platforms. Uncooled cameras are an adequate choice for many airborne environmental applications (e.g., Torgersen et al. 2001; Handcock et al. 2006; Haselwimmer et al. 2013; Hernandez et al. 2014; Tamborski et al. 2015; Neale et al. 2016) due to their lower price, compactness, portability, high spatial and good temperature resolutions (Kruse 1997; Vollmer and Möllmann 2011). However, LSWT thermography must take into consideration the following: When moving platforms, such as aircrafts are used to cover a broader area (e.g., Ferri et al. 2000; Tonolla et al. 2012; Haselwimmer et al. 2013; Emery et al. 2014; Castro et al. 2017), registration (stitching) of the image sequence is frequently required. Atmospheric boundary layer conditions, such as air temperature, humidity and atmospheric aerosol concentration, under which the thermal imagery is carried out, are constantly changing. This, together with a typical thermography altitude of O(100 m) to O(1 km) makes it more challenging to obtain reliable estimates of the atmospheric transmission coefficient than under controlled laboratory conditions. Therefore, in situ ground-

truthing is needed for radiometric calibration of the airborne thermography. The spatial variation of temperature, and consequently the grey value contrast in an IR image, is expected to be low over natural waters. Properly addressing the effects of these particular conditions requires advanced image processing.

The core of the uncooled IR sensor (micro bolometer) consists of a two-dimensional detector matrix, called the Focal Plane Array (FPA). Optical, electronic and mechanical components of the camera may affect the irradiance outputs (Milton et al. 1985; Vollmer and Möllmann 2011; Budzier and Gerlach 2015). Error sources include spatial noise, called nonuniformity, and temporal noise, called shutter-based drift (offset) (Nugent et al. 2013; Budzier and Gerlach 2015). Nonuniformity in thermal imagery results from the different photo responses of individual detectors in the FPA for the same incident radiation. Thermal cameras usually try to correct this internally by periodically placing a mechanical shutter with a uniform temperature between the camera and the lens (FLIR, last accessed 12 January 2018). This Flat Field Correction (FFC) adjusts the internal offset coefficients of the camera, subsequently providing a more uniform image. During the implementation procedure, which takes ~2 s, the thermal imagery is frozen. However, the missing internal correction between the sequential FFC operations results in a thermal drift in the images. Nonuniformity and drift corrections must be performed prior to camera temperature calibration (Vollmer and Möllmann 2011). Quantification of these noise sources, and consequently correcting the camera output, requires details of internal signal processing of the micro bolometer array, and other parameters, e.g., camera internal temperature and sensor temperature information that is usually not available. Therefore, a calibration model is needed for the camera.

Calibration models require an adjustable constant scene temperature (e.g., Perry and Dereniak 1993; Marinetti et al. 1997), rely on the IR camera internal information (e.g., Parra et al. 2011; Nugent et al. 2013; Nugent and Shaw 2014; Budzier and Gerlach 2015), or use scene-based algorithms (e.g., Torres et al. 2005; 2006). However, these algorithms are best suited for thermal imagery of high temperature contrast fields. Satellite images of lake surface waters show only small LSWT differences, typically much less than 5°C. Therefore, this kind of calibration cannot be used for image fusion and registration of over-lake IR images.

This study was carried out on Lake Geneva, the largest lake in Western Europe, (see section 2.1.). Advanced Very High Resolution Radiometer (AVHRR) satellite data were used to

investigate the diurnal/nocturnal LSWT evolution of this lake (Oesch et al. 2005; 2008). Due to the limited spatial resolution, it was suggested that the observed warm/cold LSWT regions could possibly be due to the development or attenuation of the diurnal thermocline, lake breezes and/or large-scale summertime circulations resulting from temporally and spatially variable wind forcing patterns over the lake (Lemmin and D'Adamo 1996). Meso-scale LSWT patterns can resolve the uncertainties in the LSWT data interpretation of previous investigations.

In the present study, we use a Balloon Launched Imaging and Monitoring Platform (BLIMP) with an uncooled IR camera that was developed to measure LSWTs at meso-scales. Here, we investigate its feasibility for taking meso-scale thermal imagery over Lake Geneva with an emphasis on NonUniformity Correction (NUC) and drift adjustment. We implemented an image processing workflow including NUC, drift correction, and denoising through image fusion. A feature matching-based algorithm was used for image registration (stitching). The proposed methodology was validated by comparing the corrected grey values and the simultaneous in situ water temperature data that were obtained using an autonomous craft (ZiviCat).

4.2. Materials and methods

4.2.1. Study site

Located between Switzerland and France, Lake Geneva (Local name: *Lac Léman*) is a large, deep perialpine lake at a mean surface altitude of 372 m. It is approximately 70-km long, with a maximum width of 14 km, a surface area of 582 km² and a volume of 89 km³ (Fig. 4.1). To avoid the effect of coastal mixing on the temporal and spatial patterns of LSWT, we present results for areas sufficiently far from the shores. Although land features, due to their high contrast in both visible and IR bands, are beneficial for image stitching and fusion (e.g., Tamborski et al. 2015), such complementary information is not available at the areas of interest in this study.

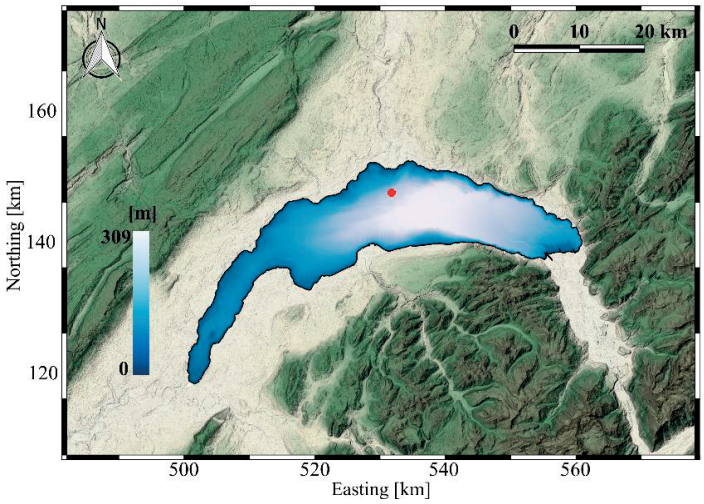

Fig. 4.1. Location and bathymetry (see the legend in the left part) of Lake Geneva, adapted from a public domain satellite image (NASA World Wind, last accessed 1 February 2018) and bathymetry data (SwissTopo, last accessed 1 February 2018). The map is given in CH1903 Swisstopo coordinates. The red dot indicates the area of the present study.

4.2.2. Measurement platforms

Field measurement campaigns were carried out using two systems: (i) an airborne balloon for thermal imagery (called BLIMP, Fig. 4.2a), and (ii) an autonomous catamaran (called ZiviCat, Fig. 4.2b) for in situ measurements.

The BLIMP was attached to a small balloon tethered to a winch on a boat, from which its height is controlled. In the present study, the balloon was placed at less than 600 m elevation. It carried a thermal imagery package (Liardon and Barry 2017) suspended beneath it (grey box in Fig. 4.2a). The package includes a *FLIR Tau2 LWIR* camera (640 × 512 pixel resolution, 14-bit digital output) and a *Raspberry Pi* RGB camera (used for visual inspection and verification), as well as other equipment for its position (GPS), orientation, tilt angles (Inertial Measurement Unit; IMU), height, and communication with the boat. All data are recorded internally in the BLIMP. The system uses either *User Datagram Protocol* (*UDP)* communication through a mobile network via a *4G* module, or serial radio transmission using an *XBee Pro 100 mW* module for real-time monitoring of the BLIMP imagery on the boat. Compared to other aerial systems such as aircraft or drones, the BLIMP system is less affected by vibration and tilting, as we confirmed by testing with a custom autonomous drone (Liardon et al. 2017). To minimize

camera movement, a self-balancing attachment system was used (Picavet rigging, last accessed 12 January 2018) that allows for passive stabilization even under moderate wind speeds. However, in our study, measurements were made under weak wind conditions, when LSWT spatial patterns are more likely to occur and, furthermore, data are less contaminated by surface waves and BLIMP lateral movements.

Simultaneous ground-truthing of the BLIMP data was achieved using the ZiviCat, an autonomously operating catamaran. It can measure in situ near-surface water temperatures (main parameter in this study), as well as lake current profiles, radiative heat flux, and surface momentum flux for physical limnology investigations. In the near-surface water layer, ten RBRsolo temperature sensors (RBR, last accessed 12 January 2018) with an accuracy of 0.002°C were mounted on a 2-m long spar and measured water temperature profiles with a frequency of up to 1 Hz in the near-surface layer (1.5 m). Thermistors were more closely spaced near the surface (shown with the arrow in Fig. 4.2b). The thermistor spar is mounted well forward of the craft to avoid hull disturbances. The ZiviCat moves with a speed of ~1 ms^{-1}. The craft is equipped with other instruments and equipment for position (GPS), stability (IMU), data recording, and communication, which allows for real-time data control, correction and analysis on the boat that accompanies the ZiviCat and on which the winch for the BLIMP is mounted. Details of the systems and sensors are presented in Barry et al. (2018, Unpublished results).

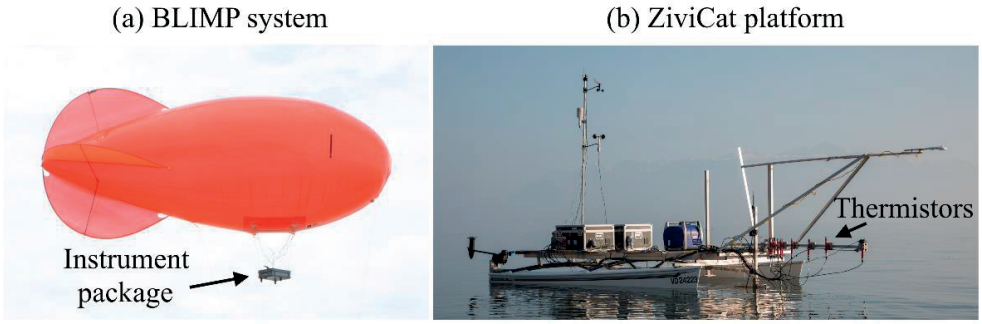

Fig. 4.2. Field measurement system: (a) BLIMP for airborne imagery, and (b) ZiviCat platform for in situ measurements. The small helium balloon (volume 9 m^3) that carries the BLIMP is tethered to a winch on the accompanying boat. The thermistor spar of the ZiviCat, which is tilted horizontally in (b) for navigation in shallow areas, is rotated vertically for measurements and includes 10 thermistors to measure the near-surface layer (down to 1.5 m depth) temperature profiles.

Several field campaigns were conducted over Lake Geneva to test the feasibility of the combined ZiviCat-BLIMP system. Results from 18 March 2016 are presented here. The BLIMP moves forward with the boat to which it is tethered and takes images every 5 s, resulting in more than 90% overlap between the sequential frames. The imagery height was kept at ~400 m, which provided IR images with ~0.8 m pixel resolution. From 11h45 to 16h30, the ZiviCat covered a ~16 km long trajectory. However, only the last 3 h of the campaign showed noticeable LSWT patterns. In order to demonstrate our methodology for the LSWT image processing, we selected a ~24 min segment, i.e., five FFC intervals, which includes 287 IR frames. It should be noted that the proposed image processing algorithm is a tool that can be applied to any comparable data set. Some examples of raw IR images from the selected period are shown in Fig. 4.3. They only cover a narrow band in the 14-bit output (16384 grey levels) of the camera (~2550 to 2720 in grey values) because of the low temperature contrast over the field of view of the IR camera. The inter-frame grey value variations, e.g., cold (Frame 1) to warm (Frame 31), or warm (Frame 61) to cold (Frame 91), reveal a clear temporal drift problem. This variation is non-linear in time (shown later), and sometimes it is within the range of the frame spatial contrast between two FFC periods (e.g., compare Frames 1 and 31 in Fig. 4.3). Nonuniformity is also evident in the raw images, e.g., cold corner areas of Frames 1, 121, and 151, or warm corners in Frame 31 (Fig. 4.3). The main LWST feature, e.g., the elongated cold streak in the middle of Frame 1 disappears in Frame 181, because the platform is moving during the thermal imagery recording. This can also be seen by following the position of the ZiviCat, indicated by a red dot in the Fig. 4.3 images, and its boat track due to water mixing. A similar track is produced by the accompanying boat navigating “below” the ZiviCat (more evident in Frames 1 and 181). This motion requires that consecutive images have to be assembled along the track of the BLIMP. We implemented an image processing procedure that combines available methods to address and correct all these issues for LSWT image registration.

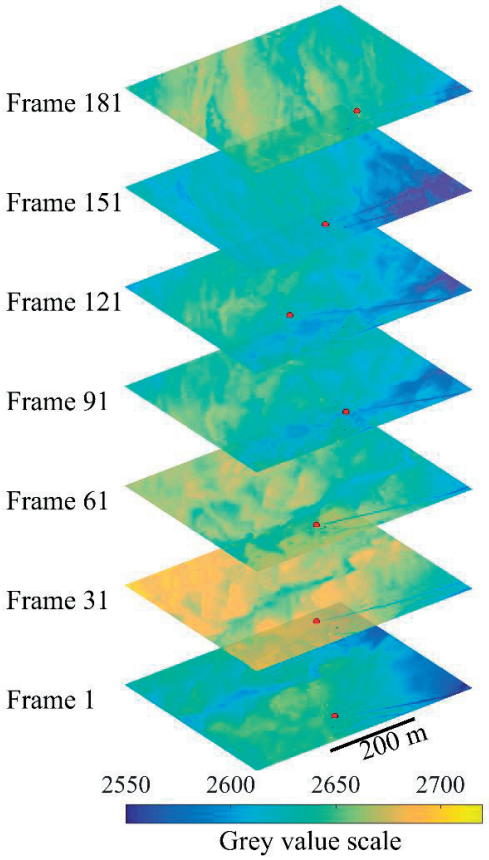

Fig. 4.3. Examples of 7 selected raw IR images 30 frames apart (collected on 18 March 2016) with a pixel resolution of ~0.8 m and a frequency of 0.2 frames per second (FPS). The color map shows the IR camera output as grey values (given in the legend). A red dot indicates the position of the ZiviCat in each frame. This figure illustrates both spatial (e.g., more pronounced in Frame 151) and temporal (e.g., grey value variation between Frames 1 and 31) noise of the thermal images. The change of the surface pattern structures among the frames is due to the moving BLIMP (e.g., take the catamaran position as a reference point to visualize the movement).

4.2.3. Image enhancement, registration and calibration procedure

The procedure developed to estimate and correct noise in images, register all the images and calibrate them is shown in Fig. 4.4. It is divided into three main steps: (i) pre-processing, (ii) image registration, and (iii) and post-processing.

In the pre-processing step, we first read the raw 14-bit thermal images collected during the field measurements. A spatial filter, e.g., Gaussian filter or median filter, is then applied to reduce the salt-and-pepper noise evident in raw thermal images (Vollmer and Möllmann 2011). The filter size, i.e., the standard deviation value (Gaussian filter) or the radius (median filter), was selected so as to retain the meso-scale patterns of LSWTs. In the next step, a preliminary NUC

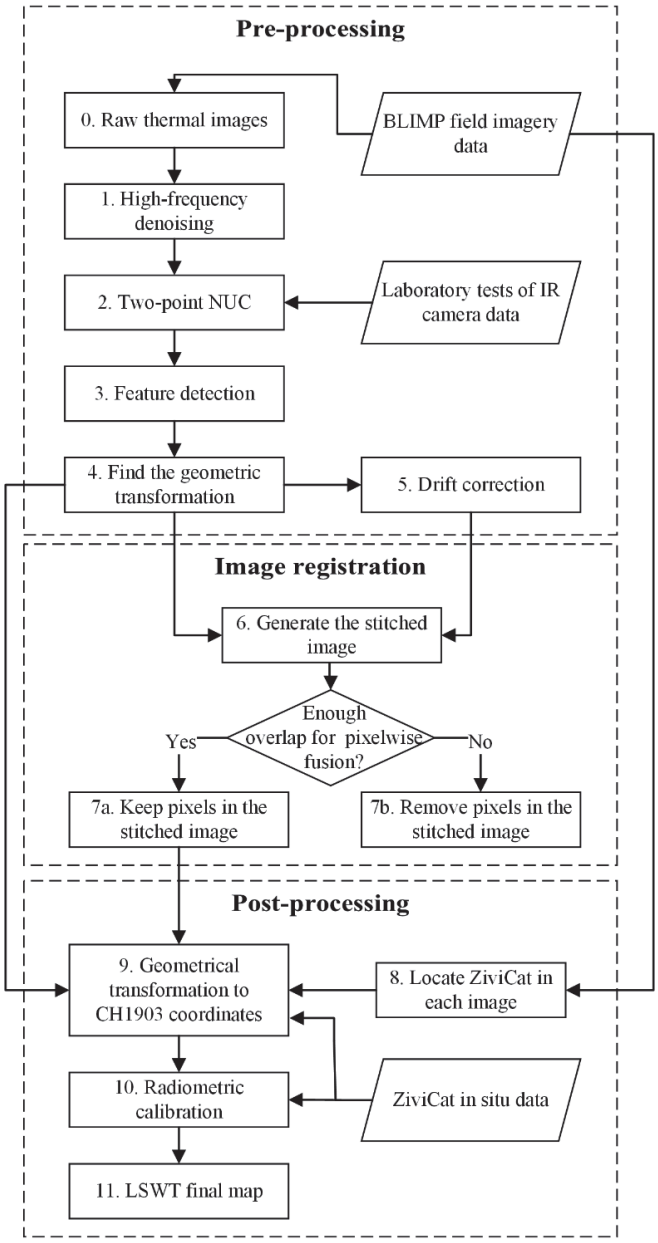

Fig. 4.4. Flowchart of the procedure for image enhancement (top), registration (center) and calibration (bottom).

investigation is performed. For this, FLIR camera images of a ~1.5 × 1.5 m metal plate were recorded under low (controlled cold room at ~4°C) and high (night-time windowless basement room at ~25°C with minimum airflow) temperatures. Then, a NUC was performed on these images following the two-point algorithm of Budzier and Gerlach (2015). In this approach, the

deviation in pixel $ij, \Delta U_{ij}$, from the mean scene value, $\langle U \rangle$, is a linear function of the pixel value:

$$\Delta U_{ij} = U_{ij} - \langle U \rangle = a_{ij} U_{ij} + b_{ij} \tag{4.1}$$

where U_{ij} denotes the pixel grey value of pixel *ij*. We used 500 frames under constant low and high temperature conditions for this calibration, and so obtained the linear regression model parameters, *a* and *b* in Eq. 4.1, for each pixel. The linear model showed mean and maximum residuals of 1.9 and 4.5 in grey values, respectively. Afterwards, the pixel value corrected for nonuniformity was calculated by subtracting the deviation, Eq. 4.1, from the measured irradiance at each frame:

$$U^k_{ij,NUC} = U^k_{ij} - \Delta U^k_{ij} = \left(1 - a_{ij}\right) U^k_{ij} - b_{ij} \tag{4.2}$$

where *k* is the frame number. An example of the NUC operation on the field data is shown in Fig. 4.5. It reveals that the preliminary NUC enhances the thermal imagery (e.g., the enhancement of the top-right cold corner and the central warm area of the image). The corresponding NUC in grey value (Fig. 4.5c) indicates that the nonuniformity errors over inland water bodies can be comparable with the frame contrast at the given scales (range of colormap in Fig. 4.5a and b). However, examining the NUC method under lower contrast conditions, e.g., in wintertime when spatial LSWT variation is minimal, indicates that some artifacts still remain in the images (not shown here). This can be due to the very low temperature contrast of LSWTs, environmental conditions different from the laboratory tests (especially humidity and higher sensor-environment temperature difference), errors associated with the parameter estimations, or the linearity assumption in the two-point NUC algorithm. In the present investigation, the large overlap area between subsequent images permits further improvement of the nonuniformity effect (discussed in section 4.3).

Compared to aircraft systems, tilting was expected to be negligible with the BLIMP Picavet rigging system. Therefore, an image with minimal (close to zero) Inertial Measurement Unit (IMU) values (negligible tilting) was selected as a first image. After applying the preliminary NUC to all selected images, the geometric transformation of the images with respect to the first

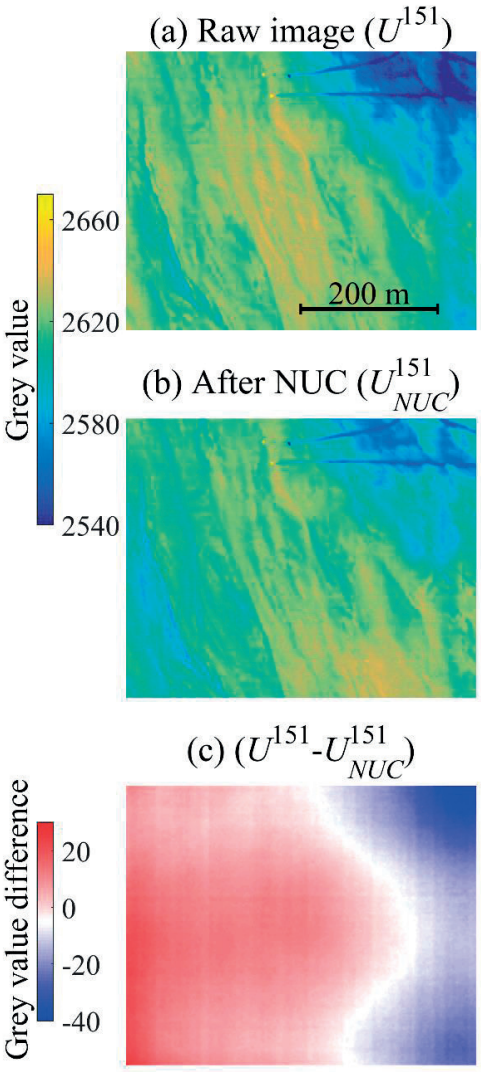

Fig. 4.5. An example of NonUniformity Correction (NUC) of Lake Geneva thermal imagery: (a) raw thermal image (Frame 151 of the selected images in Fig. 4.3, 640 × 512 pixels) with a pixel resolution of ~0.8 m, (b) the image after NUC, and (c) the difference between (a) and (b). Note that the grey value range of the legend in (a) and (b) is different from panel (c), and also Fig. 4.3.

image was calculated. To do this, a feature detection and matching technique was applied. Since strong meso-scale features (~1 m image resolution) are not likely over natural waters, we combined the Speeded-Up Robust Features (SURF) (Bay et al. 2008) and Maximally Stable Extremal Regions (MSER) (Matas et al. 2004) algorithms for feature detection in each frame. An example of features found by the SURF and MSER algorithms is shown in the Supplementary materials (Fig. S4.1). The matching of the points between two frames and their relative geometrical transformation is obtained using the Maximum Likelihood Estimation SAmple Consensus (MLESAC) (Torr and Zisserman 2000) algorithm. We applied an affine transformation, which preserves straight lines and planes. The above mentioned algorithms

require that certain parameters be specified. These were selected such that the final stitched image keeps the main patterns over the lake (by eye inspection). More importantly, an objective metric was used, i.e., that the irradiance values match well in situ temperature data measured by the ZiviCat (discussed below in section 3). All image processing in this work, including the subroutines for feature detection and estimation of the geometrical transformation, were written in Matlab (last accessed 10 February 2018). An example of three overlaid frames (20 frames apart; Fig. 4.6) demonstrates the excellent performance of the selected methods and parameters in preserving the main LSWT features in the stitched image (see the two boat tracks in the lower parts, or the streak-like features in the middle of Fig. 4.6). The change of inter-frame grey values is due to drift and will be discussed below.

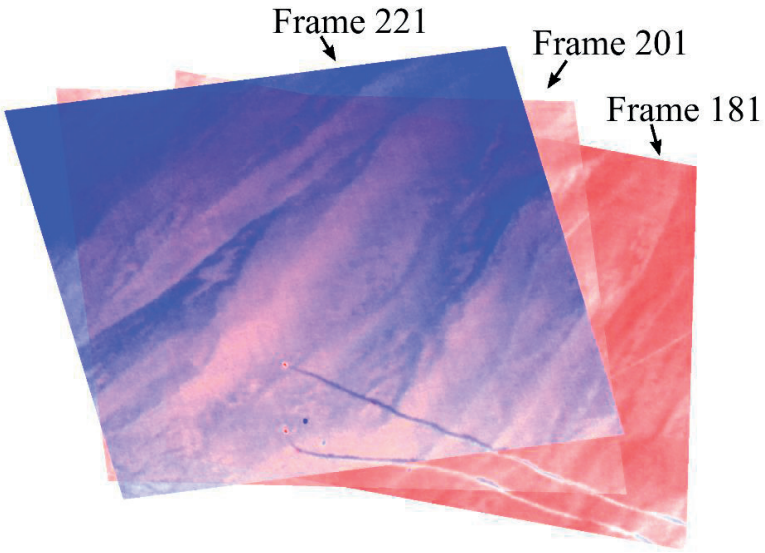

Fig. 4.6. An example demonstrating the performance of the feature-based image registration algorithm. It shows Frames 181, 201 and 221 (after the NUC was applied) overlaid based on matched features. Here we selected one image every 20 frames only for visualization purposes; a much higher amount of overlap exists between consecutive images. Note that, for example, the ZiviCat and the accompanying boat tracks appear twice to show the motion between the first two (bottom) and then between all three images.

As mentioned earlier, a problem with uncooled IR cameras is shutter-based drift. Two examples, in Figs. 4.3 and 4.6, show the problem for LSWT thermography. Even though the FLIR camera implements the internal FFC every ~5 min, drift is still evident within each FFC interval as an increase or decrease of the pixelwise grey value from frame-to-frame. To correct

this internal grey value variation that is non-physical with respect to LSWTs, the overlapped areas between consecutive pairs of frames were found using the geometric transfer functions obtained above. We then estimated and matched the probability distribution of the grey values for the overlapped area of each frame. The matching was achieved by computing the cross-correlation of the overlapped areas, finding the lag in the grey value distribution, and subsequently shifting the level of the second image to the first one. Thereafter, the corrected second image was used to correct the third image, and so on. In other words, the shutter-based drift corrected pixel value, $U^k_{ij,Sh}$, is estimated as:

$$U^k_{ij,Sh} = U^k_{ij,NUC} + c_k = \left(1 - a_{ij}\right)U^k_{ij} - b_{ij} + c_k \tag{4.3}$$

where c_k is the drift correction associated with frame number *k*, and is calculated as follows:

$$P\left(U^k_{ij,NUC} + c_k\right)_{OL} \cong P\left(U^{k-1}_{ij,Sh}\right)_{OL} \tag{4.4}$$

Here, *P* denotes the estimate of the Probability Distribution Function (PDF), and *OL* is the overlapped area. In this methodology, the drift correction for the first frame, for which we take the frame right after the FFC, is zero ($c_1 = 0$). We also tested correcting the drift by using the spatially averaged values of the overlapped area. However, errors cumulated through the image sequence and the results were slightly worse than those of the present methodology (results not shown). Figure 4.7a gives an example of the drift problem, and its correction procedure is illustrated in Fig. 4.7b. The drift correction for the whole frame sequence (287 frames in five FFC periods) is presented in Fig. 4.7c. The results suggest that the drift problem is non-linear between and within FFC intervals.

After the pre-processing step, all the selected images were registered. Image stitching was accomplished using the geometrical transform functions obtained through feature detection and matching in the pre-processing step. Pixelwise image fusion was performed to create the composite image. Although there are various methods for image fusion (Anita and Moses 2013), here we used simple averaging to fuse a set of input intensities at each pixel:

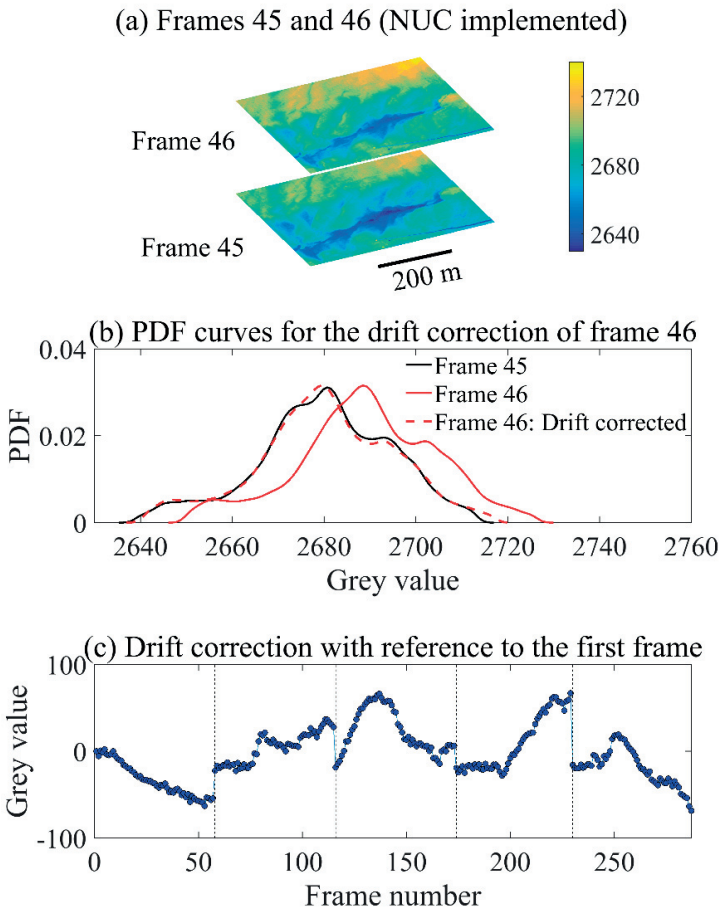

Fig. 4.7. (a) An example of drift problems in thermal imagery. Note the evidently non-physical increase of grey value from Frame 45 to Frame 46. The grey scale is given in the legend, (b) The Probability Distribution Function (PDF) of Frames 45 and 46 (solid lines), together with the PDF of the drift-corrected Frame 46 (dashed line). The corresponding correction obtained by the cross-correlation analysis is found to be ~9.1 in grey value, and (c) The drift correction for the entire selected frame series with respect to the first frame. FFC periods are indicated by dashed-vertical lines.

$$U_{pq,reg} = \frac{\sum_{m \in \{k_{pq,reg}\}} U^{m}_{pq,Sh}}{N_{pq,reg}} \tag{4.5}$$

where $U_{pq,reg}$ is the intensity value at location pq of the composite image and $N_{pq,reg}$ is the number of frames that are included in the calculation of the mean overlapped grey value at pq, i.e., $\{k_{pq,reg}\}$. Thereafter, a statistical criterion using the number of overlapped pixels was

applied to keep a pixel in the stitched image, or remove it. This is based on the statistical variation of the grey value as a function of N_{OL}, i.e., the number of overlapped images at each pixel. Results will be given in section 4.3. At the end of this step, the overall corrected LSWT thermal image in grey values is established. However, two more steps are required: (i) mapping the obtained pattern into geographic coordinates to correlate the BLIMP data to the ZiviCat data, and (ii) converting grey values to temperatures by carrying out the radiometric calibration to produce the temperature map.

For both of these steps (post-processing in Fig. 4.4) the ZiviCat measurements are needed. First, the ZiviCat location in each image was found. Solid objects, i.e., ZiviCat and the boat, usually produce pixels with the highest intensity (for example, see hot spots in Figs. 4.5 and 4.6). Due to the high overlap ratio between consecutive images (~95%), the displacement of objects is expected to be small between sequential frames. Therefore, the ZiviCat was manually located in the first image. In order to locate the ZiviCat in the second image, we searched for the pixel with the highest intensity within a small radius, i.e., ~20 pixels, around that pixel. We repeated the same procedure for the following frames always using the ZiviCat location in the previous frame (see examples in Fig. 4.3 shown by red dots). Using these locations, together with the geometric transformation for each frame from the pre-processing step, ZiviCat locations were pinpointed in the stitched image. Since the BLIMP and ZiviCat have separate data acquisition systems, the meta-data synchronization was accomplished through time matching. The corresponding GPS coordinates, recorded by the ZiviCat, permitted transforming the final stitched image from pixel coordinates to the geographic coordinates.

Conversion of pixel grey values to actual temperatures was achieved through radiometric calibration using (Horny 2003):

$$T_{pq,zc} = \frac{B}{\ln\left[R/\left(U_{pq,reg} - O\right) + F \right]} \tag{4.6}$$

where B, R, O and F are the calibration coefficients that were determined through a non-linear regression analysis. The close-to-the-surface (2 cm depth) in situ temperatures measured by ZiviCat, $T_{pq,zc}$, and the corresponding grey values in the stitched image, $U_{pq,reg}$, were used to find these parameters. Prior to that, the actual depths of the ten *RBRsolo* thermistors (Fig. 4.2b)

due to the ZiviCat frame movement were corrected using the ZiviCat IMU data. Finally, the LSWT map was obtained from the grey values of the stitched images with Eq. 4.6.

4.3. Results and discussion

To illustrate the performance of the proposed procedure for LSWT image registration and calibration, we show results for the selected IR frame series over Lake Geneva. To demonstrate the effect of each of the main steps of image processing, i.e., NUC, drift correction and image fusion, we present the resulting map with full correction, together with the thermal maps without NUC, without drift correction, or using fewer frames for image fusion.

To examine the effect of the pixelwise averaging on the image registration (image fusion), the results using all images (0.2 FPS, and an average of ~95% overlap between consecutive images) were compared with the thermal map considering only every 10th image (0.02 FPS, and an average of ~86% overlap between consecutive images). Using only every 10th image, the current algorithm of feature detection and estimation of the geometric transformation failed (results not shown). This is apparently due to lack of enough features, and also the significant movement of the ZiviCat and the boat (moving objects) between frames in the 10th image configuration. Therefore, we employed the geometrical transformations corresponding to the subset of images, i.e., every 10th image, computed using all images. According to the preliminary results, a higher number of overlapped images for a pixel results in a higher enhancement on the stitched image. For example, the edges of the stitched image, where the number of overlapped images is lower, show more non-physical spatial variability. To quantify the effect of smoothing by image fusion, and consequently to find a criterion for omitting the pixels with insufficient overlaps, we calculated the variation of the grey value, $\left(\Delta U\right)_{N_{OL}}$, as a function of the number of overlaps, N_{OL}, at each pixel:

$$\left(\Delta U_{pq,reg}\right)_{N_{OL}} = \left|\left(U_{pq,reg}\right)_{N_{OL}} - \left(U_{pq,reg}\right)_{N_{OL}-1}\right| \tag{4.7}$$

According to Eq. 4.7, at an arbitrary position, *pq*, on the registered image, the variation due to N_{OL} overlaps is defined as the change of the absolute grey value resulting from adding a new frame that includes *pq* to the registered image, i.e., using Eq. 4.5. This variation may change with location on the registered image. Therefore, we calculated the statistical parameters of

variation as a function of the number of overlapped images. Figure S4.2 presents the maps of the number of overlaps for both cases studied, using every 10th image and using all images.

The median and the range of grey value variations for each number of overlapped images were then calculated and were presented as box plots (Fig. 4.8). It is evident that using more overlaps leads to less pixelwise grey value variation. Here, the results of Fig. 4.8a at point 3 on the x-axis, should be compared with the corresponding results in Fig. 8b at point 30 on the x-axis. In this example, point 3 in Fig. 4.8a showed a median and maximum variation of ~2 and 7, respectively, and for the corresponding point in Fig. 4.8b (point 30) a median and maximum variation of ~0.2 and 0.6, respectively, were found.

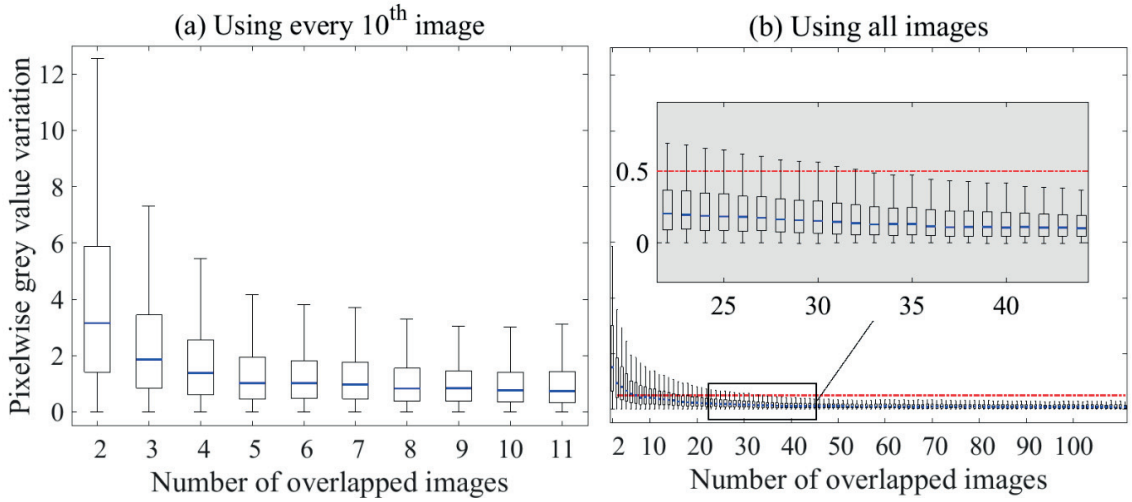

Fig. 4.8. Pixelwise grey value variation as a function of the number of overlapped images obtained by using (a) every 10th image, and (b) all images. The typical value (median, blue lines), the likely range of variation (interquartile, black boxes) and the wider range of variation (whiskers extent, solid black lines) excluding outliers are given in the box plots. The red line in (b) corresponds to 0.5 grey value variation that is used as an arbitrary threshold here. Inset: zoom on the interval of number of overlapped images where the chosen threshold intersects the maximum grey value variation.

The results of Fig. 4.8b can also be used to define a threshold for the number of overlaps in the stitched image. In this study, we considered a threshold of 35 frames for image fusion, i.e., $N_{cr,OL} = 35$ in step 7 of Fig. 4.4. This point is at the beginning of the flat part of the curve in Fig. 4.8b, and has an average maximum variation of < 0.5 grey value (as indicated by the red line in Fig. 4.8b). We applied this criterion to generate the final thermal maps shown below.

After BLIMP-ZiviCat time synchronization, as explained above, the catamaran pixel-GPS locations were used to create the final thermal map in CH1903 Swisstopo coordinates. In order to reveal the effectiveness of the proposed image processing algorithm, the results are given (Fig. 4.9) for full correction in all images, as well as the thermal maps without implementing NUC, without drift correction, and using fewer frames for image fusion. The results confirm that the high-frequency denoising (step 1 in Fig. 4.4) preserved the main features of the thermal images. For this part, we implemented both the median and Gaussian filters. The difference between the final thermal maps was insignificant at the given scale (we only show the results applying the Gaussian filter).

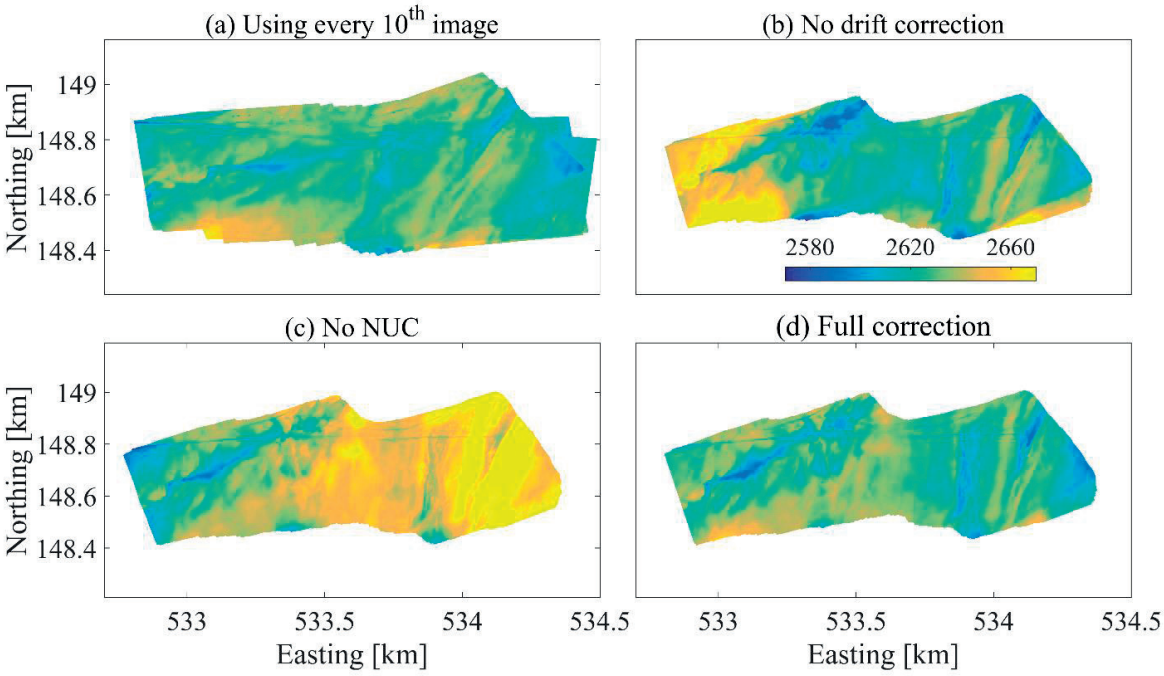

Fig. 4.9. Surface thermal maps of a section of Lake Geneva in grey value (step 9 in Fig. 4.4) obtained by: (a) Using every 10th image (to examine the effect of step 7 in Fig. 4.4), (b) Neglecting the drift correction (to examine the effect of step 5 in Fig. 4.4), (c) Neglecting NUC (to examine the effect of step 2 in Fig. 4.4), and (d) with full correction. Legend in (b) indicates the grey value scale valid for all panels.

Using fewer frames for image fusion (Fig. 4.9a) produces less image contrast difference compared to the full correction map (Fig. 4.9d), and the resulting map is not satisfactory in terms of preserving all (even the main) features in the stitched image. For example, the IR boat

tracks are not as clear as in Fig. 4.9d. In addition, due to the lack of sufficient frames for image fusion (as also shown in Fig. 4.8), some artifacts are evident in the areas with less overlap (e.g., close to the edges of Fig. 4.9a). Also, the geometrical transformation to CH1903 coordinates are slightly tilted compared to using full images (Fig. 4.9d). This is, again, due to insufficient number of frames for transformation.

Figure 4.9 also indicates that neglecting NUC or the drift correction may cause non-physical spatial gradients over the stitched image (e.g., note the warm areas in Figs. 4.9b and c). The warm areas in the left part of Fig. 4.9b result from the negative drift correction required for the first FFC interval (Fig. 4.7c), whereas in the center parts, the averaging due to a high number of overlaps (Fig. S4.2) compensates the drift problem. Fig. 4.9c illustrates a gradual warming from left (first frame) to the right (last frame) of the stitched image. This is due to the recursive behavior of the drift correction methodology. This methodology uses the PDF matching between overlapped areas of consecutive frames, but then applies the obtained correction to the whole frame. NUC is particularly effective on the edges (see Fig. 4.5c as an example), which mainly contain the non-overlapped regions of the frame. Therefore, neglecting NUC retains an error in a frame for the subsequent drift correction. This error is cumulative over subsequent frames, causing warming in this case. To confirm this, we generated a stitched image neglecting both NUC and drift correction (Fig. S4.3). It shows a map similar to Fig. 4.9b (no drift correction) with more artifacts on the edges due to omitting NUC.

To further investigate the performance of the procedure, the matching of the measured in situ near-surface temperatures (at about 2-cm depth) with the corresponding grey value on the stitched image is required. However, the in situ measurement points are contaminated by the boat track in the stitched image (note again that the measurement platform is moving). To avoid this, the average grey value of a few pixels (4 in the present analysis) above and below the actual locations of the ZiviCat were used. Therefore, locations with minimal grey value differences between pixels above and below the ZiviCat track are more appropriate. Furthermore, to cover wider temperature ranges, regions with higher along-track spatial variability are more relevant. Considering these requirements, the along-track measurement frames between 533.95 and 534.3 km in Fig. 4.9d were selected (50 frames with their locations are shown in Fig. S4.4). The comparison between the measured temperatures (from ZiviCat) and the enhanced grey values (processed BLIMP data) for the thermal maps of Figs. 4.9a and

d are shown in Fig. 4.10. It again demonstrates the poor performance by using fewer frames for image stitching and fusion and indicates a relatively low RMSD and high correlation coefficient when using the proposed method for the all image registration. The observed deviations between the grey values and LSWTs (red circles in Fig. 4.10) can be due to errors in the estimation of the geometric transformations, the difference between skin (top 10 - 500 µm layer) and near-surface temperatures (Minnett et al. 2011; Wilson et al. 2013), uncertainties in the ZiviCat measured and corrected data, and errors induced by averaging above/below pixels for the comparison.

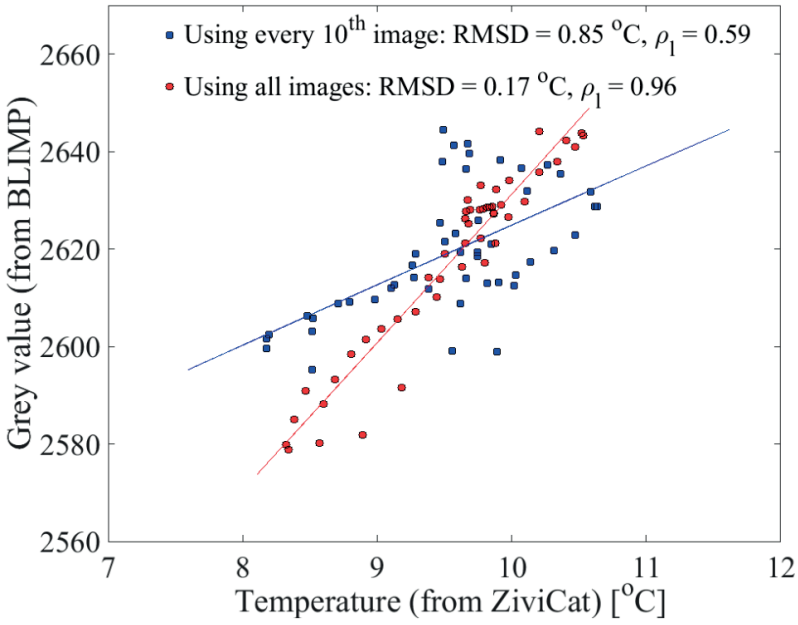

Fig. 4.10. Comparison of the grey value of the stitched image (from the airborne BLIMP) with the corresponding in situ near-surface (2-cm depth) temperatures measured by the ZiviCat using every 10th image (blue squares) and all images (red circles). The solid lines show the corresponding radiometric calibrations, Eq. 4.6, which tend to be linear for a narrow temperature range (< 3°C). The RMSDs for the non-linear regression model, and the correlation coefficients, ρ_l , for a linear curve fitting are given in the legend.

In the last step of this procedure, the radiometric calibration (step 10 in Fig. 4.4) is required to convert the obtained grey value thermal map (Fig. 4.9d) into a temperature map. A non-linear regression analysis following an ordinary least-square approach was carried out to find the best-fit parameters in Eq. 4.6. The solid lines in Fig. 4.10 show the fitted curves. We note that Eq. 4.6 was developed for a wide range of temperatures (> 50°C), confirmed by the wide range of

confidence intervals obtained for the estimated calibration parameters (not shown here). For a low-contrast scene, a linear relationship is expected and linearity within the < 3°C range of LSWTs is evident in Fig. 4.10. The red solid line parameterization in Fig. 4.10 was used to obtain the meso-scale thermal map (Fig. 4.11 with ~0.8 m resolution) over a section of Lake Geneva. The area covered in Fig. 4.11, i.e., ~0.61 km^2, resolves less than a typical satellite pixel (1 km^2). However, it shows various cold-warm patches and streak-like structures over the lake surface with a temperature contrast of > 2°C. These features are not resolved in satellite images, but may be important for atmosphere-lake heat exchange dynamics.

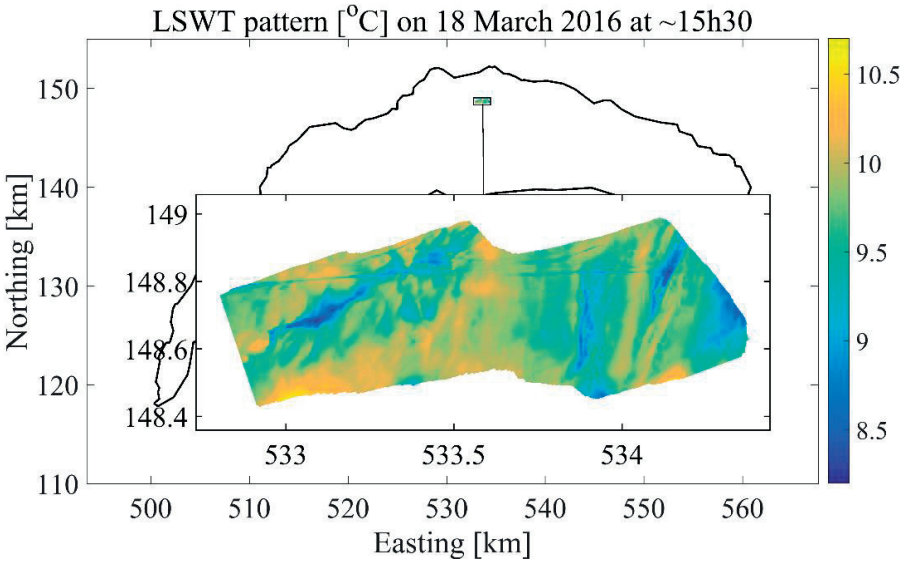

Fig. 4.11. Lake surface water temperature (LSWT) meso-scale map over a section of Lake Geneva obtained from aerial remote sensing (see Fig. 4.2 for measurement platforms). This map was created using 287 images with a resolution of ~0.8 m together with an image processing procedure (Fig. 4.4). Streaks with temperature differences of several degrees are evident. Note the boat track from west to east across the upper part of the image. The legend indicates temperature in °C.

4.4. Summary and conclusions

Airborne meso-scale thermography of LSWTs can provide suitable data for ground-truthing and spatial downscaling of satellite data. The obtained patterns are also valuable for physical limnology studies, especially the dynamics of air-water exchange phenomena at the meso-scales (~1 m resolution). In this study, we presented aerial thermography results over a section of a large lake (Lake Geneva) obtained with an in-house system consisting of a balloon-

launched platform (BLIMP) accompanied by a catamaran (ZiviCat) for ground-truthing and radiometric calibration. An uncooled microbolometer camera was used, for which the spatial noise, i.e., nonuniformity, and temporal drift are intrinsic. Correction and enhancement of the IR images were carried out before and throughout the image registration procedure (Fig. 4.4). A preliminary two-point NUC (using laboratory measurements, Fig. 4.5) together with drift estimation through PDF matching of the overlap regions of consecutive frames (Fig. 4.7) were implemented prior to image registration. The selected frames were registered to create a stitched image covering a wider area. To estimate the geometric transformations for image registration, the blob and region features are detected applying SURF and MSER techniques (Figs. 4.6 and S4.1). Then, MLESAC was employed to find the transformation functions by matching the combination of these features among frames. Due to a large degree of overlap, a simple averaging was used on the stitched image to fuse the grey value at each pixel. The results indicated that neglecting either the NUC or the drift correction can produce substantial artificial spatial gradients in the stitched image (Figs. 4.9b and c). Furthermore, using all images, providing ~95% overlap between consecutive frames allowed accurate generation of the stitched image (Figs. 4.9a and 4.10), whereas imagery with less overlap, e.g., ~86% overlap, failed. The final result (Figs. 4.10 and 4.11) showed the capability of the two-platform system and the proposed image-processing procedure to resolve meso-scale LSWT patterns over a lake. It also demonstrates that in such low-contrast moving scene cases containing only a few clearly identifiable mobile objects such as boats, a high overlap ratio (~95% in our case) combined with spatiotemporal noise reduction are essential for accurate LSWT thermography. This resulted in the generation of meso-scale LSWT maps that revealed spatial LSWT variability with unprecedented detail.

Acknowledgments

This work was supported by the FEEL Foundation [grant number 5257]. The authors would like to thank J.-L. Liardon, H.K. Wynn, P.O. Paccaud, B. Geissmann, L. Zulliger, J. Béguin, P. Klaus, N. Gujja Shaik, S. Benketaf, K. Kangur, M. Pagnamenta, L. Hostettler, N. Bongard, G. Ulrich, B. Grossniklaus, A. Rosselet, M. Bolay, J. Rossier, Y. Poffet and N. Roussel for their contribution to designing, testing, and improving of the BLIMP and ZiviCat platforms used in this research. We also wish to thank A. Ivanov and S. Tulyakov for their help and advice on BLIMP image processing.

References

Adrian, R., C. M. O'Reilly, H. Zagarese, S. B. Baines, D. O. Hessen, W. Keller, D. M. Livingstone, R. Sommaruga, D. Straile, E. Van Donk, G. A. Weyhenmeyer, and M. Winder. 2009. Lakes as sentinels of climate change. Limnol. Oceanogr. **54:** 2283-2297. doi: 10.4319/lo.2009.54.6_part_2.2283.

Anita, S. J. N., and C. J. Moses. 2013. Survey on pixel level image fusion techniques, p. 141-145. 2013 IEEE International Conference on Emerging Trends in Computing, Communication and Nanotechnology (ICECCN 2013). IEEE.

Barry, D. A., J.-L. Liardon, P. Paccaud, P. Klaus, N. S. Gujja Shaik, A. I. Rahaghi, and U. Lemmin. 2018. A low-cost, autonomous mobile platform for limnological investigations, supported by high-resolution mesoscale airborne imagery. PLoS One**:** Under review.

Bay, H., A. Ess, T. Tuytelaars, and L. Van Gool. 2008. Speeded-Up Robust Features (SURF). Comput. Vis. Image Und. **110:** 346-359. doi: 10.1016/j.cviu.2007.09.014.

Budzier, H., and G. Gerlach. 2015. Calibration of uncooled thermal infrared cameras. J. Sens. Sens. Syst. **4:** 187-197. doi: 10.5194/jsss-4-187-2015.

Castro, S. L., W. J. Emery, G. A. Wick, and W. Tandy. 2017. Submesoscale sea surface temperature variability from UAV and satellite measurements. Remote Sens. **9:** 1089. doi: 10.3390/Rs9111089.

Emery, W. J., W. S. Good, W. Tandy, M. A. Izaguirre, and P. J. Minnett. 2014. A microbolometer airborne calibrated infrared radiometer: The Ball Experimental Sea Surface Temperature (BESST) radiometer. IEEE Trans. Geosci. Remote Sens. **52:** 7775-7781. doi: 10.1109/Tgrs.2014.2318683.

Ferri, R., N. Pierdicca, and S. Talice. 2000. Mapping sea surface temperature from aircraft using a multi-angle technique: An experiment over the Orbetello lagoon. Int. J. Remote Sens. **21:** 3003-3024. doi: 10.1080/01431160050144929.

Handcock, R. N., A. R. Gillespie, K. A. Cherkauer, J. E. Kay, S. J. Burges, and S. K. Kampf. 2006. Accuracy and uncertainty of thermal-infrared remote sensing of stream temperatures at multiple spatial scales. Remote Sens. Environ. **100:** 427-440. doi: 10.1016/j.rse.2005.07.007.

Haselwimmer, C., A. Prakash, and G. Holdmann. 2013. Quantifying the heat flux and outflow rate of hot springs using airborne thermal imagery: Case study from Pilgrim Hot Springs, Alaska. Remote Sens. Environ. **136:** 37-46. doi: 10.1016/j.rse.2013.04.008.

Hernandez, P. A., S. Calvari, A. Ramos and others 2014. Magma emission rates from shallow submarine eruptions using airborne thermal imaging. Remote Sens. Environ. **154:** 219-225. doi: 10.1016/j.rse.2014.08.027.

Horny, N. 2003. FPA camera standardisation. Infrared. Phys. Techn. **44:** 109-119. doi: 10.1016/S1350-4495(02)00183-4.

Kruse, P. W. 1997. Uncooled infrared imaging arrays and systems. Academic Press. https://www.elsevier.com/books/uncooled-infrared-imaging-arrays-and-systems/willardson/978-0-12-752155-8.

Lahiri, B. B., S. Bagavathiappan, T. Jayakumar, and J. Philip. 2012. Medical applications of infrared thermography: A review. Infrared. Phys. Techn. **55:** 221-235. doi: 10.1016/j.infrared.2012.03.007.

Lemmin, U., and N. D'Adamo. 1996. Summertime winds and direct cyclonic circulation: Observations from Lake Geneva. Ann. Geophys., Ser. A **14:** 1207-1220. doi: 10.1007/s005850050384.

Liardon, J.-L., and D. A. Barry. 2017. Adaptable imaging package for remote vehicles. HardwareX **2:** 1-12. doi: 10.1016/j.ohx.2017.04.001.

Liardon, J.-L., L. Hostettler, L. Zulliger, K. Kangur, N. G. Shaik, and D. A. Barry. 2017. Lake imaging and monitoring aerial drone. HardwareX. doi: 10.1016/j.ohx.2017.10.003.

Livingstone, D. M., and M. T. Dokulil. 2001. Eighty years of spatially coherent Austrian lake surface temperatures and their relationship to regional air temperature and the North Atlantic Oscillation. Limnol. Oceanogr. **46:** 1220-1227. doi: 10.4319/lo.2001.46.5.1220.

Mahrt, L., and D. Khelif. 2010. Heat fluxes over weak SST heterogeneity. J. Geophys. Res.: Atmos. **115:** D11103. doi: 10.1029/2009jd013161.

Marinetti, S., X. Maldague, and M. Prystay. 1997. Calibration procedure for focal plane array cameras and noise equivalent material loss for quantitative thermographic NDT. Mater. Eval. **55:** 407-412. https://www.osti.gov/scitech/biblio/471095.

Matas, J., O. Chum, M. Urban, and T. Pajdla. 2004. Robust wide-baseline stereo from maximally stable extremal regions. Image Vision Comput. **22:** 761-767. doi: 10.1016/j.imavis.2004.02.006.

Milton, A. F., F. R. Barone, and M. R. Kruer. 1985. Influence of nonuniformity on infrared focal plane array performance. Opt. Eng. **24:** 855-862. doi: 10.1117/12.7973588.

Minnett, P. J., M. Smith, and B. Ward. 2011. Measurements of the oceanic thermal skin effect. Deep-Sea Res. Part II. **58:** 861-868. doi: 10.1016/j.dsr2.2010.10.024.

Mounier, E. 2011. Technical and market trends for microbolometers for thermography and night vision, p. 80121u. Proc SPIE 8012, Infrared Technology and Applications XXXVII.

Neale, C. M. U., C. Jaworowski, H. Heasler, S. Sivarajan, and A. Masih. 2016. Hydrothermal monitoring in Yellowstone National Park using airborne thermal infrared remote sensing. Remote Sens. Environ. **184:** 628-644. doi: 10.1016/j.rse.2016.04.016.

Nugent, P. W., and J. A. Shaw. 2014. Calibration of uncooled LWIR microbolometer imagers to enable long-term field deployment, p. 90710v. Proc. SPIE 9071, Infrared Imaging Systems: Design, Analysis, Modeling, and Testing XXV.

Nugent, P. W., J. A. Shaw, and N. J. Pust. 2013. Correcting for focal-plane-array temperature dependence in microbolometer infrared cameras lacking thermal stabilization. Opt. Eng. **52:** 061304. doi: 10.1117/1.Oe.52.6.061304.

Oesch, D., J. M. Jaquet, R. Klaus, and P. Schenker. 2008. Multi-scale thermal pattern monitoring of a large lake (Lake Geneva) using a multi-sensor approach. Int. J. Remote Sens. **29:** 5785-5808. doi: 10.1080/01431160802132786.

Oesch, D. C., J. M. Jaquet, A. Hauser, and S. Wunderle. 2005. Lake surface water temperature retrieval using Advanced Very High Resolution Radiometer and Moderate Resolution Imaging Spectroradiometer data: Validation and feasibility study. J. Geophys. Res.: Oceans **110:** C12014. doi: 10.1029/2004jc002857.

Parra, F., P. Meza, C. Toro, and S. Torres. 2011. Infrared focal plane array imaging system characterization by means of a blackbody radiator. Lect. Notes Comput. Sci. **7042:** 105-112. doi: 10.1007/978-3-642-25085-9_12.

Perry, D. L., and E. L. Dereniak. 1993. Linear-theory of nonuniformity correction in infrared staring sensors. Opt. Eng. **32:** 1854-1859. doi: 10.1117/12.145601.

Riffler, M., G. Lieberherr, and S. Wunderle. 2015. Lake surface water temperatures of European Alpine lakes (1989-2013) based on the Advanced Very High Resolution Radiometer (AVHRR) 1 km data set. Earth Sys. Sci. Data **7:** 1-17. doi: 10.5194/essd-7-1-2015.

Tamborski, J. J., A. D. Rogers, H. J. Bokuniewicz, J. K. Cochran, and C. R. Young. 2015. Identification and quantification of diffuse fresh submarine groundwater discharge via airborne thermal infrared remote sensing. Remote Sens. Environ. **171:** 202-217. doi: 10.1016/j.rse.2015.10.010.

Tonolla, D., C. Wolter, T. Ruhtz, and K. Tockner. 2012. Linking fish assemblages and spatiotemporal thermal heterogeneity in a river-floodplain landscape using high-resolution airborne thermal infrared remote sensing and in-situ measurements. Remote Sens. Environ. **125:** 134-146. doi: 10.1016/j.rse.2012.07.014.

Torgersen, C. E., R. N. Faux, B. A. McIntosh, N. J. Poage, and D. J. Norton. 2001. Airborne thermal remote sensing for water temperature assessment in rivers and streams. Remote Sens. Environ. **76:** 386-398. doi: 10.1016/S0034-4257(01)00186-9.

Torr, P. H. S., and A. Zisserman. 2000. MLESAC: A new robust estimator with application to estimating image geometry. Comput. Vis. Image Und. **78:** 138-156. doi: 10.1006/cviu.1999.0832.

Torres, F., C. San Martin, and S. N. Torres. 2006. A RLS filter for nonuniformity and ghosting correction of infrared image sequences. Lect. Notes Comput. Sci. **4225:** 446-454. doi: 10.1007/11892755_46.

Torres, F., S. N. Torres, and C. San Martin. 2005. A recursive least square adaptive filter for nonuniformity correction of infrared image sequences. Lect. Notes Comput. Sci. **3773:** 540-546. doi: 10.1007/11578079_56.

Tozuka, T., S. Ohishi, and M. F. Cronin. 2017. A metric for surface heat flux effect on horizontal sea surface temperature gradients. Climate Dynam. doi: 10.1007/s00382-017-3940-2.

Vollmer, M., and K.-P. Möllmann. 2011. Infrared thermal imaging: Fundamentals, research and applications. Wiley-VCH. http://eu.wiley.com/WileyCDA/WileyTitle/productCd-3527641556.html.

Williams, T. 2009. Thermal imaging cameras: Characteristics and performance. CRC Press. https://www.crcpress.com/Thermal-Imaging-Cameras-Characteristics-and-Performance/Williams/p/book/9781420071856.

Wilson, R. C., S. J. Hook, P. Schneider, and S. G. Schladow. 2013. Skin and bulk temperature difference at Lake Tahoe: A case study on lake skin effect. J. Geophys. Res.: Atmos. **118:** 10332-10346. doi: 10.1002/Jgrd.50786.

Woolway, R. I., I. D. Jones, D. P. Hamilton, S. C. Maberly, K. Muraoka, J. S. Read, R. L. Smyth, and L. A. Winslow. 2015. Automated calculation of surface energy fluxes with high-frequency lake buoy data. Environ. Model. Softw. **70:** 191-198. doi: 10.1016/j.envsoft.2015.04.013.

Supplementary Materials for Chapter 4:

LSWT imagery: Aerial remote sensing and image registration

Abolfazl Irani Rahaghi[a], Ulrich Lemmin[a], Daniel Sage[b], David Andrew Barry[a]

[a] Ecological Engineering Laboratory (ECOL), Environmental Engineering Institute (IIE), Faculty of Architecture, Civil and Environmental Engineering (ENAC), Ecole Polytechnique Fédérale de Lausanne (EPFL), 1015 Lausanne, Switzerland

[b] Biomedical Imaging Group (BIG), School of Engineering (STI), Ecole Polytechnique Fédérale de Lausanne (EPFL), 1015 Lausanne, Switzerland

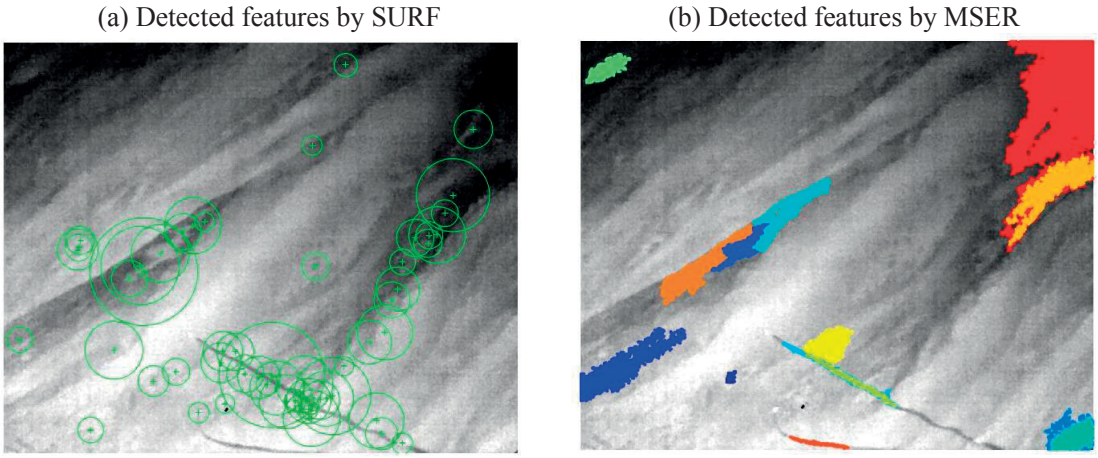

Fig. S4.1. Examples of features detected by: (a) the SURF method (blob objects), and (b) the MSER method (region objects). The SURF blob detector works by first blurring the image with the Gaussian filter at several scales, then downscaling the images, and finally detecting the blobs with a fixed size. In (a) the size of each detected feature is the radius of the drawn circle. The concept of the MSER detector in (b) is connected with thresholding. The algorithm checks for regions that remain stable over a certain number of thresholds provided as an input to this method.

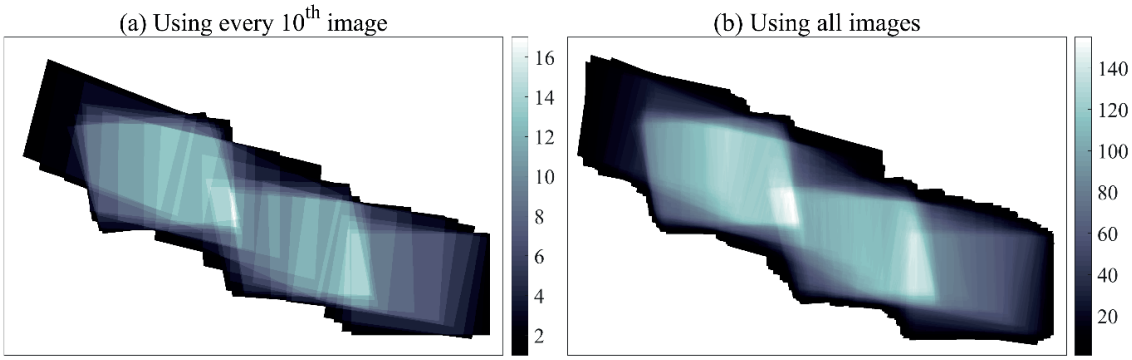

Fig. S4.2. Number of overlapped images at each pixel on the stitched image: (a) using every 10th image (29 frames), and (b) using all images (287 frames). The legend indicates the number of overlapped images, i.e., N_{OL}.

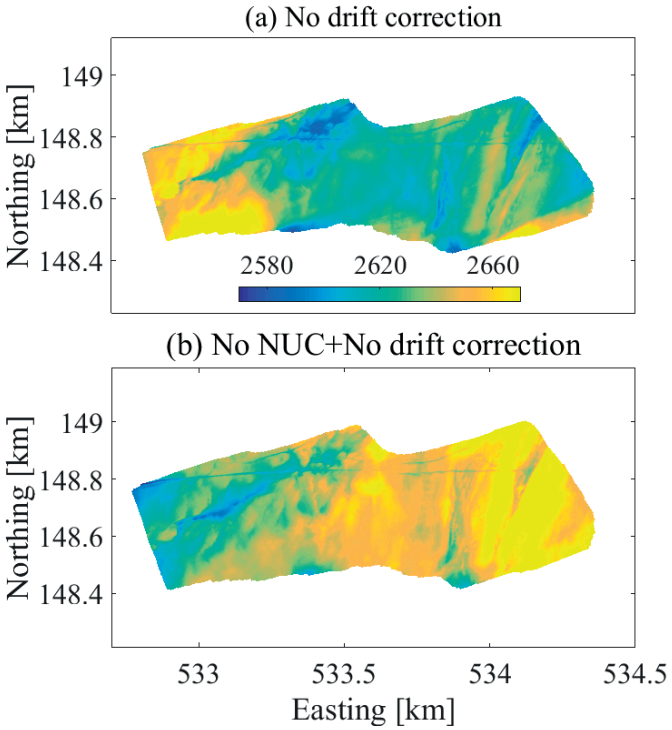

Fig. S4.3. Thermal maps in grey values by: (a) Neglecting the drift correction, and (b) Neglecting NUC and the drift correction. It shows that, as expected, the results in (b) are worse in than (a). For example, note the cold areas (artifacts) in the middle lower part of (b). The legend in (a) gives the grey value scale for (a) and (b).

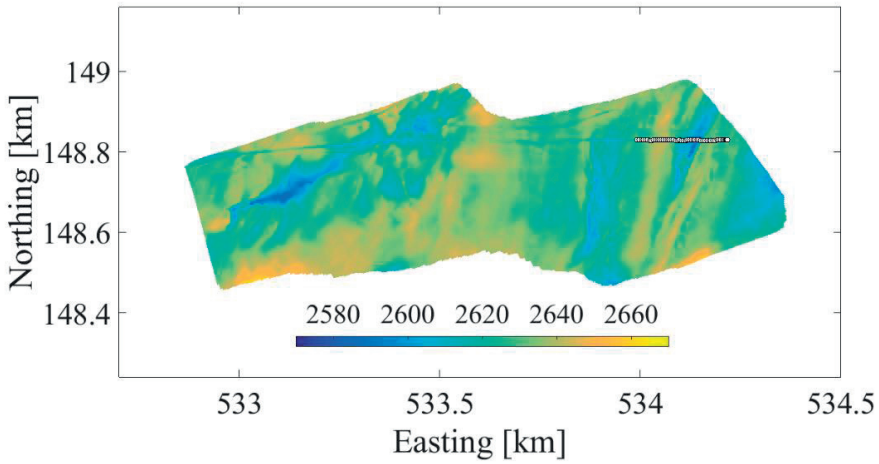

Fig. S4.4. The part of the stitched image that is used for radiometric calibration (50 frames) shown in white circles on the right side of the image. This part of the track covers the widest range of grey value (or LSWT) variability. Also, due to the streak-like structures, the differences between grey values above and below the selected points are minimal. The legend gives the grey value scale.

Chapter 5

Meso-scale surface water temperature heterogeneity effect on the surface cooling estimates of a large lake: Airborne remote sensing results from Lake Geneva

Abolfazl Irani Rahaghi[a], Ulrich Lemmin[a], David Andrew Barry[a]

[a] Ecological Engineering Laboratory (ECOL), Environmental Engineering Institute (IIE), Faculty of Architecture, Civil and Environmental Engineering (ENAC), Ecole Polytechnique Fédérale de Lausanne (EPFL), 1015 Lausanne, Switzerland

To be submitted to *Journal of Geophysical Research: Oceans*

Abstract

The effect of spatial heterogeneity of Lake Surface Water Temperature (LSWT) at meso-scale, O(1 m) on the surface cooling estimation at sub-pixel satellite area O(1 km^2) was investigated using an airborne platform. The cold season data did not show significant LSWT heterogeneity, and hence surface cooling spatial variability. However, the spring and summer results, based on three selected daytime meso-scale maps, indicated a LSWT contrast of > 2°C and > 3.5°C, corresponding to the spatial surface cooling range of > 20 Wm^{-2} and > 40 Wm^{-2}, respectively. Due to the nonlinear relationship between turbulent surface heat fluxes and LSWT, the negatively skewed LSWT distributions resulted in both negatively and positively skewed surface cooling patterns, respectively, under very stable or predominantly unstable Atmospheric Boundary Layer (ABL) conditions, and predominantly stable ABL conditions. Implementing a mean spatial filter, the effect of area-averaged LSWT on the surface cooling estimation of a typical satellite pixel was assessed. The effect of the averaging filter size on the mean spatial surface cooling values was negligible, except for predominantly stable ABL conditions when a reduction of ~3.5 Wm^{-2} from high O(1 m) to low O(1 km) pixel resolution was obtained. The results revealed that the bias in meteorological condition sampling, particularly wind speed, can affect both the mean and the range of spatial surface cooling. The error in the air temperature may also alter the surface cooling distribution from negatively skewed to positively skewed, and hence affect the area-averaged estimates.

Keywords: Lake surface water temperature, surface cooling, thermal imagery, remote sensing, Lake Geneva, atmospheric boundary layer stability

5.1. Introduction

Lake Surface Water Temperature (LSWT) is one of the main parameters for the estimation of surface cooling in lakes. Long-wave radiation and the surface turbulent heat fluxes are the major cooling components. Surface cooling estimates may be sensitive to space and time averaging of the input variables including LSWT (Gulev 1997; Hughes et al. 2012). A small (~ 1°C) variation in the LSWT, particularly under near-neutral Atmospheric Boundary Layer (ABL) stability conditions, may result in a significant modification of surface cooling of a water body (Mahrt and Khelif 2010; Brodeau et al. 2017; Mahrt and Hristov 2017).

To estimate the surface heat fluxes over water bodies, in situ point measurements (e.g., Assouline et al. 2008; Nordbo et al. 2011; Spence et al. 2011; Van Emmerik et al. 2013; Zhang and Liu 2013) or satellite surface temperature data (e.g., Lofgren and Zhu 2000; Alcantara et al. 2010; Moukomla and Blanken 2017; Rahaghi et al. 2018a) are most often used. Satellite data can depict large-scale thermal patterns, but not meso- or small-scale processes (hereinafter, meso-scale refers to horizontal structures ranging from O(1 m) to O(100 m)). Satellite thermal images are representative for a surface area with typical pixel resolution of O(1 km). Thus far, however, little attention has been given to LSWT spatial heterogeneity at sub-pixel satellite resolution. Thermography at the meso-scale level allows resolution of lake surface heterogeneity at the satellite sub-pixel scale. Past studies have examined meso-scale surface temperature variability using airborne systems. Due to the challenges intrinsic to the thermal image registration over water, which was discussed in chapter 4 (Rahaghi et al. 2018c; Unpublished work), or instrumental restrictions, they only reported along-track point (Mahrt and Khelif 2010) or area-averaged (Castro et al. 2017) measurements. The results indicated a skin temperature variation of > 1 °C within ~1 km distance, which can affect the area-averaged surface heat flux calculation. Other studies used infrared thermography to investigate small-scale (less than 1 m pixel resolution) surface water and heat flux horizontal variabilities (Garbe et al. 2003; 2004; Veron et al. 2008; Handler and Smith 2011; Schnieders et al. 2013).

Due to LSWT heterogeneity, air-water temperature differences and, consequently, the stability conditions, can be spatially variable at meso-scales. Turbulent heat fluxes are found to be more sensitive to skin temperature under near-neutral ABL stability conditions (Mahrt and Khelif 2010; Mahrt and Hristov 2017). The turbulent cooling response to the LSWT distribution also incorporates the spatial heterogeneity of the surface stress. Therefore, bulk algorithms that take

into account the stability are preferred for this study. The surface shear stress and turbulent heat flux coefficients are coupled by the Monin-Obukhov similarity theory (Monin and Obukhov 1954) with some parameterizations (e.g., Zeng et al. 1998; Fairall et al. 2003; Woolway et al. 2015), or through bulk Richardson number concepts (Mahrt and Khelif 2010; Mahrt and Hristov 2017).

In the present case study, we assess the effect of LSWT meso-scale variation on the surface cooling distribution and its area-averaged estimate without resolving the spatial variability of other meteorological parameters. A measurement system, including a balloon launched airborne platform for thermography and a catamaran for in situ ground truthing, was used for LSWT mapping and calibration. Several field campaigns were carried out over Lake Geneva, the largest lake in Western Europe (see section 5.2.2.). Four daytime (afternoon) missions covering different ABL stability conditions were selected. The surface cooling estimation is based on a 2-point calibrated model using large-scale data described in chapter 2 (Rahaghi et al. 2018b; Unpublished work). However, we investigated the effect of turbulent model parameterization on the surface cooling distribution by applying the commonly used model of Zeng et al. (1998). The uncertainty associated with the primary meteorological parameters was also quantified by a sensitivity analysis.

5.2. Materials and methods

5.2.1. Lake surface cooling formulas

The cooling from a lake surface (Q_c) contains a long-wave radiative term (Q_{br}) and two turbulent components, latent (evaporation, Q_{ev}) and sensible (convection, Q_{co}):

$$Q_c = Q_{br} + Q_{ev} + Q_{co} \tag{5.1}$$

All the heat flux terms were assumed positive upwards (out of the lake).

Back radiation, Q_{br}, was modeled with the Stefan-Boltzmann law:

$$Q_{br} = \varepsilon_w \sigma \left(T_w + 273.15\right)^4 \tag{5.2}$$

where σ and T_w are Stefan-Boltzmann constant (5.67×10^{-8} $Wm^{-2}K^{-4}$) and LSWT (°C), respectively. Following other studies in Switzerland (Livingstone and Imboden 1989; Fink et al. 2014), we used a constant water surface emissivity, ε_w, of 0.972.

Based on satellite LSWT data and meteorological parameters from a numerical model at two locations over Lake Geneva, the Monin-Obukhov similarity theory (Monin and Obukhov 1954) was found to provide the best estimates of turbulent heat fluxes over this lake (see chapter 2) (Rahaghi et al. 2018b; Unpublished work). We assume that the obtained model is also valid for the meso-scale short-term data presented here (section 5.2.2.). A set of coupled formulas is solved iteratively to find the drag, humidity and temperature bulk transfer coefficients, i.e., C_d, C_e and C_h, respectively, in order to calculate the turbulent surface heat fluxes:

$$Q_{ev} = C_e \rho_z L_v u_z \left(q_s - q_z\right) = \rho_z L_v u_* q_* \tag{5.3}$$

$$Q_{co} = \rho_z C_{p,a} C_h u_z \left(T_w - T_z\right) = \rho_z C_{p,a} u_* T_* \tag{5.4}$$

$$\tau = C_d \rho_z u_z^2 = \rho_z u_*^2 \tag{5.5}$$

where ρ, L_v, q, u, $C_{p,a}$, T and τ are air density [kgm^{-3}], latent heat of vaporization [Jkg^{-1}], specific humidity [$kgkg^{-1}$ dry air], wind speed [ms^{-1}], specific heat capacity of air at constant pressure [$Jkg^{-1}K^{-1}$], temperature [°C] and surface shear stress [Nm^{-2}], respectively. The subscript z denotes the measurement height [m] of the corresponding meteorological parameter, and the symbol q_s is the saturated specific humidity [$kgkg^{-1}$ dry air]. In this algorithm, a set of differential equations, normalized by the scaling parameters (indicated by * in Eqs. 5.3-5.5), and as a function of the ABL stability parameter (ζ) are defined and they are solved iteratively to resolve the ABL. The details of these equations, their solution procedure and their calibration can be found elsewhere (Zeng et al. 1998; Woolway et al. 2015; Rahaghi et al. 2018b). The key coupling parameter, ζ, is defined as follows:

$$\zeta = zL_w^{-1} = \left[z\kappa g \left(Q_{co} / C_{p,a} + 0.61 \left(T_z + 273.15 \right) Q_{ev} / L_v \right) \right] \Big/ \rho_z u_*^3 T_v \tag{5.6}$$

where L_w is the Monin-Obukhov length [m], and κ and T_v are, respectively, the Von Karman constant (0.41) and virtual air temperature [K], which is given by:

$$T_v = \left(T_z + 273.15\right)\left(1 + 0.61 q_z\right) \tag{5.7}$$

The relationship between LSWT (T_w) and the surface cooling terms, Q_{br} (Eq. 5.2), Q_{ev} (Eq. 5.3) and Q_{co} (Eq. 5.4), is by definition non-linear, in particular, the turbulent heat fluxes. Therefore, the response of surface cooling formulas to the LSWT distribution is expected to be non-linear. This might affect area-averaged surface cooling estimations.

5.2.2. Data set and study site

A measurement platform comprising (i) an airborne balloon for thermal imagery (called BLIMP), and (ii) an autonomous catamaran (called ZiviCat) for in situ measurements are used to resolve the LSWT at meso-scales.

The BLIMP was attached to a small balloon tethered to a winch on a boat, from which its height (typically between 300 m to 800 m) is controlled. It carried a thermal imagery package (Liardon and Barry 2017) suspended beneath it. The package includes a *FLIR Tau2 LWIR* camera (640 × 512 pixel resolution, 14-bit digital output) and a *RGB Raspberry Pi* camera (used for visual inspection and verification), as well as other equipment for its position (GPS), orientation, tilt angles (Inertial Measurement Unit; IMU), height, and communication with the boat. Unlike other aerial systems such as aircraft or drones, the BLIMP system is less affected by vibration and tilting, as we confirmed by testing with a custom made autonomous drone (Liardon et al. 2017).

Simultaneous ground-truthing of the BLIMP data was achieved using the ZiviCat, an autonomously operating catamaran. It can measure in situ near-surface (down to 1.5 m) water temperatures using 10 RBRsolo thermistors (RBR, last accessed 12 January 2018), as well as lake current profiles, radiative heat flux, wind speed, air temperature and relative humidity. However, some of these sensors were not available during some of the field measurements. The ZiviCat moves at a speed of ~1 ms^{-1}. The craft is equipped with other instruments and equipment for the position (GPS), stability (IMU), data recording, and communication, which allows for real-time data control, correction and analysis on the boat that accompanies the ZiviCat and on which the winch for the BLIMP is mounted. Details of the systems and sensors are presented in Barry et al. (2018; Unpublished work). The thermal images were then

registered and calibrated implementing an image processing procedure to create the final meso-scale temperature maps (see chapter 4) (Rahaghi et al. 2018c; Unpublished work).

This study was carried out over Lake Geneva (Local name: *Lac Léman*; Fig. 5.1). Located between Switzerland and France, it is a large, deep, crescent-shaped (Fig. 5.1) perialpine lake with a mean surface altitude of 372 m. It is approximately 70-km long, with a maximum width of 14 km, a surface area of 582 km², a volume of 89 km³, and a maximum depth of 309 m.

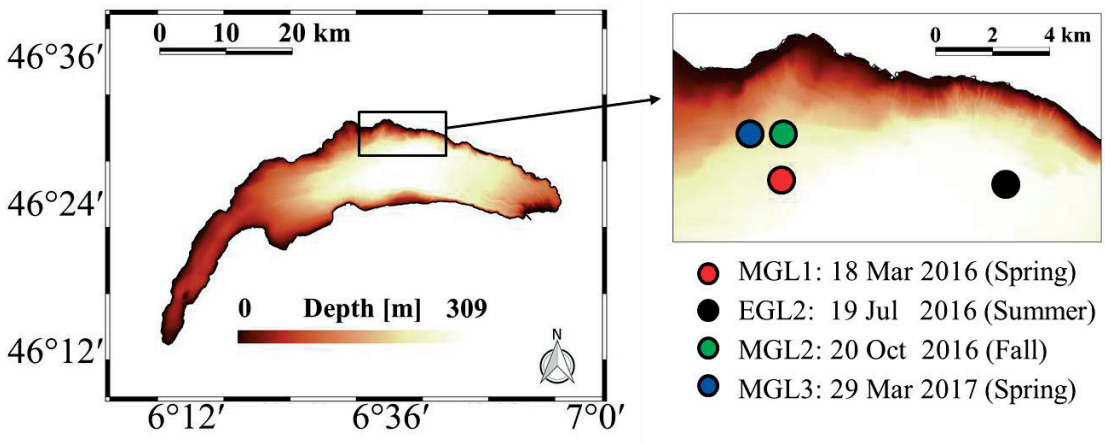

Fig. 5.1. Location and bathymetry (see the legend in the left panel) of Lake Geneva. The inset shows the area of the selected missions. The dates of the field missions are indicated in the legend of right panel.

Four field measurement data sets (Fig. 5.1 and Table 5.1) were selected for this study. Due to legal restrictions in Switzerland, the field measurements were performed during the daytime and over predefined areas on the lake. To avoid the effect of coastal mixing on the temporal and spatial patterns of LSWT, we present the results for deep (>200 m depth) areas sufficiently far from the shores. All the measurements were taken under weak wind conditions (less than ~2 ms^{-1}) when LSWT spatial patterns are more likely to occur, and data are less contaminated by surface waves and BLIMP lateral movements. Each mission usually takes ~5-6 h, but to minimize the effect of LSWT temporal variation on the presented results, a ~25-30 min segment of each data set was used, except for MGL2. Since there were insufficient features for image registration on that date, only ~7 min of the data are used. This is due to very small temporal and spatial variations of temperature (discussed in section 5.3.1). Unlike the other three missions, where we used the ZiviCat continuous temperature data for the calibration of the

BLIMP registered image (explained in chapter 4) (Rahaghi et al. 2018c; Unpublished work), the minimum and maximum in situ temperature values are used for the calibration of the MGL2 thermal images. As will be discussed in section 5.3.1, this does not affect the findings of this study.

Meteorological data, i.e., wind speed, relative humidity and air temperature, are also required for the surface cooling estimation (Eqs. 5.3-5.5). The ZiviCat platform was designed and equipped to measure along-track data, but not spatial meteorological patterns. We did not find a significant correlation between the near-surface temperatures and the measured meteorological data. Furthermore, the standard deviation of the measured data during the relatively short period of the selected segments were on average small, except for air temperature during the MGL3 mission with intense springtime radiative forcing (Table 5.1). Therefore, the average values of the meteorological data were used for the heat flux calculations. Due to technical issues, certain data were missing during MGL1 and MGL3 missions. In those cases, we used the assimilated results of a numerical weather model (COSMO, last accessed 25 February 2018) for the wind speed (at 10 m) and relative humidity (at 2 m) for the MGL1 and MGL3 missions, and the air temperature (at 2 m) of MGL1 (Table 5.1). We studied the effect of errors in meteorological sampling by performing a sensitivity analysis (section 5.3.4.). For a better comparison, the averaged values measured by ZiviCat (at ~1.8 m) were converted into the wind speed at 10 m, U_{10} (Table 5.1) assuming a power-low profile (Hsu et al. 1994):

$$U_{10} = u_z \left(10/z\right)^{0.11} \tag{5.7}$$

Table 5.1. Time, number of frames, pixel resolution and meteorological parameters for the selected field experiments in this study (see Fig. 5.1 for locations and dates). The standard deviations of the ZiviCat meteorological measurements are indicated in parenthesis.

Field campaign	Time	Number of frames	Pixel resolution [m]	U_{10} [ms^{-1}]	T_a [°C]	ϕ_{rel} [%]
MGL1	~15h30	287	0.8	0.6	9.8	60.1
EGL2	~17h30	496	0.8	1.3 (0.2)	25.2 (0.27)	60.1 (3.1)
MGL2	~14h00	81	2.7	2 (0.5)	12.3 (0.15)	50.1 (1.2)
MGL3	~13h40	315	1.4	2	13.5 (0.96)	66.7

5.3. Results and discussion

5.3.1. Spatial heterogeneity of lake surface water temperature at meso-scales

The registered thermal images for the selected missions are presented in Fig. 5.2. It shows various cold-warm patches and streak-like structures over the lake. These meso-scale features are not discernible in the satellite images. The number of frames used to create each composite map is given in Table 5.1. The comparison of the BLIMP irradiance values and the corresponding ZiviCat near-surface temperatures shows a correlation coefficient of > 89% and a Root mean Square Difference (RMSD) of < 0.17 °C (Fig. S5.1; Supporting Information (SI)).

The corresponding Probability Distribution Function (PDF) for each LSWT map is also plotted (bottom-left corner curves in Fig. 5.2). It confirms that the LSWT spatial variability within a typical satellite pixel can be significant. The spatial variability is more pronounced during the MGL1 (Fig. 5.2a) and EGL2 (Fig. 5.2b) missions with an LSWT spatial range of > 2 and > 3.5°C, respectively, over an area covering less than 1 km^2. MGL2 is a representative case for the cold season (October to February), when the spatial variability of LSWT at meso-scales is negligible (< 0.1°C). It should be noted that the measurement platform was continuously moving to cover a broader area. The observed LSWT patchiness over the measured tracks (not shown here) was spatially and temporally variable. For example, the springtime LSWT spatial

heterogeneity was found to be insignificant before 13h00 compared to the late afternoon data. In this study, we only present part of the data with significant LSWT heterogeneity.

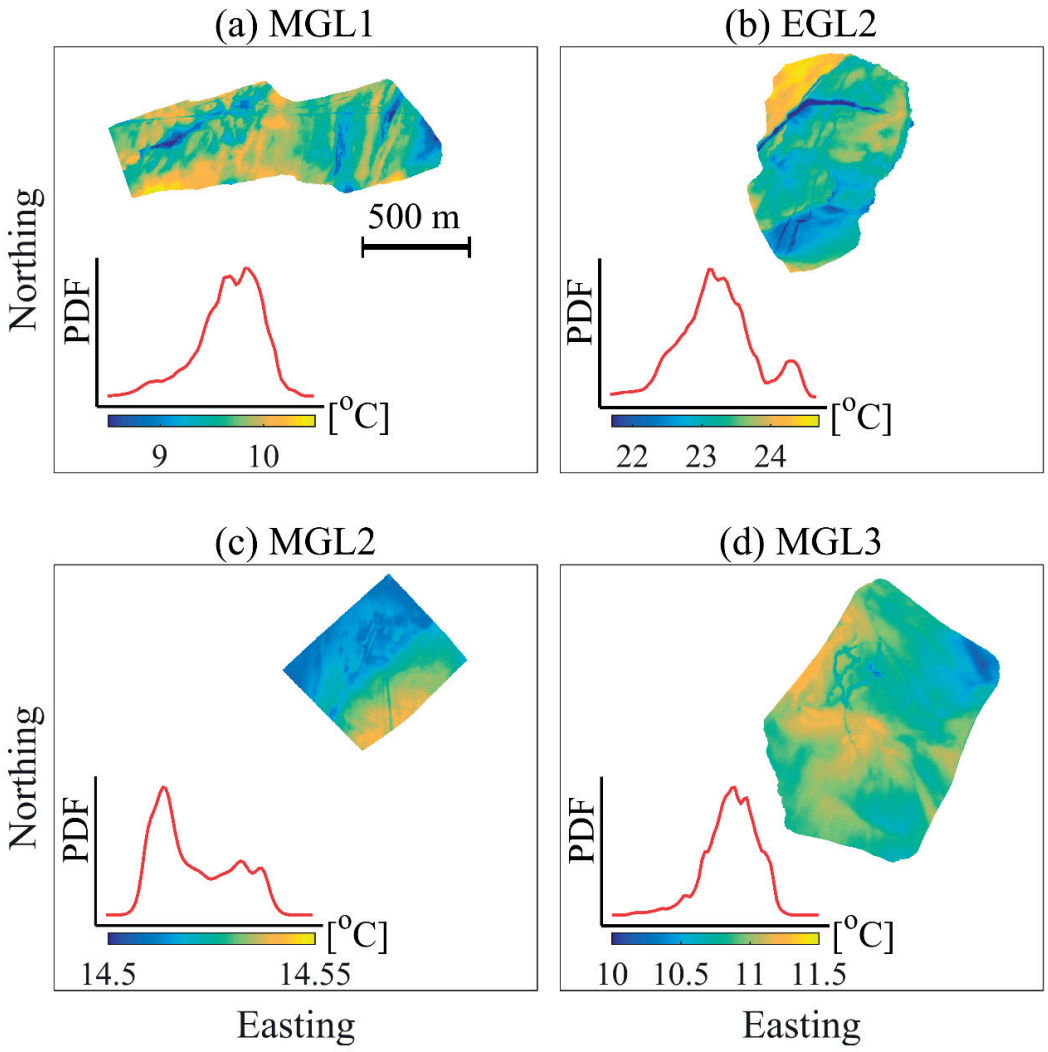

Fig. 5.2. Meso-scale lake surface water temperature patterns (top-middle maps in each panel) and their corresponding probability distribution function (PDF) (bottom-left corner of each panel) for different field missions: (a) MGL1, (b) EGL2, (c) MGL2, and (d) MGL3. For the location and the date of each panel see Fig. 5.1. Note that the temperature range of the legends and PDF plots is different in each panel, and all panels cover an approximately 2 km × 2 km area (~4 typical satellite pixels).

Except for MGL2 (Fig. 5.2c), when the spatial variability was negligible, the remaining selected LSWT patterns show a negatively skewed distribution (skewness values of -0.8, -0.4 and -0.7 for MGL1, EGL2 and MGL3, respectively). Determining the reason for such skewness is beyond the scope of this paper. However, previous studies have examined the surface temperature distribution at small-scales in the field (Veron et al. 2008) or under controlled laboratory conditions (Garbe et al. 2004; Handler and Smith 2011). Handler and Smith (2011) attributed the negative skewness of surface water temperature distribution to the elongated cold bands over the surface. Even though their measurements were taken under surface wind speeds of > 2 ms^{-1}, such cold bands were also observed in our LSWT patterns, as is particularly evident in Fig. 5.2a.

5.3.2. Meso-scale surface cooling patterns and distributions

We used Eqs. 5.1-5.5, the obtained LSWT spatial maps (Fig. 5.2) and the area-averaged meteorological data (Table 5.1) to compute the lake surface cooling (Q_c) patterns. Figure 5.3 shows the surface cooling maps as well as their corresponding distribution. Although Q_c responses preserve the larger-scale structures, the distributions (bottom-left corner plots in Fig. 5.3) are different from the LSWT PDF curves (Fig. 5.2) for some missions. This difference is more evident for the missions with higher LSWT contrasts, i.e., MGL1 and EGL2, and at the tails of the distributions. The results also demonstrate a positive skewness (value of 1.5) for the Q_c distribution of EGL2 (Fig. 5.3b) that is different from the responses to LSWT heterogeneity of MGL1 and MGL3. The spatial variation of Q_c of MGL2 (Fig. 5.3c) is negligible and reflects the small contrast of LSWT (Fig. 5.2c). The higher the LSWT contrast is, the larger the surface cooling spatial variation is (Fig. 5.3).

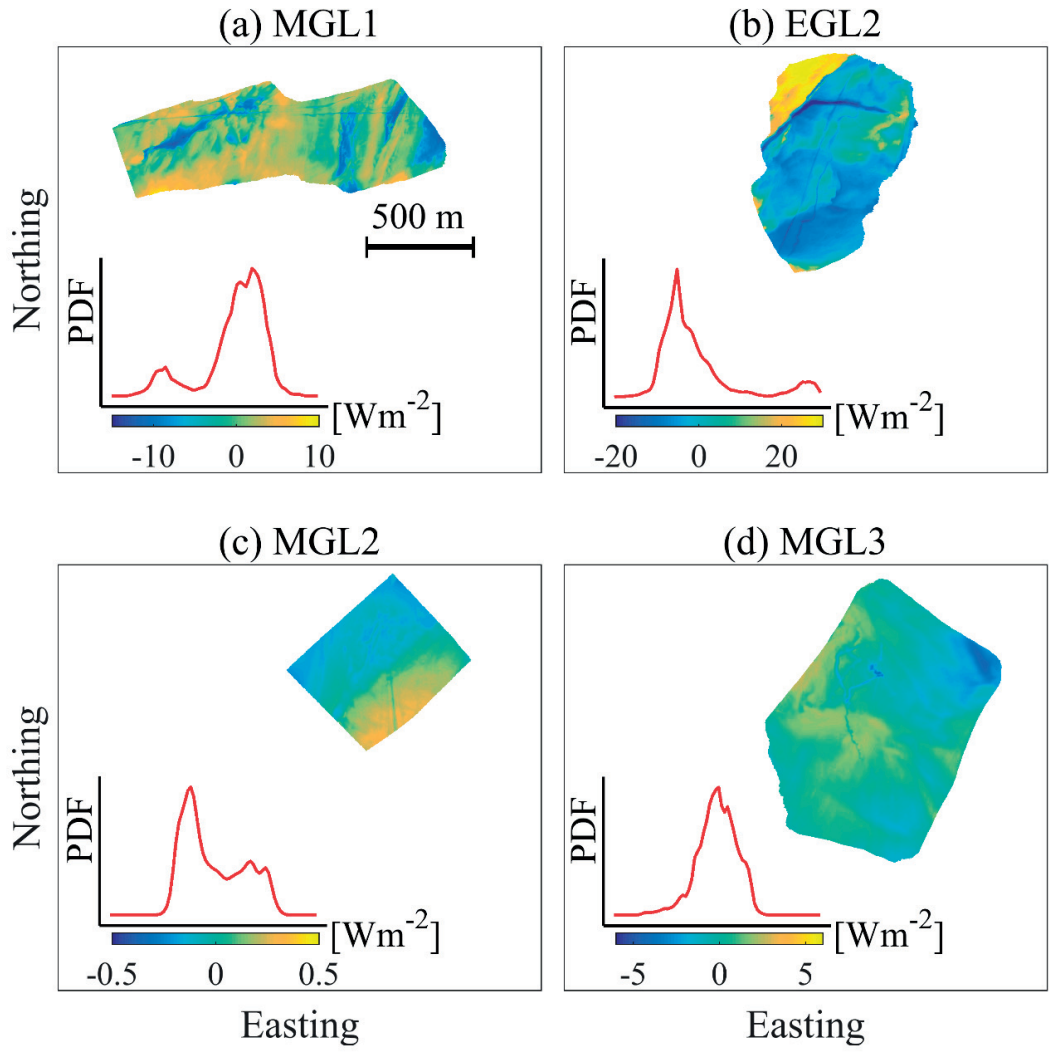

Fig. 5.3. Same as Fig. 5.2, but for lake surface cooling anomaly patterns.

The difference of the Q_c distributions as compared with the LSWT distributions is mainly due to the non-linearity in the turbulent heat flux formulas. More specifically, the Monin-Obukhov similarity theory depends on ABL stability (ζ) conditions, since ζ is coupled with the surface turbulent heat fluxes and surface momentum flux. The level of this non-linearity is higher under near-neutral conditions, i.e., small air-water temperature differences, and weak surface stress (Mahrt and Khelif 2010; Mahrt and Hristov 2017). Therefore, investigating the stability condition can be useful to interpret the obtained surface cooling distributions.

The ABL stability conditions for the selected missions are shown in Fig. 5.4. The atmospheric thermal boundary layer is defined as very unstable ($\zeta < -0.465$), unstable ($-0.465 \leq \zeta < 0$), stable ($0 \leq \zeta \leq 1$), or very stable ($0 < \zeta$) (Zeng et al. 1998; Woolway et al. 2015). The results indicate that the ABL is very unstable and very stable for the MGL2 (Fig. 5.4c) and MGL3 (Fig. 5.4d) missions, respectively, over the entire studied regions. The major part of the MGL1 thermal map (Fig. 5.4a) was very stable followed by some very stable and near-neutral regions corresponding to the cold patches (Fig. 5.2a). The ABL over EGL2 (Fig. 5.4b) was found to be mainly very stable, but very unstable and in a near-neutral condition over the warmer parts (Fig. 5.2b). Hereinafter, we call the MGL1 and EGL2 missions "predominantly unstable" and "predominantly stable", respectively. Comparison of the results in Figs. 5.2-5.4 indicates that the range of the surface cooling variation for the same LSWT range is higher under unstable than stable ABL conditions. For example, comparison of Figs. 5.2b and 5.4b in the very stable areas (Fig. 5.4b) shows a larger relative contrast in the former than the latter. The tails of the PDF curves in Figs. 5.3a and b also show higher PDF values for negative anomalies (corresponding to very stable conditions). A clear example is the second smaller mode formed in the left part of PDF plot for MGL1 (Fig. 5.3a) that is non-existent in the corresponding LSWT distribution (PDF plot in Fig. 5.2a). Furthermore, the spatial variability of LSWT, and consequently surface cooling, is much higher during the MGL1 field mission (Fig. 5.3a) than during MGL2 (Fig. 5.3c), even though both are on average very unstable. The net heat flux (including solar short-wave and atmospheric long-wave radiation) was positive for MGL1, whereas it was negative during the MGL2 mission (results not shown here). The net heating under the weak wind conditions resulted in a strong stratification during the MGL1 mission (temperature difference of up to > 2.5 °C in the 1.5 m thick surface layer; not shown here) which can enhance the water resistance to thermal mixing. This comparison suggests that the background stratification and the net surface heat flux are also important for the LSWT, and consequently surface cooling spatial heterogeneity under very unstable conditions.

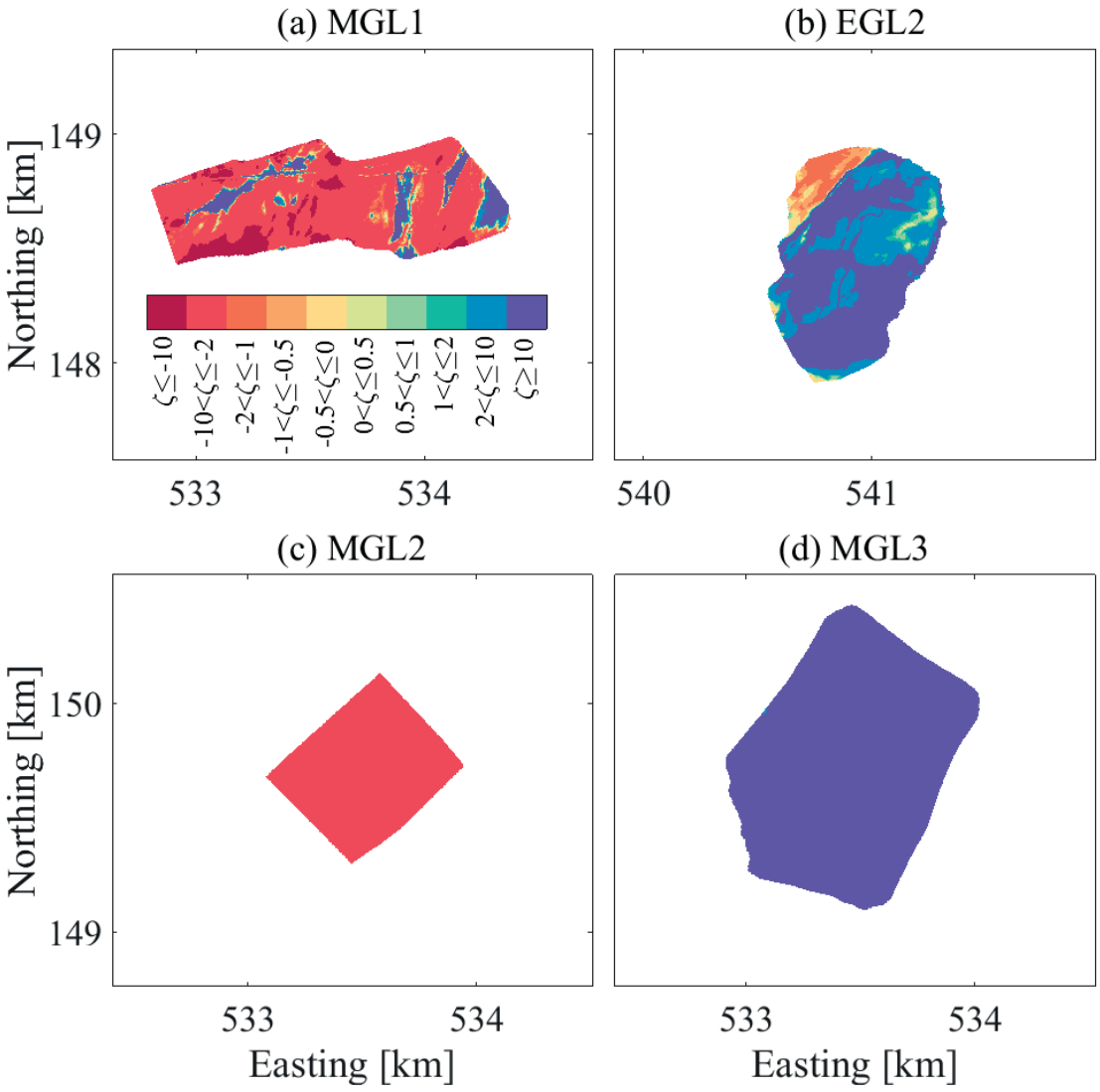

Fig. 5.4. Atmospheric boundary layer stability patterns for different field missions: (a) MGL1 (predominantly unstable), (b) EGL2 (predominantly stable), (c) MGL2 (very unstable), and (d) MGL3 (very stable). For the location and the date of each panel see Fig. 5.1. Note that all panels cover an approximately 1.8 km × 1.8 km area (less than four typical satellite pixels). The Swiss-coordinate system with km length-based units (CH1903) is used. Colors are identified in the legend in panel (a).

Figure 5.5 shows the variation of different surface cooling components, Q_{br}, Q_{ev} and Q_{co}, as a function of LSWT (T_w) for the MGL1, EGL2 and MGL3 missions (we do not show the results for MGL2, since the horizontal heterogeneity of T_w and Q_c is negligible). The results

demonstrate that the long-wave back radiation (Q_{br}; blue lines in Fig. 5.5) changes linearly over the measured temperature ranges, and is the controlling component during the MGL3 mission (Fig. 5.5c) with a very stable ABL over the entire area (Fig. 5.4d). The convective cooling (Q_{co}; green lines in Fig. 5.5) shows the least contribution among surface cooling terms. Its effect was only comparable to the other terms under very unstable conditions at the right end of Fig. 5.5a.

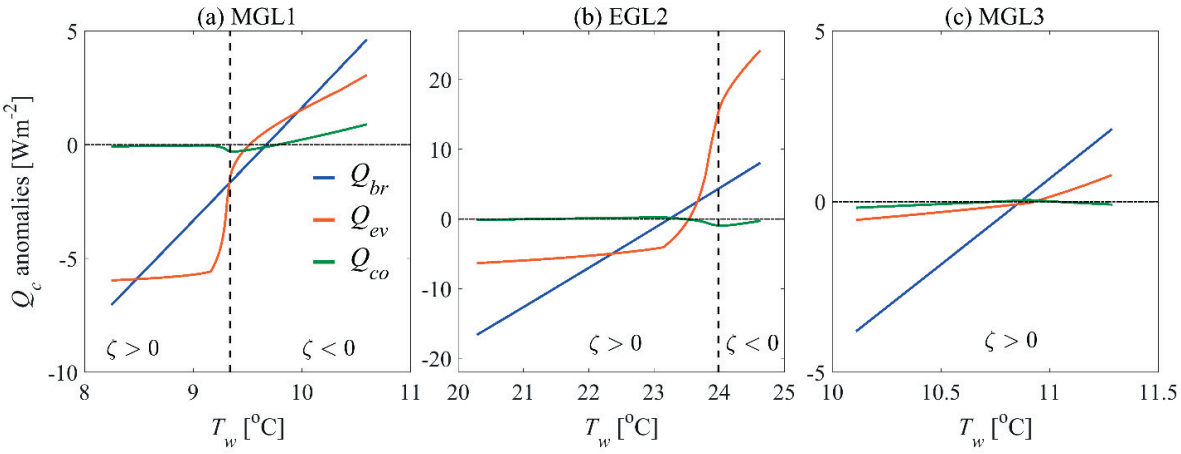

Fig. 5.5. Anomaly variation (with respect to the mean spatial surface cooling) of back radiation (Q_{br}), latent (Q_{ev}) and sensible (Q_{co}) heat fluxes as a function of lake surface water temperature, T_w, for different field missions: (a) MGL1 (predominantly unstable), (b) EGL2 (predominantly stable), and (c) MGL3 (very stable). The vertical dashed lines in (a) and (b) indicate the neutral condition, $\zeta = 0$. Colors are identified in the legend in panel (a).

A substantial variation of evaporative cooling (Q_{ev}) was found during the missions under near-neutral conditions (brown lines in Fig. 5.5a and b). The results indicate that the Q_{ev} variation as a function of LSWT can be divided into three sections: (i) a nearly flat section (left part of the curves in the very stable zone with negative Q_c anomalies), (ii) a substantial non-linear change from stable to unstable conditions (close to vertical dashed lines in the near-neutral zone), and (iii) a linear section with a positive slope (right part of the curves in the very unstable zone with positive Q_c anomalies). Part (i) explains the negative modes in the Q_c anomaly distributions (left part of the PDF plots in Fig. 5.3a and b). Since part (i) in Fig. 5.5b covers a large portion of the LSWT distribution (see Figs. 5.2b and 5.5b together), the corresponding negative mode in the PDF plot of the Q_c anomalies (Fig. 5.3b) is consequently large. This illustrates the positive skewness obtained for the Q_c anomaly distribution in Fig. 5.3b as compared to the negatively skewed LSWT pattern (Fig. 5.2b). In contrast, part (i) in Fig. 5.5a corresponds to a relatively

small segment of the LSWT pattern (see Figs. 5.2a and 5.5a together). As a result, the negative mode is relatively small, and therefore has a negligible impact on the Q_c response to the LSWT distribution, i.e., both the LSWT and Q_c anomalies show a negative skewness. The results also indicate that the evaporative cooling increases substantially from stable to unstable ABL conditions (Figs. 5.5a and b). Due to the higher wind speed during the EGL2 mission compared to MGL1, this variation is higher for EGL2.

5.3.3. Effect of area-averaged LSWT on the surface cooling estimates

Our results indicated that the sub-pixel satellite LSWT heterogeneity can be significant, in particular under weak wind and near-neutral ABL stability conditions (Fig. 5.2). It was also shown that the surface cooling response to the LSWT under such conditions is non-linear (Figs. 5.3 and 5.5). It suggests that surface cooling, and consequently the net surface heat flux, at satellite pixel resolution may be sensitive to the spatial averaging of the sub-pixel satellite LSWT variation, as has been shown for large-scales and over open waters (Gulev 1997; Mahrt and Khelif 2010; Mahrt et al. 2012). Here, we used the selected meso-scale LSWT maps obtained with our airborne remote sensing platform (Fig. 5.2) together with the calibrated bulk formulas over Lake Geneva (Eqs. 5.1-5.5) to study this effect.

A mean spatial filter with variable size was implemented on the LSWT patterns to produce thermal maps with different resolutions. In this operation, each pixel value is replaced with the mean (average) value of the predefined neighborhood pixels, including itself. We used the LSWT maps at their initial resolution (given in Table 5.1) to find the filtered patterns at 20, 100 and 500 m resolutions. Due to the negligible spatial variability of MGL2, the operation was not performed for this case. Figure 5.6 shows the resulting distributions of the LSWT anomalies (with respect to the mean spatial value at the initial resolution) with different spatial resolutions. The spatial filter preserves the mean spatial LSWT value in all missions for various filter sizes. The results indicate that the range of LSWT spatial variability decreases with increasing pixel resolution. However, the difference between the distributions with O(1 m) and 20 m resolutions was found to be negligible. It indicates that the surface temperature features with an O(10 m) horizontal scale were dominant for the selected missions. By increasing the pixel resolution, the reduction of the 0.5-99.5 percentiles ranges (solid lines in Fig. 5.6; indicative for the total range) is more pronounced than the interquartile ranges (filled rectangles in Fig. 5.6), and is mainly attributed to the fading of the cold features.

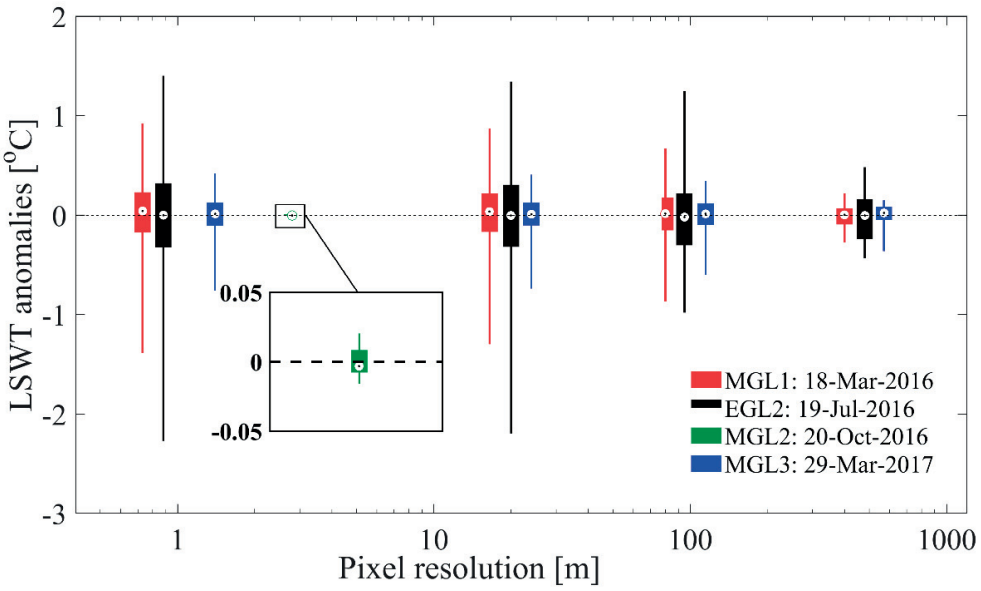

Fig. 5.6. Box plots of lake surface water temperature (LSWT), T_w, anomaly distributions as a function of pixel resolution for different field missions. The results are presented for O(1 m) (given in Table 5.1), 20 m, 100 m and 500 m pixel resolutions. The white circles, the filled rectangles and the solid lines indicate the median, interquartile range (25 to 75 percentiles) and the 0.5 to 99.5 percentiles (indicative for the total range), respectively. Note the logarithmic scale on the horizontal axis.

From the spatially filtered LSWT maps, the surface cooling (Q_c) maps at different spatial resolutions were estimated using the constant meteorological parameters given in Table 5.1. Figure 5.7 shows the calculated distributions of the Q_c anomalies for the selected missions. The surface cooling meso-scale variability is higher during the EGL2 mission with an evident positive skewness that was discussed above. Our results, similar to Mahrt and Hristov (2017), demonstrate that under near-neutral conditions (MGL1 and EGL2), the LSWT heterogeneity is more influenced by the stably stratified parts of the ABL while the turbulent heat flux spatial variability is dominated by the unstable parts of the ABL.

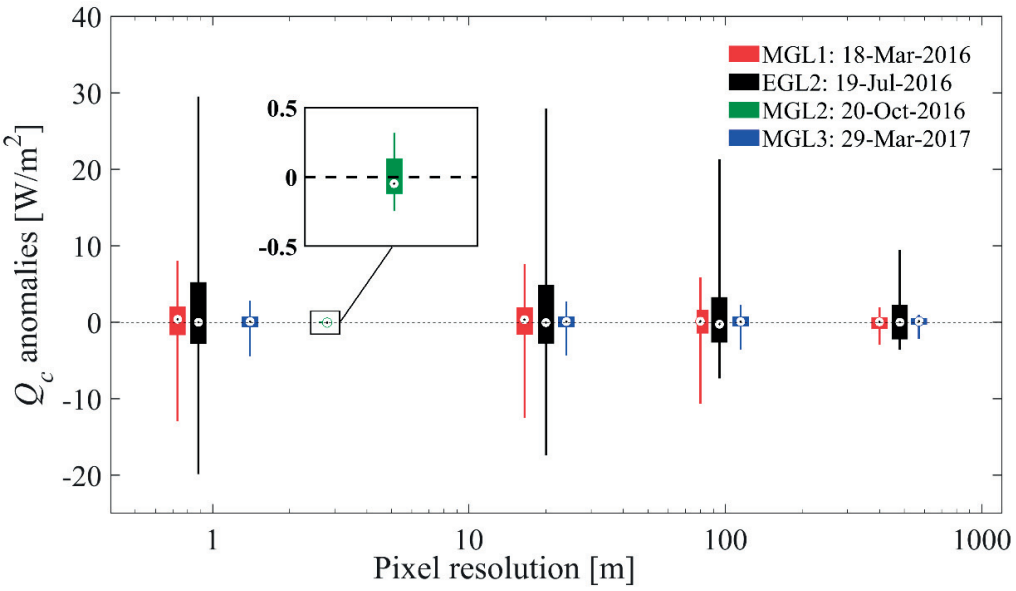

Fig. 5.7. Same as Fig. 5.6, but for surface cooling, Q_c, anomaly distributions.

The area-averaged surface cooling (Q_c) values were also calculated for various pixel resolutions and for the different field missions. The results indicate that the spatial mean Q_c for the MGL1 mission (predominantly unstable) increases by ~0.5 Wm^{-2} from meso-scale O(1 m) to large-scale O(1 km) resolution, while a decrease of ~3.5 Wm^{-2} for the same resolution range was found for EGL2 (predominantly stable). The spatial mean Q_c value also decreased, but negligibly (~0.05 Wm^{-2}) for the very stable (MGL3) mission when comparing heterogeneous with homogenous patterns. These findings demonstrate that in the surface heat flux estimation of water bodies, the errors associated with the area-averaged LSWT are expected to be higher under near-neutral conditions (Gutowski et al. 1998; Mahrt and Hristov 2017), a condition that is not common on an annual basis over lakes (Verburg and Antenucci 2010; Woolway et al. 2017; Rahaghi et al. 2018a). In order to investigate the effect of the obtained biases of surface cooling induced by LSWT meso-scale heterogeneity on the overall heat budget of a water body, especially in a long-term analysis, a more extensive data base is required.

5.3.4. Effect of biases in the meteorological parameters on the surface cooling spatial distribution

The meteorological parameters, wind speed, air temperature and relative humidity, were assumed to be spatially constant in this study. Our direct along-track measurements taken with the ZiviCat platform indicated that the spatial variability of some parameters, e.g., air temperature during the MGL3 mission (Table 5.1), can be significant even over a relatively short measurement time. Meso-scale surface maps of the meteorological parameters are required for a detailed analysis. To our knowledge, these data do not exist over Lake Geneva or other comparable lakes.

To quantify the uncertainty associated with the errors in meteorological parameter sampling, we performed a sensitivity analysis by changing each of the meteorological parameters within a reasonable range while keeping the other two constant (values in Table 5.1). The MGL1 data (predominantly unstable) was used. The wind speed (U_{10}) values were changed from 0 to 3 ms^{-1}, to cover the weak wind conditions over Lake Geneva. We studied the air temperature (T_a) values within a ±1°C range around its mean value (9.8°C). We also selected the values of 50, 65 and 80% for of the relative humidity (ϕ_{rel}) as the typical variation range over Lake Geneva.

The results (Fig. 5.8) show that by increasing the wind speed from 0 to 3 ms^{-1} , the sensible and latent surface cooling are enhanced, and the area-averaged mean and the standard deviation of the Q_c map increase by ~25 and ~3 Wm^{-2} (Fig. 5.8a). However, LSWT spatial heterogeneity is less likely under stronger wind speeds due to stronger surface mixing. The spatial mean value of Q_c shows a ~10 Wm^{-2} reduction when increasing the air-water temperature difference within a 2°C range (Fig. 5.8b). This parameter mainly affects the ABL stability conditions over the lake, and hence the skewness of the Q_c distribution. Increasing the air-water temperature difference tends to alter the ABL from unstable to stable, and therefore the negatively skewed Q_c distribution to a positively skewed one (left to right in Fig. 5.8b). The standard deviation of Q_c also showed a ~1 Wm^{-2} reduction by changing T_a from 8.8 to 10.8°C, indicating a more homogenous surface cooling pattern under stable conditions. The relative humidity had the least effect on the surface cooling variation with a decrease of ~6 and ~1 Wm^{-2} in the mean and standard deviation of the Q_c spatial map by increasing its value from 50 to 80% (Fig. 5.8c).

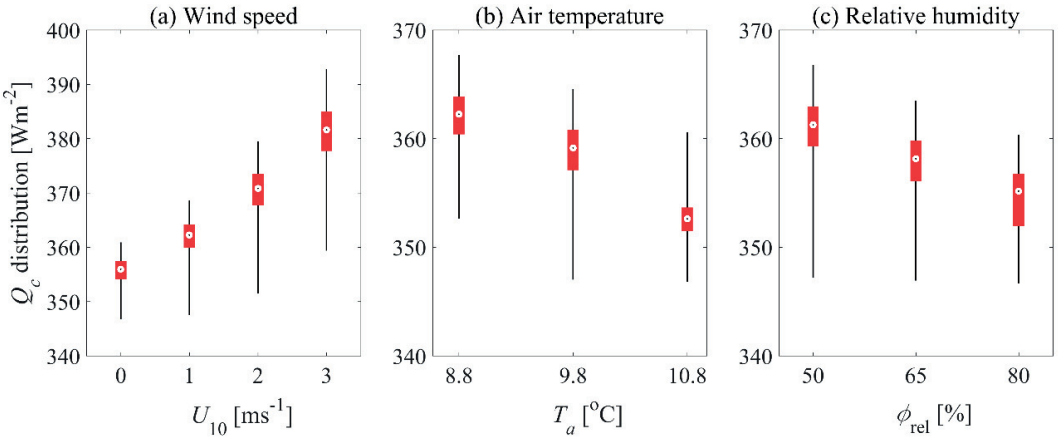

Fig. 5.8. Box plots of the variation of the surface cooling (Q_c) spatial distribution as a function of (a) wind speed (U_{10}), (b) air temperature (T_a), and (c) relative humidity (ϕ_{rel}) for the MGL1 field mission (see Table 5.1, Figs. 5.1 and 5.2 for more details). The white circles, the red filled rectangles and the solid black lines indicate the median, interquartile range (25 to 75 percentiles) and the 0.5 to 99.5 percentiles (indicative for the total range), respectively. Note that the range of ordinate axis in (a) is different from (b) and (c).

5.3.5. Effect of turbulent heat flux parameterization on the surface cooling spatial distribution

The current surface cooling estimations are based on a model calibrated at two points using large-scale satellite and meteorological data during a 7-y period (see chapter 2 for more details) (Rahaghi et al. 2018b; Unpublished work). Here, we study the effect of changing the turbulent heat flux parameterization on the results. From the various formulas and approaches that exist for carrying out such an analysis (Brodeau et al. 2017), in this study, we considered the parameterization of Zeng et al. (1998), hereinafter is referred to as ZZD. The roughness lengths of wind, humidity and temperature were estimated slightly differently by ZZD than in our study. The details of the difference between the ZZD algorithm and the parameterization used in the present paper can be found in chapter 2 (Rahaghi et al. 2018b; Unpublished work). The MGL1 and EGL2 field missions, which cover near-neutral conditions, were selected for this investigation.

The comparison between the surface cooling distributions using the ZZD algorithm and the parameterization is shown in Fig. 5.9, indicating that the two models result in a similar

distribution under very stable conditions (left segments of Fig. 5.9a and b corresponding to the flat parts in Figs. 5.5a and b). However, the ZZD algorithm estimates a higher turbulent cooling under unstable and weak wind conditions, which led to a broadening of the curve in the right segment of the PDF distribution. This comparison reveals that the main spatial features of surface cooling predicted by the two parameterizations are similar (due to the similarity in the overall shape of the PDF curves in Fig. 5.9). However, a quantitative comparison shows that the estimated spatial mean of surface cooling is ~3 and ~2 Wm^{-2} higher for MGL1 (Fig. 5.9a) and EGL2 (Fig. 5.9b), respectively, using the ZZD algorithm. The standard deviation also increases by ~3 Wm^{-2} for MGL1 and EGL2, by employing the ZZD algorithm. The results demonstrate that the turbulent heat flux parameterization can affect the meso-scale surface cooling heterogeneity (Fig. 5.9), and therefore the area-averaged results at the satellite pixel resolution (discussed in section 5.3.3). This effect was reported to be significant for the long-term heat budget analysis of aquatic systems (Brodeau et al. 2017; Rahaghi et al. 2018b).

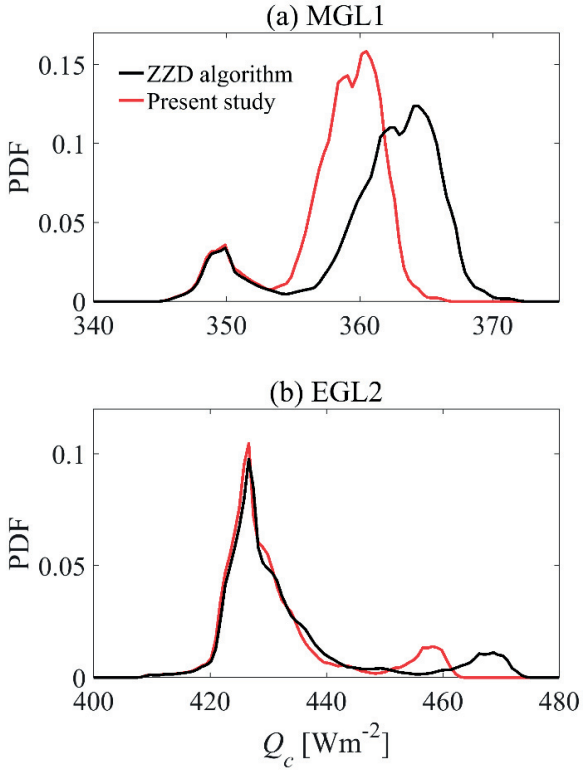

Fig. 5.9. Comparison of surface cooling distribution using two different turbulent surface heat flux parameterizations, i.e., the present study and the ZZD algorithm (see the text for more details), for (a) the MGL1 (predominantly unstable) and (b) the EGL2 (predominantly stable) field mission. Colors are identified in the legend in panel (a).

5.4. Summary and conclusions

An airborne balloon-launched remote sensing platform (BLIMP) accompanied by a catamaran (ZiviCat) for ground-truthing was used to resolve the meso-scale O(1 m), LSWT heterogeneity over Lake Geneva. Four different daytime LSWT maps covering different ABL stability conditions were selected to estimate the associated surface cooling spatial variability, and the effect of area-averaged LSWT on the surface heat flux estimation at a typical satellite pixel O(1 km) resolution. The bulk aerodynamic relationship implementing the Monin-Obukhov similarity was used to calculate the turbulent surface heat fluxes. The meteorological variables were assumed to be constant during the short-term studied periods (less than 30 min).

The measured LSWT patterns showed a maximum spatial variation of > 2°C and > 3.5°C at the beginning of spring and in the middle of summer, respectively, under near-neutral and weak wind conditions. The LSWT distributions were negatively skewed, a PDF shape that was attributed to the cold patches and fronts in the selected patterns. Comparison of the cold season and the beginning of the spring LSWT data revealed that the net surface energy, surface mixing and background stratification must be considered, in addition to the ABL stability when investigating the LSWT heterogeneity.

The corresponding calculated surface cooling patterns preserved the most prominent features of the data. However, during summer, under stable and unstable ABL conditions, the surface cooling distribution was significantly different than that of the LSWT distribution. This is related to the non-linearity in the latent heat flux estimation under near-neutral conditions, which turned the negative skewness distribution of the LSWT map into a positively skewed surface cooling one. Furthermore, this suggests that using area-averaged LSWT data (not resolving the meso-scale heterogeneity) may result in errors in the surface cooling estimation. To address this, we applied a mean spatial filter with variable size to the LSWT patterns of the selected missions. The corresponding surface cooling distributions were then calculated. The results indicate that the heterogeneous-homogeneous differences in surface cooling estimations are greater for near-neutral conditions. Under predominantly stable conditions, the area-averaged surface cooling showed a reduction of ~3.5 Wm^{-2} when comparing the heterogeneous O(1 m) resolution with homogeneous O(1 km) resolution results. For the same pixel resolution variation, the mean surface cooling estimation increased by ~0.5 Wm^{-2} for the predominantly unstable case. Integrating such overestimation or underestimation of surface cooling over the

entire surface of a large water body, e.g., Lake Geneva in our case, may significantly modify its overall heat budget analysis, especially for long-term studies.

The results of this study are affected by uncertainties associated with the model calibration and the errors in meteorological data measurement and sampling. A sensitivity analysis was performed to quantify these errors. Our results emphasize that the wind speed variation may significantly affect the mean and spatial range of the surface cooling. The errors in the air temperature data in near-neutral conditions can also change the estimated ABL stability, and hence affect the calculated surface cooling distribution over the lake. Increasing the relative humidity resulted in the reduction of the spatial mean surface cooling, but the effect was not as significant as the other two parameters. The effect of the turbulent heat flux model calibration was also studied by comparing the results with a commonly implemented parameterization in other studies (ZZD, see section 5.3.5.). Our results indicated that employing the ZZD algorithm instead of the current model results in an increase of ~2.5 and ~3 Wm^{-2} in the spatial mean and standard deviation of surface cooling patterns, respectively. It was determined that this variation is mainly due to the change of latent heat flux cooling over the segments with negative ABL stability, i.e., unstable and very unstable parts. These measurements were taken under daytime and weak wind conditions over a large inland water body. Although this study was limited to small sections of the lake, it provided unprecedented insight into the dynamics of meso-scale heterogeneity of the LSWT. Further field campaigns measurements should be carried out to confirm and extend the present results over larger areas and a wider range of conditions.

Acknowledgments

This work was supported by the Fondation pour l'Etude des Eaux du Léman (FEEL Foundation), EPFL [Grant No. 5257]. Supplementary meteorological data were kindly provided by the Federal Office of Meteorology and Climatology in Switzerland, MeteoSwiss. The authors would like to thank J.-L. Liardon, H.K. Wynn, P.O. Paccaud, B. Geissmann, L. Zulliger, J. Béguin, P. Klaus, N. Gujja Shaik, S. Benketaf, K. Kangur, M. Pagnamenta, L. Hostettler, N. Bongard, G. Ulrich, B. Grossniklaus, A. Rosselet, M. Bolay, J. Rossier, Y. Poffet and N. Roussel for their contribution to designing, testing, and improving of the BLIMP and ZiviCat platforms used in this research. We also wish to thank D. Sage, A. Ivanov and S. Tulyakov for their help and advice on BLIMP image processing.

References

Alcantara, E. H., J. L. Stech, J. A. Lorenzzetti, M. P. Bonnet, X. Casamitjana, A. T. Assireu, and E. M. L. D. Novo. 2010. Remote sensing of water surface temperature and heat flux over a tropical hydroelectric reservoir. Remote Sens. Environ. **114:** 2651-2665. doi: 10.1016/j.rse.2010.06.002.

Assouline, S., S. W. Tyler, J. Tanny, S. Cohen, E. Bou-Zeid, M. B. Parlange, and G. G. Katul. 2008. Evaporation from three water bodies of different sizes and climates: Measurements and scaling analysis. Adv. Water Resour. **31:** 160-172. doi: 10.1016/j.advwatres.2007.07.003.

Barry, D. A., J.-L. Liardon, P. Paccaud, P. Klaus, N. S. Gujja Shaik, A. I. Rahaghi, and U. Lemmin. 2018. A low-cost, autonomous mobile platform for limnological investigations, supported by high-resolution mesoscale airborne imagery. PLoS One**:** Under review.

Brodeau, L., B. Barnier, S. K. Gulev, and C. Woods. 2017. Climatologically significant effects of some approximations in the bulk parameterizations of turbulent air-sea fluxes. J. Phys. Oceanogr. **47:** 5-28. doi: 10.1175/Jpo-D-16-0169.1.

Castro, S. L., W. J. Emery, G. A. Wick, and W. Tandy. 2017. Submesoscale sea surface temperature variability from UAV and satellite measurements. Remote Sens. **9:** 1089. doi: 10.3390/Rs9111089.

Fairall, C. W., E. F. Bradley, J. E. Hare, A. A. Grachev, and J. B. Edson. 2003. Bulk parameterization of air-sea fluxes: Updates and verification for the COARE algorithm. J. Clim. **16:** 571-591. doi: 10.1175/1520-0442(2003)016<0571:Bpoasf>2.0.Co;2.

Fink, G., M. Schmid, B. Wahl, T. Wolf, and A. Wüest. 2014. Heat flux modifications related to climate-induced warming of large European lakes. Water Resour. Res. **50:** 2072-2085. doi: 10.1002/2013wr014448.

Garbe, C. S., U. Schimpf, and B. Jahne. 2004. A surface renewal model to analyze infrared image sequences of the ocean surface for the study of air-sea heat and gas exchange. J. Geophys. Res.: Oceans **109:** C08s15. doi: 10.1029/2003jc001802.

Garbe, C. S., H. Spies, and B. Jahne. 2003. Estimation of surface flow and net heat flux from infrared image sequences. J. Math. Imaging Vis. **19:** 159-174. doi: 10.1023/A:1026233919766.

Gulev, S. K. 1997. Climatologically significant effects of space-time averaging in the north Atlantic sea-air heat flux fields. J. Clim. **10:** 2743-2763. doi: 10.1175/1520-0442(1997)010<2743:Cseost>2.0.Co;2.

Gutowski, W. J., Z. Otles, and Y. B. Chen. 1998. Effect of ocean surface heterogeneity on climate simulation. Mon. Weather Rev. **126:** 1419-1429. doi: 10.1175/1520-0493(1998)126<1419:Eoosho>2.0.Co;2.

Handler, R. A., and G. B. Smith. 2011. Statistics of the temperature and its derivatives at the surface of a wind-driven air-water interface. J. Geophys. Res.: Oceans **116:** C06021. doi: 10.1029/2010jc006496.

Hsu, S. A., E. A. Meindl, and D. B. Gilhousen. 1994. Determining the power-law wind-profile exponent under near-neutral stability conditions at sea. J. Appl. Meteorol. **33:** 757-765. doi: 10.1175/1520-0450(1994)033<0757:Dtplwp>2.0.Co;2.

Hughes, P. J., M. A. Bourassa, J. J. Rolph, and S. R. Smith. 2012. Averaging-related biases in monthly latent heat fluxes. J. Atmos. Oceanic Technol. **29:** 974-986. doi: 10.1175/Jtech-D-11-00184.1.

Liardon, J.-L., and D. A. Barry. 2017. Adaptable imaging package for remote vehicles. HardwareX **2:** 1-12. doi: 10.1016/j.ohx.2017.04.001.

Liardon, J.-L., L. Hostettler, L. Zulliger, K. Kangur, N. G. Shaik, and D. A. Barry. 2017. Lake imaging and monitoring aerial drone. HardwareX. doi: 10.1016/j.ohx.2017.10.003.

Livingstone, D. M., and D. M. Imboden. 1989. Annual heat balance and equilibrium temperature of Lake Aegeri, Switzerland. Aquat. Sci. **51:** 351-369. doi: 10.1007/Bf00877177.

Lofgren, B. M., and Y. C. Zhu. 2000. Surface energy fluxes on the Great Lakes based on satellite-observed surface temperatures 1992 to 1995. J. Great Lakes Res. **26:** 305-314. doi: 10.1016/S0380-1330(00)70694-0.

Mahrt, L., and T. Hristov. 2017. Is the influence of stability on the sea surface seat flux important? J. Phys. Oceanogr. **47:** 689-699. doi: 10.1175/Jpo-D-16-0228.1.

Mahrt, L., and D. Khelif. 2010. Heat fluxes over weak SST heterogeneity. J. Geophys. Res.: Atmos. **115:** D11103. doi: 10.1029/2009jd013161.

Mahrt, L., D. Vickers, E. L. Andreas, and D. Khelif. 2012. Sensible heat flux in near-neutral conditions over the sea. J. Phys. Oceanogr. **42:** 1134-1142. doi: 10.1175/Jpo-D-11-0186.1.

Monin, A. S., and A. M. Obukhov. 1954. Basic laws of turbulent mixing in the ground layer of the atmosphere. Tr. Akad. Nauk SSSR Geofiz. Inst. **24:** 163-187.

Moukomla, S., and P. D. Blanken. 2017. The estimation of the North American Great Lakes turbulent fluxes using satellite remote sensing and MERRA reanalysis data. Remote Sens. **9:** 141. doi: 10.3390/Rs9020141.

Nordbo, A., S. Launiainen, I. Mammarella, M. Lepparanta, J. Huotari, A. Ojala, and T. Vesala. 2011. Long-term energy flux measurements and energy balance over a small boreal lake using eddy covariance technique. J. Geophys. Res.: Atmos. **116:** D02119. doi: 10.1029/2010jd014542.

Rahaghi, A. I., U. Lemmin, A. Cimatoribus, and D. A. Barry. 2018a. Multi-annual surface heat flux dynamics over Lake Geneva: The importance of spatial variability. Water Resour. Res.**:** To be submitted.

Rahaghi, A. I., U. Lemmin, A. Cimatoribus, D. Bouffard, M. Riffler, S. Wunderle, and D. A. Barry. 2018b. Improving surface heat flux estimation of a large lake through model

optimization and 2-point calibration: The case of Lake Geneva. Limnol. Oceanogr.: Methods**:** Under review.

Rahaghi, A. I., U. Lemmin, D. Sage, and D. A. Barry. 2018c. Lake surface water thermal imagery: Aerial remote sensing and image registration. Remote Sens. Environ.**:** Under review.

Schnieders, J., C. S. Garbe, W. L. Peirson, G. B. Smith, and C. J. Zappa. 2013. Analyzing the footprints of near-surface aqueous turbulence: An image processing-based approach. J. Geophys. Res.: Oceans **118:** 1272-1286. doi: 10.1002/jgrc.20102.

Spence, C., P. D. Blanken, N. Hedstrom, V. Fortin, and H. Wilson. 2011. Evaporation from Lake Superior: 2-Spatial distribution and variability. J. Great Lakes Res. **37:** 717-724. doi: 10.1016/j.jglr.2011.08.013.

Van Emmerik, T. H. M., A. Rimmer, Y. Lechinsky, K. J. R. Wenker, S. Nussboim, and N. C. van de Giesen. 2013. Measuring heat balance residual at lake surface using distributed temperature sensing. Limnol. Oceanogr.: Methods **11:** 79-90. doi: 10.4319/lom.2013.11.79.

Verburg, P., and J. P. Antenucci. 2010. Persistent unstable atmospheric boundary layer enhances sensible and latent heat loss in a tropical great lake: Lake Tanganyika. J. Geophys. Res.: Atmos. **115:** D11109. doi: 10.1029/2009jd012839.

Veron, F., W. K. Melville, and L. Lenain. 2008. Infrared techniques for measuring ocean surface processes. J. Atmos. Oceanic Technol. **25:** 307-326. doi: 10.1175/2007JTECH0524.1.

Woolway, R. I., I. D. Jones, D. P. Hamilton, S. C. Maberly, K. Muraoka, J. S. Read, R. L. Smyth, and L. A. Winslow. 2015. Automated calculation of surface energy fluxes with high-frequency lake buoy data. Environ. Model. Softw. **70:** 191-198. doi: 10.1016/j.envsoft.2015.04.013.

Woolway, R. I., P. Verburg, C. J. Merchant, J. D. Lenters, D. P. Hamilton, J. Brookes, S. Kelly, S. Hook, A. Laas, D. Pierson, A. Rimmer, J. A. Rusak, and I. D. Jones. 2017. Latitude and lake size are important predictors of over-lake atmospheric stability. Geophys. Res. Lett. **44:** 8875-8883. doi: 10.1002/2017GL073941.

Zeng, X. B., M. Zhao, and R. E. Dickinson. 1998. Intercomparison of bulk aerodynamic algorithms for the computation of sea surface fluxes using TOGA COARE and TAO data. J. Clim. **11:** 2628-2644. doi: 10.1175/1520-0442(1998)011<2628:Iobaaf>2.0.Co;2.

Zhang, Q. Y., and H. P. Liu. 2013. Interannual variability in the surface energy budget and evaporation over a large southern inland water in the United States. J. Geophys. Res.: Atmos. **118:** 4290-4302. 10.1002/jgrd.50435.

Supplemental Information for Chapter 5:

Meso-scale surface water temperature heterogeneity effect on the surface cooling estimates of a large lake: Airborne remote sensing results from Lake Geneva

Abolfazl Irani Rahaghi[a], Ulrich Lemmin[a], David Andrew Barry[a]

[a] Ecological Engineering Laboratory (ECOL), Environmental Engineering Institute (IIE), Faculty of Architecture, Civil and Environmental Engineering (ENAC), Ecole Polytechnique Fédérale de Lausanne (EPFL), 1015 Lausanne, Switzerland

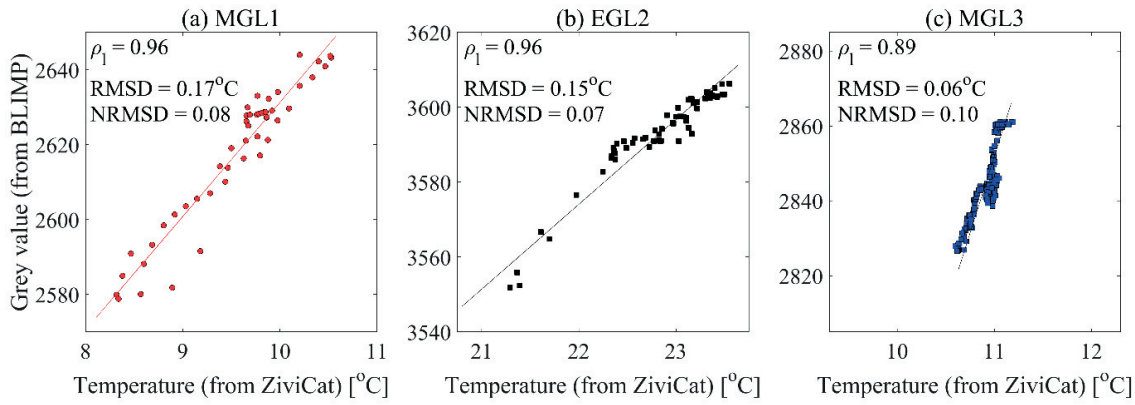

Fig. S5.1. Comparison of the grey value of the stitched image (from the airborne BLIMP) with the corresponding in situ near-surface (2-cm depth) temperatures measured by ZiviCat for the (a) MGL1, (b) EGL2, and (3) MGL3 missions. The solid lines show the corresponding radiometric calibrations, which tend to be linear for a narrow temperature range (< 4°C). The correlation coefficients for a linear curve fitting (ρ_l), the root mean square differences (RMSD) and the normalized RMSD (NRMSD) for the non-linear regression model are given in the legend. The min/max temperature range at each mission was used for RMSD normalization. The details of the calibration procedure can be found in chapter 4 (Rahaghi et al. 2018; Unpublished work).

Reference

Rahaghi, A. I., U. Lemmin, D. Sage, and D. A. Barry. 2018. Lake surface water thermal imagery: Aerial remote sensing and image registration. Remote Sens. Environ.: Under review.

Chapter 6

Conclusions and perspectives

6.1. Summary and conclusions

LSWT and meteorological parameters may exhibit significant spatial variability over large lakes. For example, the surrounding topography can exert a strong influence on the wind patterns, and hence on SurHF. LSWT spatial heterogeneity can also be considerable, especially during the summertime. Therefore, the determination of SurHF at a single location only provides a partial understanding of the energy exchange dynamics over the whole lake surface and could result in significant errors in the estimation of SurHF for the entire lake. In this thesis, the impact of LSWT and meteorological spatial variability on the air-water heat exchange of a large European lake, i.e., Lake Geneva, was studied at different spatial scales.

6.1.1. Large-scale investigation

The LSWT maps from a moderate resolution satellite, i.e., AVHRR, and the meteorological patterns from a numerical weather model, i.e., COSMO (last accessed 2 February 2018), were used for the large-scale (~1 km resolution) investigation. An optimal combination of different heat flux components was obtained through a systematic analysis of various existing formulations and parameterizations for SurHF estimation. A 7-y period (2008 to 2014) using a two-point calibration, instead of the commonly used one-point calibration was used for this investigation (chapter 2). When optimized for one lake temperature profile location, SurHF models failed to predict the temperature profile at the other location due to the spatial variability of meteorological parameters between the two locations. Consequently, the optimal SurHF models were calibrated using two profile locations. The combination of the modified parameterization of the Brutsaert equation (Brutsaert 1975) for incoming atmospheric radiation and of similarity theory based bulk parameterization algorithms for latent and sensible surface heat fluxes (Monin and Obukhov 1954) provided the most accurate SurHF estimates. The results showed that, for heat exchange analysis of large lakes, an adequately calibrated atmospheric radiation model and an appropriate turbulent SurHF model are essential. It was demonstrated that a small variation in calibration factors, especially those controlling atmospheric radiation, leads to a significant change in the heating/cooling estimation of the lake, in particular for long-term investigations, i.e., more than 3 y. This indicates that a systematic calibration of bulk models is required for each study site. The calibration improved the long-wave atmospheric radiation, and parameterization of bulk transfer coefficients (mainly

under low wind regimes) compared to other studies (e.g., Livingstone and Imboden 1989; Zeng et al. 1998; Fink et al. 2014; Woolway et al. 2015).

The optimized and calibrated bulk algorithms in chapter 2 were then used to compute the spatiotemporal SurHF of Lake Geneva (chapter 3). The results indicated an average spatial range of > 40 Wm^{-2}. During spring, much less spatial variability was evident compared to other seasons. These results are comparable with the reported values for other large lakes (Schneider and Mauser 1991; Lofgren and Zhu 2000; Moukomla and Blanken 2017). It was found that the spatial variability of SurHF values predominantly reflects the variation in wind patterns during the summer-winter period, while the LSWT variability is more important during springtime. The change of the controlling regime was evident in the ABL stability conditions curve. It demonstrates that the ABL stability patterns, in which the wind speed, LSWT and air-water temperature difference are inherent, is a better indicator of SurHF spatial variability. It was found that on average, the ABL over Lake Geneva is statically unstable 74% of the time, except during the springtime, which is in agreement with some studies in a global scale (Woolway et al. 2017). The results showed that the rate of evaporation is lower under stable ABL conditions (only ~ 10% of evaporation occurred during this period). The substantial spatial variability of SurHF obtained in chapter 3 emphasize that the spatial variability of LSWT and meteorological patterns should be taken into account when assessing the time evolution of the heat budget of large water bodies.

6.1.2. Meso-scale investigation

An airborne platform was developed to measure the LSWT patterns of inland water bodies at meso-scale (~1 m resolution). It consists of a tethered Balloon Launched Imaging and Monitoring Platform (BLIMP) equipped with an uncooled InfraRed (IR) camera for thermal imagery, and an autonomous catamaran (called ZiviCat) that measures in situ surface/near surface temperatures and permits simultaneous ground-truthing of the BLIMP data. A procedure for image enhancement, denoising, registration, georeferencing and radiometric calibration was proposed (described in chapter 4). The results indicated that neglecting either the NUC or the drift correction can produce substantial artificial spatial gradients in the stitched image. Furthermore, it was found that a high overlap ratio (~95% in our case) is also required for accurate LSWT thermography over natural water bodies.

Several field campaigns were conducted over Lake Geneva using the combined ZiviCat-BLIMP system, out of which four daily data sets were selected to be analyzed in this dissertation. The obtained meso-scale LSWT maps revealed spatial temperature variability with unprecedented detail. The measured LSWT patterns showed a maximum spatial variation of > 2°C and > 3.5°C during spring and summer, respectively, under near-neutral and weak wind conditions. The LSWT distributions were negatively skewed, a PDF shape that was attributed to the cold patches and fronts in the selected patterns. The impact of LSWT meso-scale heterogeneity on the surface cooling estimates at sub-pixel satellite scale was then assessed. The calibrated SurHF models obtained in chapter 2 was used for this study. The results indicated that the LSWT heterogeneity, and hence the surface cooling spatial range are higher under near-neutral ABL stability conditions. A spatial surface cooling range of > 20 Wm^{-2} and > 40 Wm^{-2} was found for near-neutral conditions during spring and summer, respectively. Implementing a mean spatial filter, the effect of area-averaged LSWT on the surface cooling estimation of a typical satellite pixel was also evaluated. Under predominantly unstable conditions, the area-averaged surface cooling showed an increase of ~0.5 Wm^{-2} when comparing the heterogeneous O(1 m) resolution with homogeneous O(1 km) resolution results. For predominantly stable ABL conditions a reduction of ~3.5 Wm^{-2} from high O(1 m) to low O(1 km) pixel resolution was obtained. Such overestimation or underestimation of surface cooling, when integrated over the entire surface of a large lake, e.g., Lake Geneva in our case, may significantly modify its overall heat budget analysis, especially for long-term studies. The uncertainty associated with the primary meteorological parameters was also quantified by a sensitivity analysis that revealed that the bias in meteorological condition sampling, particularly wind speed, can affect both the mean and the range of spatial surface cooling. The error in the air temperature may also alter the surface cooling distribution from negatively skewed to positively skewed, and hence affect the area-averaged estimates.

6.2. Future work

It was found that, compared to commonly used one-point approach, calibrating the SurHF models at two points enhances the heat budget analysis of a large lake in the long-term study (chapter 2). This was mainly due to the spatial variability of LSWT and meteorological parameters. However, based on the k-means clustering results in chapter 3, Lake Geneva can be partitioned into four zones, of which only two (SHL2 and GE3 points) are currently

monitored by CIPEL (last accessed 1 February 2018). Measuring the CTD profiles in the other two zones will improve the thermodynamic understanding of the lake.

The Monin-Obukhov similarity scaling (Monin and Obukhov 1954) based on the surface stability parameter was found to be the optimal method for turbulent heat flux estimation over Lake Geneva (chapter 2). However, there is a large scatter of parameterization and reported transfer coefficients parameters (e.g., Wüest and Lorke 2003; Wei et al. 2016; Brodeau et al. 2017), as discussed in chapter 2. Given that the ZiviCat platform is capable of measuring over-lake ABL data, direct measurements of sensible and latent heat fluxes can improve the results of this study. It must be mentioned that the turbulent heat fluxes are the dominant terms affecting the SurHF spatial variability (results shown in chapters 3 and 5). Although some challenges are anticipated for such field measurements, the eddy covariance (eddy correlation) technique (e.g., Assouline et al. 2008; Vercauteren et al. 2009) is suggested.

Some numerical simulation studies demonstrated the effect of using precomputed SurHF on thermodynamic modeling of large water bodies (Xue et al. 2015; Dommenget and Rezny 2018). The results of chapter 3 can be used to investigate the impact of flux correction on hydrodynamic and thermodynamic modeling of Lake Geneva. Updating the 3D model interface to use the precomputed spatiotemporal SurHF maps instead of dynamically-computed fluxes as well as re-tuning the model are required for this study.

For the meso-scale investigation of this dissertation, the meteorological data were assumed to be spatially constant (chapter 5). Although the uncertainty associated with this assumption was estimated by a sensitivity analysis, more sophisticated models, such as Bayesian inference (e.g., Ershadi et al. 2013; Kavetski et al. 2013) may improve the presented results. In addition, one may consider using scanning Doppler wind LiDAR (Light Detection and Ranging) to resolve the over-lake wind patterns (Fuertes et al. 2014). Such data, if obtained over water, simultaneously with the LSWT meso-scale maps generated by the proposed platform and image registration algorithm, can provide a better insight into the air-water exchange processes. Furthermore, an autonomous drone that carries the BLIMP imaging package (Liardon et al. 2017) can cover a wider area over the lake. However, the vibration and titling issues intrinsic with the drone system, which in turn affect the image registration (discussed in chapter 4), need to be addressed first.

References

Assouline, S., S. W. Tyler, J. Tanny, S. Cohen, E. Bou-Zeid, M. B. Parlange, and G. G. Katul. 2008. Evaporation from three water bodies of different sizes and climates: Measurements and scaling analysis. Adv. Water Resour. **31:** 160-172. doi: 10.1016/j.advwatres.2007.07.003.

Brodeau, L., B. Barnier, S. K. Gulev, and C. Woods. 2017. Climatologically significant effects of some approximations in the bulk parameterizations of turbulent air-sea fluxes. J. Phys. Oceanogr. **47:** 5-28. doi: 10.1175/Jpo-D-16-0169.1.

Brutsaert, W. 1975. Derivable formula for long-wave radiation from clear skies. Water Resour. Res. **11:** 742-744. doi: 10.1029/Wr011i005p00742.

Dommenget, D., and M. Rezny. 2018. A caveat note on tuning in the development of coupled climate models. J Adv Model Earth Sy **10:** 78-97. doi: 10.1002/2017MS000947.

Ershadi, A., M. F. McCabe, J. P. Evans, G. Mariethoz, and D. Kavetski. 2013. A Bayesian analysis of sensible heat flux estimation: Quantifying uncertainty in meteorological forcing to improve model prediction. Water Resour. Res. **49:** 2343-2358. doi: 10.1002/wrcr.20231.

Fink, G., M. Schmid, B. Wahl, T. Wolf, and A. Wüest. 2014. Heat flux modifications related to climate-induced warming of large European lakes. Water Resour. Res. **50:** 2072-2085. doi: 10.1002/2013wr014448.

Fuertes, F. C., G. V. Iungo, and F. Porté-Agel. 2014. 3D turbulence measurements using three synchronous wind lidars: Validation against sonic anemometry. J. Atmos. Oceanic Technol. **31:** 1549-1556. doi: 10.1175/jtech-d-13-00206.1.

Kavetski, D., S. W. Franks, and G. Kuczera. 2013. Confronting input uncertainty in environmental modelling, p. 49-68. Calibration of Watershed Models. American Geophysical Union. doi: 10.1029/WS006p0049.

Liardon, J.-L., L. Hostettler, L. Zulliger, K. Kangur, N. G. Shaik, and D. A. Barry. 2017. Lake imaging and monitoring aerial drone. HardwareX. doi: 10.1016/j.ohx.2017.10.003.

Livingstone, D. M., and D. M. Imboden. 1989. Annual heat balance and equilibrium temperature of Lake Aegeri, Switzerland. Aquat. Sci. **51:** 351-369. doi: 10.1007/Bf00877177.

Lofgren, B. M., and Y. C. Zhu. 2000. Surface energy fluxes on the Great Lakes based on satellite-observed surface temperatures 1992 to 1995. J. Great Lakes Res. **26:** 305-314. doi: 10.1016/S0380-1330(00)70694-0.

Monin, A. S., and A. M. Obukhov. 1954. Basic laws of turbulent mixing in the ground layer of the atmosphere. Tr. Akad. Nauk SSSR Geofiz. Inst. **24:** 163-187.

Moukomla, S., and P. D. Blanken. 2017. The estimation of the North American Great Lakes turbulent fluxes using satellite remote sensing and MERRA reanalysis data. Remote Sens. **9:** 141. doi: 10.3390/Rs9020141.

Schneider, K., and W. Mauser. 1991. On the estimation of energy fluxes at the surface of Lake Constance using NOAA-AVHRR data, p. 373-376. IGARSS 91-Remote Sensing : Global Monitoring for Earth Management. IEEE Xplore Conference, Espoo, Finland. doi: 10.1109/IGARSS.1991.579158.

Vercauteren, N., E. Bou-Zeid, H. Huwald, M. B. Parlange, and W. Brutsaert. 2009. Estimation of wet surface evaporation from sensible heat flux measurements. Water Resour. Res. **45:** W06424. doi: 10.1029/2008wr007544.

Wei, Z. W., A. Miyano, and M. Sugita. 2016. Drag and bulk transfer coefficients over water surfaces in light winds. Bound-Lay. Meteor. **160:** 319-346. doi: 10.1007/s10546-016-0147-8.

Woolway, R. I., I. D. Jones, D. P. Hamilton, S. C. Maberly, K. Muraoka, J. S. Read, R. L. Smyth, and L. A. Winslow. 2015. Automated calculation of surface energy fluxes with high-frequency lake buoy data. Environ. Model. Softw. **70:** 191-198. doi: 10.1016/j.envsoft.2015.04.013.

Woolway, R. I., P. Verburg, C. J. Merchant, J. D. Lenters, D. P. Hamilton, J. Brookes, S. Kelly, S. Hook, A. Laas, D. Pierson, A. Rimmer, J. A. Rusak, and I. D. Jones. 2017. Latitude and lake size are important predictors of over-lake atmospheric stability. Geophys. Res. Lett. **44:** 8875-8883. doi: 10.1002/2017GL073941.

Wüest, A., and A. Lorke. 2003. Small-scale hydrodynamics in lakes. Ann. Rev. Fluid Mech. **35:** 373-412. doi: 10.1146/annurev.fluid.35.101101.161220.

Xue, P. F., D. J. Schwab, and S. Hu. 2015. An investigation of the thermal response to meteorological forcing in a hydrodynamic model of Lake Superior. J. Geophys. Res.: Oceans **120:** 5233-5253. doi: 10.1002/2015JC010740.

Zeng, X. B., M. Zhao, and R. E. Dickinson. 1998. Intercomparison of bulk aerodynamic algorithms for the computation of sea surface fluxes using TOGA COARE and TAO data. J. Clim. **11:** 2628-2644. doi: 10.1175/1520-0442(1998)011<2628:Iobaaf>2.0.Co;2.

Appendix A

Temporal variation of lake surface heat flux and heat content

Abolfazl Irani Rahaghi[a], Ulrich Lemmin[a], Andrea Cimatoribus[a], David Andrew Barry[a]

[a] Ecological Engineering Laboratory (ECOL), Environmental Engineering Institute (IIE), Faculty of Architecture, Civil and Environmental Engineering (ENAC), Ecole Polytechnique Fédérale de Lausanne (EPFL), 1015 Lausanne, Switzerland

In this appendix, the temporal evolution of lake-wide mean SurHF terms and their individual effect on the total heat content variation is discussed. The obtained spatiotemporal results of chapter 3 was used for this investigation.

A1. Temporal variation of surface heat flux components

The spatial mean values (solid lines in Fig. 3.3) were analyzed first. The mean annual temporal variation of different SurHF terms and the net SurHF was calculated and plotted in Fig. A1. To investigate the dominant heat flux terms controlling the temporal variation of lake-wide mean SurHF (solid line, Fig. 3.3f), correlation coefficients of different heat flux components with respect to total SurHF for the lake-wide mean were calculated first. We obtained 0.93, 0.7, -0.55, 0.24 and 0.84 for Q_{sn}, Q_{an}, Q_{br}, Q_{ev} and Q_{co}, respectively. Figure A1, together with the calculated correlation coefficients, demonstrate that solar radiation is the leading component underlying the mean total SurHF evolution, mainly in the spring and summer. The temporal variation in the convective flux, Q_{co}, also shows a high correlation with the total SurHF despite its relatively smaller range of values. Its effect is more significant during fall and winter, where the small perturbations in the net SurHF curve follow the jumps in sensible and latent heat flux. Atmospheric longwave radiation reaches its maximum in summer, leading back radiation by approximately 6 months. Q_{an} and Q_{br} extrema are delayed by approximately 1-2 months relative to Q_{sn}, which can explain the low correlation coefficients obtained above. We quantified the time-lags between different terms and net SurHF below.

To further analyze the temporal variation of SurHF, the surface heat exchange due to radiative heating, $Q_{sn} + Q_{an} + Q_{br}$, and non-radiative (turbulent) cooling, $-(Q_{ev} + Q_{co})$, are plotted separately (red and blue lines in Fig. A2, respectively). The radiative surface heating shows a seasonal variation mainly controlled by solar shortwave radiation with a maximum during May-July and a minimum during December-January. In contrast, the SurHF cooling due to the non-radiative terms, $-(Q_{ev} + Q_{co})$, decreases rapidly from January to mid-April. It then increases rapidly until mid-July, and fluctuates over a short period until the following January (Fig. A2, blue lines). In addition, even though using a 30-d running average filters out the extreme weather events, some long-lasting cooling events are still observed, e.g., beginning of 2012 and end of 2013.

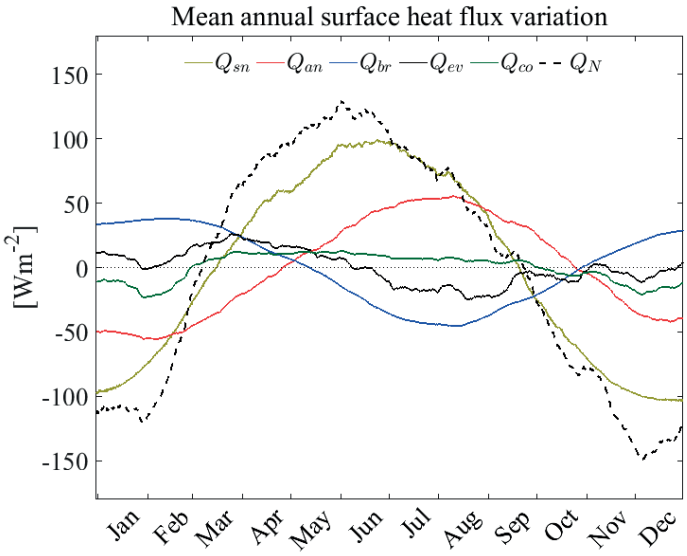

Fig. A1. Temporal evolution of lake-wide mean surface heat flux (SurHF) terms and net SurHF of Lake Geneva averaged over 1 January 2009 to 31 December 2014. Temporal variation smoothed with a 30-d running mean window. For better legibility, the mean annual values of SurHF terms (given in section 3.3.1.) were subtracted in all plots.

Comparison with Fig. S3.4 demonstrates that the low air temperatures and high wind speeds, and consequently a rapid decrease in the atmospheric radiation (Fig. 3.3b) and non-radiative terms (Fig. 3.3d-e), account for these events. A five-month delay between radiative heating and non-radiative cooling was reported for Lake Superior (Blanken et al. 2011), a larger inland water body than Lake Geneva. A cross correlation analysis was performed to obtain this delay for Lake Geneva (Fig. A3) which reveals a ~4-month lag between maximum summer radiative heating and maximum non-radiative cooling. However, computing the 99% confidence intervals for the obtained cross-correlation values (Ebisuzaki 1997) showed that the results are not statistically significant. The wide range of the significance limits is due to high seasonality, and therefore, the high auto-correlation values. Nonetheless, we speculate that the higher delay for Lake Superior is due its larger volume and ice coverage during winter (lower mean temperature), consequently a higher thermal inertia.

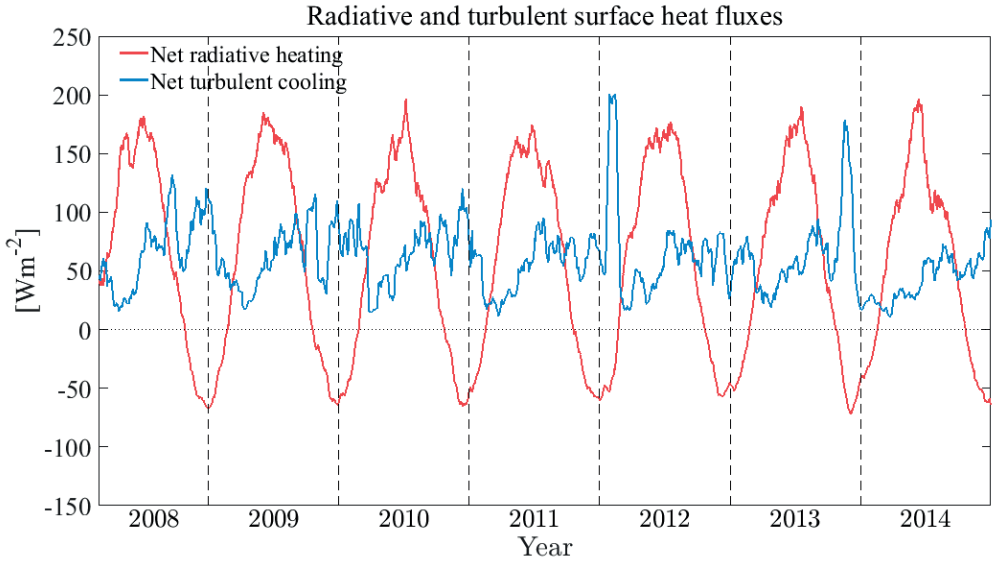

Fig. A2. Time series of the lake-wide average net surface radiative heat flux (red line, positive into the lake), and net flux of the non-radiative (turbulent) components (blue line, positive outward), smoothed with a 30-d running mean.

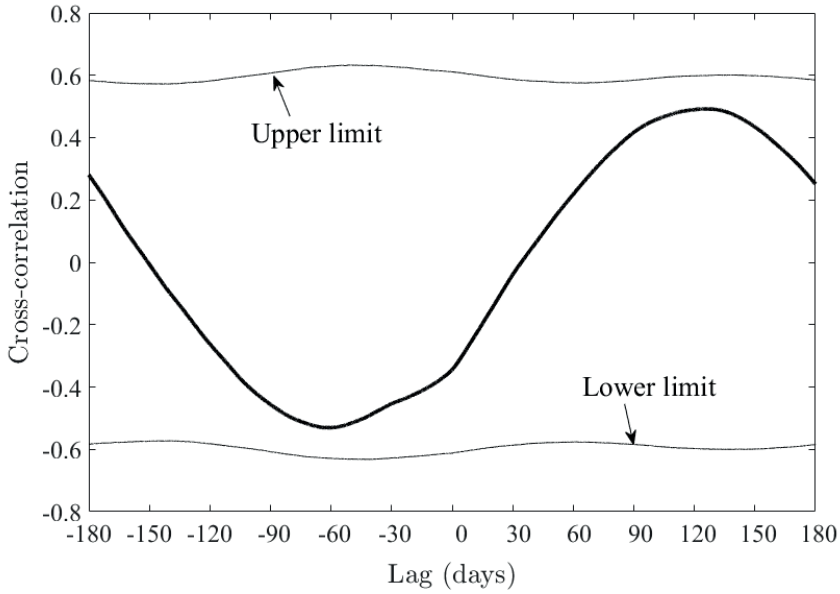

Fig A3. Cross-correlation curve between radiative and non-radiative surface heat fluxes (SurHF). The hourly spatially mean data were used for this analysis (the smoothed results were shown in Fig. A2).Thin lines show the upper and lower limits of 99% confidence intervals (values within these limits are not statistically significant). It indicates that the obtained values including peaks at ~4- and ~2- month are statistically insignificant.

A2. Temporal variation of Lake surface thermal energy (heat content)

In Fig. 3.5 a small negative mean spatiotemporal heat flux of -1 Wm^{-2} is seen for the studied period, i.e., on average the lake cooled during 2009-2014 if we neglect the uncertainties associated with the used data and models, and if it is assumed that the SurHF dominates the lake's energy budget, compared to other heat sources such as inflow, precipitation and geothermal heat flux. The smoothed SurHF results (Figs. 3.3f and A2) does not readily reflect this low rate of cooling. For this reason, the cumulative SurHF, i.e., lake surface thermal energy (heat content) was considered. The surface thermal energy variation, *G,* is calculated by time-integration of the SurHF terms for a given period (Eq. 3.2). Fig. A4a shows the temporal variation of the total heat content in Lake Geneva due to surface heat exchange for the study period (2008-2014). It indicates a net cooling for 2008 to 2012 and the onset of a warming period in 2013. To put this behavior in the context of the lake's longer term heat budget, the observed heat content at SHL2 was estimated (Eq. 2.1) using historical measurements of the vertical temperature profile measured by the CIPEL (Fig. A4b).

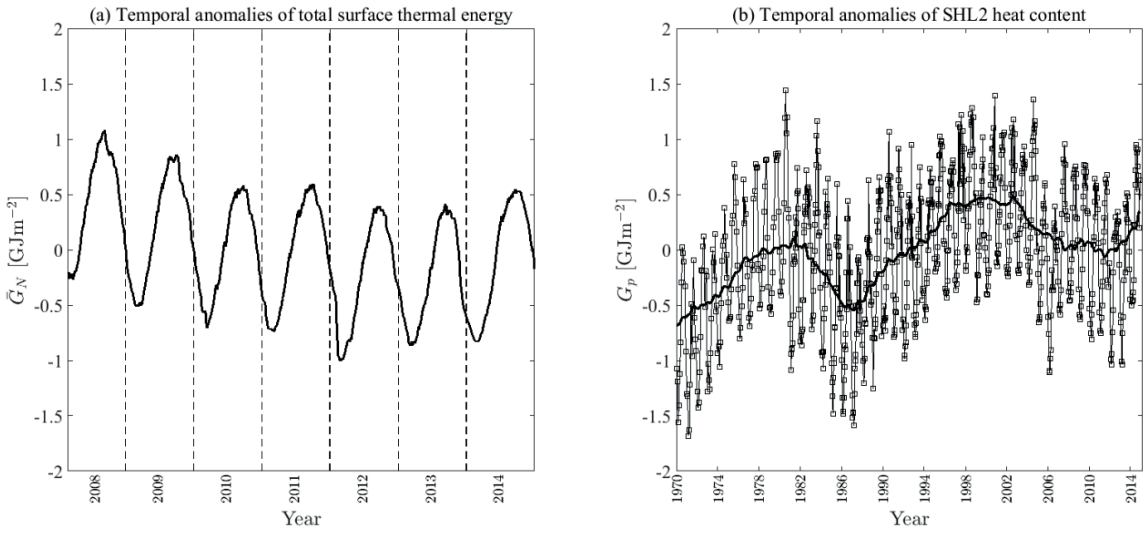

Fig. A4. (a) Temporal anomalies (zero-mean) of total heat content of Lake Geneva due to surface heat exchange (cumulative net SurHF) for 1 March 2008 to 31 December 2014, and (b) heat content variation of Lake Geneva by using historical temperature profile measurements at SHL2 for the 1970 to 2014 period. For better comparison, the mean values over the periods shown in each plot were subtracted. The bold line in (b) indicates the temporal variation smoothed with a 50-point running mean.

Figure A4b shows the long-term heat content variation at SHL2, where several cooling and warming periods during 1970-2014 are apparent. Although our previous results showed that the pointwise analysis may result in significant errors in estimation of SurHF and heat content of large lakes (Fig. 3.4, for example), we can still use the long-term heat content variation to underscore the lake response to global and regional climate change. The trend in cooling for 1998-2012 (Figs. A4a and b) is consistent with global cooling (Desbruyeres et al. 2014; Drijfhout et al. 2014; Watanabe et al. 2014).

The contribution of individual SurHF terms leading to the calculated total surface thermal energy variation (Fig. A4a) was also studied. The hourly spatially mean time series of each SurHF component were used to find the corresponding surface thermal energy variation (Fig. A5a). For a better comparison, the linear trends of each curve were removed. The results indicate that the range of thermal energy variation induced by radiative terms (especially solar radiation) is higher than non-radiative components. Also, the contribution of longwave atmospheric radiation (ΔG_{an}) and back radiation from the water (ΔG_{br}) are negatively correlated.

A time-lag among different curves of Fig. A5a is apparent, e.g., as shown by the peaks of the different curves. We computed the cross-correlations between each of these curves and the total surface energy variation (Fig. A4a), which are shown in Fig. A5b. Because of potentially high auto-correlation values (due to seasonality), the 99% confidence intervals for the cross-correlation analysis were also estimated following the statistical method proposed by Ebisuzaki (1997). The cross-correlation curve for solar shortwave radiation (ΔG_{sn}), which reaches a high value of >0.8 at ~zero-lag, was not statistically significant. Therefore, we removed this curve from Fig. A5b. For other components, the cross-correlations are statistically significant only close to their peaks. The contributions of sensible heat flux (ΔG_{co}) on the total heat content variation of the lake was found to be without any pronounced delay (i.e., no time lag). However, a high cross-correlation of >0.9 was obtained for ΔG_{br} and ΔG_{an} at ~ -50-d time-lag, i.e., total surface thermal energy leads ΔG_{br} and ΔG_{an}. This seems to be linked to the seasonal thermal lag resulting from the thermal inertia of the water body (Rouse et al. 2003). The results also indicate a ~90-d time-lag between ΔG_{ev} and ΔG_{N}. Interestingly, by following the peaks and general trend of different plots (Fig. A5a), we note that only evaporative cooling and longwave

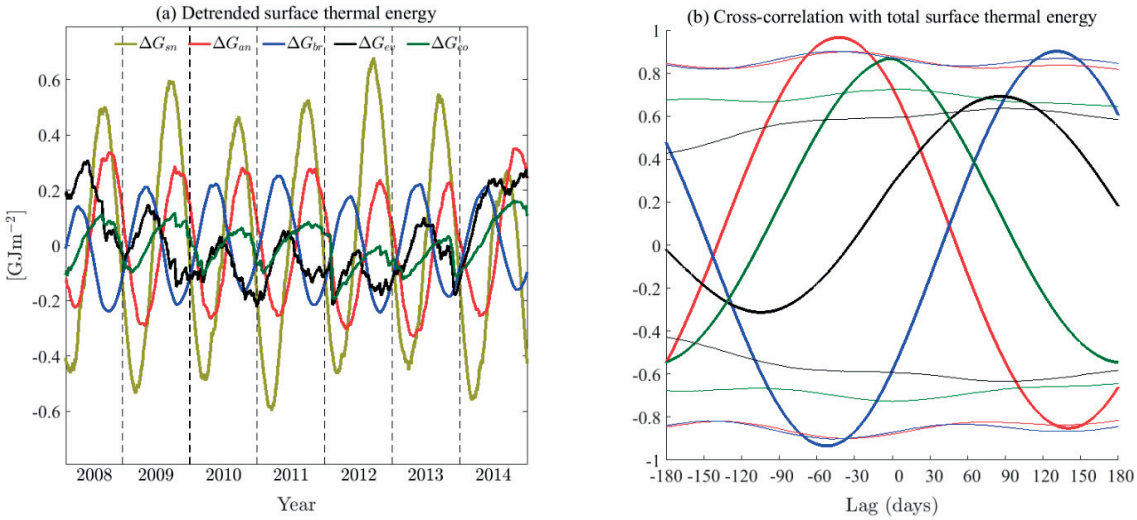

Fig. A5. (a) Temporal evolution of the spatially mean surface thermal energy (cumulative surface heat flux) due to different surface heat flux terms, and (b) cross-correlation curve between each term and the net surface thermal energy presented in Fig. A4a. For better legibility, the linear trends of the surface thermal energy variation were subtracted in all plots in (a). Also, thin lines in (b) show the limits of 99% confidence intervals for the calculated cross-correlation values, i.e., the values between these lines are not statistically significant. A high cross-correlation value (~0.8) between surface thermal energy variation due to solar radiation (ΔG_{sn}) and total surface thermal energy at ~zero-lag was also found. However, since it was statistically insignificant we did not show it.

atmospheric heating (and to a lesser extent convective cooling) have the same trend as total surface thermal energy variation (Fig. A4a). This suggests that the overall trends of the lake total heat content can be predicted by the surface thermal energy variation induced by latent heat flux (~90-d lead-time, Fig. A5b), and that the results can be used to forecast the cumulative atmospheric longwave radiation (~50-d lag-time, Fig. A5b), if, again, the SurHF is assumed to dominate the lake total heat content variation.

References

Blanken, P. D., C. Spence, N. Hedstrorn, and J. D. Lenters. 2011. Evaporation from Lake Superior: 1. Physical controls and processes. J. Great Lakes Res. **37:** 707-716. doi: 10.1016/j.jglr.2011.08.009.

Desbruyeres, D. G., E. L. McDonagh, B. A. King, F. K. Garry, A. T. Blaker, B. I. Moat, and H. Mercier. 2014. Full-depth temperature trends in the northeastern Atlantic through the early 21st century. Geophys. Res. Lett. **41:** 7971-7979. doi: 10.1002/2014GL061844.

Drijfhout, S. S., A. T. Blaker, S. A. Josey, A. J. G. Nurser, B. Sinha, and M. A. Balmaseda. 2014. Surface warming hiatus caused by increased heat uptake across multiple ocean basins. Geophys. Res. Lett. **41:** 7868-7874. doi: 10.1002/2014GL061456.

Ebisuzaki, W. 1997. A method to estimate the statistical significance of a correlation when the data are serially correlated. J. Clim. **10:** 2147-2153. doi: 10.1175/1520-0442(1997)010<2147:Amtets>2.0.Co;2.

Rouse, W. R., C. M. Oswald, J. Binyamin, P. D. Blanken, W. M. Schertzer, and C. Spence. 2003. Interannual and seasonal variability of the surface energy balance and temperature of central Great Slave Lake. J. Hydrometeorol. **4:** 720-730. doi: 10.1175/1525-7541(2003)004<0720:Iasvot>2.0.Co;2.

Watanabe, M., H. Shiogama, H. Tatebe, M. Hayashi, M. Ishii, and M. Kimoto. 2014. Contribution of natural decadal variability to global warming acceleration and hiatus. Nat. Clim. Change **4:** 893-897. doi: 10.1038/Nclimate2355.

Curriculum Vitae

Abolfazl IRANI RAHAGHI

Research interests

- Environmental fluid mechanics
- Aquatic physics
- Energy conversion
- Remote sensing

Key technical skills

- Fieldwork experience
- Data analysis
- Computational fluid dynamics
- Image processing

Contact information

abolfazl.iranirahaghi@epfl.ch
irani.abolfazl@gmail.com

Rue Etraz 14, 1003, Lausanne, Switzerland

(+41) 78 961 93 24

abolfazl.irani

Education

2013-2018	Ph.D., Civil and Environmental Engineering, Ecole Polytechnique Fédérale de Lausanne, Lausanne, Switzerland Research topic: *Large-scale and meso-scale surface heat flux patterns of Lake Geneva*	▪ Physical limnology ▪ Air-water heat exchange of water bodies ▪ Airborne & spaceborne lake thermography ▪ Data analysis ▪ Numerical modeling of inland waters
2007-2009	M.Sc., Mechanical Engineering, Energy Conversion, Sharif University of Technology, Tehran, Iran Honor: **Ranked 1st**, GPA: 19.1/20 Thesis topic: *1D and 2D numerical modeling of micro-scale combustion*	• Numerical modeling of Advective-diffusive-reactive systems, e.g., a micro-combustor • Microfluidics • Optical techniques for flow visualization, e.g., PIV, LIF and MTV
2003-2007	B.Sc., Mechanical Engineering, Sharif University of Technology, Tehran, Iran Honor: **Ranked 3rd**, GPA: 18.3/20 Thesis topic: *1D numerical simulation of a porous media burner*	➢ Energy and exergy analysis of closed systems, e.g., power plants and buildings ➢ Computational Fluid Dynamics (CFD) ➢ Heating, Ventilation and Air Conditioning (HVAC) calculation and design

Professional experience

2011-2013	Research Center of Intelligent Signal Processing (RCISP), Tehran, Iran	Research assistant: Modeling and conceptual design of a micro-scale power generation system
2007-2008	Petro Paydar Energy, Tehran, Iran	Part-time engineer: Energy auditing of industrial units

Projects & Internships

2011-2012	Ramin power plant (Iran's biggest supercritical power plant), Ahwaz, Iran	Energy and exergy analysis of the units with the aim of optimizing the cycle efficiency

2011	National Iranian South Oilfields Company (NISOC), Ahwaz, Iran	Enhancement of the air conditioning systems using the two-wheel dehumidification technology
2010	Shahid Salimi power plant, Neka, Iran	Steam units thermal balance comprehensive study, and software development using on-site monitored data
2008	Iran Khodro Industrial Group, Tehran, Iran	4-month internship: Ventilation system calculations and design for automobile assembly shops
2007-2008	Iran Khodro Industrial Group, Tehran, Iran	4-month internship: Increasing the permeability of ultra filtration for ED paint pool by analyzing the automobile body temperature distribution
2007	Bisotoun Power Plant, Kermanshah, Iran	Analysis of water supply for reheat spray from the mid-stage of feed water pump

Publications

Journal Publications (Published, submitted, or in preparation for submission)

- ✓ Rahaghi, A. I., U. Lemmin, , A. Cimatoribus, D. Bouffard, M. Riffler, S. Wunderle, and D. A. Barry. 2018a. Improving surface heat flux estimation of a large lake through model optimization and 2-point calibration: The case of Lake Geneva. Limnol. Oceanogr.: Methods: Under review.
- ✓ Rahaghi, A. I., U. Lemmin, A. Cimatoribus, and D. A. Barry. 2018b. Multi-annual surface heat flux dynamics over Lake Geneva: The importance of spatial variability. Water Resour. Res.: To be submitted.
- ✓ Rahaghi, A. I., U. Lemmin, D. Sage, and D. A. Barry. 2018c. Lake surface water thermal imagery: Aerial remote sensing and image registration. Remote Sens. Environ.: Under review.
- ✓ Barry, D. A., J.-L. Liardon, P. Paccaud, P. Klaus, N. S. Gujja Shaik, A. I. Rahaghi, and U. Lemmin. 2018. A low-cost, autonomous mobile platform for limnological investigations, supported by high-resolution mesoscale airborne imagery. PLoS One: Under review.
- ✓ Rahaghi, A. I., U. Lemmin, and D. A. Barry. 2018d. Lake surface water thermal imagery: Aerial remote sensing and image registration. J. of Geophys. Res.: Oceans: To be submitted.
- ✓ Rahaghi, A. I., M.S., Saidi, M.H., Saidi and M.B., Shafii, 2009. Two-dimensional numerical investigation of a micro combustor. Sci. Iran. **17**: 433-442. http://scientiairanica.sharif.edu/article_3366.html.

Conference Publications and Presentations

- Rahaghi, A. I., U. Lemmin, D. Bouffard, M. Riffler, S. Wunderle, and D. A. Barry. 2017. Small-scale and mesoscale lake surface water temperature structure: Thermography and in situ measurements from Lake Geneva, Switzerland. *European Geosciences Union (EGU)*. Vienna, Austria. April 2017.
- Rahaghi, A. I., U. Lemmin, M. Riffler, S. Wunderle, and D. A. Barry. 2015. Multiscale surface water temperature data acquisition platform: Tests on Lake Geneva, Switzerland. *American Geophysical Union (AGU)*. San Fransisco, USA. December 2015.
- Rahaghi, A. I., U. Lemmin, D. Bouffard, M. Riffler, S. Wunderle, and D. A. Barry. 2015. Seasonal spatial patterns of surface water temperature, surface heat fluxes and meteorological forcing over Lake Geneva. *American Geophysical Union (AGU)*. San Fransisco, USA. December 2015.
- Rahaghi, A. I., U. Lemmin, D. Bouffard, M. Riffler, S. Wunderle, and D. A. Barry. 2015. Surface thermal patterns of Lake Geneva, Switzerland, from 2008 to 2012. *9th Symposium for European Freshwater Sciences*. Geneva, Switzerland. July 2015.

- Rahaghi, A. I., U. Lemmin, D. Bouffard, M. Riffler, S. Wunderle, and D. A. Barry. 2015. Surface heat flux variability of a large lake: Lake Geneva, Switzerland. *American Geophysical Union (AGU)*. San Fransisco, USA. December 2014.
- Behroozinia, P., A. I. Rahaghi, M. H. Saidi. 2012, One-dimensional numerical investigation of a cylindrical micro-combustor applying electrohydrodynamics effect. *World Academy of Science, Engineering and Technology*. vol 6 (7). 2012. scholar.waset.org/1307-6892/740.
- Rahaghi, A. I., M. Saediamiri, M. S. Saidi, M. H. Saidi, and M. B. Shafii. 2009. One-dimensional numerical investigation of a cylindrical micro combustor. *ASME Summer Heat Transfer Conference*. San Francisco, USA. July 2009. doi: 10.1115/HT2009-88415.
- Saidi, M. S., M. H. Saidi, P. Hanafizadeh, B. Sajadi, and A. I. Rahaghi. 2009. Ventilation system design for automobile assembly shops. *17th Annual (International) Conference on Mechanical Engineering-ISME2009*. Tehran, Iran. May 2009.
- Saidi. M. H., A. I. Rahaghi, S. M. Mousavi. 2008. Retrofitting a steam power cycle by using water from the interstage feed water pump as reheat spray. *ASME Power 2008 Conference*. Orlando, USA. July 2008. doi: 10.1115/POWER2008-60060.
- Saidi, M. S., M. H. Saidi, P. Hanafizadeh, B. Sajadi, and A. I. Rahaghi. 2008. Transient prediction of automobile body temperature distribution in the ED paint dryers: Analytical-numerical approach. *4th International Conference on Energy Research and Development (ICERD4)*. Kuwait City, Kuwait. November 2008.
- Rahaghi, A. I., M. S. Saidi, M. H. Saidi, and M. B. Shafii. 2008. One-dimensional numerical study of a two-stage porous burner: A new approach in combustion modeling. *16th Annual (International) Conference on Mechanical Engineering-ISME2008*. Kerman, Iran. May 2008.

Teaching experience

(i) Ecole Polytechnique Fédérale de Lausanne (EPFL)

- TA: Soil science, Fall 2015-2017
- Supervisor: Design project, Spring 2015-2016

(iii) Sharif Center of Technical and Applied Educations (SCTAE)

- Part-time lecturer: HVAC systems calculation and design, Spring 2008-2010

(ii) Sharif University of Technology (SUT)

- Lecturer: Fluid mechanics, Fall 2012
- Instructor: Thermodynamics laboratory, 2011
- TA: Heat transfer-I, Spring 2010
- TA: Refrigeration systems, Fall 2010
- TA: Fluid mechanics-I, Fall 2009
- TA: CFD, Fall 2008
- TA: Thermal power plants, Fall 2007-2009

Computer and programming skills

Detailed knowledge: Matlab, Delft-3D Flow, Fortran, Thermoflow, HAP-Carrier, EES, ANSYS Fluent, MS Office

Basic knowledge: MITgcm, C++, Linux operating system, UDF programming in Fluent, Chemkin, Gas Turbine Simulation Program (GSP), Tecplot, Solid Works, Autocad, Catia

Languages

Persian: Native

English: Fluent

French: Upper intermediate (B1/B2 level, progressive learner)

Deutsch: Beginner (A1/A2 level)

Arabic: Beginner (A1/A2 Level)

Hobbies and extracurricular activities

Personal details

Date of birth: 31 March 1985

Civil status: Married

Nationality: Iranian

Swiss permit: Type B (valid till 5 October 2018)

"Additional information and references will be provided upon request"

10 May 2018